Collisionless Plasma Turbulence: Insights from Magnetohydrodynamic and Hall Magnetohydrodynamic Simulations and Observations of the Earth's Magnetosphere

by

Julia E. Stawarz

B.S., University of New Hampshire, 2011

M.S., University of Colorado, 2013

A thesis submitted to the

Faculty of the Graduate School of the

University of Colorado in partial fulfillment

of the requirements for the degree of

Doctor of Philosophy

Department of Astrophysical and Planetary Sciences

2016

This thesis entitled:
Collisionless Plasma Turbulence: Insights from Magnetohydrodynamic and Hall Magnetohydrodynamic Simulations and Observations of the Earth's Magnetosphere
written by Julia E. Stawarz
has been approved for the Department of Astrophysical and Planetary Sciences

_____

Prof. Robert E. Ergun

_____

Dr. Annick Pouquet

_____

Prof. Mark Rast

_____

Prof. Phil Armitage

_____

Prof. Juri Toomre

Date _____

The final copy of this thesis has been examined by the signatories, and we find that both the content and the form meet acceptable presentation standards of scholarly work in the above mentioned discipline.

Stawarz, Julia E. (Ph.D., Astrophysical and Planetary Sciences)

Collisionless Plasma Turbulence: Insights from Magnetohydrodynamic and Hall Magnetohydrodynamic Simulations and Observations of the Earth's Magnetosphere

Thesis directed by Prof. Robert E. Ergun

Turbulence is a ubiquitous phenomenon that occurs throughout the universe, in both neutral fluids and plasmas. For collisionless plasmas, kinetic effects, which alter the nonlinear dynamics and result in small-scale dissipation, are still not well understood in the context of turbulence. This work uses direct numerical simulations (DNS) and observations of Earth's magnetosphere to study plasma turbulence.

Long-time relaxation in magnetohydrodynamic (MHD) turbulence is examined using DNS with particular focus on the role of magnetic and cross helicity and symmetries of the initial configurations. When strong symmetries are absent or broken through perturbations, flows evolve towards states predicted by statistical mechanics with an energy minimization principle, which features two main regimes; one magnetic helicity dominated and one with quasi-equipartition of kinetic and magnetic energy. The role of the Hall effect, which contributes to the dynamics of collisionless plasmas, is also explored numerically. At scales below the ion inertial length, a transition to a magnetically dominated state, associated with advection becoming subdominant to dissipation, occurs. Real-space current, vorticity, and electric fields are examined. Strong current structures are associated with alignment between the current and magnetic field, which may be important in collisionless plasmas where field-aligned currents can be unstable.

Turbulence within bursty bulk flow braking events, thought to be associated with near-Earth magnetotail reconnection, are then studied using the THEMIS spacecraft. It is proposed that strong field-aligned currents associated with turbulent intermittency destabilize into double layers, providing a collisionless dissipation mechanism for the turbulence. Plasma waves may also radiate from the region, removing energy from the turbulence and potentially depositing it in the aurora.

Finally, evidence for turbulence in the Kelvin-Helmholtz instability (KHI) on the Earth's magnetopause is found using data from the Magnetospheric Multiscale (MMS) mission. With MMS, spatial properties, including spatial intermittency and anisotropy, can be examined along with temporal properties and ion and electron velocity spectra can be examined observationally into the kinetic scales. Quasi-two-dimensional anisotropy perpendicular to the magnetic field is found. Field-aligned current instabilities and wave radiation may also be relevant in the KHI.

Dedication

I dedicate this thesis to my parents for all of their support over the course of my graduate, as well as undergraduate careers.

Acknowledgements

I am particularly grateful to my two advisors Bob Ergun and Annick Pouquet. Discussions with them were always enlightening. I am glad to have had the opportunity to learn how to perform numerical simulations from Annick, as well as from Duane Rosenberg, and to have been encouraged to examine the role of turbulence at kinetic scales by Bob. While having two advisors with somewhat different areas of expertise was daunting at times, it was also extremely rewarding. I am also thankful to Bob for offering funding after graduation, while I prepare for my new postdoctoral position at Imperial College London.

I would like to thank all of the people within the group at LASP, particularly Fran Bagenal, Laila Andersson, Stefan Eriksson, Rick Wilder, Rob Wilson, David Malaspina, Katy Goodrich, Andrew Sturner, and Steve Schwartz for all of their help, as well as Raffaele Marino at NCAR. I would also like to gratefully acknowledge the wide variety of co-authors I have had the pleasure to work with over my time in graduate school, and the tremendous amount of work done by the entire THEMIS and MMS teams in order to produce the observational data that was used in this thesis. Finally, I would like to thank my entire thesis committee.

Funding for this work was provided by a National Science Foundation Graduate Research Fellowship (Grant No. DGE 1144083), NASA grants for the THEMIS mission, NASA grant NNX11AD73G, and the NASA MMS project. Numerical computations were performed at the National Center for Atmospheric Research and on the Janus supercomputer at the University of Colorado, Boulder.

Contents

Chapter

Tables

Table

Figures

Figure

Chapter 1

Introduction

Turbulence is a ubiquitous phenomenon that occurs in a variety of systems, ranging from terrestrial environments such as the oceans [*Gargett*, 1989; *D'Asaro*, 2014] and atmosphere [*Riley and Lelong*, 2000; *Staquet and Sommeria*, 2002; *Sun et al.*, 2015] to astrophysical environments such as the solar corona [*Cranmer*, 2009; *Cranmer et al.*, 2015], solar wind [*Matthaeus et al.*, 1995; *Tu and Marsch*, 1995; *Bruno and Carbone*, 2013], planetary magnetospheres [*Borovsky et al.*, 1997; *Borovsky and Funsten*, 2003; *Weygand et al.*, 2005; *Saur et al.*, 2002, 2003], and the interstellar medium [*Falgarone et al.*, 2009; *Falceta-Gonçalves et al.*, 2014]. Despite its pervasiveness and extensive scientific study, turbulent dynamics are still not completely understood. The focus of this work is to examine the behavior of turbulence in systems of charged particles, known as plasmas, with particular interest in applications to collisionless space plasmas. To do this a two-pronged approach is used, employing both numerical simulations and observations of the Earth's magnetosphere from the Time History of Events and Macroscale Interactions During Substorms (THEMIS) and Magnetospheric Multiscale (MMS) satellites. While numerical simulations can be limited in some respects in their ability to accurately describe the physical systems, they allow for a more in depth probing of the dynamics through the examination of quantities that are not easily obtained from observations. Not only that, but the use of simplified plasma approximations, which isolate particular aspects of the physics, can aid in developing an understanding of how individual effects alter the dynamics. Alternatively, the analysis of observational data provides the "ground truth" for any theoretical examination of collisionless plasma turbulence and, since it is often difficult to

accurately simulate turbulence along with all the possible collisionless effects, observations allow one to explore what physics is relevant in the real system and guide additional theoretical inquiries. The following sections of this chapter discuss the relevant conceptual background and provide an outline for the thesis.

1.1 Collisionless Plasmas

Collections of ionized particles, known as plasmas, are present in many space and astrophysical systems. The presence of freely moving electrons and ions means the dynamics of the system are both influenced by and can generate electric (**E**) and magnetic (**B**) fields. Although plasmas are made up of charged particles, at large enough length scales, above what is known as the Debye length, plasmas can generally be considered charge neutral due to nearly equal amounts of positive and negative charge, a property known as quasineutrality. Plasma physics can have important consequences for understanding the dynamics throughout the universe, for example, in extreme environments such as magnetars and supernovae [*Uzdensky and Rightley*, 2014] or in the context of star formation [*McKee and Ostriker*, 2007] and stellar activity [*Nelson et al.*, 2013]. This work focuses on the plasma physics of the near-Earth environment where, for example, the interaction of the solar wind emanating from the Sun with the Earth's magnetic field generates the magnetosphere [*Chapman and Ferraro*, 1931] and changes in solar wind activity can lead to so-called "space weather," which can affect infrastructure at Earth [*Joselyn*, 2001]. Aurora at the Earth [*Ergun et al.*, 2004] and other planets [*Delamere et al.*, 2015] are also a manifestation of plasma dynamics. The wide range of length scales and potentially highly nonlinear dynamics present in many space and astrophysical systems means that turbulence (discussed in more detail in Chapter 1.2) can be important for understanding the dynamics of these systems, particularly as we continue to probe ever smaller length and time scales.

At the most fundamental level, the mathematical description of a plasma involves solving Newton's laws for every particle in the system coupled with Maxwell's equations governing the electric and magnetic fields (as well as, the equations for any other forces that may be relevant

to a given system). However, for large systems this method is cumbersome and a hierarchy of approximations have been developed that have varying degrees of accuracy (see, for example, *Chen* [1984] for an overview of plasma descriptions). At length and time scales larger than the gyromotion associated with ions orbiting **B**, the dynamics of a plasma can be described as a fluid, meaning it is sufficient to consider the statistical behavior of ensembles of particles as opposed to the individual motions of every particle. Two types of fluid approximations are utilized in the numerical work of Chapters 3 and 4; the magnetohydrodynamic (MHD) equations and Hall magnetohydrodynamic (HMHD) equations discussed in further detail in Chapter 2.1. In the MHD equations, ion and electron motions are described as a single fluid, which is coupled to the magnetic field. While HMHD remains a single-fluid description similar to MHD, it incorporates the effects of differing ion and electron motions in the small scales. Some additional fluid models include the two-fluid equations [*Chen*, 1984], where ions and electrons are treated as two coupled fluids and hybrid models [*Harned*, 1982], where the much less massive electrons are treated as a fluid and the ions are treated as particles.

If collisions between particles occur frequently enough, viscous and resistive effects that dissipate energy into heat can occur. However, many space plasmas are nearly collisionless (meaning the frequency of collisions is so rare, they effectively can be neglected) and the fluid approximation breaks down before viscosity and resistivity can dissipate the energy. The breakdown of the fluid approximation means that it is necessary to resolve the individual particle motion and leads to so-called "kinetic" effects, which can alter the dynamics and result in alternative mechanisms for the dissipation of energy. One example, is the instability of currents aligned with **B**, which become unstable as a result of kinetic effects and can generate electrostatic waves and nonlinear kinetic structures (see Chapter 2.2.2). Kinetic effects can be described using the Maxwell–Vlasov equations, discussed in Chapter 2.2, which govern the evolution of the distribution of ion and electron particle velocities in the presence of electromagnetic fields. Note that the Maxwell–Vlasov equations also include the effects described by the fluid approximations.

1.2 Turbulence

The study of turbulence has a long history, particularly in hydrodynamics [e.g. *Reynolds*, 1883; *Richardson*, 1926; *Taylor*, 1938; *Kolmogorov*, 1941]. Turbulent environments are characterized by strong nonlinearities that dominate over dissipation for a wide range of scales. The highly nonlinear dynamics lead to complex, unpredictable behavior and the transfer of energy to different length scales. The need to resolve a wide range of scales with relatively little dissipation makes fluid models like MHD a useful tool for studying the large scales of plasma turbulence and it has been shown that fluid descriptions can capture some of the essential physics of collisionless plasma turbulence [e.g. *Zeldovich and Ruzmaĭkin*, 1987; *Matthaeus et al.*, 2003, 2015; *Wu et al.*, 2013; *Parashar et al.*, 2015].

In the classic theory of turbulence, energy is transferred to incrementally smaller length scales until dissipation can dominate over the nonlinear interactions. The dynamics of turbulent flows can be divided into three general regimes; (1) the large "driving scales" where energy is injected into the system, (2) the "inertial range" where nonlinear dynamics dominate and energy cascades to smaller scales in an energy conserving manner, and (3) the "dissipation range" where dissipation of energy becomes more important than the nonlinear dynamics [*Pope*, 2000, and references therein]. Turbulence therefore provides a means through which energy can be dissipated in systems where dissipation would otherwise be considered insignificant. In the context of collisionless plasmas, the transfer of energy to the small scales means that turbulence may be important for understanding the observed kinetic scale behavior of plasmas. In some cases, such as two-dimensional (2D) hydrodynamics [*Kraichnan*, 1967] or MHD [*Frisch et al.*, 1975; *Pouquet et al.*, 1976], it is also possible for energy or other conserved quantities, such as the magnetic helicity, to be transferred from small to large scales, referred to as an inverse cascade. Inverse cascades can be important for dynamos, where large-scale magnetic fields are built up from small-scale perturbations [*Brandenburg and Subramanian*, 2005].

Kolmogorov [1941] showed that the distribution of energy as a function of wavenumber k,

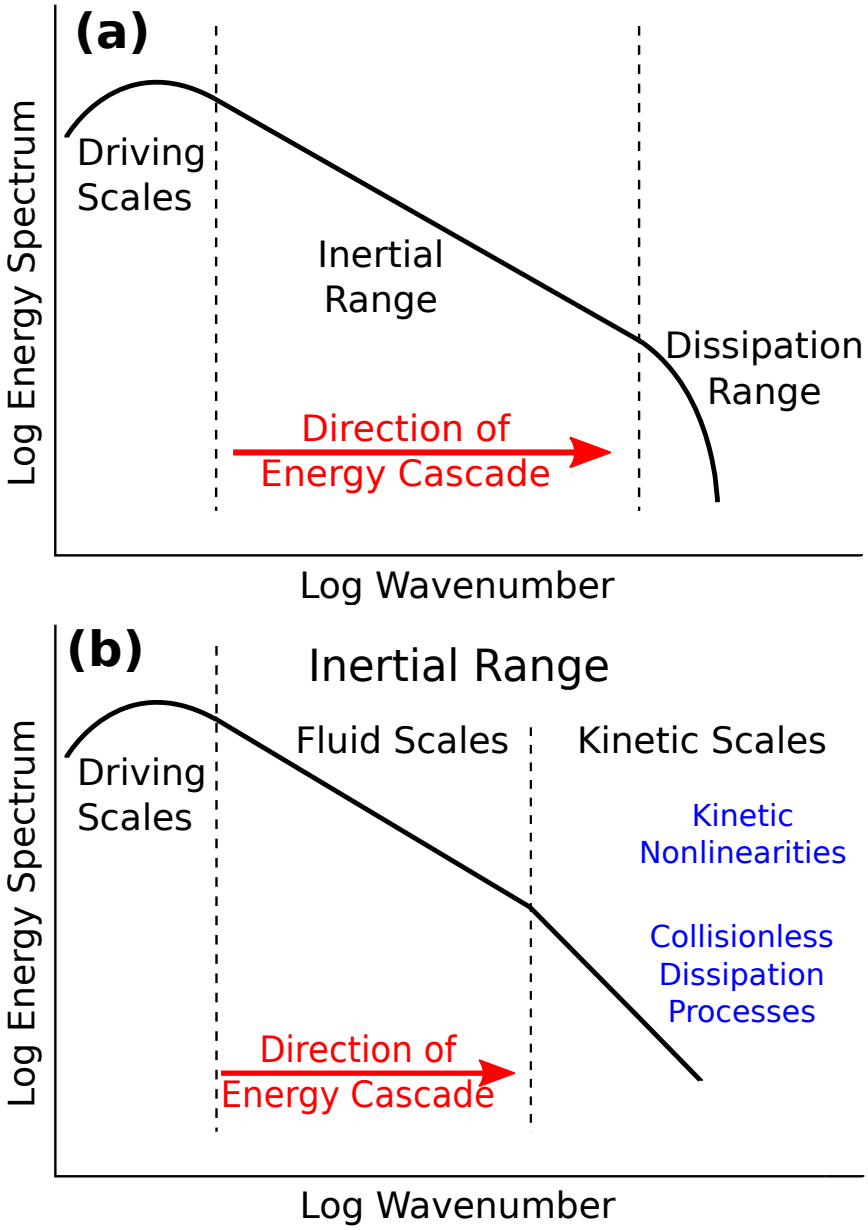

Figure 1.1: (a) Diagram of the energy spectrum in the classic theory of turbulence in which collisional viscosity provides dissipation. (b) Energy spectrum diagram for collisionless plasma turbulence. At kinetic scales, changes in power law are expected due to changes in the nonlinear dynamics and ultimately collisionless processes provide dissipation. Multiple changes in power law and different behavior of the magnetic field, electric field, or velocities could occur at kinetic scales and are not included in this simplified diagram. While these diagrams show energy cascading from small to large wavenumbers, it is also possible in some cases to have inverse cascades from large to small wavenumbers.

known as the energy spectrum, within the inertial range of hydrodynamic turbulence follows a power law, scaling as $k^{-5/3}$. Figure 1.1a shows a schematic representation of the energy spectrum in hydrodynamic turbulence with the three regions labeled. The power law nature of the inertial range spectrum is a feature that carries over into plasma turbulence theory; however, as is discussed in Chapter 2.3.1, the exact exponent can vary depending on the physics of the nonlinear interactions.

Understanding how kinetic processes interact with a turbulent environment is currently an active area of research [*Kiyani et al.*, 2015] and from a numerical standpoint is made difficult by the computational challenges associated with both obtaining the large scale separations inherent to turbulent flows, and accurately describing the kinetic scales of the plasma. However, some aspects of turbulent kinetic dynamics are anticipated. Nonlinearities associated with turbulence are thought to be important down into the kinetic scales [*Sahraoui et al.*, 2009, 2010; *Karimabadi et al.*, 2013]. Kinetic effects can result in observed changes to the power law of the energy spectrum and ultimately contribute to the dissipation of energy from the turbulence [*Leamon et al.*, 1999; *Bale et al.*, 2005; *Howes et al.*, 2011; *Biskamp et al.*, 1996; *Gary et al.*, 2010; *Kasper et al.*, 2008; *Alexandrova et al.*, 2013]. As an example, the Hall effect is expected to steepen the magnetic component of the energy spectrum to $k^{-7/3}$ at scales smaller than the ion inertial length [*Ghosh et al.*, 1996; *Galtier*, 2006]. As will be seen in Chapters 5 and 6, the spectrum for other quantities can have different behavior than the **B** spectrum. For example, **E** spectra tend to become shallower at kinetic scales, while **B** spectra steepen. Figure 1.1b shows a simplified diagram of the energy spectrum with the addition of kinetic effects. Inertial range dynamics may continue within the kinetic scales. However, kinetic effects are ultimately responsible for dissipation, although the exact signatures of kinetic dissipation in the spectrum are not entirely known.

Turbulence is also known to generate intense coherent structures known as intermittency (see Chapter 2.3.2), as have been studied in MHD [*Politano et al.*, 1995; *Sorriso-Valvo et al.*, 2000; *Mininni et al.*, 2006a; *Greco et al.*, 2009] and kinetic [*Karimabadi et al.*, 2013; *Matthaeus et al.*, 2015] simulations. In plasmas, intermittent structures include intense, thin current sheets or other strong gradients. Signatures of intermittency have also been observed in space plasmas [*Burlaga*, 1991;

Sorriso-Valvo et al., 1999; *Weygand et al.*, 2005; *Abramenko*, 2008; *Bruno and Carbone*, 2013]. Intermittency, particularly in the currents, is thought to have an important role in collisionless plasma turbulence, where it can set up configurations favorable for kinetic scale phenomena. The tangling of the magnetic field by turbulence can drive magnetic reconnection and the likely locations would be intermittent current sheets [*Matthaeus and Lamkin*, 1986; *Servidio et al.*, 2010; *Donato et al.*, 2012; *Osman et al.*, 2014]. Intermittency may also be linked to collisionless dissipation and the formation of kinetic scale instabilities associated with field-aligned currents (as explored in this work) or temperature anisotropy [*Osman et al.*, 2012, 2013; *Wan et al.*, 2012; *TenBarge and Howes*, 2013]. The implications of intermittency for the kinetic scales and its role in collisionless dissipation is one topic explored in this thesis.

Traditionally, turbulence theory utilizes assumptions such as statistical homogeneity and isotropy of the turbulent fluctuations; however, plasma turbulence can potentially violate these assumptions. The presence of a strong background magnetic field can introduce anisotropy to the turbulent fluctuations [*Fyfe and Montgomery*, 1976; *Galtier et al.*, 2000, 2002; *Goldreich and Sridhar*, 1995; *Matthaeus et al.*, 1990; *Weygand et al.*, 2009]. Inhomogeneities in the plasma could take the form of large-scale velocity shears, as explored in the solar wind [*Wan et al.*, 2009, 2010; *Stawarz et al.*, 2011], or confined regions of turbulence that could loose energy through the radiation of waves [*Klimchuk*, 2006; *Karimabadi et al.*, 2013; *Lecoanet and Quataert*, 2013]. In this work, the possibility of plasma wave radiation in the context of magnetospheric turbulence is considered.

1.3 Earth's Magnetosphere

The observational studies performed in Chapters 5 and 6 use satellite data from the Earth's magnetosphere. The magnetosphere is the region of space carved out of the solar wind by the Earth's magnetic field [*Chapman and Ferraro*, 1931]. Because plasmas interact with magnetic fields, Earth's magnetic field acts as an obstacle to the flow of plasma emanating from the Sun and the flow is deflected around the Earth. The solar wind is supersonic and super-Alfvénic and therefore a bow shock forms upstream of Earth, which slows the flow before the plasma encounters

the magnetosphere. The region of slowed solar wind, also referred to as shocked solar wind, is known as the magnetosheath and the boundary between the magnetosheath and magnetospheric plasma is known as the magnetopause. The solar wind interaction compresses what would otherwise be Earth's nearly dipolar field on the dayside and stretches it out on the nightside.

At the subsolar magnetopause, magnetic reconnection can occur, where the connectivity of magnetic field lines change and link magnetospheric magnetic field to the solar wind magnetic field. Magnetic reconnection allows for the transfer of plasma between the solar wind and magnetosphere and releases magnetic tension. The motion of the solar wind drags the newly reconnected field lines over the Earth forming a long "magnetotail" behind Earth. The build-up of magnetic flux in the magnetotail results in reconnection in the tail and the release of magnetic energy transports magnetic flux and plasma back towards Earth and around to the dayside where the process can repeat. This cycle of magnetic reconnection in the magnetosphere is referred to as the Dungey cycle [*Dungey*, 1961].

The equatorial region of the magnetotail contains a slab of hot plasma, which stretches down the tail known as the plasma sheet. At the center of the plasma sheet, the stretched out magnetic field changes direction from Earthward to anti-Earthward driving a current across the magnetotail. This region is known as the neutral sheet and is where tail reconnection occurs. Above and below the plasma sheet are the lobes, which have very low plasma densities and very high magnetic field strength.

1.3.1 Bursty Bulk Flows

Bursty bulk flow (BBF) events are high-speed bulk flows observed in Earth's plasma sheet [*Baumjohann et al.*, 1990; *Angelopoulos et al.*, 1992]. The flows have velocities ranging from hundreds of km/s up to in excess of 1000 km/s and often occur pre-midnight with velocities dominantly in the Earthward direction (although farther down tail similar anti-Earthward flows could also occur). BBFs are observed as bursts in time [*Angelopoulos et al.*, 1992], with durations of about 10 minutes indicating they are spatially localized in the direction of the flow. *Angelopoulos et al.* [1996]

argued based on energy flux arguments that the cross section perpendicular to the flow should be 1–2 R_E^2 and *Angelopoulos et al.* [1997] inferred a scale size in the east-west direction across the tail of < 3 R_E based on multipoint measurements from closely spaced satellites.

BBF events can have a significant impact on the magnetosphere, with an observed positive correlation between the occurrence rate of BBFs and geomagnetic activity [*Baumjohann et al.*, 1990; *Angelopoulos et al.*, 1994]. Even though these flows are bursty, constituting only a small fraction of the observations, they can contribute a large fraction of the observed mass, energy, and magnetic flux transport towards Earth in the magnetotail [*Angelopoulos et al.*, 1994]. An understanding of the evolution of BBF events is therefore important in understanding the dynamics of the magnetosphere as a whole.

The exact source of BBF events has not been definitively established; however, they are thought to be reconnection jets generated by near-Earth magnetic reconnection in the tail at distances greater than approximately 20 R_E [*Baumjohann et al.*, 1990; *Chen and Wolf*, 1993]. BBF events are associated with the dipolarization of the magnetic field (i.e. the depletion of the stretched component in favor of the dipolar component) [*Angelopoulos et al.*, 1992]. As the flow nears Earth, force balance between the pressure of the dipolar field close to Earth and magnetic tension of the stretched field driving the flow causes the BBF to slow and deflect [*Shiokawa et al.*, 1997]. The region over which the flow is slowed and diverted is referred to as the BBF braking region.

The process of flow braking can generate fluctuations and turbulence within the region. Observations [*Panov et al.*, 2010] and MHD simulations [*Birn et al.*, 2011] show the braking of such flows can result in the rebounding of the flow tailward and the development of large-scale vortices. BBF events and BBF braking events have been associated with instabilities and turbulent fluctuations using both observations and simulations [*Swift and Lin*, 2001; *Shiokawa et al.*, 2005; *Volwerk et al.*, 2007; *Vörös et al.*, 2004, 2007; *El-Alaoui et al.*, 2013]. Evidence for fluctuations exhibiting properties of MHD scale and kinetic scale Alfvén waves that may be participating in a turbulent cascade have been found associated with BBF events [*Chaston et al.*, 2012, 2014].

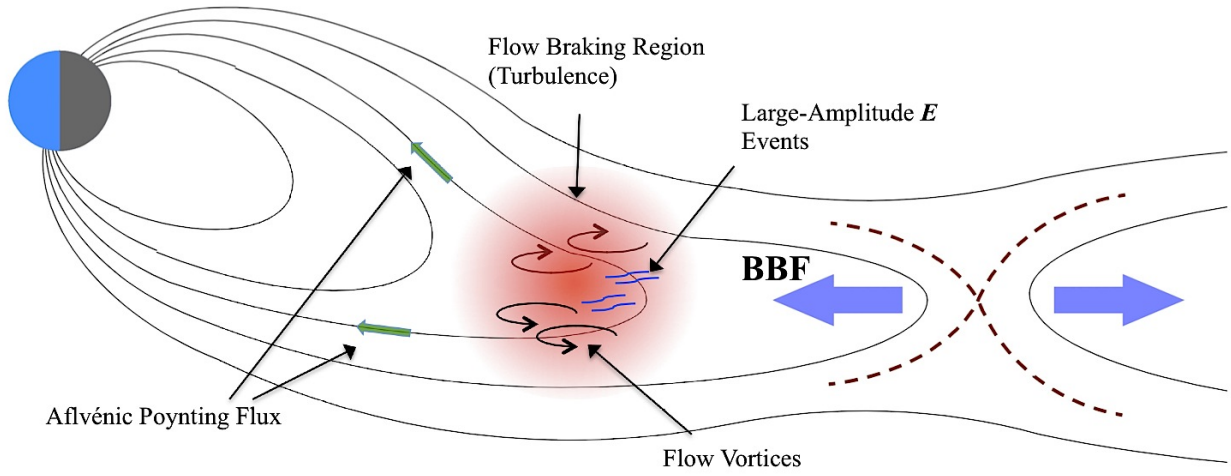

Figure 1.2: Diagram of the evolution of a BBF event as discussed by *Ergun et al.* [2015] and in Chapter 5. BBFs are generated by the magnetic tension released from reconnection in the tail. Near Earth the flow brakes, generating flow vortices and turbulence. The turbulence generates intermittency in the form of strong localized magnetic-field-aligned currents, which destabilize into large-amplitude **E** structures. Alfvénic Poynting flux radiates from the region along the magnetic field towards the Earth's auroral region.

Whistler waves are also associated with dipolarization fronts [*Nishimura et al.*, 2008]. For a review of magnetic field fluctuation observations throughout the Earth's magnetotail see *Zelenyi et al.* [2014].

A number of energy channels are available for the transfer or dissipation of energy from BBF events, which are considered in Chapter 5. One of these is adiabatic heating of ions and electrons through the conservation of magnetic moment as the magnetic field strength increases in the equatorial region. A second, which may be of geophysical significance, is the propagation of Alfvén waves out of the BBF braking region and along magnetic field to the auroral region where they can participate in auroral dynamics. A third path may be the deflection of flow out of the braking region and a fourth path is the dissipation of energy through a turbulent cascade, within the braking region itself. In Chapter 5 the role of turbulent intermittency in generating observed large-amplitude **E** structures (see Chapters 2.2.2 and 5.1) is considered. A diagram outlining the evolution of a BBF event from the reconnection site to the BBF braking region is shown in Figure 1.2.

1.3.2 The Kelvin-Helmholtz Instability

The Kelvin-Helmholtz instability (KHI) is a velocity shear driven instability that can occur in hydrodynamics, as well as in plasmas [e.g. *Chandrasekhar*, 1961; *Miura and Pritchett*, 1982]. The KHI is known to occur on the equatorial flanks of the Earth's magnetopause (see diagram in Figure 1.3) [e.g. *Hasegawa et al.*, 2004]. As the solar wind deflects around the magnetosphere a velocity shear can form across the magnetopause with a tailward flow in the magnetosheath and a nearly stationary flow in the magnetosphere. The magnetic tension associated with a component of **B** in the plane of the velocity shear provides a stabilizing force and, therefore the most unstable configuration occurs when **B** is in the direction perpendicular to the velocity shear (although, a strong enough shear can overcome an in-plane **B**). The development of the KHI on the surface of the magnetopause begins as an anti-sunward propagating surface wave, which "rolls-up" into a train of vortices in the wave's nonlinear phase. The KHI is also believed to be important for coupling

the magnetospheres of Jupiter and Saturn to the solar wind. In the case of Jupiter and Saturn, strong rotation of the magnetospheric plasma induced by the rotation of the planet's magnetic field can enhance or reduce the velocity shears on opposite sides of the magnetosphere resulting in asymmetry [*Masters et al.*, 2010; *Desroche et al.*, 2012; *Delamere et al.*, 2013].

The presence of the KHI can have consequences for the coupling of the magnetosphere to the magnetosheath; leading to magnetic reconnection even for northward interplanetary magnetic field where the magnetosheath and magnetospheric fields are nearly parallel and allowing momentum and mass transport across the magnetopause [e.g. *Nykyri and Otto*, 2001; *Nakamura et al.*, 2013; *Nakamura and Daughton*, 2014; *Kavosi and Raeder*, 2015]. Magnetic reconnection can occur at current sheets formed in several areas of the KHI. The presence of even a small in-plane **B** with shear in the direction of **B** across the boundary can form strong compressed current sheets at regions of converging flow between each of the vortices resulting in the formation of periodic current sheets along the train of vortices. Periodic current sheets are a common signature of the KHI in observations (see Chapter 6). Reconnection on these periodic current sheets is sometimes referred to as "type I" reconnection [*Pu et al.*, 1990; *Nakamura et al.*, 2013]. So-called "type II" reconnection occurs on current sheets formed by the in-plane components of **B** that get wrapped-up inside the vortices [*Nykyri and Otto*, 2001; *Nakamura and Fujimoto*, 2005; *Faganello et al.*, 2008].

KHI simulations show the development of turbulence within the vortices, which is thought to be driven by secondary instabilities that form as the KH vortices roll-up [*Karimabadi et al.*, 2013; *Nakamura and Daughton*, 2014; *Daughton et al.*, 2014]. In the later stages of development, a layer of turbulence can form that envelops the train of vortices. Turbulence provides a pathway for the transfer of energy from the large-scale KH vortices to small scales where collisionless processes can lead to dissipation and particle heating. Simulations show that turbulence aids in plasma mixing within the KHI [*Matsumoto and Hoshino*, 2004; *Matsumoto and Seki*, 2010]. The tangling of magnetic fields due to turbulence may also lead to additional reconnection sites in the KHI, which may be similar to the type II reconnection described above [*Servidio et al.*, 2010; *Donato et al.*, 2012]. While some observational studies suggest the presence of turbulence [*Chaston et al.*,

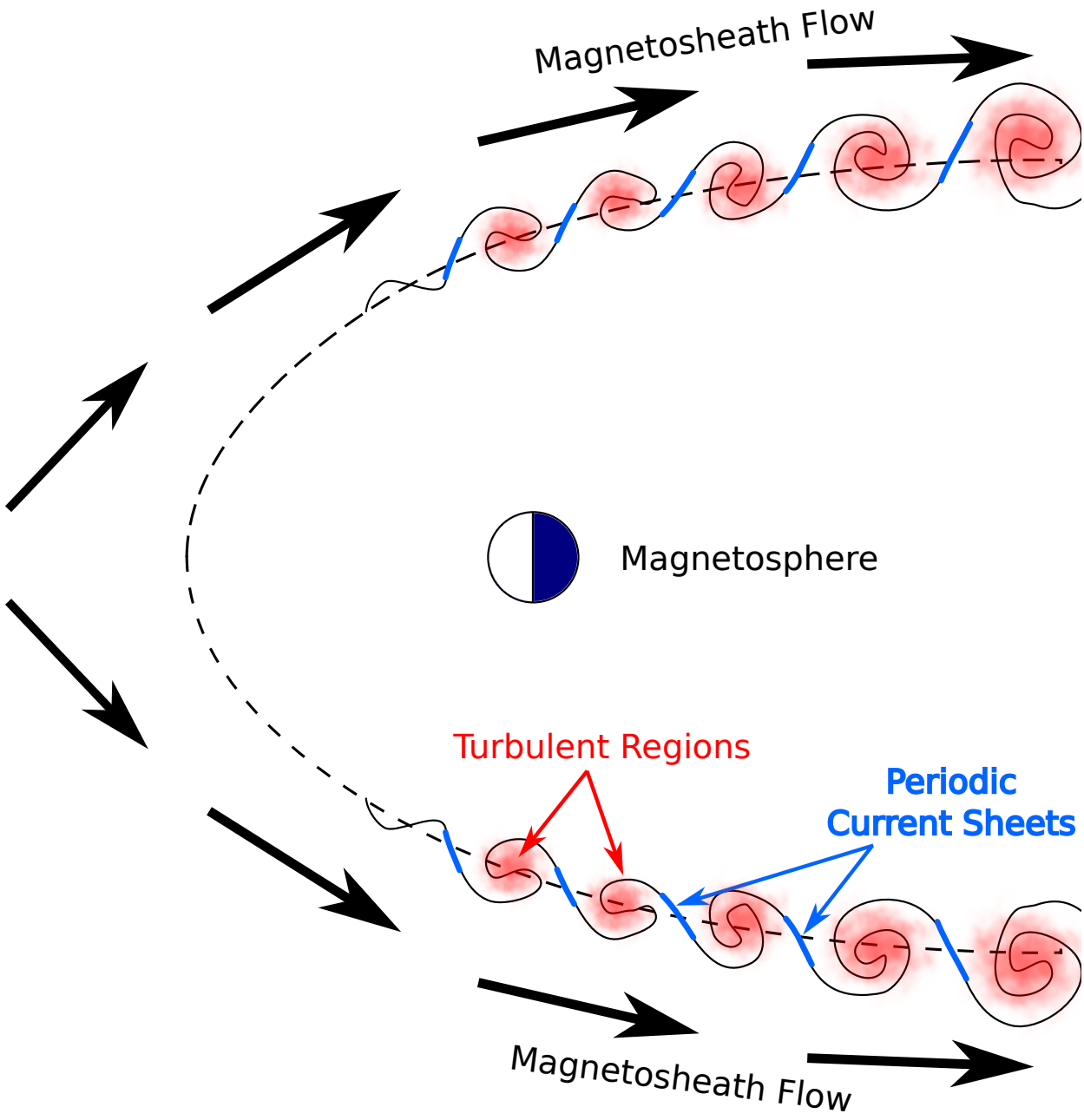

Figure 1.3: Diagram of the Kelvin-Helmholtz instability on the flanks of Earth's magnetopause as viewed looking down at the equatorial plane. The dashed line is the unperturbed magnetopause. Arrows show the magnetosheath flow deflected around the magnetosphere, which creates a relative shear with the nearly stationary magnetospheric flow and drives the KHI. As the KHI surface wave propagates down-tail, it rolls up into vortices. Periodic current sheets can form between the vortices and secondary instabilities within the vortices can drive turbulence.

2007a; *Hwang et al.*, 2011], extensive observational examination of the properties of KHI related turbulence has not been performed previously and is explored in Chapter 6.

1.4 The THEMIS and MMS Missions

Two multi-spacecraft missions are used for the observational studies in this thesis; the THEMIS and MMS missions. Both missions orbit the Earth and are mainly located within the Earth's magnetosphere. The formation of the THEMIS mission is configured with relatively large separations between the spacecraft so as to examine the large-scale dynamics of the magnetosphere. The MMS spacecraft, on the other hand, orbit such that they have a tight formation aimed at examining small-scale plasma dynamics.

1.4.1 THEMIS

The THEMIS mission [*Angelopoulos*, 2008], which launched on February 17, 2007, consists of five identical spacecraft, referred to as THEMIS A–E. The THEMIS orbits are highly elliptical with apogees arranged in the order THEMIS B (31 R_E), THEMIS C (20 R_E), THEMIS D (12 R_E), THEMIS E (12 R_E), and THEMIS A (10 R_E). Due to the orbital periods, once every 4 days at least 4 of the spacecraft align at apogee during the prime mission. As the Earth orbits the Sun, the apogees rotate around the Earth, going from the nightside (magnetotail) to the dayside and back again. In 2011, the outer two THEMIS spacecraft were removed from the THEMIS configuration and diverted to the Moon forming the ARTEMIS mission [*Angelopoulos*, 2011]. In this work, THEMIS data from the magnetotail are used to study the BBF braking region.

The instruments on the THEMIS spacecraft include the Fluxgate Magnetometer (FGM) measuring low-frequency magnetic fields up to frequencies of 64 Hz [*Auster et al.*, 2008], Search-Coil Magnetometer (SCM) measuring high-frequency magnetic fields from 0.1 Hz to 4 kHz [*Roux et al.*, 2008], Electric Field Instrument (EFI) measuring electric fields with frequencies up to 8 kHz [*Bonnell et al.*, 2008], Electrostatic Analyzer (ESA) measuring ion and electron particle distributions from 5 eV to 25 keV for ions and 5 eV to 30 keV for electrons [*McFadden et al.*, 2008a], and the

Solid State Telescope (SST) measuring ion and electron particle distributions from 25 keV to 6 MeV for ions and 25 keV to 1 MeV for electrons. The distributions from the ESA and SST can be used to compute fluid moments such as densities, flow velocities, and temperatures.

Data from the THEMIS spacecraft are sent to Earth in 4 data rate modes. Low time resolution "Slow Survey" and "Fast Survey" data are available over long periods of time. The nominally available data is Slow Survey and the data rate transitions to Fast Survey during spacecraft conjunctions. Two high resolution data rates known as "Particle Burst" and "Wave Burst" are also available, which are triggered by on-board algorithms. Particle Bursts are roughly 10 minute long segments of data measuring electric and magnetic fields every 1/128 seconds and particle distributions every 3 seconds. In the magnetotail, Particle Bursts are triggered by enhancements in the B_z component and therefore triggers mainly on dipolarization events. Wave Bursts are seconds to tens of seconds in length providing electric and magnetic field measurements every 1/8192 seconds. Wave bursts can be triggered during the Particle Bursts based on the amplitudes of the fields. Due to telemetry constraints, the Wave Burst data is limited in occurrence.

1.4.2 MMS

The MMS mission [*Fuselier et al.*, 2014; *Burch et al.*, 2015] was recently launched on March 12, 2015 and is made up of four identical spacecraft referred to as MMS1–MMS4. Currently, all four spacecraft are in elliptical orbits with apogee at 12 R_E in order to study magnetic reconnection on the dayside magnetopause. As the apogee rotates around the Earth, MMS encounters the flanks of the magnetosphere where the KHI can occur (studied in this work), as well as the sub-solar magnetopause and magnetotail. Later in the mission in 2017, the apogee of the spacecraft will be raised to 25 R_E in order to examine reconnection in the magnetotail. Near apogee the MMS spacecraft orbit in a tetrahedral formation. At different times during the mission, the distance between spacecraft in this formation ranges from roughly 160 km down to 10 km.

The FIELDS instruments [*Torbert et al.*, 2014] on MMS include the Fluxgate Magnetometers (FGM) [*Russell et al.*, 2014] measuring low-frequency magnetic fields up to 64 Hz, the Search-Coil

Magnetometer (SCM) [*Le Contel et al.*, 2014] measuring high-frequency magnetic fields from 1 Hz to 6 kHz, and the Electric Field Double Probes (EDP) [*Ergun et al.*, 2014; *Lindqvist et al.*, 2014] capable of measuring electric fields with frequencies up to 100 kHz. The Fast Plasma Instrument (FPI) [*Pollock et al.*, 2016] is also used in this work and measures ion and electron distribution functions from 10 eV to 30 keV.

MMS data is also available in several data rate modes. Two low time resolution survey modes are available referred to as "Slow Survey" and "Fast Survey." Fast Survey data is collected for roughly half of each orbit around apogee. Burst data is also available, but unlike THEMIS which used automated triggers, MMS uses manual selections based on the Fast Survey data made by a "scientist-in-the-loop" (SITL) [*Baker et al.*, 2015]. The burst data provides electric and magnetic field measurements every 1/8192 seconds, electron distributions and moments every 30 ms, and ion distributions and moments every 150 ms.

The objective of the MMS mission is to study the kinetic scale behavior of plasmas in and around the magnetosphere, with particular emphasis on the phenomenon of magnetic reconnection. To achieve this goal, MMS makes use of the extraordinarily high time resolution and small-scale spatial formation described above. These capabilities also make MMS an excellent mission for exploring the kinetic scales of plasma turbulence. Because turbulence transports energy to small-scales and can drive kinetic scale phenomena, a better understanding of turbulence will likely aid in interpreting the data obtained from MMS. As such, it is necessary to extend our understanding of turbulence using theoretical and numerical approaches that go beyond the MHD framework.

1.5 Outline

In Chapter 2, the theoretical background necessary for understanding this work is presented. Various sets of equations that can be used to describe plasmas are discussed in Chapters 2.1 and 2.2. The equations focused on are the MHD and HMHD equations, which are used in the numerical simulations of Chapters 3 and 4. The Maxwell-Vlasov equations also are discussed with particular focus on the linear wave solutions and current instabilities, which are used in examining observation

from the Earth's magnetotail. Finally, elements of turbulence theory including strong and weak turbulence, power law predictions, intermittency, and statistical equilibria are shown in Chapter 2.3.

Chapters 3 and 4 present two numerical investigations. The study in Chapter 3 focuses on MHD and examines the question, "What states do decaying turbulent plasmas relax to after long times?" The work builds on previous studies by *Frisch et al.* [1975] and *Stribling and Matthaeus* [1990, 1991], but at significantly higher spatial resolutions (meaning more turbulent environments). The effect of small perturbations on highly symmetric initial configurations is also examined. Results from Chapter 3 have been published in *Stawarz et al.* [2012]. Chapter 4 looks at the HMHD equations numerically, along with analogous MHD runs for comparison, in order to understand how the Hall effect alters the turbulent dynamics in the small-scales of collisionless plasmas. The behavior is examined both in Fourier space and in configuration (real) space. Results from Chapter 4 have been published in *Stawarz and Pouquet* [2015]

In Chapters 5 and 6 two observational studies are performed. Chapter 5 uses THEMIS data to examine turbulence in the BBF braking region, focusing on the role of intermittency in setting up field-aligned current instabilities that can create kinetic structures observed in the region. The radiation of plasma waves from the region is also discussed. Results from Chapter 5 have been published in *Stawarz et al.* [2015]. Chapter 6 presents observational evidence for turbulence in a KHI event using MMS data. Both the temporal and spatial characteristics of the turbulence are examined. Similar to the BBF braking region, intermittent field-aligned currents and wave radiation may be important in the KHI. Results from Chapter 6 are submitted for publication in *Stawarz et al.* [2016]. Chapter 7 summarizes the conclusions of all of the studies and discusses future work.

Chapter 2

Plasma and Turbulence Theory

In this chapter, the mathematical framework used by the studies in the following chapters is discussed; beginning with the fluid approximations in Chapter 2.1, the kinetic Maxwell-Vlasov equations in Chapter 2.2, and finally elements of turbulence theory in Chapter 2.3. In this work, the plasma is taken to consist of only protons and electrons. The subscript i is used to denote ion specific quantities and a subscript e denotes electron specific quantities.

In analyzing the equations, it is often useful to consider the Fourier transforms of quantities, which decomposes the domain into an orthonormal basis of sine and cosine functions. The spatial transform is of particular interest in turbulence and the Fourier transform of a function $g(\mathbf{x})$ is defined such that

$$g(\mathbf{k}) = \int_{-\infty}^{\infty} g(\mathbf{x}) e^{-i\mathbf{k}\cdot\mathbf{x}} d^3\mathbf{x} \tag{2.1}$$

$$g(\mathbf{x}) = \int_{-\infty}^{\infty} g(\mathbf{k}) e^{i\mathbf{k}\cdot\mathbf{x}} d^3\mathbf{k} \tag{2.2}$$

where $i = \sqrt{-1}$ and $\mathbf{k}$ is the wavevector. Here the Fourier transform has been written for an infinite and continuous domain, which is useful for theoretical work. However, a discrete formulation defined on finite domain sizes is also available, which is useful in applying Fourier transforms to simulation or observational data, and is discussed in Appendix A.1. Similarly, a temporal Fourier transform, which is of particular importance when considering linear wave solutions, can be defined such that

$$g(\omega) = \int_{-\infty}^{\infty} g(t) e^{i\omega t} dt \tag{2.3}$$

$$g(t) = \int_{-\infty}^{\infty} g(\omega) e^{-i\omega t} d\omega \tag{2.4}$$

where ω is the angular frequency, which is related to the ordinary frequency by $\omega = 2\pi f$.

2.1 Magnetohydrodynamics and Hall Magnetohydrodynamics

The numerical studies in Chapters 3 and 4 make use of the incompressible MHD and HMHD equations with a uniform mass density ρ. The 0–order fluid moment equation describes the evolution of ρ (conservation of mass) and is given by

$$\frac{D\rho}{Dt} + \rho\nabla\cdot\mathbf{u} = 0 \tag{2.5}$$

where $D/Dt = \partial/\partial t + \mathbf{u}\cdot\nabla$ is the convective derivative operator describing the Lagrangian time rate of change of a quantity along the flow trajectory and $\mathbf{u}$ is the fluid velocity. In the incompressible approximation, $D\rho/Dt = 0$ resulting in the incompressibility condition

$$\nabla\cdot\mathbf{u} = 0. \tag{2.6}$$

A convenient way to express the incompressible single fluid equations is in Alfvén units, where the magnetic field is expressed in units of velocity such that $\mathbf{b} = \mathbf{B}/\sqrt{\mu_0\rho}$ with μ_0 the vacuum permeability. The current $\mathbf{J}$ in Alfvén units is given by $\mathbf{j} = \mathbf{J}\sqrt{\mu_0/\rho}$ and the electric field is given by $\mathbf{e} = \mathbf{E}/\sqrt{\mu_0\rho}$. In addition to Eq. 2.6, the incompressible MHD and HMHD systems can be described by the equations

$$\frac{\partial\mathbf{b}}{\partial t} = \nabla\times(\mathbf{u}\times\mathbf{b}) - d_i\nabla\times(\mathbf{j}\times\mathbf{b}) + \eta\nabla^2\mathbf{b} - \eta'\nabla^4\mathbf{b} \tag{2.7}$$

$$\frac{\partial\mathbf{u}}{\partial t} = -\mathbf{u}\cdot\nabla\mathbf{u} - \frac{1}{\rho}\nabla P + \mathbf{j}\times\mathbf{b} + \nu\nabla^2\mathbf{u} - \nu'\nabla^4\mathbf{u} \tag{2.8}$$

$$\nabla\cdot\mathbf{b} = 0 \tag{2.9}$$

where P is the particle pressure and $\mathbf{j} = \nabla\times\mathbf{b}$ is the current. The ion inertial length is denoted by $d_i = \sqrt{m_i/(\mu_0 q^2 n)}$ with m_i the proton mass, q the proton charge, and n the particle number density. By setting $d_i = 0$, the MHD equations are obtained, whereas $d_i \neq 0$ gives the HMHD equations. The advection term can alternatively be written as $-\mathbf{u}\cdot\nabla\mathbf{u} = \mathbf{u}\times\boldsymbol{\omega} - \nabla|\mathbf{u}|^2$, where $-\nabla|\mathbf{u}|^2$ can be incorporated into the pressure term and $\boldsymbol{\omega} = \nabla\times\mathbf{u}$ is the vorticity. From Faraday's

Law, $\mathbf{e}$ is related to the time derivative of the magnetic vector potential $\mathbf{a}$, where $\mathbf{b} = \nabla \times \mathbf{a}$, such that

$$\mathbf{e} = -\mathbf{u} \times \mathbf{b} + d_i \mathbf{j} \times \mathbf{b} + \eta \mathbf{j} - \eta' \nabla^2 \mathbf{j}. \tag{2.10}$$

In Eq. 2.7 and 2.8, two types of dissipative terms have been included, which will be used in the simulations of Chapters 3 and 4. The dissipation coefficients ν and η are the traditional kinematic viscosity and magnetic diffusivity respectively, whereas ν' and η' are hyperviscosity and hyperdiffusivity coefficients respectively associated with Laplacian–squared dissipative terms. In the numerical studies, $\nu = \eta$, $\nu' = \eta'$, and only one form of dissipative term is used in any given run (that is to say if $\nu \neq 0$, then $\nu' = 0$ and vice versa). In Chapter 3, the MHD system is considered and only the $\nu\nabla^2\mathbf{u}$ and $\eta\nabla^2\mathbf{b}$ dissipative terms are used. In Chapter 4, both HMHD and MHD are considered and in the HMHD case the $\nu'\nabla^4\mathbf{u}$ and $\eta'\nabla^4\mathbf{b}$ are employed, as well.

The reason for using the hyperdiffusive terms in HMHD is because the timescale associated with the Hall term dimensionally scales as k^{-2}, which is the same as the scaling for the diffusive timescale associated with Laplacian dissipation. As such, it has been suggested that from a numerical perspective utilizing hyperdiffusivity may produce better results, in that it will allow dissipation to cut in more sharply in the small scales resulting in a better developed HMHD inertial range [*Ghosh et al.*, 1996; *Birn et al.*, 2001; *Meyrand and Galtier*, 2012]. The results may then be more comparable to the sub-ion scale nonlinear dynamics present in collisionless plasmas, while still providing sufficient dissipation for the numerics.

For $\nu = \eta$, the average energy dissipation in the system for both MHD and HMHD is given by $\nu\Omega_T$, where $\Omega_T = \langle|\mathbf{j}|^2\rangle + \langle|\boldsymbol{\omega}|^2\rangle$ is the total enstrophy. For decaying turbulence, the time at which Ω_T is maximum corresponds to when the turbulence is most fully developed. In the hyperdiffusive case, when $\nu' = \eta'$, the average energy dissipation in the system is given by $\nu'\mathcal{P}_T$ where $\mathcal{P}_T = \langle|\nabla^2\mathbf{b}|^2\rangle + \langle|\nabla^2\mathbf{u}|^2\rangle$ is the total palinstrophy.

By taking the divergence of Eq. 2.8, the incompressible approximation gives a Poisson equa-

tion for P written as

$$\nabla^2 P = \rho \nabla \cdot (-\mathbf{u} \cdot \nabla \mathbf{u} + \mathbf{j} \times \mathbf{b}) \,. \tag{2.11}$$

The physical significance of this Poisson equation is that P instantaneously adjusts to any dynamical changes in the flow, whereas in a compressible system pressure changes would be transmitted by compressive fluctuations such as sound waves. The incompressible equations can therefore be interpreted as the limit where the fluctuations of interest are much slower than the sound speed and the sound speed is effectively infinite.

Defining the characteristic length scale L_c, timescale t_c, velocity $U_c \equiv L_c/t_c$, and pressure $P_c \equiv \rho U_c^2$, the equations can be made dimensionless and the parameters

$$Re \equiv \frac{U_c L_c}{\nu} \,,\; Re' \equiv \frac{U_c L_c^3}{\nu'} \tag{2.12}$$

$$Rm \equiv \frac{U_c L_c}{\eta} \,,\; Rm' \equiv \frac{U_c L_c^3}{\eta'} \tag{2.13}$$

$$\epsilon_H \equiv \frac{d_i}{L_c} \tag{2.14}$$

appear in the equations. Re and Re' are the Reynolds numbers for viscosity and hyperviscosity respectively, Rm and Rm' are the magnetic Reynolds numbers for magnetic diffusivity and hyperdiffusivity, and ϵ_H is the dimensionless ion inertial length.

Since multiple nonlinear terms are present in the system, three distinct "dissipation" scales can be defined by comparing the timescales associated with the nonlinear terms to the dissipation timescale. Using dimensional analysis, the conditions for these scales can be written as

$$\frac{1}{\nu}\sqrt{\frac{E_V(k_A)}{k_A}} = 1, \qquad \frac{E_M(k_L)}{\nu\sqrt{k_L E_V(k_L)}} = 1, \qquad \frac{d_i\sqrt{k_H E_M(k_H)}}{\eta} = 1 \tag{2.15}$$

for traditional viscosity and diffusivity and as

$$\frac{1}{\nu'}\sqrt{\frac{E_V(k_A)}{k_A^5}} = 1, \qquad \frac{E_M(k_L)}{\nu'\sqrt{k_L^5 E_V(k_L)}} = 1, \qquad \frac{d_i}{\eta'}\sqrt{\frac{E_M(k_H)}{k_H^3}} = 1 \tag{2.16}$$

for hyperviscosity and hyperdiffusivity. $E_V(k)$ and $E_M(k)$ are the kinetic and magnetic energy spectra respectively, k_A is the dissipation wavenumber associated with the advection term $(\mathbf{u}\cdot\nabla\mathbf{u})$, k_L is the dissipation wavenumber associated with the Lorentz force $(\mathbf{j}\times\mathbf{b})$, and k_H is the dissipation

wavenumber associated with the Hall term ($d_i \nabla \times [\mathbf{j} \times \mathbf{b}]$). For $\nu = \eta$ or $\nu' = \eta'$, k_A is identical to the dissipation wavenumber for $\nabla \times (\mathbf{u} \times \mathbf{b})$. In MHD, where the Hall term is absent and there is generally near equipartition between magnetic and kinetic energy in the small scales (see Figure 3.6, for example), all of the dissipation scales coincide. The largest of the wavenumbers k_A, k_L, and k_H corresponds to the overall dissipation scale of the system where all nonlinearities are subdominant to dissipation.

The HMHD equations can alternatively be written in the form [*Mahajan and Yoshida*, 1998]

$$\frac{\partial \mathbf{b}}{\partial t} = \nabla \times [(\mathbf{u} - d_i \mathbf{j}) \times \mathbf{b}] + \eta \nabla^2 \mathbf{b} - \eta' \nabla^4 \mathbf{b} \tag{2.17}$$

$$\frac{\partial}{\partial t}(\mathbf{b} + d_i \boldsymbol{\omega}) = \nabla \times [\mathbf{u} \times (\mathbf{b} + d_i \boldsymbol{\omega})] + \nabla^2 [\eta \mathbf{b} + d_i \nu \boldsymbol{\omega}] - \nabla^4 \left[\eta' \mathbf{b} + d_i \nu' \boldsymbol{\omega}\right]. \tag{2.18}$$

In the ideal system (neglecting dissipative terms), the fields $\boldsymbol{\Omega}_R \equiv \mathbf{b}$ and $\boldsymbol{\Omega}_L \equiv \mathbf{b} + d_i \boldsymbol{\omega}$ are frozen into the fields $\mathbf{u}_R \equiv \mathbf{u} - d_i \mathbf{j}$ and $\mathbf{u}_L \equiv \mathbf{u}$ respectively. That is to say, they obey the flux-conservation equations

$$\partial_t \boldsymbol{\Omega}_R = \nabla \times [\mathbf{u}_R \times \boldsymbol{\Omega}_R] \ , \ \partial_t \boldsymbol{\Omega}_L = \nabla \times [\mathbf{u}_L \times \boldsymbol{\Omega}_L] \ . \tag{2.19}$$

The fields $\mathbf{u}_{R,L}$ are equivalent to the HMHD version of the Elsässer variables in the limit $d_i k \gg 1$ [*Galtier*, 2006].

2.1.1 Ideal Invariants

The ideal invariants for the MHD system are the total energy (E_T), magnetic helicity (H_M), and cross helicity (H_C) defined as [*Woltjer*, 1958a,b]

$$E_T = E_V + E_M = \frac{1}{2}\langle |\mathbf{u}|^2 + |\mathbf{b}|^2 \rangle, \qquad H_M = \frac{1}{2}\langle \mathbf{a} \cdot \mathbf{b} \rangle, \qquad H_C = \frac{1}{2}\langle \mathbf{u} \cdot \mathbf{b} \rangle \tag{2.20}$$

where, in this definition of energy, mass has been normalized out for convenience and $\langle ... \rangle$ denotes a volume average. In HMHD, H_C is no longer conserved and instead the generalized helicity defined as

$$H_G = \frac{1}{2}\langle (\mathbf{a} + d_i \mathbf{u}) \cdot (\mathbf{b} + d_i \boldsymbol{\omega}) \rangle = H_M + 2 d_i H_C + d_i^2 H_V \tag{2.21}$$

is conserved [*Turner*, 1986]. $H_V = \langle \mathbf{u} \cdot \boldsymbol{\omega} \rangle / 2$ is the kinetic helicity, which is an invariant in ideal hydrodynamics [*Moffett*, 1969]. While these quantities are no longer conserved in the dissipative system, they play an important role in understanding turbulence because they are conserved by the nonlinear interactions (see for example Chapters 2.3.3 and 3).

Relative helicities are defined as

$$\sigma_M = \frac{\mathbf{a} \cdot \mathbf{b}}{|\mathbf{a}||\mathbf{b}|}, \qquad \sigma_C = \frac{\mathbf{u} \cdot \mathbf{b}}{|\mathbf{u}||\mathbf{b}|}, \qquad \sigma_G = \frac{(\mathbf{a} + d_i \mathbf{u}) \cdot (\mathbf{b} + d_i \boldsymbol{\omega})}{|\mathbf{a} + d_i \mathbf{u}||\mathbf{b} + d_i \boldsymbol{\omega}|}, \qquad \sigma_V = \frac{\mathbf{u} \cdot \boldsymbol{\omega}}{|\mathbf{u}||\boldsymbol{\omega}|} \tag{2.22}$$

and measure the degree of alignment (cosine of angle) between the vectors in the conserved helicities. Additional alignments considered in these studies are

$$\sigma_R = \frac{\mathbf{u}_R \cdot \boldsymbol{\Omega}_R}{|\mathbf{u}_R||\boldsymbol{\Omega}_R|}, \qquad \sigma_L = \frac{\mathbf{u}_L \cdot \boldsymbol{\Omega}_L}{|\mathbf{u}_L||\boldsymbol{\Omega}_L|}, \qquad \sigma_{jb} = \frac{\mathbf{j} \cdot \mathbf{b}}{|\mathbf{j}||\mathbf{b}|}. \tag{2.23}$$

These alignments inform us on the strength of the nonlinear terms appearing in the primitive equations. In Fourier space these alignments are defined using cross-spectra. The magnetic polarization, which measures the direction of circular polarization relative to the magnetic field, is given by $P_M = \sigma_M \sigma_C$ computed in Fourier space. $P_M > 0$ and $P_M < 0$ correspond to left and right circularly polarized fluctuations respectively [*Meyrand and Galtier*, 2012].

2.1.2 Linear Solutions

Linearized wave solutions to the equations can be obtained by decomposing the fields and flow into homogeneous, time-independent backgrounds and infinitesimally small perturbations around the background, such that

$$\mathbf{b}(\mathbf{x}, t) = \mathbf{V}_A + \mathbf{b}_1(\mathbf{x}, t), \quad \mathbf{u}(\mathbf{x}, t) = \mathbf{u}_1(\mathbf{x}, t), \quad P(\mathbf{x}, t) = P_0 + P_1(\mathbf{x}, t), \quad \mathbf{e}(\mathbf{x}, t) = \mathbf{e}_1(\mathbf{x}, t) \tag{2.24}$$

where $\mathbf{V}_A = \mathbf{B}_0 / \sqrt{\mu_0 \rho}$ is known as the Alfvén velocity, subscript 0 denotes the background quantities, and subscript 1 denotes the small perturbations. The background $\mathbf{u}$ and $\mathbf{e}$ are taken to be zero. Applying the decomposition, Fourier transforming, and rearranging the equations results in

$$-\omega \mathbf{u}_1(\mathbf{k}, \omega) \quad = \quad V_A k_{||} \mathbf{b}_1(\mathbf{k}, \omega) - \mathbf{k} \left[\frac{\mathbf{V}_A \cdot \mathbf{b}_1(\mathbf{k}, \omega)}{2} + \frac{P_1(\mathbf{k}, \omega)}{\rho} \right] \tag{2.25}$$

$$-\omega \mathbf{b}_1(\mathbf{k},\omega) = V_A k_{||} \left[\mathbf{u}_1(\mathbf{k},\omega) - i d_i \mathbf{k} \times \mathbf{b}_1(\mathbf{k},\omega)\right] \tag{2.26}$$

$$\mathbf{k} \cdot \mathbf{u}_1(\mathbf{k},\omega) = 0, \quad \mathbf{k} \cdot \mathbf{b}_1(\mathbf{k},\omega) = 0. \tag{2.27}$$

From Eq. 2.27, the solutions are restricted to transverse fluctuations, which omits the compressive branches of the dispersion relations that in MHD give rise to the fast and slow magnetosonic waves. The longitudinal component of Eq. 2.25 sets a relation between the magnetic fluctuations and pressure, while the transverse components of Eq. 2.25 and 2.26 give rise to wave solutions. For MHD, the only wave mode is the Alfvén wave, which satisfies the dispersion relation

$$\omega = V_A k_{||}. \tag{2.28}$$

The Alfvén wave satisfies the relationships

$$\mathbf{b}_1 = \mathbf{u}_1, \quad \mathbf{b}_1 = V_A \mathbf{e}_1 \tag{2.29}$$

and as a result, the Alfvén wave features equipartition between the magnetic and kinetic energy.

The addition of the Hall term breaks the symmetry between right and left circularly polarized fluctuations and the linearized incompressible HMHD equations support two types of wave modes; the right circularly polarized whistler wave and the left circularly polarized ion cyclotron wave described by the dispersion relation [*Sahraoui et al.*, 2006]

$$\omega = V_A k_{||} \frac{k d_i}{2} \left(1 \pm \sqrt{1 + \frac{4}{k^2 d_i^2}}\right) \tag{2.30}$$

where + and − give the whistler and ion cyclotron modes respectively. For the whistler wave $P_M = -1$ and for the ion cyclotron wave $P_M = 1$. At small wavenumbers the two modes merge onto the same dispersion relation consistent with MHD where circular polarization is not a relevant parameter and there is only one wave mode, the Alfvén wave. The linear ratio of magnetic to kinetic energy is given by

$$\frac{E_M(k)}{E_V(k)} = \frac{k^2 d_i^2}{4} \left(\pm 1 + \sqrt{1 + \frac{4}{k^2 d_i^2}}\right)^2 \tag{2.31}$$

with again + or − giving the whistler and ion cyclotron modes respectively. In the limit of $k d_i \gg 1$, the whistler mode is magnetically dominated with $E_M(k)/E_V(k) \approx k^2 d_i^2$ and the ion cyclotron mode is kinetically dominated with $E_M(k)/E_V(k) \approx (k^2 d_i^2)^{-1}$.

An alternative way to "linearize" the HMHD system is if the fluctuations have perfect alignment between u_R and Ω_R and between u_L and Ω_L, which makes all nonlinear terms zero [*Mahajan and Yoshida*, 1998; *Krishan and Mahajan*, 2005]. This type of configuration is referred to as a double curl Beltrami solution and gives equivalent solutions to the small-amplitude linear fields, but for arbitrary amplitude fluctuations. The necessary alignments would need to occur as a result of the nonlinear dynamics and it is not obvious the alignment should occur in any arbitrary turbulent system. The alignments associated with the double curl Beltrami configurations are examined in Chapter 4.

2.2 The Maxwell-Vlasov Equations

The Maxwell-Vlasov equations are used to describe the evolution of collisionless plasmas under the influence of only electromagnetic forces. The system consists of the coupled Vlasov equations describing the evolution of the particle distribution functions for each particle species in the plasma and Maxwell's equations describing the evolution of $\mathbf{E}$ and $\mathbf{B}$. The system of equations can be written (with quantities no longer expressed in Alfvén units) as

$$\frac{\partial F_s}{\partial t} + \mathbf{v}\cdot\nabla F_s + \frac{q_s}{m_s}(\mathbf{E}+\mathbf{v}\times\mathbf{B})\cdot\frac{\partial F_s}{\partial \mathbf{v}} = 0 \tag{2.32}$$

$$\nabla\times\mathbf{E} = -\frac{\partial \mathbf{B}}{\partial t} \tag{2.33}$$

$$\nabla\times\mathbf{B} = \mu_0\mathbf{J} + \epsilon_0\mu_0\frac{\partial \mathbf{E}}{\partial t} \tag{2.34}$$

$$\nabla\cdot\mathbf{E} = \rho_c/\epsilon_0 \tag{2.35}$$

$$\nabla\cdot\mathbf{B} = 0 \tag{2.36}$$

where $F_s(\mathbf{x},\mathbf{v},t)$ is the phase-space density (in six-dimensional position-velocity space) for species s with $\mathbf{v}$ the velocity of a given particle and $\partial/\partial\mathbf{v}$ is the gradient with respect to velocity. The quantities q_s and m_s are the charge and mass of s respectively and ρ_c is the charge density. Eq. 2.32 is the Vlasov equation and Eq. 2.33–2.36 are Maxwell's equations. The Vlasov equation couples to

Maxwell's equations through $\mathbf{J}$ and ρ_c, which are related to moments of F_s by

$$\rho_c = \sum_s q_s \int F_s d\mathbf{v} \tag{2.37}$$

$$\mathbf{J} = \sum_s q_s \int \mathbf{v} F_s d\mathbf{v}. \tag{2.38}$$

Note that the nonlinearities in the system that give rise to turbulence are introduced within the Vlasov equation.

The fluid variables discussed in Chapter 2.1 are given by moments of F_s. For a given species, fluid variables are defined as

$$n_s = \int F_s d\mathbf{v} \tag{2.39}$$

$$\mathbf{u}_s = \frac{1}{n_s} \int \mathbf{v} F_s d\mathbf{v} \tag{2.40}$$

$$P_s = \frac{m_s}{3} \int (\mathbf{v} - \mathbf{u}_s)^2 F_s d\mathbf{v}. \tag{2.41}$$

For the case of a proton-electron plasma that is quasineutral (e.g. $n \equiv n_i \approx n_e$), single-fluid variables are defined as

$$\rho = (m_i + m_e)\, n \tag{2.42}$$

$$\mathbf{u} = \frac{m_i \mathbf{u}_i + m_e \mathbf{u}_e}{m_i + m_e} \tag{2.43}$$

$$P = P_i + P_e. \tag{2.44}$$

Since protons are much more massive than electrons by a factor of ≈ 1800, $\rho \approx m_i n$ and $\mathbf{u} \approx \mathbf{u}_i$. The ideal versions of the fluid equations can be derived by taking moments of the Vlasov equation (see for example *Chen* [1984]). To derive the fluid equations including viscosity and resistivity, collisional terms must be included in Eq. 2.32, which are neglected in the Vlasov equation [*Braginskii*, 1965; *Boyd and Sanderson*, 2003].

2.2.1 Linear Solutions of the Kinetic Equations

The linearized Maxwell-Vlasov equations give rise to a wide variety of wave modes. The linear theory of electromagnetic waves in kinetic plasmas is well established, as, for example, outlined in

Stix [1992]. The solutions are again decomposed into homogenous backgrounds and infinitesimally small perturbations, such that

$$F_s(\mathbf{x},\mathbf{v},t) = F_{s0}(\mathbf{v}) + F_{s1}(\mathbf{x},\mathbf{v},t), \quad \mathbf{B}(\mathbf{x},t) = \mathbf{B}_0 + \mathbf{B}_1(\mathbf{x},t), \quad \mathbf{E}(\mathbf{x},t) = \mathbf{E}_1(\mathbf{x},t). \tag{2.45}$$

The effects of the currents generated by the plasma can be compactly written in terms of an effective dielectric tensor ($\boldsymbol{\epsilon}$). When Ampère's and Faraday's Laws are combined, this leads to

$$\begin{pmatrix} \epsilon_{xx} - N_\parallel^2 & \epsilon_{xy} & \epsilon_{xz} + N_\parallel N_\perp \\ \epsilon_{yx} & \epsilon_{yy} - N^2 & \epsilon_{yz} \\ \epsilon_{zx} + N_\parallel N_\perp & \epsilon_{zy} & \epsilon_{zz} - N_\perp^2 \end{pmatrix} \begin{pmatrix} E_{x1} \\ E_{y1} \\ E_{z1} \end{pmatrix} = 0 \tag{2.46}$$

where $\mathbf{N} = \mathbf{k}c/\omega$ is the index of refraction with c denoting the speed of light and the coordinate system is oriented with $\mathbf{k}$ in the xz-plane, which can be done without loss of generality. $\mathbf{B}_0$ is along the z-axis and as such the components of $\mathbf{k}$ have been written as the components parallel and perpendicular to $\mathbf{B}_0$. Defining the determinant of the matrix in Eq. 2.46 as $D(\mathbf{k},\omega)$, then the condition $D(\mathbf{k},\omega) = 0$ results in the dispersion relation for the wave and the associated eigenvector gives the polarization of $\mathbf{E}_1$.

In order to determine the components of the dielectric tensor, the currents must be evaluated from the Vlasov equation. Although the manipulation of Maxwell's equations to obtain Eq. 2.46 required no assumption about the amplitude of the fluctuation, the Vlasov equation is nonlinear and thus the equation must be linearized to obtain the small amplitude wave solution. Once linearized, Eq. 2.32 becomes

$$\frac{\partial F_{s1}}{\partial t} + \mathbf{v}\cdot\nabla F_{s1} + \frac{q_s}{m_s}(\mathbf{v}\times\mathbf{B}_0)\cdot\frac{\partial F_{s1}}{\partial \mathbf{v}} = -\frac{q_s}{m_s}(\mathbf{E}_1 + \mathbf{v}\times\mathbf{B}_1)\cdot\frac{\partial F_{s0}}{\partial \mathbf{v}}. \tag{2.47}$$

Assuming the background distribution functions are Maxwellians with no average velocity for each species, the following expressions are obtained for the components of the dielectric tensor [*Stix*, 1992]

$$\epsilon_{xx} = 1 + \sum_s \frac{\omega_{ps}^2}{\omega k_\parallel \sqrt{2} V_{T,s}} \sum_{l=-\infty}^{\infty} l^2 \frac{\Gamma_l(k_\perp^2\rho_s^2)}{k_\perp^2\rho_s^2} Z(\xi_{ls}) \tag{2.48}$$

$$\epsilon_{yy} = \epsilon_{xx} - \sum_s \frac{\omega_{ps}^2}{\omega k_\parallel \sqrt{2} V_{T,s}} \sum_{l=-\infty}^{\infty} 2k_\perp^2 \rho_s^2 \Gamma_l'(k_\perp^2 \rho_s^2) Z(\xi_{ls}) \tag{2.49}$$

$$\epsilon_{zz} = 1 - \sum_s \frac{\omega_{ps}^2}{\omega k_\parallel \sqrt{2} V_{T,s}} \sum_{l=-\infty}^{\infty} \Gamma_l(k_\perp^2 \rho_s^2) \xi_{ls} Z'(\xi_{ls}) \tag{2.50}$$

$$\epsilon_{xy} = -\epsilon_{yx} = i \sum_s \frac{\omega_{ps}^2}{\omega k_\parallel \sqrt{2} V_{T,s}} \sum_{l=-\infty}^{\infty} l\Gamma_l'(k_\perp^2 \rho_s^2) Z(\xi_{ls}) \tag{2.51}$$

$$\epsilon_{xz} = \epsilon_{zx} = -\sum_s \frac{\omega_{ps}^2}{\omega k_\parallel \sqrt{2} V_{T,s}} \sum_{l=-\infty}^{\infty} l \frac{\Gamma_l(k_\perp^2 \rho_s^2)}{\sqrt{2} k_\perp \rho_s} Z'(\xi_{ls}) \tag{2.52}$$

$$\epsilon_{yz} = -\epsilon_{zy} = i \sum_s \frac{\omega_{ps}^2}{\omega k_\parallel \sqrt{2} V_{T,s}} \sum_{l=-\infty}^{\infty} \frac{k_\perp \rho_s}{\sqrt{2}} \Gamma_l'(k_\perp^2 \rho_s^2) Z'(\xi_{ls}) \tag{2.53}$$

where $\omega_{ps} = n_{0s} q_s^2 / \epsilon_0 m_s$ is the plasma frequency for particle species s, $\xi_{ls} = (\omega - l\omega_{cs})/(k_\parallel \sqrt{2} V_{T,s})$, $V_{T,s} = \sqrt{k_b T_{0s}/m_s}$ is the thermal velocity of the species, $\omega_{cs} = q_s B_0 / m_s$ is the species' cyclotron frequency, and $\rho_s = V_{T,s}/\omega_{cs}$ is the gyroradius of the species. T_{0s} and n_{0s} are the background temperature and number density for a species and k_b is Boltzman's constant. ω_{cs} and ρ_s can be positive or negative depending on the sign of the particle's charge. The functions $\Gamma_l(k_\perp^2 \rho_s^2) \equiv e^{-k_\perp^2 \rho_s^2} I_l(k_\perp^2 \rho_s^2)$ are related to the modified Bessel functions of the first kind and the function $Z(\xi_{ls})$ is the plasma dispersion function, which can be written as

$$Z(\xi_{ls}) \equiv i2e^{\xi_{ls}} \int_{-i\xi_{ls}}^{\infty} e^{-z^2} dz. \tag{2.54}$$

The plasma dispersion function introduces imaginary terms that lead to Landau and cyclotron damping. Superscript $'$ on these functions denote derivatives with respect to the arguments such that $\Gamma_l'(k_\perp^2 \rho_s^2) = e^{-k_\perp^2 \rho_s^2}[I_l'(k_\perp^2 \rho_s^2) - I_l(k_\perp^2 \rho_s^2)]$ and $Z'(\xi_{ls}) = -2[1 + \xi_{ls} Z(\xi_{ls})]$.

Eq. 2.46–2.53 now describe all of the linear wave modes that can exist in a homogeneous Maxwellian plasma in the presence of a uniform magnetic field. One such wave mode, which will be discussed in Chapter 5.2, is the kinetic Alfvén wave. The kinetic Alfvén wave is the generalization of the MHD Alfvén wave (see Chapter 2.1.2) to perpendicular length scales approaching or smaller than ρ_i. Chapter 5.2 examines numerical solutions to the kinetic Alfvén wave. Further details about solving the linear Maxwell–Vlasov equations numerically are provided in Appendix A.2.

2.2.2 Current-Driven Instabilities

Currents aligned with the background magnetic field are known to be a mechanism for generating high-frequency electric field activity both in the form of electrostatic wave modes and nonlinear kinetic structures. The linear instability analysis for electrostatic waves (in particular for the electrostatic ion acoustic wave and the electrostatic ion cyclotron wave) in a Maxwellian plasma was performed by *Kindel and Kennel* [1971]. The basic concept is very similar to that outlined in Chapter 2.2.1 for the derivation of linear kinetic waves, except that in this case a bulk velocity difference between the ion and electron distributions is introduced and the equations can be simplified in the electrostatic case by enforcing that the electric field can be expressed as the gradient of a potential. The dispersion relation is given by the solutions to the equation [*Stix*, 1992]

$$0 = k^2 + \sum_s \frac{\omega_{ps}^2}{V_{T,s}^2}\left[1 + \sum_{l=-\infty}^{\infty} \frac{\omega - k_\parallel V_{D,s}}{k_\parallel \sqrt{2} V_{T,s}} \Gamma_l\left(k_\perp^2 \rho_s^2\right) Z\left(\frac{\omega - k_\parallel V_{D,s} - l\omega_{cs}}{k_\parallel \sqrt{2} V_{T,s}}\right)\right] \tag{2.55}$$

where $V_{D,s}$ is a uniform bulk velocity parallel to $\mathbf{B}_0$ associated with the distribution function for species s, which for a proton–electron plasma is related to the field aligned current by $J_\parallel = n_0 q(V_{D,i} - V_{D,e})$. One can choose to work in a reference frame where $V_{D,i} = 0$ such that $V_{D,e}$ represents the relative drift velocity between the ion and electron distribution functions. The margin of stability (or in other words, the transition between a negative and positive growth rate) occurs when $\omega_i = 0$, with ω_i being the imaginary part of the frequency. To find the threshold for instability, one must therefore find the combination of ω, $k_\parallel$, and $k_\perp$ which minimizes the value of $V_{D,e}$ subject to the constraints that ω_i is zero and Eq. 2.55 is satisfied.

Kindel and Kennel [1971] found that the critical electron velocity for instability is dependent on the ratio T_{0e}/T_{0i} and that the threshold value of $V_{D,e}/\sqrt{2}V_{T,e}$ decreases as the ratio T_{0e}/T_{0i} increases. Between $T_{0e}/T_{0i} = 0.1$ and $T_{0e}/T_{0i} = 8$ it was found that the electrostatic ion cyclotron wave was the most unstable wave mode with a critical drift velocity of $V_{D,e}/\sqrt{2}V_{T,e} \sim 1$ when $T_{0e}/T_{0i} = 0.2$ and $V_{D,e}/\sqrt{2}V_{T,e} \sim 0.3$ when $T_{0e}/T_{0i} = 1$.

Another form of current instability involves the formation of nonlinear kinetic scale structures known as double layers. These structures consist of a separation of two layers of charge along a

field line. An electric field forms between the separated layers of charge corresponding to a "ramp" in the electric potential [*Block*, 1978]. Double layers have been observed to be present in space plasma environments such as the Earth's auroral region [*Ergun et al.*, 2001], as well as within BBF braking events [*Ergun et al.*, 2009, 2015].

From theoretical considerations, strong currents on the order of the electron thermal speed are expected to be required for the formation of double layers [*Block*, 1978]. Early kinetic simulations confirmed this result with double layers forming for currents with drifts above the electron thermal velocity while currents less than this did not form these structures [*Goertz and Joyce*, 1975]. More recent kinetic simulations have demonstrated that density perturbations in the presence of such currents (which are roughly at the Buneman instability threshold) can lead to the spontaneous generation of double layers [*Newman et al.*, 2001]. The generation of double layers from density perturbations results from the fact that the presence of a strong current means there is a difference in the bulk velocities associated with ions and electrons. The differential motion results in the ion and electron density perturbations offsetting from each other for an initially quasineutral density perturbation. If the offset occurs fast enough, such that the charged particles cannot equilibrate, then the resulting charge separation will form a self consistent double layer. The presence of double layers within a plasma environment is therefore suggestive of the presence of field-aligned currents.

Electron phase space holes are often observed in conjunction with double layers and are another type of nonlinear kinetic structure. These structures take the form of a potential well (or hill since electrons are negatively charged). The electron distribution function generated to support this potential structure consists of a depletion of electrons within phase space. *Newman et al.* [2001] showed that electron phase space holes can be generated by a beam plasma instability resulting from the acceleration of electrons through the double layer. Generally many electron phase space holes are generated by a single double layer and therefore, in observations it is often much more common to see the electron phase space holes than the associated double layer. Even when double layers are not directly observed, electron phase space holes can be taken as a signature that double layers may be present in the region.

There are several additional mechanisms for the generation of either electron phase space holes or double layers. Electron phase space holes are observed in many boundary regions or kinetically active regions, for example the plasma sheet [*Matsumoto et al.*, 1994], the auroral region [*Ergun et al.*, 1998], bow shock [*Bale et al.*, 1998], as well as the magnetopause and the cusp [*Cattell et al.*, 1999, 2002]. Electron phase space holes can be developed by electron beams [*Omura et al.*, 1996], two-stream instabilities [*Goldman et al.*, 1999], or Buneman instabilities [*Drake et al.*, 2003]. Double layers have been observed primarily in the auroral region in association with field-aligned currents. The field-aligned currents can be generated globally by large-scale current systems or locally by Alfvén waves. In laboratory plasmas, current-free double layers can be generated at the boundary between two plasma populations with differing electron temperatures [*Charles and Boswell*, 2003].

However, the combination of double layers adjacent to electron phase space holes, such as reported by *Ergun et al.* [2009, 2015] and simulated by *Newman et al.* [2001], have only been observed (other than in the BBF braking region) in the downward current region of the auroral zone, often associated with Alfvénic activity [*Ergun et al.*, 2004]. It can only be concluded that strong field-aligned currents are not a unique mechanism of developing double layers and electron phase space holes, but a strong candidate.

Note that the instability threshold associated with electrostatic wave modes, as examined by *Kindel and Kennel* [1971] generally, is comparable to or less than the instability threshold associated with the generation of double layers. Therefore, it is conceivable that if field-aligned currents are strong enough to generate double layers, then there is also likely the generation of electrostatic wave modes occurring in the region.

2.3 Turbulence Theory

In the linearized systems, fluctuations at different length and time scales are independent of one another and do not exchange energy. However, the presence of nonlinearities in the equations allows for the coupling of wavenumbers, which results in the cascade of energy in turbulent systems.

This feature can be illustrated by considering the Fourier transform of the multiplication of two function $g(\mathbf{x})$ and $h(\mathbf{x})$, which utilizing the convolution theorem gives

$$[g(\mathbf{x})h(\mathbf{x})]_k = \int g(\mathbf{x})h(\mathbf{x})e^{i\mathbf{k}\cdot\mathbf{x}}d^3\mathbf{x} = \int g(\mathbf{k}')h(\mathbf{k}-\mathbf{k}')d^3\mathbf{k}' \tag{2.56}$$

with $[...]_k$ representing the Fourier transform of the nonlinear term. Therefore the value of the nonlinear terms, and as a result evolution of the quantities described by the equations in Chapters 2.1, at wavevector $\mathbf{k}$ contain contributions from all other wavevectors. In many turbulent systems, it is postulated that the nonlinearities are dominated by local interactions, that is to say, only wavevectors near $\mathbf{k}$ contribute to $[g(\mathbf{x})h(\mathbf{x})]_k$. However, in general, it is possible for non-local interactions to play a role [*Alexakis et al.*, 2005; *Mininni et al.*, 2005].

Turbulence theories can be divided into two broad categories, "strong" and "weak" (or wave) turbulence [*Nazarenko*, 2011]. In strong turbulence, nonlinear fluctuations dominate the dynamics while in weak turbulence linear fluctuations (i.e. waves) dominate the dynamics with a small but nonzero nonlinear coupling. The condition which separates these two regimes is given by $\chi = \tau_L/\tau_{NL}$ where $\tau_L = \omega^{-1}$ is the timescale associated with the waves and τ_{NL} is the timescale associated with the nonlinear terms. If χ is less than 1, the linear timescale is shorter than the nonlinear timescale and the turbulence is weak and if χ is large, the nonlinear timescale is shorter than the linear timescale and the turbulence is strong.

2.3.1 The Energy Spectrum and Length Scales of Turbulence

In turbulence theory, energy spectra are expected to follow power laws as a function of k. Predicted power laws are based on assumptions for the nonlinear energy transfer timescale (τ_{tr}). If the physics associated with nonlinear interactions changes, as occurs at the transition from fluid to kinetic scales, the power law is expected to change. Based on phenomenological arguments, the inertial range energy spectrum for quantity Q (for example the velocity or magnetic field) is dimensionally given by $E_Q(k) \sim Q^2(k)/k \sim \tau_{tr}\mathcal{E}/k$ where $\mathcal{E} \sim Q^2(k)/\tau_{tr}$ is the energy cascade rate. For strong hydrodynamic turbulence, *Kolmogorov* [1941] argued that $\tau_{tr} \sim \tau_{NL}$

where $\tau_{NL} \sim [ku(k)]^{-1}$ (often referred to as the eddy turnover time) is the timescale associated with the nonlinear term $\mathbf{u}\cdot\nabla\mathbf{u}$ based on dimensional analysis. The resulting kinetic energy spectrum is given by

$$E_V(k) = C_K \mathcal{E}^{2/3} k^{-5/3} \tag{2.57}$$

where C_K is an order unity constant that cannot be determined from dimensional arguments. Based on experiments $C_K \approx 1.6$ [*Sreenivasan*, 1995].

The MHD equations are dimensionally the same as in the hydrodynamic case, that is, the additional nonlinear terms ($\mathbf{j}\times\mathbf{b}$ in Eq. 2.8 and $\nabla\times(\mathbf{u}\times\mathbf{b})$ in Eq. 2.7) are dimensionally equivalent to $\mathbf{u}\cdot\nabla\mathbf{u}$. Therefore, one might expect, based on the *Kolmogorov* [1941] arguments, that for strong MHD turbulence, the total energy spectrum ($E_T(k) = E_V(k) + E_M(k)$) will follow the form seen in Eq. 2.57. Spectra with a $k^{-5/3}$ form have been observed in both simulations of MHD turbulence [e.g. *Biskamp and Müller*, 2000], as well as in observations of the spectrum in the solar wind [*Matthaeus and Goldstein*, 1982].

The Hall term introduces the nonlinear timescale $[d_i k^2 b(k)]^{-1}$ to Eq. 2.7, which depending on the ratio of the magnetic field to velocity fluctuations should be shorter than the MHD timescale at roughly $k > d_i^{-1}$. Therefore, using the phenomenology of Kolmogorov, $\tau_{tr} \sim [d_i k^2 b(k)]^{-1}$ in the small scales of HMHD turbulence, giving a magnetic energy spectrum of [*Galtier*, 2006]

$$E_M(k) = C_H \left(\frac{\mathcal{E}}{d_i}\right)^{2/3} k^{-7/3} \tag{2.58}$$

where C_H is again a constant. Therefore, a steepening of the magnetic spectrum may be expected to occur at scales near d_i because of the change in nonlinear timescale.

In weak turbulence theory, $\tau_{tr} \sim \tau_{NL}/\chi = \tau_{NL}^2/\tau_L$. Since in weak turbulence χ is a small number this lengthens the amount of time it takes to transfer energy in k-space compared to strong turbulence. *Iroshnikov* [1964] and *Kraichnan* [1965] argued that in the presence of a strong $\mathbf{B}$, Alfvén waves become important to the dynamics. Under the assumption of isotropy, it was argued that $\tau_{tr} \sim kV_A/[ku(k)]^2$ and that equipartition between $E_M(k)$ and $E_V(k)$ should be present as

expected from Alfvén waves, leading to

$$E_T(k) = C_{IK}\sqrt{\mathcal{E}V_A}k^{-3/2} \tag{2.59}$$

where $C_{IK} \sim 1.4$ is an order unity constant [*Matthaeus and Zhou*, 1989].

Eq. 2.59 gives a weak turbulence energy spectrum prediction based on dimensional analysis arguments; however, in weak turbulence theory significant headway can be made analytically. Under the assumption of weak nonlinearity, the equations governing the dynamics of the system (for example the MHD equations for the large scales in a plasma or the Maxwell-Vlasov equations for the kinetic scales in a plasma) can be solved perturbatively out to second order and expressions can be derived for the statistical quantities such as the energy spectrum [*Nazarenko*, 2011]. The weak turbulence formalism was applied to MHD scale Alfvén waves by *Galtier et al.* [2000] and it was found that the spectrum for shear Alfvén waves was given by

$$E_T(k_\parallel, k_\perp) = f(k_\parallel)C_w\sqrt{\mathcal{E}_\perp V_A}k_\perp^{-2} \tag{2.60}$$

where C_w is again a constant, $\mathcal{E}_\perp$ is the energy cascade rate per $k_\perp$ plane, and $E_T(k_\parallel, k_\perp)$ must be integrated over both $k_\parallel$ and $k_\perp$ to obtain energy. The function $f(k_\parallel)$ is a non-universal function that cannot be determined from weak turbulence theory because at lowest order, resonant interactions do not transfer energy in the $k_\parallel$ direction. However, as noted for example by *Oughton et al.* [2004] and *Galtier et al.* [2005], in reality energy transfer can occur in the $k_\parallel$ direction, although in an anisotropic fashion. Assuming isotropy and performing dimensional analysis on Eq. 2.60 results in a spectrum of the form seen in Eq. 2.59.

Eq. 2.57–2.60 provide the energy spectrum predictions in several regimes discussed in this work and illustrate the basic steps involved in determining the spectrum of turbulence; however, a variety of predictions have been derived in various regimes of plasma turbulence. *Galtier* [2006] has applied the weak turbulence formalism to HMHD. Weak turbulence of kinetic Alfvén waves has been appealed to in the explanation of the observed steepening of the wavenumber spectrum to a power law index of ~ -2.5 at kinetic scales in the solar wind [*Voitenko*, 1998; *Voitenko and*

de Keyser, 2011]. Phenomenological arguments based on kinetic Alfvén waves in the regime where $\chi \sim 1$ (often referred to as critical balance) have also been considered by several authors to account for the steeper power laws at kinetic scales [*Howes et al.*, 2011; *Boldyrev and Perez*, 2012].

Based on the energy spectrum the integral scale can be defined as

$$L_{int} = 2\pi \frac{\int [E_V(k)/k]\, dk}{\int E_V(k) dk}, \tag{2.61}$$

which is simply an energy weighted average of $2\pi/k$. L_{int} can be interpreted as a characteristic large scale associated with the turbulent flow and, as such, will often be used as L_c in the computation of Re or as a length scale for defining a characteristic eddy turnover time.

The real-space analog of the energy spectrum is the autocorrelation function, which for a vector $\mathbf{Q}$ is defined as

$$A_Q(\Delta\mathbf{x}) = \frac{\sum\limits_{i=x,y,z} \langle Q_i(\mathbf{x}) Q_i(\mathbf{x}+\Delta\mathbf{x})\rangle}{\langle |\mathbf{Q}(\mathbf{x})|^2 \rangle} \tag{2.62}$$

where $\Delta\mathbf{x}$ is the spatial lag. Since A_Q is by definition an even function, the convolution theorem tells us that the wavenumber energy spectrum of $\mathbf{Q}$ is given by the Fourier transform of $\langle |\mathbf{Q}(\mathbf{x})|^2 \rangle A_Q$. The shape of A_Q provides information about the length scales associated with the turbulence. A correlation length can be defined as the integral of $A_Q(\Delta\mathbf{x})$ over $\Delta\mathbf{x}$ and gives a measure of the characteristic large scale associated with $\mathbf{Q}$. The Taylor scale, which is the characteristic scale associated with gradients in $\mathbf{Q}$, can also be measured based on the curvature near $\Delta\mathbf{x} \approx 0$.

2.3.2 Turbulent Intermittency

Another concept from turbulence is intermittency, which refers to the formation of small-scale coherent structures within a turbulent flow. Intermittency is associated with strong, localized gradients in $\mathbf{u}$ and $\mathbf{b}$ and is often characterized by the development of non-Gaussian statistics for small scale differences of these quantities [e.g. *Frisch*, 1995; *Politano and Pouquet*, 1995; *Pope*, 2000; *Abramenko*, 2008; *Rast and Pinton*, 2009]. In resistive/viscous systems, velocity gradients and currents are directly responsible for the local dissipation of energy [*Politano et al.*, 1995; *Sorriso-Valvo et al.*, 2000; *Mininni and Pouquet*, 2009] (see also, *Davidson* [2004]) and in collisionless plasmas,

the current structures in particular are thought to play a key role in dissipation [*Osman et al.*, 2012; *Wan et al.*, 2012; *TenBarge and Howes*, 2013]. Intermittency is therefore characterized by small regions of exceptionally strong dissipation and relatively large areas with little dissipation [*Ishihara et al.*, 2009]. In fact, numerical evidence seems to suggest that turbulent systems may tend towards finite dissipation in the limit of $Re \to \infty$ and $Rm \to \infty$ [*Mininni and Pouquet*, 2009]. Therefore, in the resistive/viscous context, since dissipation is given by $\eta\langle|\mathbf{j}|^2\rangle + \nu\langle|\boldsymbol{\omega}|^2\rangle$, intermittency could be thought of as a manifestation of the tendency of turbulence to form exceptionally strong $\mathbf{j}$ and $\boldsymbol{\omega}$ to compensate for vanishing η and ν.

MHD simulations, in both 2D and 3D, show the spatial distributions of currents, have super-Gaussian wings indicating increased probability (compared to Gaussian) of having particularly strong currents. When related back to the physical configuration, these distributions correspond to the above picture where large regions have relatively little current and localized regions have exceptionally strong ones [*Greco et al.*, 2008, 2009; *Uritsky et al.*, 2010]. Recent simulations of kinetic plasmas in both 2D and 3D have shown that the development of non-Gaussian current distributions and intermittency continues into the kinetic regime [*Wan et al.*, 2012; *Karimabadi et al.*, 2013]. Intermittent current structures are also likely sites for kinetic phenomena such as magnetic reconnection [*Osman et al.*, 2014]. The role of intermittency in driving kinetic phenomena, in particular the field-aligned current instabilities discussed in Chapter 2.2.2, is one of the topics explored in Chapters 4, 5, and 6 and ultimately may be important for understanding turbulent dissipation in collisionless plasmas.

One way of examining intermittency is by considering the distribution and moments of temporal or spatial increments in the magnetic field given by [*Sorriso-Valvo et al.*, 1999; *Weygand et al.*, 2005]

$$\frac{\Delta B_i(\Delta\mathbf{x},\tau)}{\Delta B_{i,rms}} = \frac{B_i(\mathbf{x},t) - B_i(\mathbf{x}+\Delta\mathbf{x},t+\tau)}{\sqrt{\langle(B_i(\mathbf{x},t) - B_i(\mathbf{x}+\Delta\mathbf{x},t+\tau))^2\rangle}} \tag{2.63}$$

where i denotes a component of $\mathbf{B}$, and τ and $\Delta\mathbf{x}$ are time and space lags respectively. In a turbulent system, distributions of $\Delta B_i/\Delta B_{i,rms}$ are expected to be Gaussian at large lags where

fluctuations are uncorrelated and have super-Gaussian wings at small lags, which is associated with the coherent structures. Intermittency is traditionally examined in the spatial domain [*Politano et al.*, 1995]; however, signatures of intermittency are observed in temporal increments of the velocity or magnetic field in both hydrodynamic and MHD simulations. The signatures in the temporal distributions can be associated with the advection of spatial structures past the observer by small-scale turbulent motions [*Chevillard et al.*, 2005; *Homann et al.*, 2007; *Yoshimatsu et al.*, 2011]. Observational evidence for intermittency has also been found in space plasmas, such as the solar wind [*Tsurutani and Smith*, 1979; *Sorriso-Valvo et al.*, 1999; *Greco et al.*, 2009; *Osman et al.*, 2012] and magnetosphere [*Weygand et al.*, 2005], where signatures in the distribution of temporal magnetic increments have been attributed to intermittency.

2.3.3 Statistical Mechanics of Ideal MHD Turbulence

Another way of trying to understand the behavior of turbulence is by considering the statistical equilibria of the ideal system (i.e. neglecting dissipative terms). While the exact quantitative solutions obtained through this approach may not be applicable to the dissipative system, they have been shown to provide useful qualitative insight into the dynamics in the presence of dissipation, as for example was done in hydrodynamics [*Kraichnan*, 1967] and 3D MHD [*Frisch et al.*, 1975; *Stribling and Matthaeus*, 1990, 1991]. *Frisch et al.* [1975] derived the statistical equilibria for 3D MHD and were able to predict the inverse cascade of H_M.

Statistical equilibria are the long-time solutions to a truncated system of Fourier modes, with k_{min} and k_{max} the minimum and maximum wavenumbers respectively. These modes are coupled through the nonlinear ideal MHD equations (Eq. 2.6–2.9 with $d_i = 0$, $\nu = \eta = 0$, and $\nu' = \eta' = 0$) and subject to the conservation of the quadratic invariants; E_T, H_M, and H_C. The idea here is that the nonlinear couplings will exchange energy between the modes, allowing the system to explore phase space and driving it towards statistical equilibrium. Defining $\alpha \neq 0$, ϑ and γ as the Lagrange multipliers (analogous to the inverse of the temperature in statistical mechanics) associated with

the E_T, H_M and H_C invariants, a canonical ensemble can be defined such that

$$w = \frac{\exp\left(-\alpha E_T - \vartheta H_M - \gamma H_C\right)}{W} \tag{2.64}$$

where w is the phase space density and W is the partition function (i.e. the integral of the numerator over all of phase space). In this context, phase space consists of the real and imaginary parts of the transverse components of $\mathbf{u}(\mathbf{k})$ and $\mathbf{b}(\mathbf{k})$ for each wavevector in the range from k_{min} to k_{max}. The longitudinal components are constrained in the incompressible system. Based on Eq. 2.64, equilibrium spectra can be computed (*Frisch et al.* [1975] and *Stribling and Matthaeus* [1990] outline several methods for performing this computation), which, assuming that the magnetic helicity is non-zero ($\vartheta \neq 0$), can be expressed as

$$\begin{aligned}
H_M(k) &= -\frac{8\pi\vartheta}{\alpha^2\Gamma^4}\frac{1}{\mathcal{D}(k)}, && (2.65)\\
H_J(k) &= k^2 H_M(k), && (2.66)\\
H_C(k) &= \frac{\gamma\Gamma^2}{2\vartheta} H_J(k), && (2.67)\\
H_V(k) &= \frac{\gamma^2}{4\alpha^2} H_J(k), && (2.68)\\
E_M(k) &= -\frac{\alpha\Gamma^2}{\vartheta} H_J(k) = \frac{8\pi k^2}{\alpha\Gamma^2}\frac{1}{\mathcal{D}(k)}, && (2.69)\\
E_V(k) &= \left(\Gamma^2\mathcal{D}(k) + \frac{\gamma^2}{4\alpha^2}\right) E_M(k) = \left(1 - \frac{\vartheta^2}{4\alpha^2\Gamma^2}\frac{1}{k^2}\right) E_M(k) && (2.70)
\end{aligned}$$

where $H_J = \int k^2 H_M(k) dk$ is the current helicity, and

$$\alpha > 0\ , \qquad \Gamma^2 = 1 - \frac{\gamma^2}{4\alpha^2} > 0\ ; \qquad \mathcal{D}(k) = \left(1 - \frac{\vartheta^2}{\alpha^2\Gamma^4}\frac{1}{k^2}\right) > 0 \quad , \forall k \in [k_{min}, k_{max}]\ . \tag{2.71}$$

H_M and H_C are not definite positive, and furthermore, H_M does not have the same physical dimension as E_T and H_C, and hence ϑ does not have the same physical dimension as α and γ. In order to fulfill realizability conditions (positivity of energy, and Schwarz inequalities involving the helicities), necessary relationships between coefficients can be derived, involving k_{min} (see *Frisch et al.* [1975]).

When $\vartheta \equiv 0$ and thus $H_M(k) \equiv 0$, $H_J(k) \equiv 0$, one finds that the kinetic helicity is also equal to zero, that there is equipartition of energy at all wavenumbers with $E_M(k) = E_V(k) =$

$8\pi k^2/(\alpha\Gamma^2)$, and that $H_C(k) = -4\pi\gamma k^2/(\alpha^2\Gamma^2)$. Therefore, the relative cross helicity $2H_C(k)/E_T(k)$ is constant in this case. When $\gamma \equiv 0$ and thus $H_C(k) \equiv 0$, the kinetic helicity is also equal to zero and the kinetic energy has its non-helical expression, $E_V(k) = 8\pi k^2/\alpha$. The magnetic energy and helicity can peak at low wavenumber when ϑ is large enough, and the relative magnetic helicity $kH_M(k)/E_M(k) \sim 1/k$, i.e. it is stronger in the largest scales of the flow, a result that persists in the general case ($\vartheta \neq 0, \gamma \neq 0$).

When considering $H_J(k)$ (instead of $H_M(k)$), note that all Fourier spectra are strictly proportional, with coefficients uniquely determined by initial conditions given the values of the invariants, except for the kinetic energy. For all k, $E_V(k) \leq E_M(k)$ with the equality arising only when there is either no magnetic helicity, maximal H_C, or for $k_{max} \to \infty$. Similarly, the residual helicity defined as

$$H_R(k) = H_V(k) - H_J(k) = -\Gamma^2 H_J(k) \ ,$$

is of the sign opposite to that of the current and of the magnetic helicity, and $H_R(k)$ becomes equal to zero only for maximal cross-correlation ($\Gamma^2 = 0$), except for the trivial non-helical case of course. The relative helicity $H_R(k)$, integrated over the small scales, is the motor of the nonlinear dynamo problem, i.e. the growth of large-scale magnetic energy because of small-scale helical motions. Note that H_R reduces to the kinetic helicity in the kinematic regime when the magnetic field is weak, thus recovering the so-called "alpha" effect (see *Brandenburg and Subramanian* [2005] for a recent comprehensive review).

It was shown by *Stribling and Matthaeus* [1990, 1991], based on the statistical mechanics described above, that in the ($2H_C/E_T$, $k_{min}H_M/E_T$) parameter space, configurations minimizing the total energy lay on the curve

$$\frac{2H_C}{E_T} = \begin{cases} \sqrt{1 - 4\left(\left|\frac{k_{min}H_M}{E_T}\right| - 0.5\right)^2}, & \left|\frac{k_{min}H_M}{E_T}\right| > 0.5 \\ \pm 1, & \left|\frac{k_{min}H_M}{E_T}\right| \leq 0.5 \end{cases} . \tag{2.72}$$

It was argued that over long time-scales, the dissipative system would evolve so as to minimize E_T and, therefore, would evolve towards the states defined by Eq. 2.72, with the exact location

on the curve depending on the initial values of $2H_C/E_T$ and $k_{min}H_M/E_T$. Three main regions of parameter space can be seen as attractors to the dynamics; a magnetic helicity dominated region, an alignment (strong H_C) region, and an intermediate region. The first two extreme cases (which are dominated by either H_M or H_C) are associated with the so-called selective decay [*Matthaeus and Montgomery*, 1980] and dynamic alignment [*Dobrowolny et al.*, 1980] relaxation processes, respectively. In selective decay, certain invariants are viewed as more sturdy than others; thus, they may influence the long-term dynamics of decaying turbulent flows. This hypothesis is based on the fact that invariants may have different physical dimensions. For example, H_M has one less factor of length in its dimensions than E_T and, therefore might be expected to be weighted more towards the large scales, where dissipation is weaker. H_M would then dissipate more slowly than E_T leaving behind a magnetically dominated and strongly helical (i.e. force free) "Taylor state" [*Taylor*, 1986] after long times. A similar argument can also be made in 2D MHD where $\langle|\mathbf{a}|^2\rangle$ replaces H_M as an invariant. On the other hand, dynamic alignment is associated with a tendency for the system to develop strong alignment between $\mathbf{u}$ and $\mathbf{b}$ fluctuations as a result of the turbulent dynamics. This type of behavior leads to an "Alfvénic" state with equipartition of magnetic and kinetic energy. The intermediate region corresponds to the more general case where both H_M and H_C play a role in the dynamics. In addition to the three regions mentioned above, *Stribling and Matthaeus* [1990, 1991] found that initial conditions with $H_C \approx 0$ and $H_M \approx 0$ tended to remain in this state for long times and not evolve towards the minimum energy prediction of Eq. 2.72. In Chapter 3, the long-time relaxation of 3D MHD will be explored in further detail numerically.

Chapter 3

Long-Time Relaxation of Magnetohydrodynamic Turbulence

While turbulence is known to transfer energy to the small scales where it can be dissipated, the question remains as to what types of configurations the turbulence drives the system towards. In this chapter, the long-time relaxation of turbulent flows (i.e. the configuration that is left behind once the turbulence has decayed away) is examined through the use of 3D direct numerical simulations (DNS) of the incompressible MHD equations (Eq. 2.6–2.9 with $d_i \equiv 0$). An understanding of the relaxation of MHD turbulence may be relevant for space plasmas where turbulence is sporadically driven (such as in the case of the bursty bulk flow braking region discussed in Chapter 5) or in the solar wind where turbulence decays as it is advected away from the Sun by the bulk solar wind flow. The majority of the simulation runs performed in this chapter make use of the Geophysical High-Order Suite for Turbulence code (GHOST) [*Mininni et al.*, 2011], which is a pseudospectral code and the main simulation code utilized throughout this thesis. Further details about GHOST can be found in Appendix A.1. Additionally, several runs in this chapter use the Taylor-Green Symmetric code (TYGRS) [*Brachet et al.*, 1983; *Cichowlas et al.*, 2005] for comparison with the GHOST runs. TYGRS is a similar code to GHOST except that it enforces the four-fold symmetry present in the Taylor-Green (TG) initial condition (see Sec. 3.1) throughout the computation and, therefore aids in examining the role of symmetries in long-time relaxation. By enforcing the symmetries, TYGRS allows for a substantial gain in memory and CPU resources at a given Reynolds number.

Exploring the long-time states of decaying turbulence is a challenging problem numerically because it can require computations out to hundreds of nonlinear timescales, which, for a given

amount of compute time, severely reduces the maximum number of grid points in the computational domain. Since dissipation in a DNS must occur at scales larger than the grid scale, reduced grid sizes mean that the Reynolds number must also be reduced. While some previous numerical work has been performed on the relaxation of MHD turbulence [*Stribling and Matthaeus*, 1990, 1991], these studies only included $\approx$ 100 interacting wavevectors, so it is unclear if similar results are obtained for higher Reynolds number systems. In this chapter, the numerical study of long-time MHD relaxation is extended to grid sizes of up to 512^3 points (corresponding to over a million interacting wavevectors).

A variety of initial conditions are examined to study the various regimes of turbulent relaxation discussed in Chapter 2.3.3. The initial conditions consist of combinations and/or perturbations to well studied configurations in turbulence, which have various initial values of $2H_C/E_T$ and $k_{min}H_M/E_T$. Of particular interest is the examination of the three MHD extensions of the highly symmetric TG flow, which all have $H_C \approx 0$ and $H_M = 0$ initially. In the decaying case, *Lee et al.* [2010] found that three different power laws are observed with these configurations ($k^{-5/3}$, $k^{-3/2}$, and k^{-2}) despite using the same velocity field and having the same ideal invariants. Similar results are found to hold in the forced case as well, for which long-time averaging is feasible [*Krstulovic et al.*, 2014]. Will similar relaxation dynamics to those discussed by *Stribling and Matthaeus* [1990, 1991] occur, when starting with the three flows studied in *Lee et al.* [2010], which statistically are equivalent but which display different inertial range dynamics? Through the examination of these TG flows and small perturbations to them, this question is explored. The TG configurations also allow for a closer examination of the ($H_C = 0$, $H_M = 0$) region of parameter space.

3.1 Initial Conditions

Table 3.1 summarizes the main characteristics of the 41 runs discussed in this chapter. All runs use GHOST except for those marked with TYGRS in the remarks column. Values of $2H_C/E_T$, $k_{min}H_M/E_T$, and E_T at several times in the computation are given in the Table 3.1. The time $t_{100} = 100\tau_{NL}$, with τ_{NL} the timescale of the advection term defined based on the initial conditions,

and t_F is the final time of the computation. The simulation box is scaled to size $(2\pi)^3$, which can be done without loss of generality, so that $k_{min} = 1$ and the parameter $k_{min}H_M/E_T$ will simply be referred to as H_M/E_T. For all runs $\nu = \eta$ (i.e. the magnetic Prandtl number is unity), $\nu' = \eta' = 0$ (i.e. hyperdiffusivity is not employed), and $E_M = E_V = 0.125$ initially. The groups divided by horizontal lines in Table 3.1 correspond to different line styles in Figure 3.1, 3.2, and 3.4. All runs are performed on a grid of 64^3 points with $\nu = 2 \times 10^{-3}$, unless otherwise noted in the remarks column. The viscosity is changed inversely to the resolution and three runs are done on grids of 512^3 points, with two in a series (R17** and R25**) with resolutions 64^3, 128^3, 256^3, and 512^3. Run R17+ is a variant of run R17** on a grid of 512^3 points, with a helical velocity perturbation placed at wavenumber $k = 1$ instead of $k = 3$. In the second column, /D and /S stand for double and single precision computations. The variety of different initial conditions examined in this study are discussed in detail below and abbreviated descriptions are given in column two of Table 3.1. The purpose here is to vary H_C and H_M of well-studied configurations in MHD turbulence with a fixed value of E_T.

The Taylor-Green velocity is given by

$$\mathbf{u}^{TG} = \overline{u}^{TG} \left[\sin(k_v x)\cos(k_v y)\cos(k_v z),\ -\cos(k_v x)\sin(k_v y)\cos(k_v z),\ 0\right] \tag{3.1}$$

and the three different Taylor-Green magnetic field initial conditions are

$$\begin{aligned} \mathbf{b}^I &= \overline{b}^I \left[\cos(k_m x)\sin(k_m y)\sin(k_m z),\ \sin(k_m x)\cos(k_m y)\sin(k_m z),\right. \\ &\qquad \left. -2\sin(k_m x)\sin(k_m y)\cos(k_m z)\right] \end{aligned} \tag{3.2}$$

$$\mathbf{b}^A = \overline{b}^A \left[\cos(k_m x)\sin(k_m y)\sin(k_m z),\ -\sin(k_m x)\cos(k_m y)\sin(k_m z),\ 0\right] \tag{3.3}$$

$$\begin{aligned} \mathbf{b}^C &= \overline{b}^C \left[\sin(k_m x)\cos(k_m y)\cos(k_m z),\ \cos(k_m x)\sin(k_m y)\cos(k_m z),\right. \\ &\qquad \left. -2\cos(k_m x)\cos(k_m y)\sin(k_m z)\right]. \end{aligned} \tag{3.4}$$

I, A and C (notation also used in column two of Table 3.1) refer to the insulating, alternate insulating, and conducting boundary conditions of the TG flows studied by *Lee et al.* [2010] respectively. By insulating or conducting, it is meant that in the computational box, the current is either parallel

Table 3.1: Initial conditions of the 41 runs and values of various parameters at $t = 100\tau_{NL}$ and at the final time t_F. All runs are done on grids of 64^3 points unless otherwise indicated (see last column). Two series (indicated by $**$) with Re (and grids) varied by a factor 8 are performed. Values listed for these series are those for the highest resolution (512^3) grid. Three runs are done with the TYGRS code. Horizontal lines divide groups with different types of initial conditions. /D or /S stand for double or single precision. I, A & C are for the TG flows and "$+10^{-x}$" indicates runs with added noise of amplitude 10^{-x} relative to the initial conditions. Runs R15–R17 are A flows with either weak (w) or intermediate (i) helical perturbations added to $\mathbf{b}$ ($\mathbf{u}$ is also weakly perturbed in the sH cases). H1, 2, or 3 stands for the ABC configuration at $k = 1$, 2, or 3. The last 4 runs have an OT $\mathbf{u}$ and a mixture of OT and ABC for $\mathbf{b}$. See text for more details.

		Initial Values				Values at $t_{100} = 100\tau_{NL}$					Values at t_F				
Run	Type	$2H_C/E_T$	H_M/E_T	k_V	k_M	E_M/E_V	$2H_C/E_T$	H_M/E_T	10^4E_T	t_F	E_M/E_V	$2H_C/E_T$	H_M/E_T	10^6E_T	Remarks
R1a	I/D	0.00	0.00	2	2	23.7	0.00	0.00	30.9	500	37.2	0.00	0.00	3.84	
R1b	I/D/T	0.00	0.00	2	2	23.7	0.00	0.00	30.9	500	37.2	0.00	0.00	3.84	TYGRS
R2	I/S	0.00	0.00	2	2	23.5	0.00	0.00	30.9	500	1.91	0.06	0.01	2.26	
R3	I/D+10^{-6}	0.00	0.00	2	2	0.76	-0.01	-0.02	6.18	500	0.99	-0.48	0.08	7.49	
R4	I/D+10^{-3}	0.00	0.00	2	2	0.54	-0.02	0.02	7.83	500	0.58	-0.26	0.08	16.2	
R5a	C/D	0.00	0.00	2	3	0.27	-0.75	0.00	4.80	500	0.84	-1.00	0.00	2.56	
R5b	C/D/T	0.00	0.00	2	3	0.27	-0.75	0.00	4.80	500	0.84	-1.00	0.00	2.56	TYGRS
R6	C/S	0.00	0.00	2	3	0.27	-0.75	0.00	4.80	500	0.84	-1.00	0.00	2.56	
R7	C/D+10^{-4}	0.00	0.00	2	3	0.71	0.05	0.03	2.90	500	0.54	0.21	0.03	6.89	
R8	C/D+10^{-3}	0.00	0.00	2	3	0.75	-0.22	0.01	4.64	500	1.00	-0.71	0.02	16.0	
R9a	C/D+10^{-2}	0.00	0.00	2	3	1.32	0.06	-0.03	4.69	500	1.71	-0.25	-0.11	8.27	
R9b	C/D+10^{-2}	0.00	0.00	2	3	2.33	0.15	-0.12	8.98	100	–	–	–	–	256^3; $\nu = 6.67 \times 10^{-4}$
R10a	A/D	0.00	0.00	2	3	2.36	0.00	0.00	1.14	500	28.0	0.00	0.00	0.36	
R10b	A/D/T	0.00	0.00	2	3	2.36	0.00	0.00	1.14	500	28.0	0.00	0.00	0.36	TYGRS
R10c	A/D	0.00	0.00	2	3	0.64	0.00	0.00	0.40	1000	0.69	0.00	0.00	1.21×10^{-8}	32^3; $\nu = 4 \times 10^{-3}$
R10d	A/D	0.00	0.00	2	3	4.86	0.00	0.00	1.50	100	–	–	–	–	128^3; $\nu = 1 \times 10^{-3}$
R11a	A/S	0.00	0.00	2	3	2.36	0.00	0.00	1.14	500	28.0	0.00	0.00	0.36	
R11b	A/S	0.00	0.00	2	3	0.64	0.00	0.00	0.40	1000	0.69	0.00	0.00	1.21×10^{-8}	32^3; $\nu = 4 \times 10^{-3}$
R12	A/D+10^{-4}	0.00	0.00	2	3	1.47	-0.07	0.01	1.50	500	0.65	-0.14	-0.15	3.73	
R13	A/D+10^{-3}	0.00	0.00	2	3	1.45	0.22	-0.01	2.35	500	0.98	0.48	0.06	8.08	
R14	A/D+10^{-2}	-0.01	0.00	2	3	1.44	-0.24	0.08	2.84	500	0.98	-0.45	0.25	7.36	
R15	B wH	0.00	0.00	2	3	0.46	-0.26	-0.02	7.99	500	0.12	-0.16	-0.02	57.7	
R16	B iH	0.00	0.04	2	3	9.30	0.05	0.85	25.8	500	74.81	0.05	0.98	443	
R17**	U&B sH	-0.09	0.02	2, 3	3	8.08	-0.29	0.52	64.9	100	–	–	–	–	4 runs, 64^3 to 512^3 grids
R17+	U&B sH +	-0.09	0.00	1, 2	3	–	–	–	–	50	4.68	-0.12	0.45	8940	512^3; $\nu = 2.5 \times 10^{-4}$ variant
R18	B H1	0.00	0.50	2	1	1428	0.00	1.00	817	100	–	–	–	–	
R19	B H2	0.00	0.25	2	2	1379	-0.01	0.57	535	100	–	–	–	–	128^3; $\nu = 1 \times 10^{-3}$
R20	U H2, B H2	0.11	0.25	2	2	177	0.15	0.57	282	500	155	0.13	0.99	1018	
R21a	B H3	0.00	0.17	3	3	20.5	0.00	0.85	316	150	60.2	0.00	0.94	2.71×10^5	192^3; $\nu = 6.67 \times 10^{-4}$
R21b	B H3	0.00	0.17	3	3	17.4	0.00	0.80	363	150	49.7	0.00	0.92	3.03×10^5	256^3; $\nu = 5 \times 10^{-4}$
R22	OT	0.41	0.00	1	1, 2	1.00	0.99	0.00	21.0	250	0.99	1.00	0.00	337	
R23a	0.99OT+0.01H1	0.41	0.00	1	1, 2	0.98	0.99	0.12	19.7	150	1.02	1.00	0.13	957	
R23b	0.99OT+0.01H1	0.41	0.00	1	1, 2	1.05	0.99	0.10	62.4	150	1.04	1.00	0.12	4032	256^3; $\nu = 5 \times 10^{-4}$
R24	0.95OT+0.05H1	0.41	0.02	1	1, 2	1.95	0.92	0.51	32.0	150	2.03	0.92	0.57	1863	
R25**	0.5OT+0.5H1	0.40	0.31	1	1, 2	–	–	–	–	50	10.89	0.53	0.89	8.11×10^4	4 runs, 64^3 to 512^3 grids

or normal to the boundaries. In all cases, except for the TYGRS runs, the symmetries of the TG initial conditions are not enforced and can be broken.

Runs where noise of amplitude 10^{-x} relative to the energy in the host flow is added to both the kinetic and magnetic energy are denoted by "$+10^{-x}$" in the second column of Table 3.1. This noise has randomly generated phases with an energy spectrum of the form

$$E_{noise}(k) = \overline{E}_{noise} \exp\left(-\frac{(\log k - \log 2)^2}{2(\log 2)^2}\right) \ . \tag{3.5}$$

The noise introduces small perturbations in the initial magnetic helicity and cross helicity relative to the total energy depending on the random phases generated and the amplitude of the noise. Runs R1a–R14 involve TG initial condition either with or without noise.

Since the Taylor-Green runs have no helicity, different initial conditions are also studied in order to examine configurations with significant amounts of helicity. The "B Hx" type is one for which the velocity is a modified TG velocity, such that $u_x^{TG'} = -u_y^{TG}$, $u_y^{TG'} = -u_x^{TG}$, and $u_z^{TG'} = 0$, centered at wavenumber 2 or 3, and the magnetic field is the helical Beltrami ABC configuration centered at wavenumber $k_m = x$ with x equal to either 1, 2, or 3. The ABC magnetic field is given by

$$\begin{aligned} \mathbf{b}^{ABC} &= \overline{b}^{ABC} [B\cos(k_m y) + C\sin(k_m z),\ C\cos(k_m z) + A\sin(k_m x), \\ &\qquad A\cos(k_m x) + B\sin(k_m y)] \, . \end{aligned} \tag{3.6}$$

with $A = 0.9$, $B = 1.0$, and $C = 1.1$. Runs R18, R19, and R21a,b use this initial configuration

The OT type (used in run R22) denotes the generalization of the Orszag-Tang vortex to three dimensions, as studied in *Politano et al.* [1995], with the velocity and magnetic fields defined as

$$\mathbf{u}^{OT} = \overline{u}^{OT} [-2\sin(k_v y),\ 2\sin(k_v x),\ 0] \tag{3.7}$$

$$\mathbf{b}^{OT} = \overline{b}^{OT} [-2\sin(2k_m y) + \sin(k_m z),\ 2\sin(k_m x) + \sin(k_m z),\ \sin(k_m x) + \sin(k_m y)] \, . \tag{3.8}$$

For $\overline{u}^{OT} = \overline{b}^{OT}$ and $k_m = k_v$, $2H_C/E_T = 0.41$.

Finally, initial conditions that are mixtures of the above types are also studied. Runs R15 and R16 have the TG velocity and perturb the TG A magnetic field with an ABC Beltrami field

such that

$$\begin{aligned} b_x^{A+ABC} &= \overline{b}^{A+ABC} \left(\psi_1 \cos(k_{m1}x)\sin(k_{m1}y)\sin(k_{m1}z)\right. \\ &\qquad \left. +\psi_2 \left[B\cos(k_{m2}y) + C\sin(k_{m2}z)\right]\right) \\ b_y^{A+ABC} &= \overline{b}^{A+ABC} \left(-\psi_1 \sin(k_{m1}x)\cos(k_{m1}y)\sin(k_{m1}z)\right. \\ &\qquad \left. +\psi_2 \left[A\sin(k_{m2}x) + C\cos(k_{m2}z)\right]\right) \\ b_z^{A+ABC} &= \overline{b}^{A+ABC} \psi_2 \left[A\cos(k_{m2}x) + B\sin(k_{m2}y)\right]. \end{aligned} \tag{3.9}$$

The parameters ψ_1 and ψ_2 set the relative fractions of the Taylor-Green and ABC portions of the initial condition. Run R15 has $\psi_1 = 0.99$ and $\psi_2 = 0.01$ and run R16 has $\psi_1 = 0.9$ and $\psi_2 = 0.1$. Both of these flows have k_{m1} and k_{m2} such that both portions of the initial condition are at $k = 3$. Initial conditions such as these allow a perturbation in H_M without significantly perturbing H_C. In column two of Table 3.1, these initial conditions are referred to as "B wH" and"B iH" indicating that a weak (1%) or intermediate (10%) helical perturbation is added.

The series of runs labeled R17** use **b** from Eq. 3.9, but have a velocity that combines the TG and ABC flows in a similar fashion

$$\begin{aligned} u_x^{TG+ABC} &= \overline{u}^{TG+ABC} \left(\psi_1 \sin(k_{v1}x)\cos(k_{v1}y)\cos(k_{v1}z)\right. \\ &\qquad \left. +\psi_2 \left[B\cos(k_{v2}y) + C\sin(k_{v2}z)\right]\right) \\ u_y^{TG+ABC} &= \overline{u}^{TG+ABC} \left(-\psi_1 \cos(k_{v1}x)\sin(k_{v1}y)\cos(k_{v1}z)\right. \\ &\qquad \left. +\psi_2 \left[A\sin(k_{v2}x) + C\cos(k_{v2}z)\right]\right) \\ u_z^{TG+ABC} &= \overline{u}^{TG+ABC} \psi_2 \left[A\cos(k_{v2}x) + B\sin(k_{v2}y)\right]. \end{aligned} \tag{3.10}$$

In the case of the R17 runs, both **b** and **u** initial conditions have $\psi_1 = 0.93$ and $\psi_2 = 0.07$. The magnetic field is such that both portions of the initial condition are at $k = 3$, but the velocity has the Taylor-Green portion of the flow at $k = 2$ and the ABC portion at $k = 3$ initially. This initial condition allows for a perturbation in both H_M and H_C. Run R17+ is the same but with the ABC portion of the velocity at $k = 1$. These initial condition types are referred to as "U&B sH" in column two of Table 3.1 referring to a small (7%) helical perturbation.

R20 involves a velocity that is a combination of the modified TG velocity and a Beltrami ABC flow, such that

$$\begin{aligned} u_x^{TG'+ABC} &= \overline{u}^{TG'+ABC} \left(\psi_1 \cos(k_{v1}x)\sin(k_{v1}y)\cos(k_{v1}z)\right. \\ &\qquad \left. +\psi_2 \left[B\cos(k_{v2}y) + C\sin(k_{v2}z)\right]\right) \\ u_y^{TG'+ABC} &= \overline{u}^{TG'+ABC} \left(-\psi_1 \sin(k_{v1}x)\cos(k_{v1}y)\cos(k_{v1})\right. \\ &\qquad \left. +\psi_2 \left[A\sin(k_{v2}x) + C\cos(k_{v2}z)\right]\right) \\ u_z^{TG'+ABC} &= \overline{u}^{TG'+ABC} \psi_2 \left[A\cos(k_{v2}x) + B\sin(k_{v2}y)\right]. \end{aligned} \tag{3.11}$$

In run R20, $\psi_1 = 0.97$, $\psi_2 = 0.03$, and k_{v1} and k_{v2} are set such that both the TG and ABC portions are at $k = 2$. When combined with an ABC magnetic field this configuration results in $2H_C/E_T = 0.11$. This initial condition type is referred to as "U H2, B H2".

The type "ψ_1 OT+ψ_2 H1" (used in Runs R23a–R25**) is an initial condition where $\mathbf{u}$ is the OT vortex and $\mathbf{b}$ is a combination of OT and ABC, such that

$$\begin{aligned} b_x^{OT+ABC} &= \overline{b}^{OT+ABC} \left(\psi_1 \left[-2\sin(2k_{m1}y) + \sin(k_{m1}z)\right] + \psi_2 \left[B\cos(k_{m2}y) + C\sin(k_{m2}z)\right]\right) \\ b_y^{OT+ABC} &= \overline{b}^{OT+ABC} \left(\psi_1 \left[2\sin(k_{m1}x) + \sin(k_{m1}z)\right] + \psi_2 \left[A\sin(k_{m2}x) + C\cos(k_{m2}z)\right]\right) \\ b_z^{OT+ABC} &= \overline{b}^{OT+ABC} \left(\psi_1 \left[\sin(k_{m1}x) + \sin(k_{m1}y)\right] + \psi_2 \left[A\cos(k_{m2}x) + B\sin(k_{m2}y)\right]\right) \end{aligned} \tag{3.12}$$

where ψ_1 and ψ_2 set the relative fractions of OT and ABC respectively. Each of the flows of this type have $k_{m1} = k_{m2} = 1$.

3.2 Numerical Results

Figure 3.1 shows the temporal evolution of the Reynolds number and the ratio of magnetic to kinetic energy for roughly half the runs. Since the runs are performed at relatively modest Reynolds numbers and numerical resolutions, but for long times, the Reynolds numbers eventually enter a regime of exponential decay where nonlinearities are weak. The burst of energy for run R20 at $t \sim 250$ is associated with the end of a plateau in the ratio E_M/E_V and with a weak Lamb vector $(\mathbf{v} \times \boldsymbol{\omega})$ (see Figure 3.4). Examining E_M/E_V, it is clear that two main regimes develop in

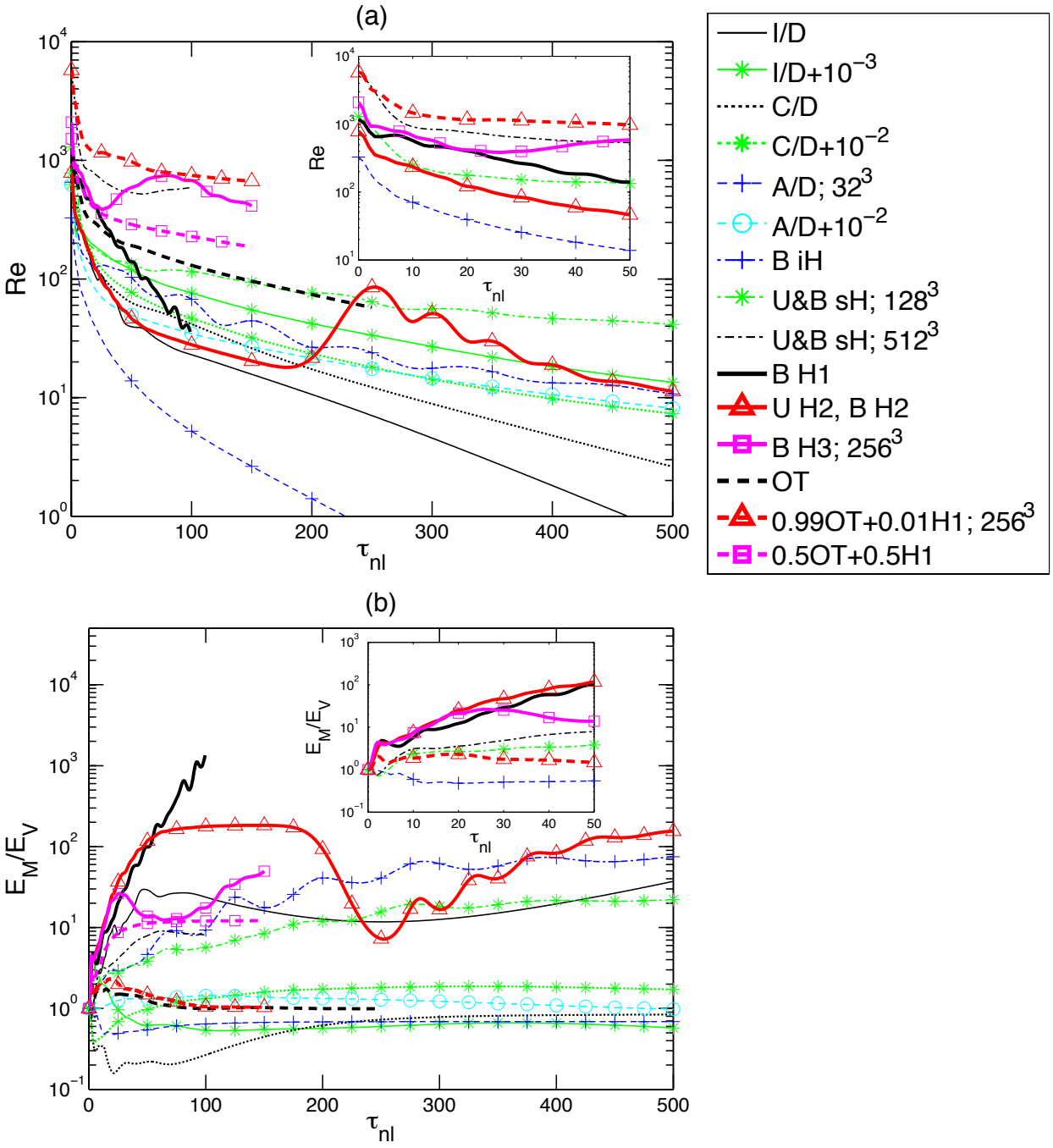

Figure 3.1: (a) Evolution of $Re \equiv u_{rms} L_{int}/\nu$ as a function of time for roughly half of the flows from Table 3.1. The plot has linear-logarithmic axes and time is measured in units of τ_{NL} for each run. The inset shows a blow-up of the results at early times for a subset of the plotted runs. Each run is indicated by symbols and colors that are given in the legend, a choice that is also followed in Figure 3.4. (b) E_M/E_V for the same runs and again with linear-logarithmic axes. Many runs gather around quasi-equipartition, either above or below. For some runs, mostly those in which H_M/E_T grows significantly (such as runs R16 – R21b), E_M/E_V gets substantially larger than unity.

these runs; one with near equipartition of energy (within a factor of 2) and one where the magnetic energy dominates by a substantial amount. Values of E_M/E_V are given at several points during the computation for all of the runs in Table 3.1. The two runs (R10c and R11b) performed on a grid of 32^3 points have Re getting too low and as a result behave considerably differently from the other TG A runs on grids of 64^3 and 128^3 points. Also note that run R15, which is the TG A flow perturbed by 1% ABC magnetic field, moves towards a kinetically dominated state; by the end of the run, this flow has kinetic energy dominating over magnetic energy by approximately a factor of 10 in the gravest mode.

3.2.1 The Role of Accuracy and Symmetries

The ensemble of runs analyzed in this chapter is shown in Figure 3.2 in a plane first introduced in *Stribling and Matthaeus* [1990, 1991], which delineates, in terms of E_T, the relative importance of H_M and H_C. A peculiar feature of the I and A Taylor-Green runs is that, unless perturbed, they stay where they started, even though in these runs the symmetries are not imposed at all times. This may be related to the fact that it can be shown in the context of the hydrodynamic equations that symmetries are preserved by the dynamical evolution, a result that one may be able to extend to the MHD case [*Bardos et al.*, 2013]. In the presence of perturbations, they do cover parameter space and evolve towards configurations with either strong H_M (and thus high ratio E_M/E_V, as in the case of runs R16 and R17**), or strong H_C with near equipartition of kinetic and magnetic energy.

In single precision and for long times, the I flow is perturbed by the accumulated round-off errors and it evolves toward another attractor (see Figure 3.3). Whereas the accurate computation that maintains all symmetries evolves toward presumably a magnetically-dominated Taylor state, the perturbations introduced by lower precision lead to a quasi-equipartition of energy. This same behavior, where the single precision computation evolves towards a different attractor after sufficiently long times, is not evident in either the A or C Taylor-Green flows; however similar effects are observed when random noise is explicitly added to these initial conditions.

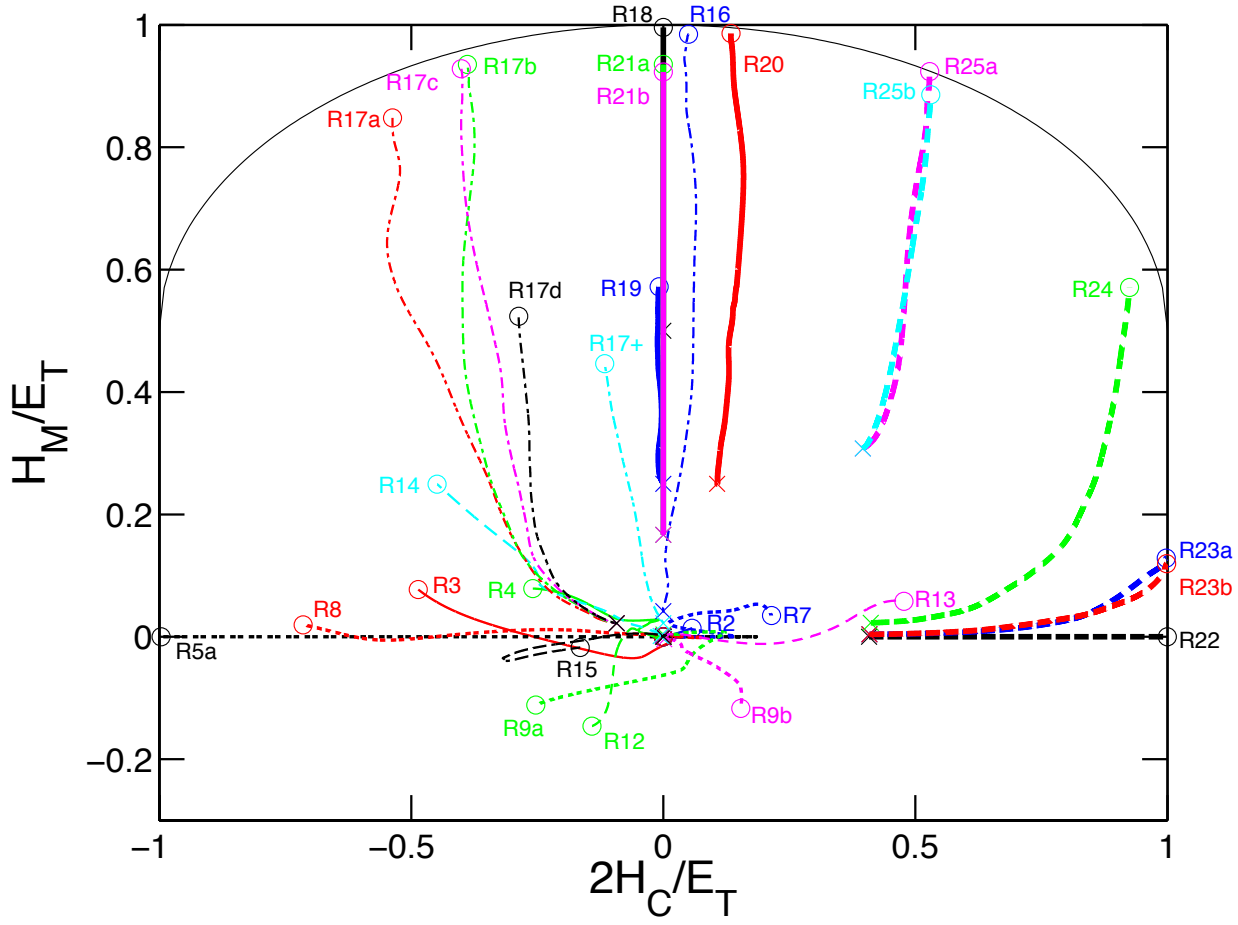

Figure 3.2: Trajectories taken through the $(2H_C/E_T,\ H_M/E_T)$ parameter space for the runs in Table 3.1. The start positions for each run are marked with "x" and the positions at the final time of the run are marked with "o." Each curve is labeled with the run number from Table 3.1 near the end point. Three runs (R5a,b and R6) follow the black dotted line which goes from the origin to the point (-1,0) and 8 runs (R1a,b, R10a–R10d, and R11a,b) remain at the origin of the parameter space. The two series (R17** and R25**) have "**" replaced with letters that increase from a to d for increasing resolutions to mark the individual runs. Only the 64^3 and 512^3 runs are shown from R25** because all resolutions followed nearly identical trajectories. The energy minimization principle predicts that flows will move towards the boundaries of this space; that is $2H_C/E_T = \pm 1$ when the end value of $H_M/E_T < 0.5$, and on the marked ellipsoidal curve bounding the upper portion of the plot when the end value of $H_M/E_T \geq 0.5$. The parameter space is symmetric for negative values of H_M/E_T.

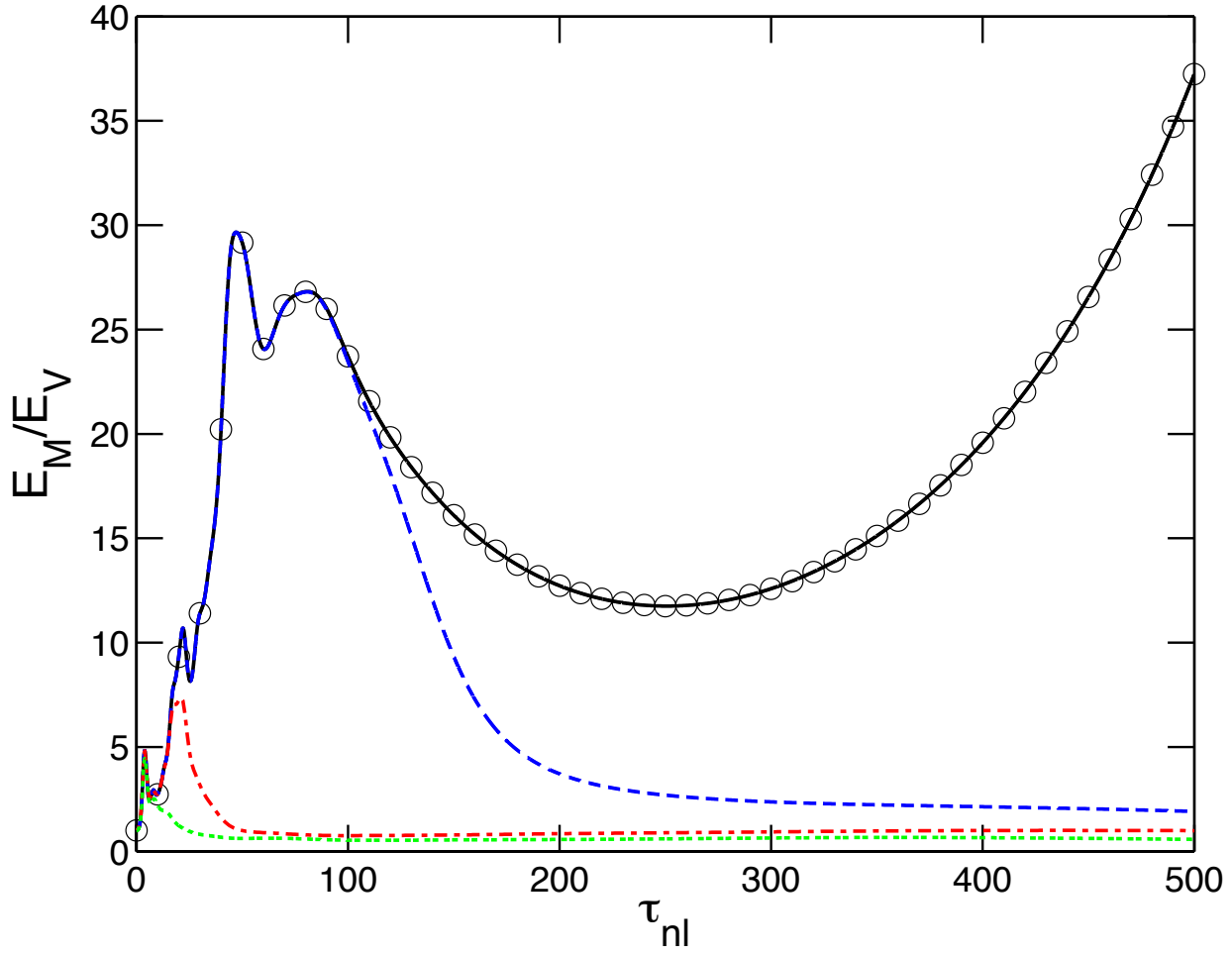

Figure 3.3: Comparison of E_M/E_V for the Taylor-Green I flow between the two codes, one implementing symmetries (run R1b, black circles), the other one not, (run R1a, black solid line), both in double precision. Another run using single precision (run R2) is given by the blue dashed line. The double precision in GHOST is sufficient to maintain the symmetries up to $t = 500\tau_{NL}$. Note the excellent agreement between the three computations up to $t \sim 100\tau_{NL}$, after which the single precision run departs from the others and evolves towards quasi-equipartition (at the final time, $E_M/E_V \sim 2$, as often observed in the solar wind [*Matthaeus and Goldstein*, 1982]).The red dashed-dotted line and the green dotted line are the Taylor-Green I flow with added random noise of relative amplitude 10^{-6} (run R3) and 10^{-3} (run R4) respectively. Note that added noise behaves similarly to the single precision computation, but departs from the other runs and goes towards quasi-equipartition at earlier times.

The C flow also exhibits unique behavior as compared to the I and A flows in that, over the course of the computation, the accurate double precision run does not remain at the origin of the plane and instead moves to a state with $2H_C/E_T = -1$ and $H_M/E_T = 0$. As a result, the C flow without perturbations reaches an equipartitioned state, as opposed to a magnetically dominated state.

Runs are also performed with a more controlled and specific perturbation of the Taylor-Green symmetries by adding a fraction of a Beltrami ABC flow to **b** and/or **u** of the TG initial condition in the A configuration, which perturbs the flow explicitly with non-zero H_M and H_C (runs R15–R17+ and R18–R21b). By varying the amount of helical ABC relative to non–helical Taylor-Green in the magnetic field, the value of H_M/E_T can be adjusted in a controlled manner at $t = 0$. By also adding a fraction of ABC to **u**, a set amount of $2H_C/E_T$ can additionally be introduced to the flow. With larger perturbations to H_M and H_C, such as in runs R16 and R17$**$, the symmetries are clearly broken and the runs reach the boundaries of the parameter space as predicted by the energy minimization principle (see Figure 3.2). Note that run R17d, which is performed on a grid of 512^3 points, is only run for $100\tau_{NL}$. If this run were continued to longer times, as the other three R17** runs are, this run would likely reach the boundary. In the case of run R16, only the magnetic field initial condition is perturbed with 10% ABC, and the flow achieves a magnetically dominated state with nearly maximal H_M/E_T. The four R17** runs, which all have 7% ABC in both the velocity and magnetic field initial conditions, but are performed at different Re, evolve to a state on the boundary with both nonzero H_M/E_T and $2H_C/E_T$ when given enough time. Note that although the four runs have the same initial conditions, they have taken different paths through the parameter space with differing Re due to the effect of small perturbations.

3.2.2 Relative Growth of Magnetic Helicity

According to the equations written in Chapter 2.3.3, the helical invariants play a central role in the evolution of MHD turbulence. Since the unperturbed Taylor-Green flows have no helicity, the evolution of several helical configurations that have been studied in the literature are examined,

namely the ABC (Beltrami) flows, the Orszag-Tang vortex, and some perturbations of such flows (see Chapter 3.1 and Table 3.1 for definitions).

The Orszag-Tang vortex, which has $H_M = 0$, becomes highly correlated, but with the inclusion of some H_M, it evolves toward states which, as H_M/E_T increases, are increasingly dominated by E_M. With very small additions of magnetic helicity (runs R23a and R23b), H_M/E_T grows to modest values at which $2H_C/E_T$ can still obtain a value of one and the flow has equipartition between E_M and E_V. However, with even a slightly larger addition of H_M (see runs R24 and R25**), the growth of H_M/E_T begins to dominate and the flow moves towards more magnetically dominated states. Similarly, unperturbed ABC flows, with strong H_M, remain uncorrelated if initially so; but when perturbing them by adding some H_C, as in run R20, they follow similar evolutions but stay away from the singularity that occurs at maximum H_M/E_T and $H_C = 0$.

3.2.3 Vector Alignment in MHD Turbulence

Relative alignments of dynamical fields (see Chapter 2.1.1 for definitions) are shown in Fig. 3.4 for many runs, using the same line style and color encoding as in Fig. 3.1. Several runs reach an Alfvénic states ($\sigma_C \sim \pm 1$) and a few stay at low values. It has been known for some time that the correlation between $\mathbf{u}$ and $\mathbf{b}$ tends to grow with time [e.g. *Pouquet*, 1993].

H_M seems more discriminating insofar as the long-time behavior of the runs: either H_M/E_T remains rather low, or else it approaches its maximal value. The runs that approach near maximal values of H_M/E_T are those in which a sufficient amount of magnetic helicity is present in the initial condition. In Figure 3.2, as well as in Figure 3.4, it can be seen that all the runs which attain large values of H_M/E_T have at least slightly larger initial values of magnetic helicity than those that remain near zero. On the other hand, σ_V shows a more varied set of behavior, with sometimes strong fluctuations between aligned and perpendicular fields, as for example in Run R20 (thick solid line, red triangles), which evolves towards strong H_M (see the map in Fig. 3.2). Note that Run R25 (thick dash line, purple squares) is likely to evolve in a similar manner.

Aside from the global alignments examined in Figure 3.4, the build up of point-wise correla-

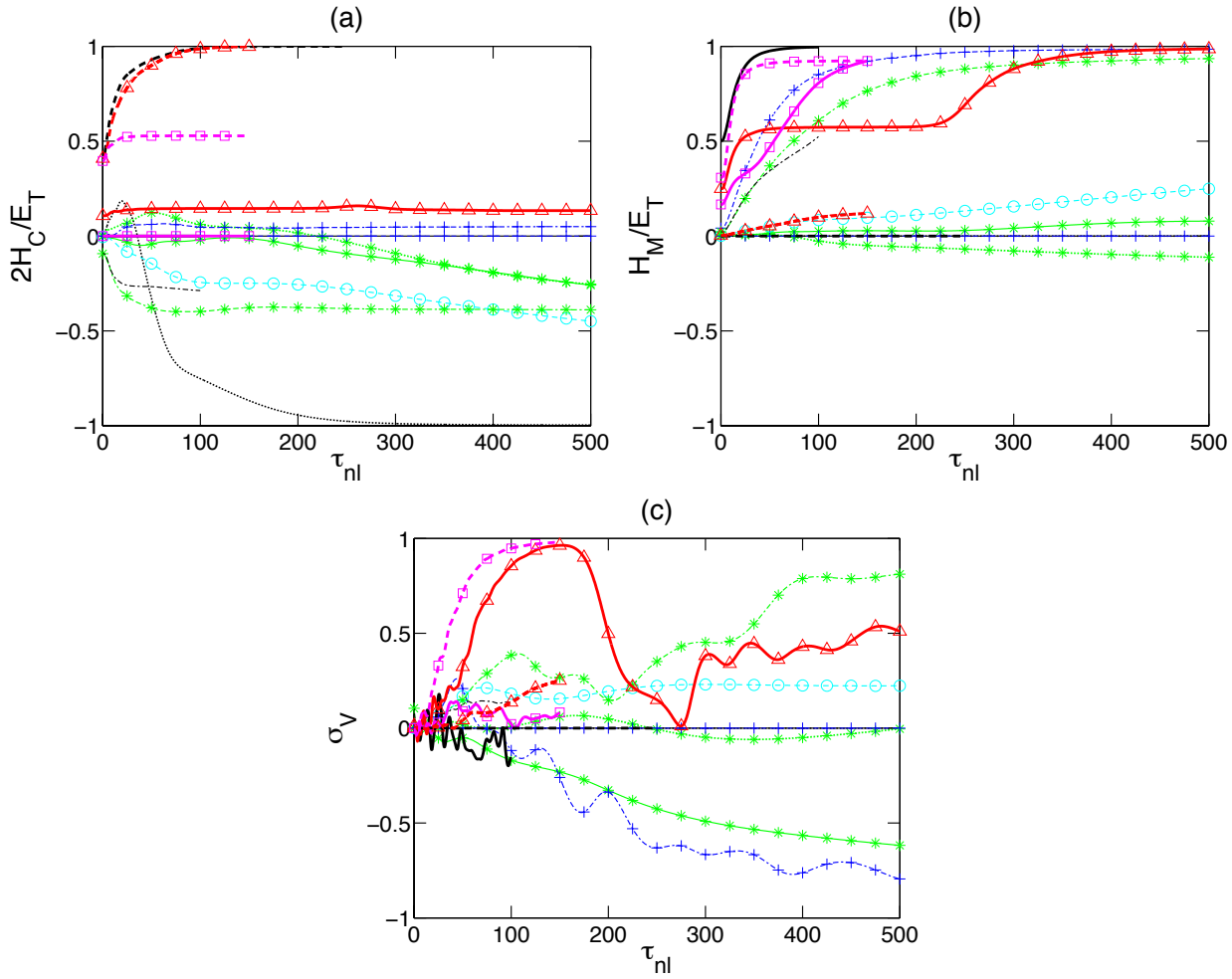

Figure 3.4: Temporal evolution of helicity in relative terms for the same runs as in Figure 3.1 showing (a) $2H_C/E_T$, (b) H_M/E_T, and (c) σ_V. The symbols and color scheme are the same as that in Figure 3.1. Note the clear distinction between the evolution for the two invariant quantities (either staying at values close to zero or close to their extrema) and the more varied evolution for σ_V, although its evolution is also influenced by magnetic helicity (see Eq. 2.65).

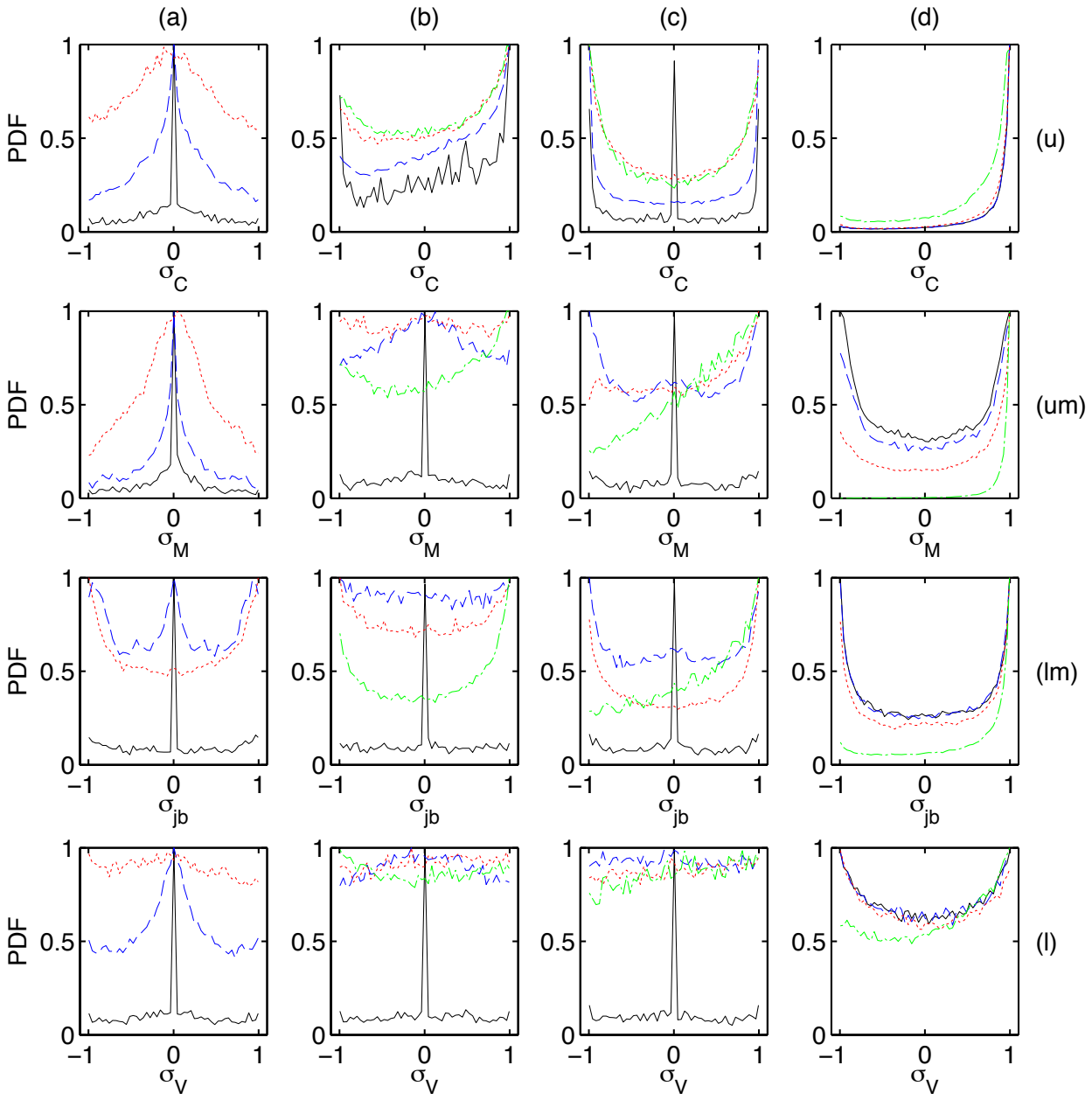

Figure 3.5: Probability distribution functions at $t = 10\tau_{NL}$ of vector alignments (cosine of angle) σ_C (row u), σ_M (row um), σ_{jb} (row lm), and σ_V (row l). Vector alignments are defined in Eq. 2.22 and 2.23. All PDFs are normalized to their maximum value to aid in comparison. Column (a) shows Taylor-Green "I" runs R1a (black solid line), R3 (blue dashed line), and R4 (red dotted line). Column (b) shows Taylor-Green "C" runs R5a (black solid line), R7 (blue dashed line), R8 (red dotted line), and R9a (green dashed-dotted line). Column (c) shows Taylor-Green "A" runs R10a (black solid line), R12 (blue dashed line), R14 (red dotted line), and R16 (green dashed-dotted line). Column (d) shows OT flow runs R22 (black solid line), R23a (blue dashed line), R24 (red dotted line), and R25 (green dashed-dotted line). See Table 3.1 for the nomenclature of the runs.

tions between vectors is known to occur in turbulent flows. *Matthaeus et al.* [2008] examined rapid alignment over a few τ_{NL} in σ_C, which was linked to alignment of $\mathbf{b}$ with either pressure gradients or shear, and evidence for this type of alignment was found in both DNS of MHD flows and the solar wind. Point-wise alignments were further studied in detail by *Servidio et al.* [2008] with 3D computations, where the strongest alignment was found to be σ_{jb} (corresponding to a weakening of the Lorentz force).

Figure 3.5 shows probability distribution functions (PDFs) of several vector alignments for several of the flows (see caption) at $t = 10\tau_{NL}$. Row (u) examines the alignment between $\mathbf{u}$ and $\mathbf{b}$ (related to H_C), row (um) examines the alignments between $\mathbf{a}$ and $\mathbf{b}$ (related to H_M), row (lm) looks at the alignment between $\mathbf{b}$ and $\mathbf{j}$ (related to the Lorentz force), and row (l) considers the alignment between $\mathbf{u}$ and $\boldsymbol{\omega}$ (related to H_V). At $t = 0$, all unperturbed flows have a strong central peak corresponding to orthogonality of vectors and thus strong nonlinearities, except for the OT case (column d) for which σ_M peaks symmetrically at values slightly greater and slightly less than zero and σ_C indicates that there is a significant fraction of highly aligned velocity and magnetic field vectors.

These PDFs confirm the results illustrated in Figure 3.2 in showing an evolution towards either alignment of $\mathbf{u}$ and $\mathbf{b}$, or of $\mathbf{b}$ and $\mathbf{a}$, once the flows are perturbed. The runs have a tendency for more alignment with larger perturbations and, in many cases, for smaller scale quantities (as when contrasting σ_M and σ_{jb}). The "I" flows (column a) are in fact the harder to perturb insofar as alignment does not really develop and one only observes a widening of the PDFs around zero, i.e. a distribution of angles that remain close to $\pi/2$. Although, $\mathbf{b}$ and $\mathbf{j}$ develop some alignment, particularly for the stronger perturbation. For the "C" flow family of runs (column b), a perturbation at the level of 10^{-4} simply widens the distribution of σ_M (blue dashed curve), but increasing this perturbation can lead to an increased amount of alignment ($\sigma_M = \pm 1$). The perturbations are less significant for σ_C in the sense that the PDF is changed but the overall distribution (its shape) is similar in all cases.

Concerning the A configuration (column c), almost symmetric PDFs of σ_C develop with more

alignment ($\sigma_C \sim \pm 1$) in the perturbed cases. Clear asymmetry for σ_M and σ_{jb} develops with the strongest perturbations (runs R14 and R16). Finally, the Orszag-Tang flow (column d) starts from a different configuration of vectors, and its evolution as it is more perturbed is not so dramatically different (except for the green dash-dotted line which corresponds to an initial condition with a 50% OT-50% ABC mixture).

On the other hand, σ_V does not seem to follow such a clear-cut organization, unless H_M is strong and then H_V does follow H_M and grows in relative terms, under the influence presumably of Alfvén waves due to the large-scale magnetic field, as predicted in *Pouquet et al.* [1976]. However, the A and C flows show less weakening of the advection term than for the other alignments, with rather flat PDFs for σ_V.

3.2.4 Ratios of Timescales and Energies

Finally the relative role of **u** and **b**, in terms of energy spectra and timescales, is examined for the runs performed at the highest Reynolds number, and thus with the largest extent of the inertial range (and numerical grid resolution). Two ratios are examined; $E_M(k)/E_V(k)$ and of the eddy turnover time to the Alfvén time ($\tau_{NL}(k)/\tau_A(k)$), with $\tau_A(k)$ being based on the magnetic field in the largest scale mode. These computations are performed near the peak of dissipation, when the turbulence is developed and the Reynolds number has not yet substantially decreased.

The ratio of timescales behaves as expected when evaluating the turnover time on the energy spectrum variation with wavenumber, which can be seen in Figure 3.6. For all flows, $\tau_{NL}(k)/\tau_A(k)$ increases with increasing wavenumber because of the way these two characteristic times change with scale, i.e. $1/k$ for τ_A and $[k^3 E_V(k)]^{-1/2}$ for the eddy turnover time. On the other hand, and again for all flows, $E_M(k)/E_V(k)$ is constant and of order unity (but systematically slightly above, as also regularly observed in the solar wind) for most of the wavenumber range except at the largest scales. The large scales are dominated by the initial conditions and the reinforcement of E_M in the case of runs dominated by an evolution towards the top of the map displayed in Fig. 3.2, corresponding to cases with strong H_M. $E_T(k)$, $E_M(k)$, and $E_V(k)$ for the R17** run is also shown in Fig. 3.6c; of

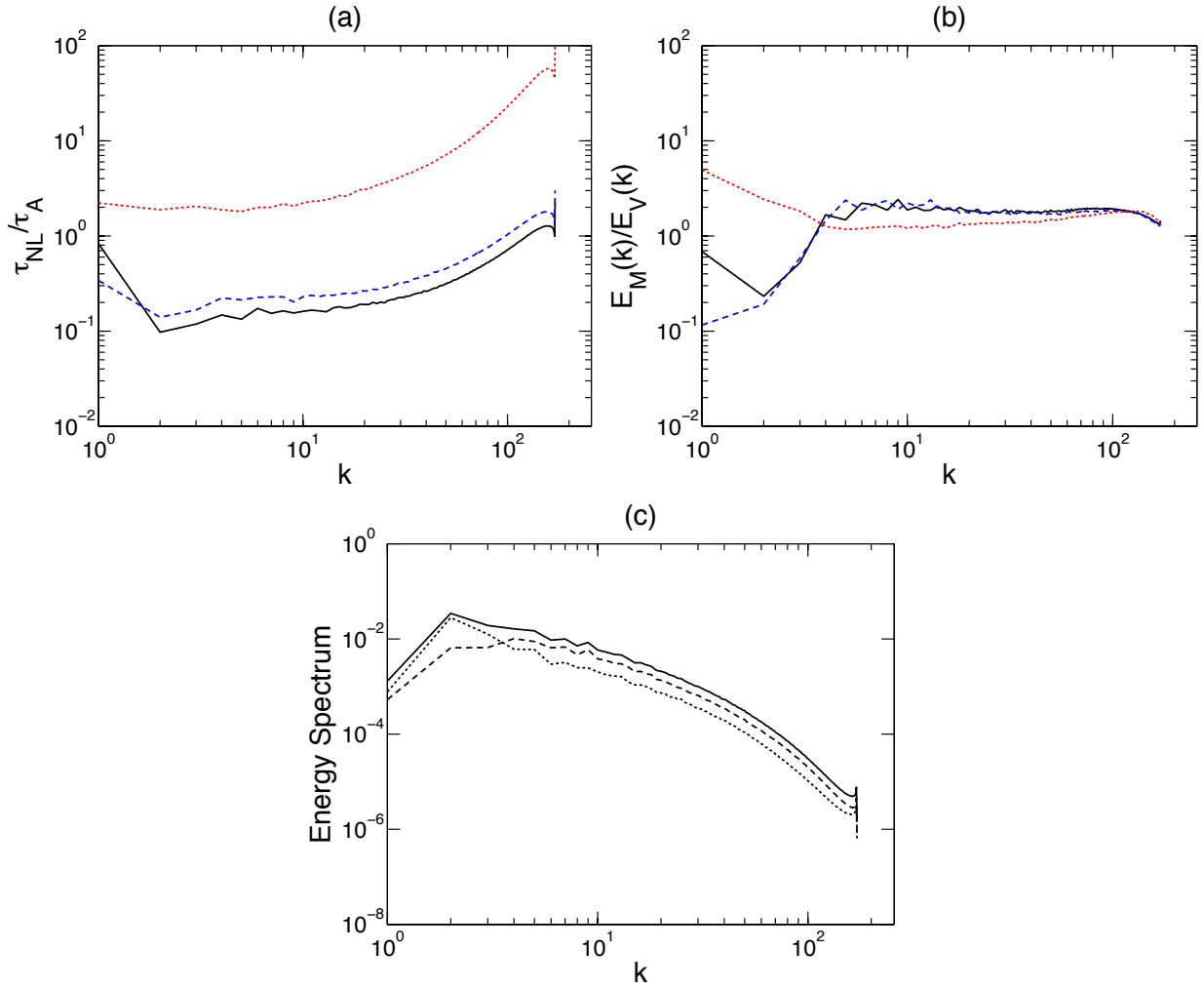

Figure 3.6: (a) $\tau_{NL}(k)/\tau_A(k)$ and (b) $E_M(k)/E_V(k)$ as a function of wavenumber at peak of dissipation for the following computations performed on grids of 512^3 points (see Table 3.1 for the nomenclature): run R17** (A flow with 7% ABC, black solid line), run R17+ (variant of A flow with 7% ABC, blue dashed line), and run R25 (50% OT and 50% ABC, red dotted line). Note the constancy of quasi-equipartition of energy throughout the inertial range, to be contrasted with the increase in the ratio of characteristic time scales in that same range. In panel (c), $E_T(k)$ (solid line), $E_M(k)$ (dashed line), and $E_V(k)$ (dotted line) for R17** on the 512^3 grid are given.

course, the resolution of these runs makes it difficult to distinguish whether a $k^{-5/3}$ or $k^{-3/2}$ scaling is favored here. Note that at later times of the order of three times the peak of dissipation, these results still holds but with, in all cases displayed here, an increase in $E_M(k)/E_V(k)$ at the largest excited scales, by a factor of 2 to 40 (not shown). All other runs of this study behaved similarly, as long as the Reynolds number is sufficiently high for turbulent mixing to take place.

3.3 Conclusions

In this chapter, we tackled the problem of long-time properties of turbulent flows in MHD at unit magnetic Prandtl number, using direct numerical simulations with grids of up to 512^3 points and periodic boundary conditions appropriate for homogeneous turbulence. We chose a variety of flows and examined the effect of perturbing the initial conditions with different levels of random noise, as well as modifying the ideal invariants in the fluid at constant E_T, namely H_M and H_C. We show that, independent of the Reynolds number (up to a maximum Reynolds number of $\approx 1.2 \times 10^4$), flows evolve to a state based on basic physical principles, namely using the statistical equilibria of a truncated number of modes with the given invariants combined with an energy minimization principle [*Stribling and Matthaeus*, 1990].

The Taylor-Green configurations, studied in *Lee et al.* [2010] for their energetic properties, depart from their strong symmetries given a strong-enough perturbation, as can be encountered in high Reynolds number flows. *Dallas and Alexakis* [2013], building on the work presented here, have examined in greater detail the role of Reynolds number in breaking the Taylor-Green symmetries over short timescales. With symmetries broken, the turbulence then can evolve toward different characteristic behaviors as to the amount of magnetic and cross helicity it can support, which can depend on the perturbation (whether it has H_C or H_M), leading the flows to different end-states. It is not clear however if, when studying these flows at substantially higher Reynolds numbers, as was done in *Lee et al.* [2010] for the Taylor-Green flows in MHD but, contrary to *Lee et al.* [2010], not imposing the symmetries at all time, one will still have three different scaling laws for the total energy spectra for these three configurations. This work also confirms that statistical

mechanics, with an energy minimization principle, is an excellent predictor for the behavior of turbulent flows, as argued in *Stribling and Matthaeus* [1990], and studied at lower resolutions resolutions in *Stribling and Matthaeus* [1991]. The conclusion on the validity of statistical mechanics for dissipative turbulent flows in MHD is reached using a parametric study for a variety of initial conditions and with grids of up to 512^3 points and Reynolds numbers of up to 12000 (values taken at $t = 0$), a substantial improvement over previous studies.

It could be asked, "How generic are the flows studied in this chapter?" One could think in terms of random initial conditions, as initially done in *Stribling and Matthaeus* [1990, 1991]. The view in the random case is that noise is generic in experimental, geophysical, and astrophysical flows, and the question is what emerges over time through the nonlinear interactions of random modes. However, turbulence would be a boring subject if it was purely Gaussian. In fact, phase relations are known to play an important role in the structuring of turbulent flows, with a wealth of well-defined structures, be it vortex filaments for fluids, or vortex and current sheets in MHD; which can roll-up at sufficiently high Reynolds number, as observed in high-resolution DNS of MHD flows [*Pouquet et al.*, 2010]. The instabilities of such structures eventually lead to energy dissipation, as measured in the solar wind [e.g. *Sorriso-Valvo et al.*, 2007; *Marino et al.*, 2008; *Stawarz et al.*, 2009, 2010; *Osman et al.*, 2011].

On the other hand, the initial conditions of a turbulent event, in the solar wind, magnetosphere, or interstellar medium, for example, may well come from an instability when, for some reason, the fluid exceeds a threshold. One can think, for example, of the Kelvin-Helmholtz instability as discussed in the context of magnetospheric turbulence in Chapter 6. Another example could be nonlinear couplings of weak waves, overturning, and Kelvin-Helmoltz instabilities, which lead to enhanced diffusion in stably stratified media such the atmosphere or oceans of Earth [*Ivey et al.*, 2008]. Such instabilities near threshold may well be represented by a few large-scale modes, which may result in different alignment properties. Finally, one could point out that, in principle, universality (within a given class) holds whatever the initial conditions.

Quasi-equipartition between E_V and E_M is expected, on the basis of mixing of complex

systems with a large number of degrees of freedom, although as shown in *Frisch et al.* [1975], H_M, alone or in the presence of H_C, may well prevent this from happening. What this study has shown is that, in some cases with strong phase relationships such that the nonlinear terms are weakened considerably through alignment of the relevant fields (vorticity, velocity, magnetic field, and current), other solutions are reachable with quite different properties.

Chapter 4

Small-Scale Behavior in Hall Magnetohydrodynamic Turbulence

One way to begin looking at kinetic effects in a turbulent environment numerically is to consider more accurate approximations to the kinetic equations, such as the HMHD equations discussed in Chapter 2.1. While not a complete model of the kinetic scales, HMHD begins to incorporate kinetic effects by allowing for the decoupling of ion and electron motions at scales below the ion inertial length through the addition of the Hall term in Ohm's Law. The Hall effect has been studied extensively in the context of laminar magnetic reconnection using Harris sheet configurations and HMHD is found to be the minimum plasma model necessary to obtain fast reconnection rates comparable to those obtained from more complete kinetic plasma simulations [*Biskamp et al.*, 1997; *Shay and Drake*, 1998; *Birn et al.*, 2001]. Signatures of the Hall term have been found in the Earth's magnetosphere [*Mozer et al.*, 2002; *Borg et al.*, 2005] and in laboratory plasmas [*Yamada et al.*, 2006]. Under some parameter regimes in the solar wind, a steepening of the spectral slope of the turbulence from either a Kolmogorov spectrum [*Matthaeus and Goldstein*, 1982] or the Iroshnikov-Kraichnan spectrum [*Mininni and Pouquet*, 2007], has been associated with the ion inertial length [*Chen et al.*, 2014]. So-called plasmoids, as observed in the magnetotail by the Cluster spacecrafts, are viewed as the signature of multiple reconnection events in the Hall regime and are linked to substorms [*Liu et al.*, 2013]. The Hall effect and turbulence has also been found to have an impact on accretion in protoplanetary discs [*Simon et al.*, 2015].

As discussed in Chapter 2.3.1, spectra of HMHD turbulence are expected to be steeper than MHD at scales below d_i in both the strong and weak turbulence regimes, with a power law slope

of $-7/3$ (see Eq. 2.58) for the magnetic field in strong turbulence [*Galtier*, 2006]. Steepening of the solar wind spectra above ω_{ci} has been attributed to HMHD effects [*Ghosh et al.*, 1996; *Krishan and Mahajan*, 2005; *Alexandrova et al.*, 2008]. Some numerical simulations have reported power law slopes similar to $-7/3$ [*Hori and Miura*, 2008; *Shaikh and Shukla*, 2009; *Miura and Hori*, 2009]; however, it is difficult to determine the spectral slope for HMHD at the numerical resolutions available today. *Meyrand and Galtier* [2012] found that right and left circularly polarized fluctuations have different power law slopes with right polarizations showing a $-7/3$ slope and left polarizations showing a $-11/3$ slope and showed heuristically that the magnetic field should follow these power laws.

Previous studies of HMHD turbulence have found that although MHD scales control some important average properties of the system, such as the energy decay rate [*Matthaeus et al.*, 2003], the structures present in the flow can be significantly altered. *Miura and Hori* [2009] and *Miura and Araki* [2011] examined the current and vorticity structures and found that there are smaller scale structures present in HMHD; they speculated the much lower amplitude vorticity structures were excited by the enhanced small-scale magnetic field activity in HMHD. Larger scale vorticity structures were found to be potentially more tubular than in MHD, although roll-up of vorticity sheets as well as current sheets have also been observed in MHD turbulence [*Mininni and Pouquet*, 2009]. 2D simulations have found reconnection sites in the turbulence become similar in structure to laminar studies of HMHD reconnection, which exhibit bifurcated current sheets and quadrupolar magnetic fields [*Donato et al.*, 2012]. *Dmitruk and Matthaeus* [2006] found that while the magnetic field was largely unchanged by the addition of the Hall effect, the electric field was more intermittent. Using theoretical calculations and low resolution simulations, *Mininni et al.* [2007] found that the Hall effect alters the coupling between the magnetic field and velocity and can result in a backscattering of energy which is not seen in MHD. Reduced HMHD models, which describe the system in the presence of a strong background magnetic field, have also been examined and it was found that in this context structures widen and generate internal eddies and currents resulting in an apparent reduction in intermittency [*Martin et al.*, 2012; *Rodriguez Imazio et al.*, 2013; *Martin*

et al., 2013].

In this chapter, 3D DNS are used to examine the behavior of HMHD turbulence in the absence of forcing. The GHOST code discussed in Appendix A.1 is again used for the computations in this chapter. The features in both Fourier and configuration space are examined to better understand the small-scale behavior. In Chapter 4.1 the initial conditions used in the DNS are discussed. Chapter 4.2.1 presents the numerical results in Fourier space and provides an interpretation for the behavior. Chapter 4.2.2 discusses the numerical results in configuration space. Chapter 4.2.3 briefly presents runs using hyperdiffusivities and compares the results to the traditional diffusivity runs presented in Chapter 4.2.1 and Chapter 4.2.2. Chapter 4.3 summarizes the results and discusses some possible implications for collisionless plasmas. In this chapter, values of d_i are given as the dimensionless ϵ_H, where the value of L_c is set such that the dimensionless simulation box size is $(2\pi)^3$.

4.1 Initial Conditions

Two types of initial conditions are examined in this chapter, one using a prescribed set of phase relationships, and the other one using randomly phased fluctuations. Details about the runs are listed in Table 4.1. The first set of initial conditions are a modification of the Orszag-Tang vortex based on *Biskamp and Welter* [1989] and extended to 3D in a manner similar to *Politano et al.* [1995]

$$\mathbf{b}^{OT} = \overline{b}\left[\sin(y+4.1)+\sin(z),\ -2\sin(2x+2.3)+\sin(z),\ \sin(x)+\sin(y)\right]\ , \tag{4.1}$$

$$\mathbf{u}^{OT} = \overline{u}\left[\sin(y+0.5),\ -\sin(x+1.4),\ 0\right]\ . \tag{4.2}$$

The values of $\overline{b}$ and $\overline{u}$ are set such that $\langle|\mathbf{b}^{OT}|^2\rangle = 0.64$ and $\langle|\mathbf{u}^{OT}|^2\rangle = 1.36$ initially, resulting in nearly equal values of $\langle|\mathbf{j}|^2\rangle$ and $\langle|\boldsymbol{\omega}|^2\rangle$. Runs are performed at resolutions using 256^3, 512^3, and 768^3 grid points in a cubic box and with periodic boundary conditions. At all resolutions $\epsilon_H = 0.0$ or 0.2. Additionally at 256^3, runs with $\epsilon_H = 0.1$ and 0.5 are performed. At 768^3, the initial condition for the $\epsilon_H = 0.2$ run is taken to be the peak of dissipation from the 768^3 $\epsilon_H = 0.0$ run.

Table 4.1: Resolution, value of ν (which is the same as the value of η), value of ϵ_H, and eddy turn-over time τ_{NL} at the peak of Ω_T (or $\mathcal{P}_T$ for the hyperdiffusive runs) for the 16 runs performed in this chapter. In the Run ID, OT stands for the Orszag-Tang initial condition, R stands for the random initial condition, M stands for MHD, H stands for HMHD, the number after H gives $10\epsilon_H$, and K4 indicates the use of hyperdiffusivity. Run OTH2c is started from the OTMc peak of Ω_T.

Run ID	Resolution	ν or ν'	ϵ_H	τ_{NL}
OTMa,b,c	256^3, 512^3, 768^3	1×10^{-2}, 5×10^{-3}, 3.3×10^{-3}	0.0	5.77, 4.39, 4.01
OTH1	256^3	1×10^{-2}	0.1	5.88
OTH2a,b	256^3, 512^3	1×10^{-2}, 5×10^{-3}	0.2	6.07, 5.11
OTH2c	768^3	3.3×10^{-3}	0.2	4.11
OTH5	256^3	1×10^{-2}	0.5	6.26
RMa,b,c	128^3, 256^3, 512^3	2×10^{-2}, 1×10^{-2}, 5×10^{-3}	0.0	3.61, 3.43, 3.16
RH2a,b,c	128^3, 256^3, 512^3	2×10^{-2}, 1×10^{-2}, 5×10^{-3}	0.2	3.26, 3.07, 2.84
RH2K4a,b	256^3	2.5×10^{-5}, 7×10^{-6}	0.2	2.53, 2.30

This method of starting an HMHD run from the peak of dissipation was tested at 256^3 resolution and produced comparable results to a 256^3 HMHD run started from scratch using the Orszag-Tang initial conditions. The initial relative helicities for all Orszag-Tang runs are $\sigma_M \sim \sigma_C \sim -0.2$, and $\sigma_V \sim 0.0$. Furthermore, at $\epsilon_H = 0.2$, $\sigma_G \sim -0.28$ whereas for both $\epsilon_H = 0.1$ and 0.5, $\sigma_G \sim -0.26$ initially. Runs using this initial condition are denoted with an OT in Table 4.1.

The second set of initial conditions initialize the fields $\mathbf{u}_L$ and $\mathbf{u}_R$ with random phases and power spectra which follow the form $E_{L,R}(k) = C_{L,R}k^4\exp(-k^2/k_0^2)$. The wavenumber k_0 is set such that the spectra peak at $k = 2$ and C_L and C_R are set such that $\langle|\mathbf{u}_L|^2\rangle = 1.00$ and $\langle|\mathbf{u}_R|^2\rangle = 0.5$. Noting that $\epsilon_H^2\langle|\mathbf{j}|^2\rangle = \langle|\mathbf{u}_R|^2\rangle + \langle|\mathbf{u}_L|^2\rangle - 2\langle\mathbf{u}_R\cdot\mathbf{u}_L\rangle$, the correlation between $\mathbf{u}_L$ and $\mathbf{u}_R$ is set such that the initial $\langle|\mathbf{j}|^2\rangle$ and $\langle|\boldsymbol{\omega}|^2\rangle$ are nearly equal. In the case of MHD, identical initial conditions to the HMHD case are used even though $\epsilon_H = 0$ in MHD. Random runs are performed at resolutions 128^3, 256^3, and 512^3 with $\epsilon_H = 0.0$ and 0.2 in all cases. Initially $\sigma_M \sim 0.24$, $\sigma_C \sim 0.01$, $\sigma_V \sim -0.04$, and $\sigma_G \sim 0.17$. Two HMHD runs with this initial condition have also been performed using hyperdiffusivity for comparison with the regular diffusivity results. This initial condition is denoted with an RM or RH (for MHD and HMHD respectively) in Table 4.1.

Physically the OT configuration is structured with an X-point centered on a stagnation point (with a sinusoidal variation in the third direction) so that current sheets are known to form rather

rapidly. In the formulation of the OT configuration presented here, phase shifts are introduced that break some of the symmetry present in the traditional configuration. On the other hand, random initial conditions are possibly more representative of a natural flow, with less symmetries and thus possibly more complicated to analyze in terms of structures in physical space. Both types of initial conditions are studied here to cover a larger dynamical range. The relative helicity coefficients are chosen so as to represent generic data; indeed, if zero or one, they represent very specific and unlikely configurations unless one imposes symmetries (such as in the case of the Taylor-Green or Beltrami configurations discussed in Chapter 3). Moreover, when taking the relative helicities close to unity, the nonlinear terms are strongly damped and the evolution out of that state will be slow [*Podvigina and Pouquet*, 1994]. Table 4.1 also gives the value of $\tau_{NL} \equiv L_{int}/\left\langle |\mathbf{u}|^2 \right\rangle^{1/2}$ for each run computed at the peak of Ω_T or $\mathcal{P}_T$.

4.2 Numerical Results

Figure 4.1 plots E_T and Ω_T as a function of time for runs RH2c and RMc. The results of this study are focused on data taken from near the peak of Ω_T (for the two runs shown in Figure 4.1 this corresponds to $t \sim 1.925$ for run RH2c and $t \sim 1.75$ for run RMc in simulation units) unless otherwise noted. Despite HMHD showing enhanced small scale activity (see Figure 4.2), HMHD tends to show slightly smaller Ω_T than MHD resulting in slightly different profiles of E_T. The smaller Ω_T is linked to the steepening of the HMHD spectrum at scales below the ion inertial length. The predicted spectral slope for magnetic fluctuations in HMHD is steeper than -2. In the DNS presented here the total energy spectrum also tends to become steeper than k^{-2} at near $1/\epsilon_H$ and since $\Omega_T(k) = k^2 E_T(k)$, the peak of the Ω_T spectrum will be near $1/\epsilon_H$. The steepening of the spectrum is not necessarily present in MHD until dissipation becomes significant and therefore a broader profile to the $\Omega_T(k)$ spectrum can be formed resulting in a larger average value of Ω_T when the spectrum is integrated. Even with smaller values of Ω_T on average, locally currents are enhanced significantly in HMHD (see Chapter 4.2.2). Figure 4.1 also shows the ratios of magnetic to kinetic energy and mean square current to mean square vorticity for the same runs. In both

MHD and HMHD the flows tend to be magnetically dominated as interpreted from either ratio; for the random initial condition it is slightly less so in HMHD. The OT initial conditions and other resolutions (not displayed) behave similarly except for some slight differences in the ratios.

The behavior of the relative helicities as a function of time are similar between MHD and HMHD and therefore are not displayed. In all cases, σ_M shows the most growth over the course of the run. The value of σ_G also shows significant growth over the course of the HMHD runs likely associated with the presence of H_M in the definition of H_G.

4.2.1 Behavior in Fourier Space

Figure 4.2 shows $E_T(k)$ for the runs analyzed in this study. The most distinct feature of the HMHD spectra is the excess of energy relative to MHD in the small scales in all cases, which is associated with the magnetic energy. The excess of energy becomes more pronounced as ϵ_H is increased (Figure 4.2a). While the spectra are similar for small wavenumbers, at moderate wavenumber above $1/\epsilon_H$, the HMHD spectra tend to be slightly steeper than MHD consistent with theory (however the exact spectral slope cannot be determined at the resolutions here) [*Galtier*, 2006]. For reference, in the case of run RH2c, the steeper region lasts from roughly $k \sim 6$ to $k \sim 20$ as shown in Figure 4.2d. However, dissipation in the MHD cases quickly causes the MHD spectra to become steeper than HMHD; indeed, we take the same viscosity for the MHD and HMHD runs, but due to the fact that in MHD the production of small scales is not as intense as for HMHD, the runs have a larger dissipation range. In runs OTH1 and OTH2a, the steeper region is likely not evident because of the location of the dissipation scale. Run OTH2c likely does not show a steeper region because the run was continued from the peak of dissipation of the MHD version and the small to moderate wavenumbers did not change significantly in the time it takes to reach the new peak in Ω_T.

As suggested by *Meyrand and Galtier* [2012], another way of examining the spectra in HMHD is to look at the energy spectra of strongly circularly polarized fluctuations. Figure 4.3 plots energy spectra constructed using only wavevectors with $P_M > 0.3$ and $P_M < -0.3$ or $P_M > 0.7$ and

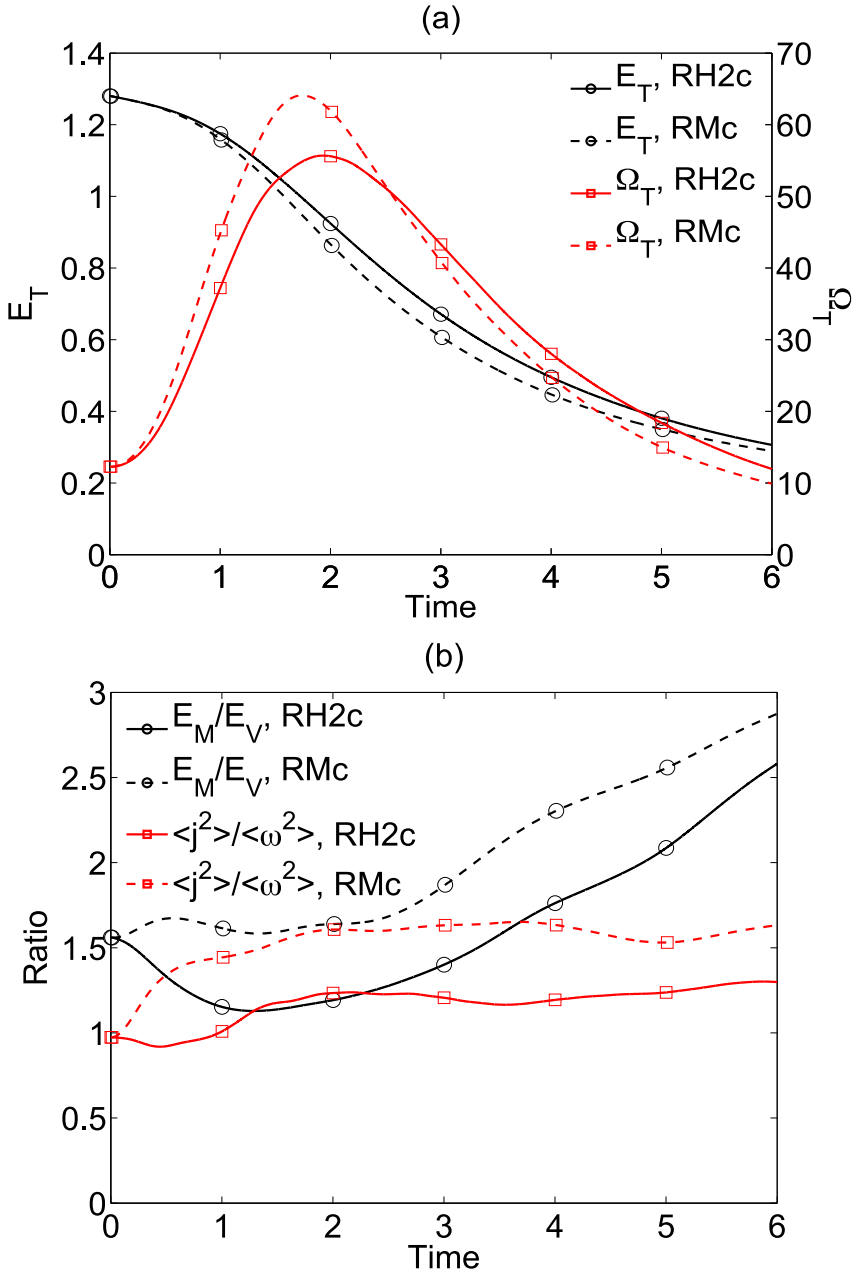

Figure 4.1: (a) Total energy (black circles) and enstrophy (red squares) as a function of time for RMc (dashed lines) and RH2c (solid lines). (b) Ratio of magnetic to kinetic energy and ratio of mean square current to mean square vorticity as a function of time for the same runs and in the same format as in Panel a.

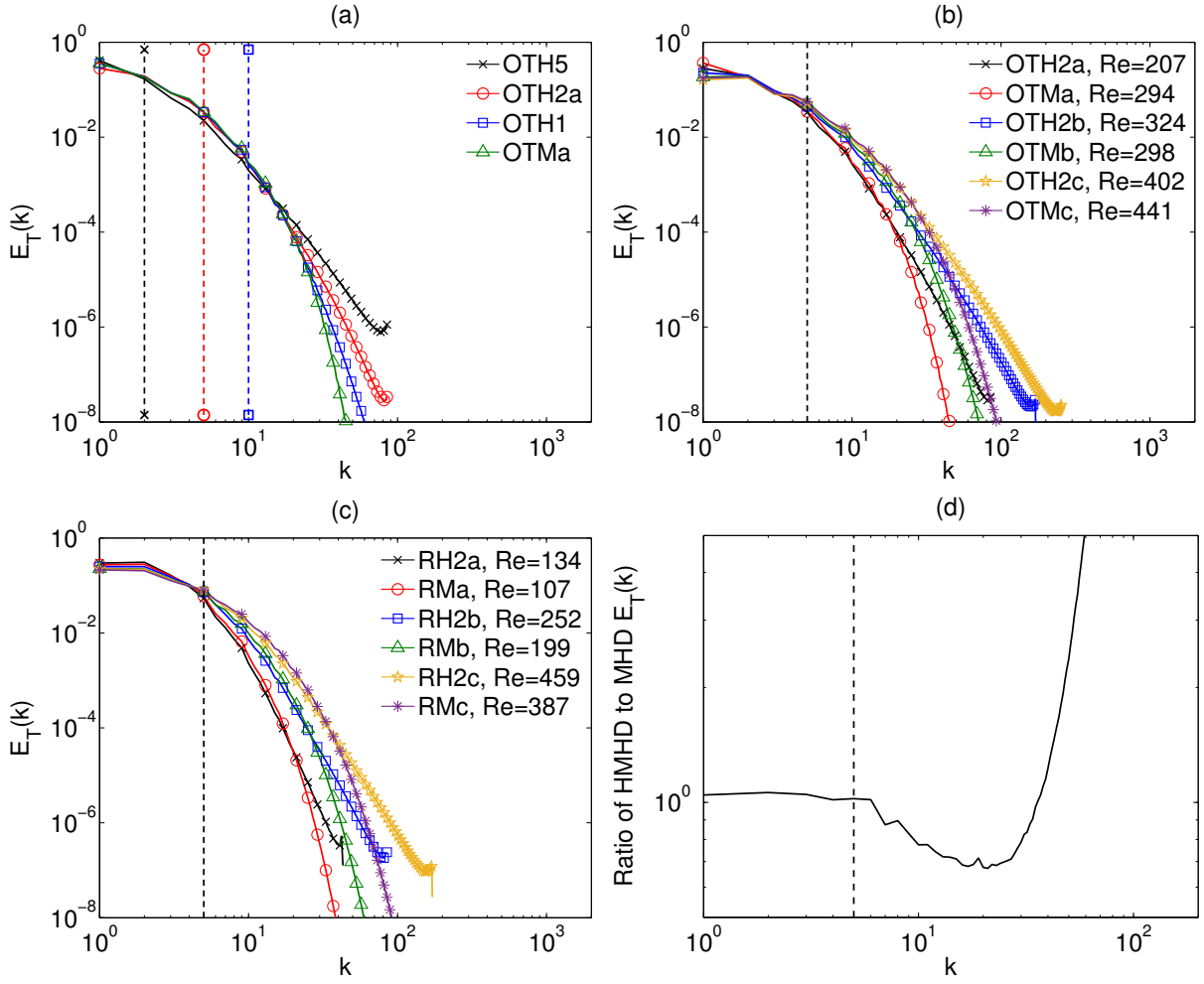

Figure 4.2: (a) $E_T(k)$ for runs OTMa, OTH1, OTH2a, and OTH5, which have varying values of ϵ_H. Vertical dashed lines mark $1/\epsilon_H$ with colors and markers corresponding to the run. (b) $E_T(k)$ for runs OTMa,b,c and OTH2a,b,c, which have varying Reynolds numbers. (c) $E_T(k)$ for runs RMa,b,c and RH2a,b,c, which have varying Reynolds numbers. In panels b and c, Reynolds numbers $Re = \langle|\mathbf{u}|^2\rangle L_{int}/\nu$ at the peak of Ω_T are given in the legend. (d) Ratio of $E_T(k)$ for run RH2c to $E_T(k)$ for run RMc. The region of negative slope indicates where HMHD is steeper than MHD. In all panels vertical dashed lines show $1/\epsilon_H$.

$P_M < -0.7$. In both the random and OT initial conditions the left polarized spectra are steeper than the right polarized spectra, as was found by *Meyrand and Galtier* [2012] using hyperdiffusivities, indicating the excess energy at small scales seen in Figure 4.2 is associated with right polarized fluctuations. However, in the random case the left polarized spectrum dominates in the large scales, whereas right and left polarizations are roughly in equipartition in the large scales of the OT runs. This behavior is likely related to the mean square values of $\mathbf{u}_R$ and $\mathbf{u}_L$ which are roughly equal initially in the OT runs and set to be a factor of two apart initially in the random runs. Using a threshold of $|P_M| > 0.3$, short regions where the right and left spectra may be compatible with spectral slopes of $-7/3$ and $-11/3$ respectively can be found (Fig. 4.3b), consistent with the results of *Meyrand and Galtier* [2012]. When the threshold is set to 0.7 (Fig. 4.3c), the $-7/3$ scaling extends over a wide range in the right polarized spectrum in run RH2c, but the left polarized spectrum is even steeper than $-11/3$. The break in the $-7/3$ spectrum for run RH2c in panel c at $k \sim 65$ roughly corresponds with the wavenumber k_H (the dissipation wavenumber for the Hall term, see Eq. 2.15).

Figure 4.4 plots $E_M(k)/E_V(k)$ for a variety of HMHD runs. The spectra in MHD are found to be in near equipartition (within a factor of 2) at all scales (similar to the spectra seen in Figure 3.6), and this is the case for all of the MHD runs performed in this study (not shown). In HMHD, the spectra are in near equipartition at large scales and then transition to a magnetically dominated state in the small scales, where the spectra exactly match the whistler wave linear prediction (see Eq. 2.31). In the context of a shell model for HMHD, *Galtier and Buchlin* [2007] also noted that a magnetically dominated regime could be obtained under certain parameter regimes. The wavenumber at which the transition occurs is above $1/\epsilon_H$ in most cases and moves to larger wavenumber as the Reynolds number is increased. In the region of near equipartition, the random runs have relatively more kinetic energy than the OT runs, likely because $\mathbf{u}_R < \mathbf{u}_L$ and left polarized fluctuations (expected to be kinetically dominated from linear theory) dominate the spectra in the large scales. Based on Figure 4.3, it is not surprising the small scales are magnetically dominated since the left polarizations fall off more steeply than the right polarizations.

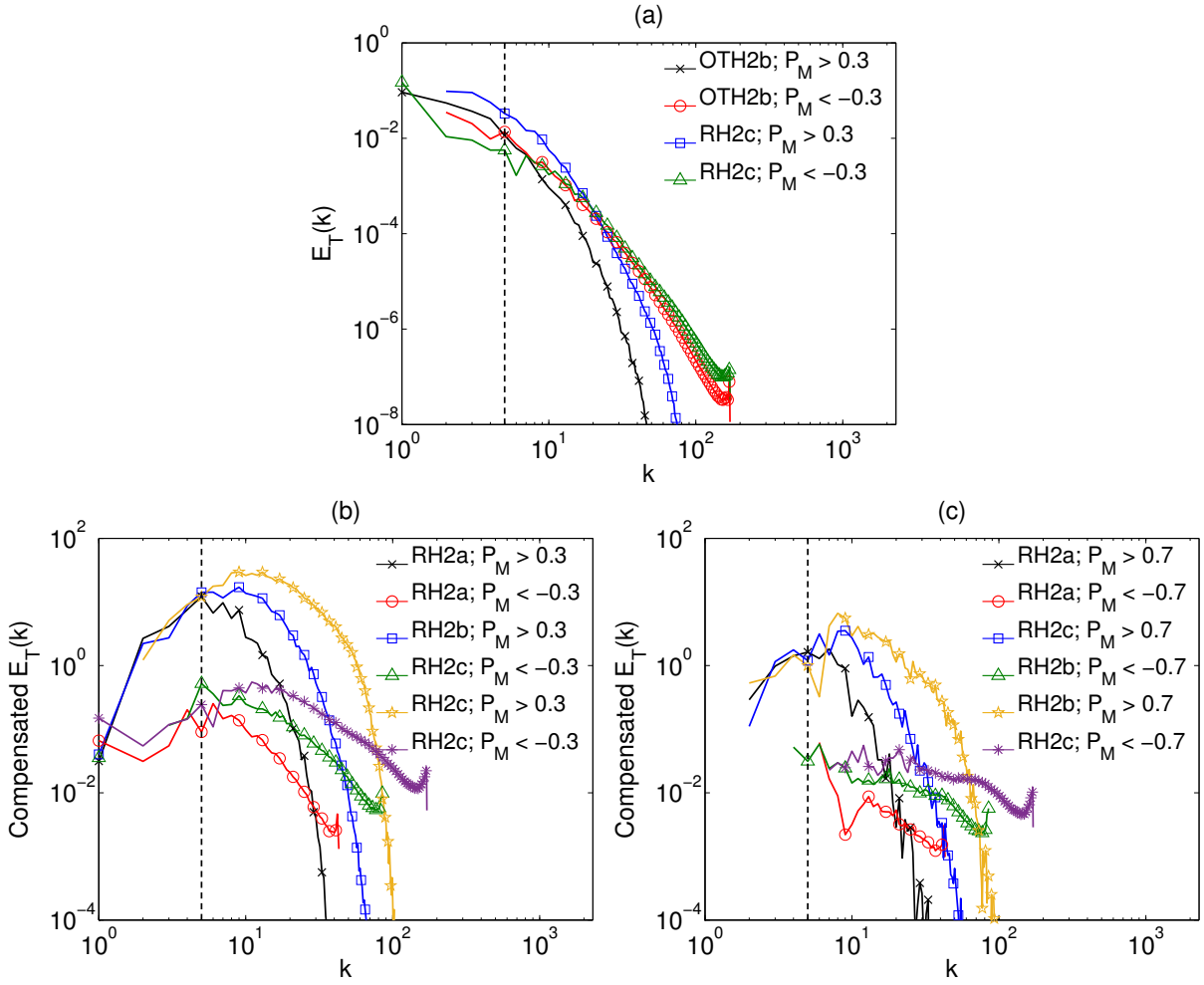

Figure 4.3: (a) Spectra for fluctuations with $|P_M| > 0.3$ for runs OTH2b and RH2c. (b) Spectra for the same values of P_M as panel a, but compensated by either $k^{11/3}$ for positive P_M (left polarized ion cyclotron fluctuations) or $k^{7/3}$ for negative P_M (right polarized whistler fluctuations) as predicted and observed in hyperdiffusive simulations by *Meyrand and Galtier* [2012]. (c) Spectra with $|P_M| > 0.7$ compensated by either $k^{11/3}$ for positive P_M or $k^{7/3}$ for negative P_M. The compensated spectra are for runs RH2a, RH2b, and RH2c, which have various Reynolds numbers. In all panels, vertical dashed lines mark $1/\epsilon_H$.

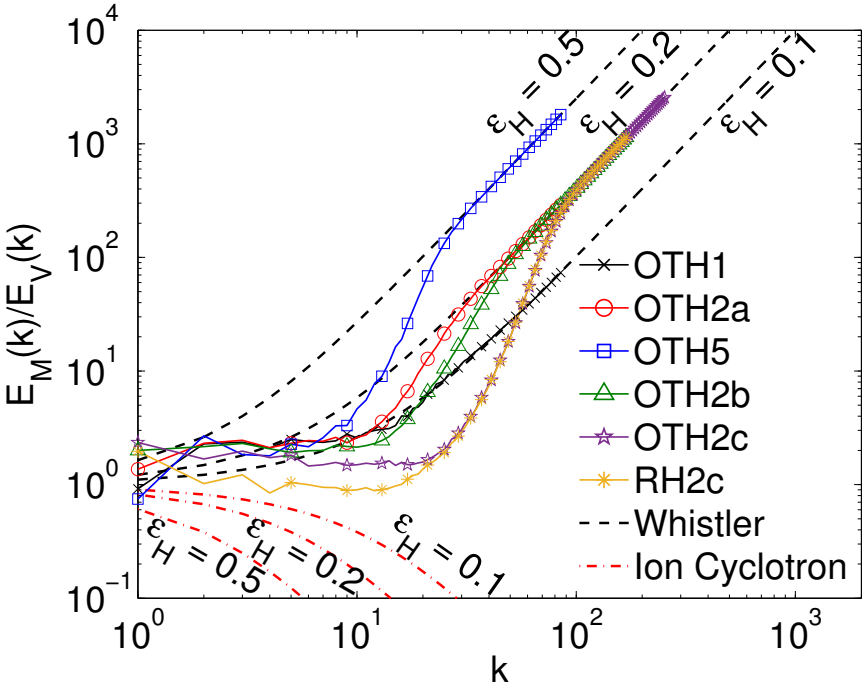

Figure 4.4: Ratio of magnetic to kinetic energy spectra near the peak of Ω_T for runs OTH1, OTH2a, OTH2b, OTH2c, OTH5, and RH2c. For all runs, the ratio at large wavenumbers matches the linear prediction for whistler waves. At lower wavenumbers the energy is roughly in equipartition, consistent with the behavior of MHD. The random HMHD runs tend to be more kinetically dominated than the OT runs or the random MHD runs at low wavenumbers.

One possible explanation for the seemingly linear behavior observed in the small scales in Figure 4.4 is through the presence of the double curl Beltrami configuration (see Chapter 2.1.2) in the small scales. To examine the role of this configuration in the dynamics of HMHD turbulence, Figure 4.5 plots σ_R and σ_L computed in Fourier space (see Eq. 2.23 for the real-space formulation) for run RH2c. Absolute values are performed before averaging over spherical shells in Fourier space to create the spectra so as to avoid cancellations of positive and negative alignment. All HMHD runs analyzed behave similarly to the displayed curves. If both σ_R and σ_L correspond to full alignment, the nonlinear dynamics stop and in the presence of a uniform background magnetic field B_0, the linear solution is obtained. In the simulations presented here, no B_0 is explicitly imposed; however, it is possible for the largest-scale magnetic fluctuations to appear as a quasi-uniform field to the small-scale fluctuations, provided there is enough scale separation [*Mininni and Pouquet*, 2007]. Starting at roughly $1/\epsilon_H$, σ_R and σ_L are constant at a value of roughly 1/2. At $k \sim 40$ for run RH2c, σ_L begins to decrease significantly and then increases somewhat at $k \sim 100$. The lack of both large σ_R and σ_L in the small scales seems to contradict the idea that the small scales are in a double curl Beltrami state. However, the effect may be obscured by the difficulty of separating B_0 from the fluctuations in the current simulations. The theory of *Krishan and Mahajan* [2005] only requires the nonlinear fluctuations, and not the background field, to have the double curl Beltrami alignments.

To better understand the change in behavior present in Figure 4.4, consider the Fourier transform of the induction and vorticity equations (Eq. 2.7 and the curl of Eq. 2.8) neglecting dissipation

$$\frac{\partial \mathbf{b}(\mathbf{k})}{\partial t} = i\mathbf{k} \times \left([\mathbf{u} \times \mathbf{b}]_k - \epsilon_H \, [\mathbf{j} \times \mathbf{b}]_k \right) \tag{4.3}$$

$$\frac{\partial \boldsymbol{\omega}(\mathbf{k})}{\partial t} = i\mathbf{k} \times \left([\mathbf{u} \times \boldsymbol{\omega}]_k + [\mathbf{j} \times \mathbf{b}]_k \right). \tag{4.4}$$

From dimensional analysis, one might expect the Hall term to dominate the induction equation at scales below the ion inertial length ($\epsilon_H k \gg 1$), so at small scales the $[\mathbf{u} \times \mathbf{b}]_k$ term will be neglected and $\mathbf{u}$ no longer influences the evolution of $\mathbf{b}$. However, it is unclear from dimensional

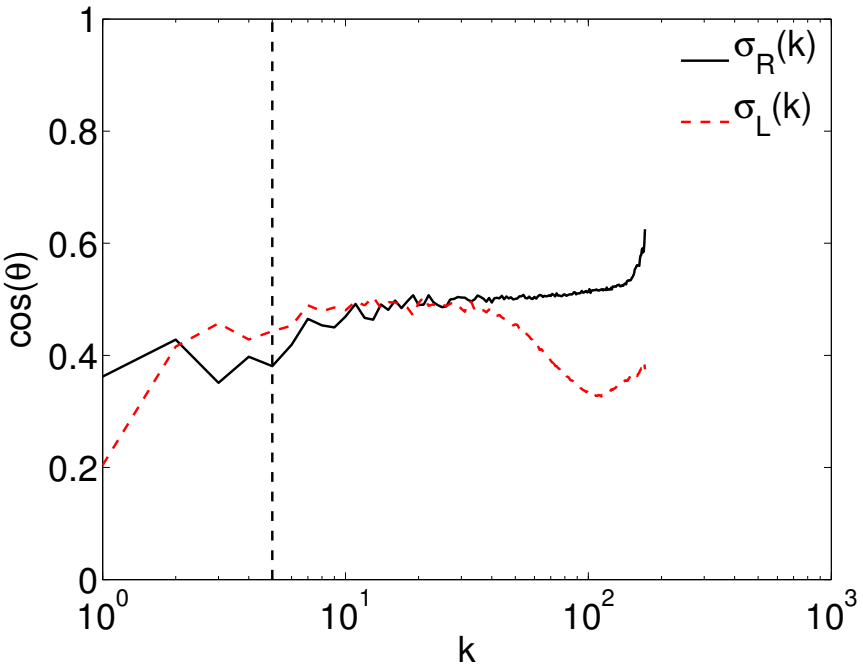

Figure 4.5: Spectra of the alignments associated with the double curl Beltrami state [*Mahajan and Yoshida*, 1998] for run RH2c. The solid black curve gives σ_R and the red dashed curve gives σ_L. An absolute value is taken before averaging over spherical shells to avoid cancellation of positive and negative alignment. The vertical dashed line marks $1/\epsilon_H$.

analysis alone which terms may be important in the vorticity equation. An important distinction between the MHD scales and HMHD scales is that in terms of powers of k the nonlinear terms in the induction equation scale as the momentum equation at MHD scales and the vorticity equation at HMHD scales.

Different behaviors of the vorticity and therefore the velocity fluctuations will occur depending on the relative importance of the $[\mathbf{u} \times \boldsymbol{\omega}]_k$ and $[\mathbf{j} \times \mathbf{b}]_k$ terms. If $\mathbf{k} \times [\mathbf{j} \times \mathbf{b}]_k$ dominates the vorticity equation, which could happen if $\mathbf{u}$ is significantly more aligned with $\boldsymbol{\omega}$ than $\mathbf{b}$ is with $\mathbf{j}$, if $|\mathbf{u}||\boldsymbol{\omega}| \ll |\mathbf{j}||\mathbf{b}|$, or if the angles between the nonlinear terms and $\mathbf{k}$ are significantly different, then the vorticity equation (with a factor of $-\epsilon_H$) will evolve identically to the induction equation. We can then write $-\epsilon_H \partial_t \boldsymbol{\omega}(\mathbf{k}) = \partial_t \mathbf{b}(\mathbf{k})$, which assuming small scale fluctuations are initially zero can be integrated to obtain $-\epsilon_H \boldsymbol{\omega}(\mathbf{k}) = \mathbf{b}(\mathbf{k})$. Since each component of $\boldsymbol{\omega}(\mathbf{k})$ and $\mathbf{b}(\mathbf{k})$ are equal, the magnitudes must be equal and using the fact that $|\boldsymbol{\omega}(\mathbf{k})| = k|\mathbf{u}(\mathbf{k})|$, an expression for the ratio of magnetic to kinetic energy can be written

$$\frac{E_M(k)}{E_V(k)} = \epsilon_H^2 k^2 \ . \tag{4.5}$$

This expression is true for both linear and nonlinear small-scale HMHD fluctuations where the $[\mathbf{j} \times \mathbf{b}]_k$ term dominates over the $[\mathbf{u} \times \boldsymbol{\omega}]_k$ term in the vorticity equation. Eq. 4.5 can similarly be obtained from the magnetic vector potential and velocity equations if the pressure term is neglected. In the linear solution, obtaining the lower frequency and kinetic energy dominated ion cyclotron wave requires the influence of the $[\mathbf{u} \times \mathbf{b}]_k$ term, which has been neglected in obtaining Eq. 4.5. Eq. 4.5 is equivalent to the linear prediction for whistler waves in the limit $\epsilon_H k \gg 1$, which is the region where the ratios in Figure 4.4 match up with the linear prediction. *Galtier and Buchlin* [2007] also found a relationship between magnetic and kinetic energy consistent with Eq. 4.5 for some parameters, as well as an alternative kinetically dominated regime in other parameter regimes based on shell model results and it was noted through heuristic arguments involving the balance of nonlinear timescales that various behaviors of $E_M(k)/E_V(k)$ may be linked to the wide range of spectral slopes observed at sub-ion scales in the solar wind. The DNS results presented in this

study only show a transition to the magnetically dominated state.

To understand the state described by Eq. 4.5 in more physical terms, first note that $\mathbf{u}$ is a mass weighted average of ion and electron velocities and since ions have much more mass than electrons, $\mathbf{u} \sim \mathbf{u}_i$. Also note that $\epsilon_H \mathbf{j} = \mathbf{u}_i - \mathbf{u}_e$. Therefore, the dominance of the Hall term in the induction equation corresponds to a state where ions are approximately stationary compared to electrons and only electron motions are carrying the currents in the small scales. With the Lorentz force dominating over advection in the vorticity equation, small-scale fluctuations in $\mathbf{u}$ are simply responding to the magnetic field fluctuations and in turn $\mathbf{u}_e$ fluctuations without any significant advection or feedback on the evolution of $\mathbf{b}$. This behavior is similar in some ways to the so-called electron MHD approximation.

The relative importance of the various nonlinear terms in run RH2c is examined in Figures 4.6a,b, which show the ratios of the spectra associated with the nonlinear terms $[\mathbf{j} \times \mathbf{b}]_k$, $[\mathbf{u} \times \boldsymbol{\omega}]_k$, and $[\mathbf{u} \times \mathbf{b}]_k$ and their curls. In the magnetic vector potential equation, $\epsilon_H [\mathbf{j} \times \mathbf{b}]_k$ dominates over $[\mathbf{u} \times \mathbf{b}]_k$ at wavenumbers larger than $1/\epsilon_H$. Since the derivative in time of $\mathbf{a}$ is given by the electric field, this means that the Hall term is dominating the electric field at wavenumbers above $1/\epsilon_H$. The actual wavenumber where the Hall term becomes dominant occurs at $k \sim 8$, which is consistent with the energy in the initial conditions mainly being located between $k = 1$ and $k = 2$, making L_c slightly smaller than 2π. In the induction equation, $\epsilon_H \mathbf{k} \times [\mathbf{j} \times \mathbf{b}]_k$ is comparable to the $\mathbf{k} \times [\mathbf{u} \times \mathbf{b}]_k$ at wavenumbers above $1/\epsilon_H$ and does not become dominant until larger wavenumbers. Based on the linear solution, left polarized waves have equipartition between $\epsilon_H \mathbf{k} \times [\mathbf{j} \times \mathbf{b}]_k$ and $\mathbf{k} \times [\mathbf{u} \times \mathbf{b}]_k$ at wavenumbers above $1/\epsilon_H$ (similar to the midrange wavenumbers in Figure 4.6b), while in the right polarized waves the Hall term dominates.

In the velocity equation, the term $[\mathbf{j} \times \mathbf{b}]_k$ is found to be comparable to $[\mathbf{u} \times \boldsymbol{\omega}]_k$ into the Hall regime, but in the small scales $[\mathbf{j} \times \mathbf{b}]_k$ is dominant. The wavenumber at which the ratio $[\mathbf{j} \times \mathbf{b}]_k^2 \,/\, [\mathbf{u} \times \boldsymbol{\omega}]_k^2$ begins to increase roughly corresponds to the wavenumber where $E_M(k)/E_V(k)$ begins to increase towards the prediction of Eq. 4.5. In the vorticity equation, the ratio of $\mathbf{k} \times [\mathbf{j} \times \mathbf{b}]_k$ to $\mathbf{k} \times [\mathbf{u} \times \boldsymbol{\omega}]_k$ decreases with $\mathbf{k} \times [\mathbf{u} \times \boldsymbol{\omega}]_k$ dominating at wavenumbers above $1/\epsilon_H$; however,

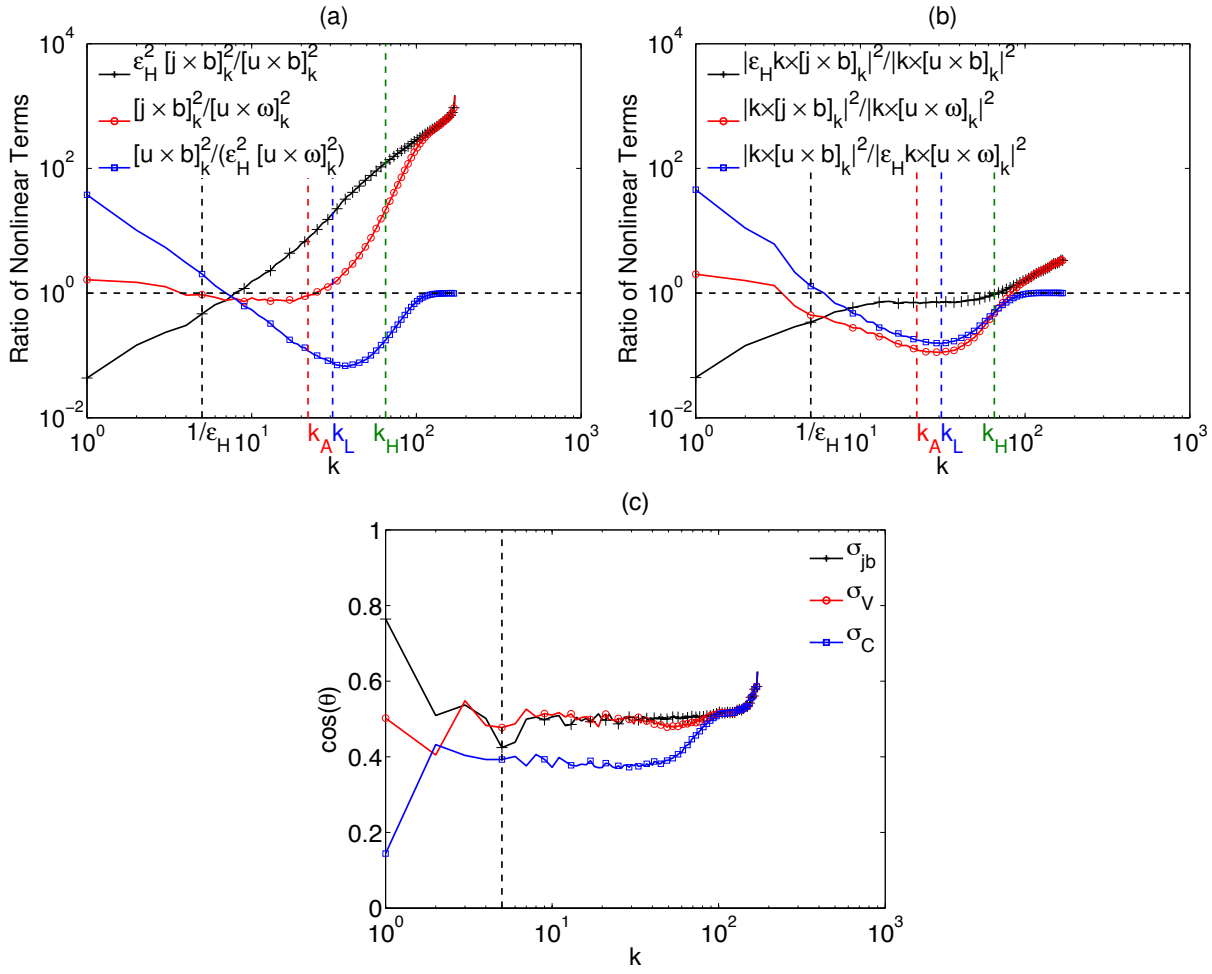

Figure 4.6: (a) Ratios of the spectra of the nonlinear terms present in the magnetic vector potential, velocity, and "uncurled" $\mathbf{\Omega}_L$ equations. The horizontal dashed line marks a value of unity, and the vertical dashed lines mark the ion inertial length ($1/\epsilon_H$), and dissipation scales given by Eq. 2.15 (k_A, k_L, and k_H). (b) Same as panel a but for the nonlinear terms in the induction, vorticity, and $\mathbf{\Omega}_L$ equations. (c) Spectra of the cosine of the angles between the vectors involved in the nonlinear terms (σ_{jb}, σ_V, and σ_C). In creating the spectra, the absolute value of the correlation is taken before averaging over spherical shells so as to avoid cancellation of positive and negative alignment. The vertical dashed line gives $1/\epsilon_H$. All three plots are for run RH2c. Other HMHD runs show the same general behavior.

the ratio begins to increase at moderate wavenumbers and $\mathbf{k} \times [\mathbf{j} \times \mathbf{b}]_k$ dominates at the largest wavenumbers. The change in behavior of the nonlinear terms in the vorticity equation seems to be associated with the change in behavior in the nonlinear terms of the velocity equation. The scale at which these changes in behavior occur appear to be associated with the scale k_A, which roughly is consistent with where $E_M(k)/E_V(k)$ begins to increase. The association with k_A is consistent with the transition to the magnetically dominated state occurring at larger wavenumber for higher Reynolds number as seen in Figure 4.4. While $\mathbf{k} \times [\mathbf{j} \times \mathbf{b}]_k$ does not dominate the vorticity equation at the scale where the energy begins to become magnetically dominated, $\mathbf{k} \times [\mathbf{j} \times \mathbf{b}]_k$ does dominate the vorticity equation at the scales where $E_M(k)/E_V(k)$ follows Eq. 4.5 as expected. k_A is smaller than the overall dissipation wavenumber of the system (in this case k_H) indicating that the interplay of dissipation with the various nonlinear terms can lead to different regimes of HMHD turbulence. Similar results to run RH2c are found for the other HMHD runs. Figure 4.6c shows spectra of σ_{jb}, σ_V, and σ_C, which are the alignments associated with the nonlinear terms. The spectra of σ_{jb} and σ_V are similar at small scales indicating it is the magnitudes of the vectors that are causing $[\mathbf{j} \times \mathbf{b}]_k$ to dominate the velocity equation rather than the angles between the vectors.

Although in the example shown k_L seems to roughly correspond to a change in behavior in $[\mathbf{u} \times \mathbf{b}]_k^2/(\epsilon_H^2 [\mathbf{u} \times \boldsymbol{\omega}]_k^2)$ and in $|\mathbf{k} \times [\mathbf{j} \times \mathbf{b}]_k|^2/|\mathbf{k} \times [\mathbf{u} \times \boldsymbol{\omega}]_k|^2$, examination of other runs reveals that k_L is not associated with strong changes in behavior as is the case with k_A. In the runs at resolution 512^3, k_H seems to be associated with Hall term dominating the induction equation, however at lower resolutions this is not necessarily the case.

The decrease in σ_L in Figure 4.5 may be associated with the increase in the importance of the $\mathbf{u} \times \mathbf{b}$ compared to the $\epsilon_H \mathbf{u} \times \boldsymbol{\omega}$ term (Figure 4.6a) and increase in σ_C to the value of σ_V (Figure 4.6c). Both of these quantities are relevant to σ_L and show significant changes in behavior at $k \sim 40$, which is where σ_L begins to decrease. σ_L begins to increase again when $\sigma_C \sim \sigma_V$.

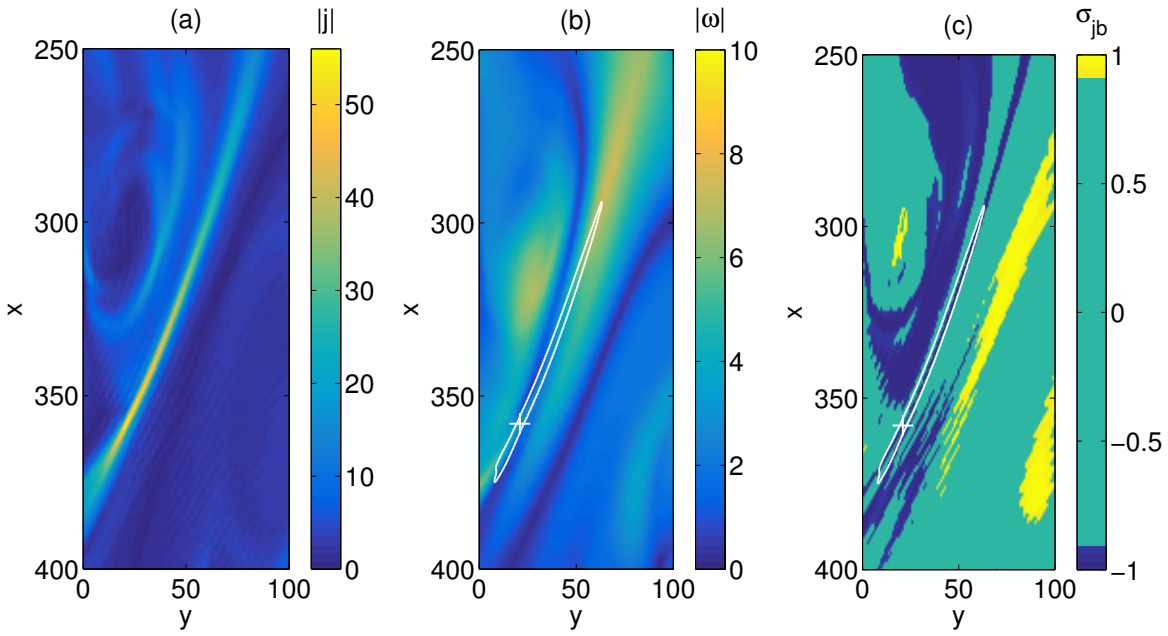

Figure 4.7: 2D cuts of (a) $|\mathbf{j}|$, (b) $|\boldsymbol{\omega}|$, and (c) σ_{jb} at the location of maximum current near the peak of Ω_T for run OTH2b. White crosses mark the location of maximum current and white curves give the half-maximum contours of the current. Values of $|\sigma_{jb}| < 0.9$ are masked out to highlight the highly-aligned structures. The x and y axes are in units of grid points.

4.2.2 Behavior in Configuration Space

Figure 4.7 shows 2D cuts for the current, vorticity, and σ_{jb} near the peak of Ω_T for run OTH2b. The 2D cuts are for a subset of the domain located around the current structure containing the maximum current. For the cut in σ_{jb}, alignments less than 0.9 are masked out to highlight the most aligned structures. In Figure 4.7, white curves mark the half-maximum current contours and the white + marks the location of the maximum current. It is found that for both types of initial conditions, strong currents tend to be associated with regions of highly-aligned magnetic field and current ($\sigma_{jb} \approx \pm 1$). σ_R shows similar results to σ_{jb}; however, this is expected since in the small scales the Hall term dominates, which should give $\sigma_R \sim -\sigma_{jb}$. We also observe that in the vicinity of regions of high alignment, σ_{jb} can vary in sign (corresponding to parallel or anti-parallel configurations of the fields), as was observed in MHD for the velocity-magnetic field correlation [*Meneguzzi et al.*, 1996].

To further examine this association, Figure 4.8 plots probability distributions (PDFs) for various alignments conditioned on the strength of the current being greater than 75% of the maximum for runs OTH2b and RH2c. Since only a limited number of current structures form within the domain for the runs presented in this study, it is possible to obtain false peaks near strong alignment in the conditional PDFs if the current structures randomly coincide with regions of strong alignment. However, if the current structures are not fundamentally associated with a given alignment, the shape of the conditional PDF can significantly change in time as current structures move or new current structures form. Based on the simulations presented here, times slightly after the peak of Ω_T appear to have more strong current structures providing better statistics in the conditional PDFs. Conditional PDFs have been examined at additional times for both types of initial conditions (see Figures 4.8a,b for an example) and while the PDFs for most of the alignments change shape with time, peaks at strong alignment consistently occur for σ_{jb}. Examination of conditional PDFs in the MHD runs (not shown), reveals that, while there may be some association between strong currents and highly-aligned σ_{jb}, the association tends to be stronger in HMHD. Evidence

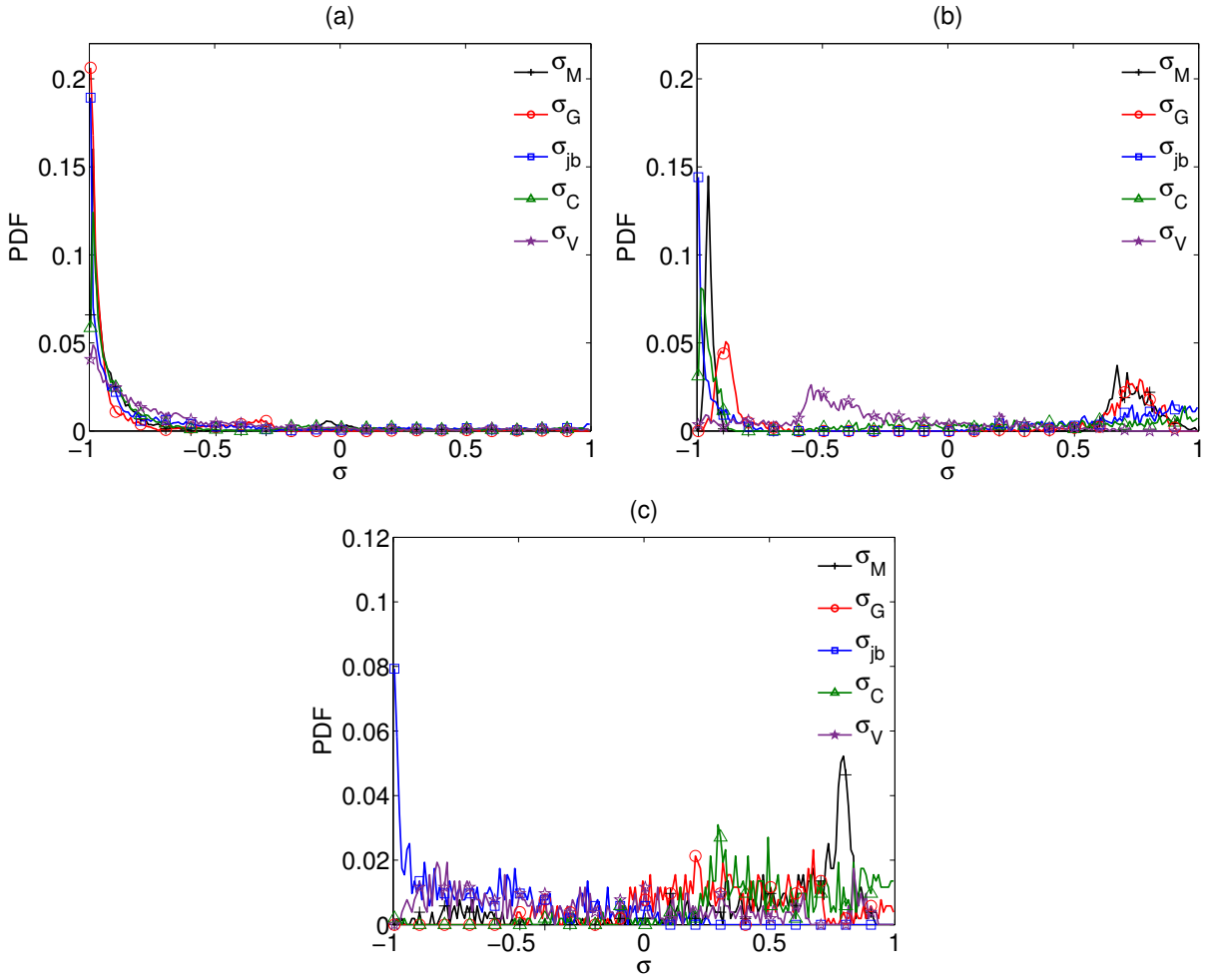

Figure 4.8: Conditional PDFs of σ_M, σ_G, σ_{jb}, σ_C, and σ_V for points where $|\mathbf{j}|$ is greater than 75% of the maximum. Panels (a) and (b) show run OTH2b at the time of peak Ω_T and 1.2 times the time of peak Ω_T respectively. Panel (c) shows run RH2c at the time of peak Ω_T. At all times and initial conditions examined, peaks in the conditional PDF for σ_{jb} are present at either +1 or at -1 (as plotted here).

has also been found that the inclusion of the Hall term can generate magnetic field-aligned currents in laminar reconnection [*Ma and Lee*, 2001; *Ma and Otto*, 2013].

Figure 4.9 shows PDFs of the parallel and perpendicular magnitudes of the current with respect to the magnetic field ($|j_{||}| = |\mathbf{j} \cdot \mathbf{b}|/|\mathbf{b}|$ and $|j_{\perp}| = \sqrt{|\mathbf{j}|^2 - |j_{||}|^2}$) for runs OTH2b, OTMb, RH2c, and RMc. Both $|j_{||}|$ and $|j_{\perp}|$ have similar PDFs, particularly for the random initial conditions. Even though on average Ω_T is weaker in HMHD, the PDFs extend to greater magnitudes in the case of HMHD consistent with more intermittent behavior. The value of $|j_{||}|$ reaches nearly the magnitude of the maximum current consistent with the findings of Figure 4.7. As is explored in Chapters 5 and 6 [see also *Stawarz et al.*, 2015], the destabilization of field-aligned currents plays a key role in the dissipation of collisionless plasma turbulence, particularly in the Earth's magnetotail. The association of intense currents with σ_{jb} and enhancement in current magnitudes in HMHD may mean that Hall physics helps to enhance this dissipation mechanism in collisionless plasmas.

From Figure 4.7 it appears that not only are the currents significantly more intense than the vorticity in HMHD, but the structures are also significantly thinner. One way of quantifying the size of structures on average in a turbulent system is by considering the autocorrelation function defined in Eq. 2.62. Figure 4.10a plots the autocorrelation functions for $\mathbf{j}$, $\boldsymbol{\omega}$, and $\mathbf{e}$ for runs OTH2b and OTMb. While in MHD $\mathbf{j}$ and $\boldsymbol{\omega}$ have virtually identical autocorrelation functions consistent with structures of similar size, HMHD has a narrower $\mathbf{j}$ autocorrelation function and wider $\boldsymbol{\omega}$ autocorrelation function. At larger separations the HMHD $\mathbf{j}$ autocorrelation crosses both the MHD autocorrelation functions indicative of more peaked current structures in HMHD. For MHD the correlation length, defined as the integral of the autocorrelation function, is 0.042 for both $\mathbf{j}$ and $\boldsymbol{\omega}$. For HMHD, the correlation lengths are 0.04 for $\mathbf{j}$ and 0.049 for $\boldsymbol{\omega}$ (compared to the total box size of 2π). The behavior of $\mathbf{j}$ and $\boldsymbol{\omega}$ autocorrelation functions is likely a manifestation of the effect described in Chapter 4.2.1 which causes $\boldsymbol{\omega}$ to scale identically to $\mathbf{b}$ in the small scales. If $\boldsymbol{\omega} \sim \mathbf{b}$, then $\mathbf{j}$, which is the curl of $\mathbf{b}$ will end up being at smaller scale (unless the field is force-free).

The HMHD autocorrelation function for the electric field $\mathbf{e}$ is nearly identical to that of $\mathbf{j}$

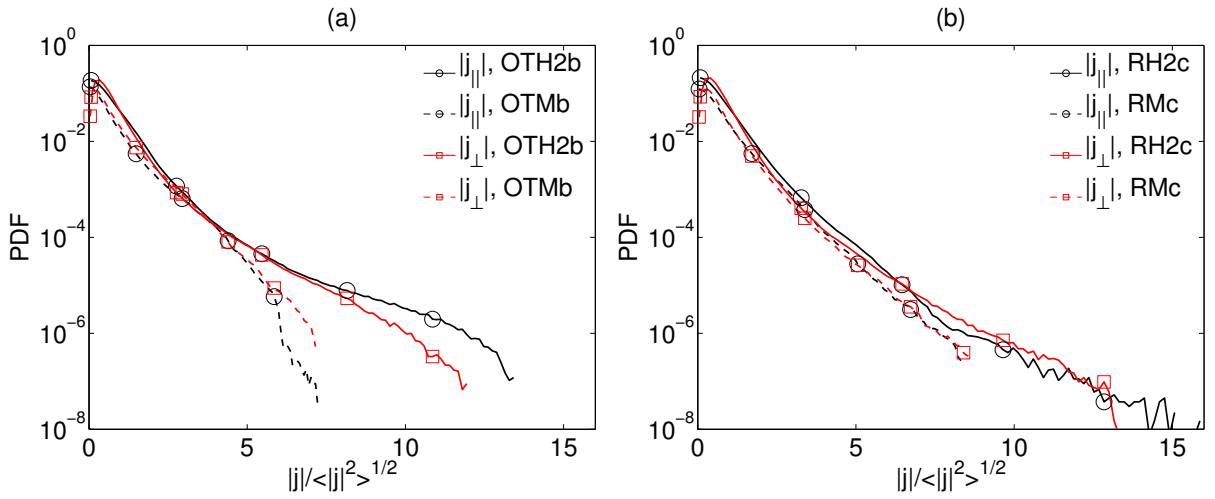

Figure 4.9: (a) Distributions of $|j_{||}| = |\mathbf{j}\cdot\mathbf{b}|/|\mathbf{b}|$ (black circles) and $|j_{\perp}| = \sqrt{|\mathbf{j}|^2 - |j_{||}|^2}$ (red squares) for runs OTH2b (solid lines) and OTMb (dashed lines). (b) Same as (a) but for runs RH2c (solid lines) and RMc (dashed lines). The magnitudes are normalized to the standard deviation of the current. The HMHD runs have wider wings to the distributions than the MHD runs.

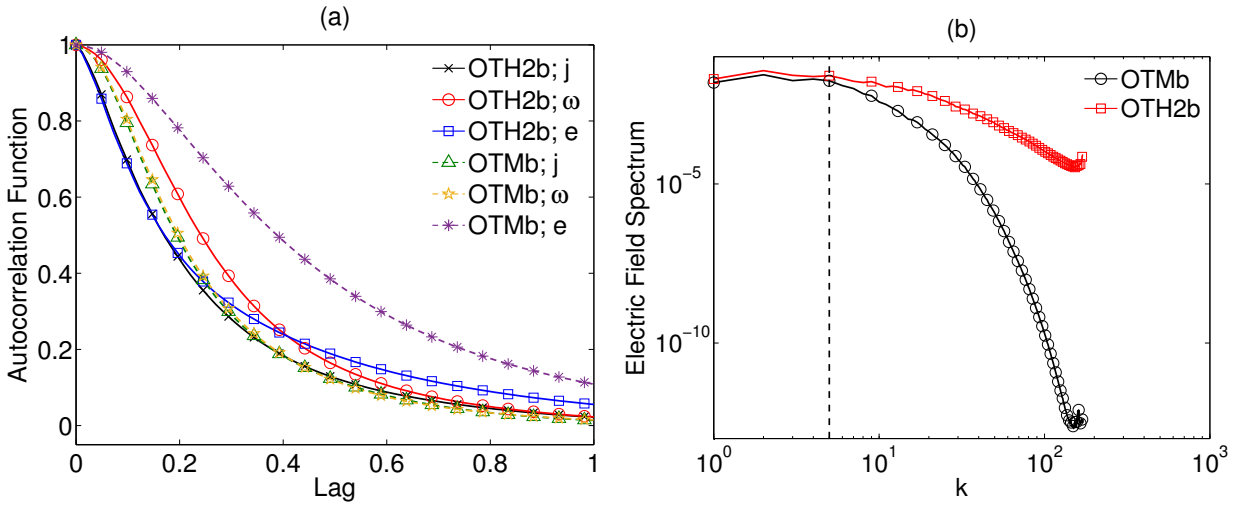

Figure 4.10: (a) Autocorrelation functions of the current, vorticity, and electric field for runs OTH2b (solid lines) and OTMb (dashed lines). In MHD, the current and vorticity autocorrelation functions are nearly identical consistent with current and vorticity structures that are of similar scales. In HMHD, the current autocorrelation function is narrower and the vorticity autocorrelation function is wider consistent with thinner current structures and wider vorticity structures. Electric field structures are much narrower and follow the current autocorrelation function at small separations in HMHD. (b) Spectra of $\mathbf{e}$ (Fourier transform of $\mathbf{e}$ autocorrelation function) for runs OTMB (black circles) and OTH2b (red squares). The vertical dashed line marks $1/\epsilon_H$.

at small separations and then departs from **j**, ultimately becoming wider with a correlation length of 0.048. The presence of **j** structures narrower than **e** structures is consistent with the findings of *Bhattacharjee et al.* [2001] in 2D HMHD laminar reconnection. The MHD **e** autocorrelation function is significantly wider than HMHD with a correlation length of 0.081. At small separations the MHD **e** autocorrelation is not identical to **j**. Enhanced small-scale **e** activity has also been observed in 3D HMHD turbulence simulations by *Dmitruk and Matthaeus* [2006]. Smaller scale **e** activity in HMHD is expected because the Hall term, present in Eq. 2.10, is important at small scales.

The **e** spectra, which are the Fourier transform of the autocorrelation function, are also shown in Figure 4.10b. At wavenumbers below $1/\epsilon_H$ the HMHD and MHD electric field spectra are similar and at wavenumbers above $1/\epsilon_H$ HMHD has significantly enhanced electric field activity over MHD. The behavior of the electric field spectra are consistent with that reported by *Dmitruk and Matthaeus* [2006].

4.2.3 Comparison to Hyperdiffusive Runs

In order to test if the method of dissipation (regular Laplacian dissipation or hyperdiffusive Laplacian-squared dissipation) alters the results of the previous sections, two hyperdiffusive HMHD runs (see Table 4.1 for parameters) are performed and compared to the runs using regular diffusivity. The hyperdiffusive runs are analyzed at the time of maximum $\mathcal{P}_T$.

In general, runs using hyperdiffusivity give comparable results to the regular diffusivity runs. Some examples are shown in Figure 4.11. Figure 4.11a gives the energy spectra for Fourier modes with $|P_M| > 0.3$. While 512^3 resolution regular diffusivity runs seen in Figure 4.3 show only short regions that may be consistent with $k^{-7/3}$ scaling for $P_M < -0.3$, the hyperdiffusive runs show regions consistent with $k^{-7/3}$ scaling from just above $1/\epsilon_H$ until $k \sim 30$ in the case of run RH2K4b. However, $P_M > 0.3$ still does not show a significant range of $k^{-11/3}$ scaling. Figure 4.11b shows $E_M(k)/E_V(k)$ for both the hyperdiffusive runs with regular diffusivity runs RH2b and RH2c for comparison. In all runs a transition occurs at scales much smaller than the ion inertial length

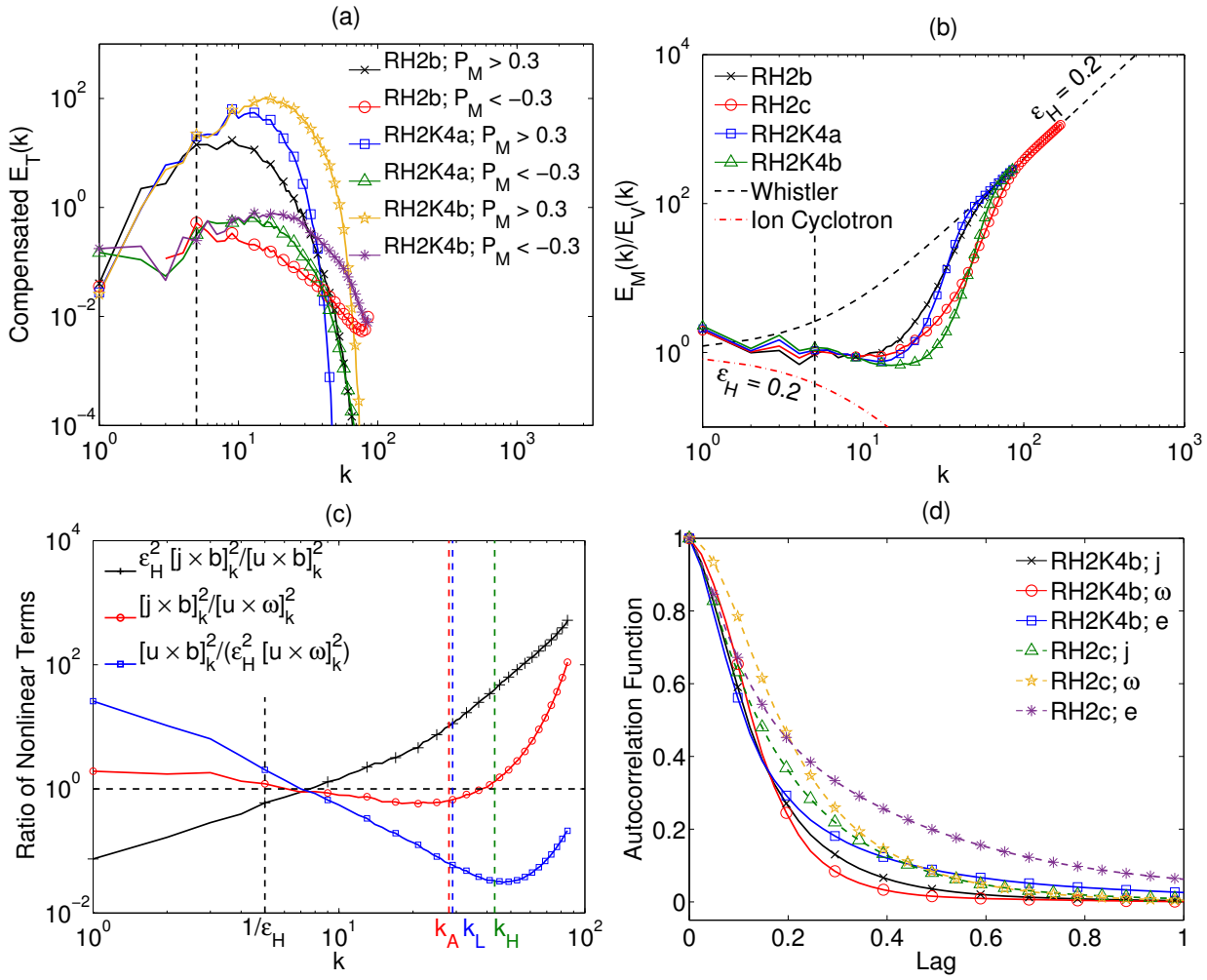

Figure 4.11: (a) Energy spectra for Fourier modes with $|P_M| > 0.3$ for the two hyperdiffusive runs, as well as run RH2b for comparison. The spectra for negative P_M are compensated by $k^{7/3}$ and the positive P_M spectra are compensated by $k^{11/3}$. The vertical dashed line marks $1/\epsilon_H$. (b) $E_M(k)/E_V(k)$ for the two hyperdiffusive runs with runs RH2b and RH2c (note that this run has 512^3 resolution) for comparison. The vertical dashed line marks $1/\epsilon_H$. (c) Ratio of nonlinear terms in the magnetic vector potential equation, momentum equation, and "uncurled" $\mathbf{\Omega}_L$ equation for run RH2K4b. The horizontal dashed line denotes unity and the four vertical dashed lines mark the wavenumbers $1/\epsilon_H$, k_A, k_L, and k_H. (d) Autocorrelation functions for the current, vorticity, and electric field in run RH2K4b and RH2c for comparison.

to a magnetically dominated state following the prediction of Eq. 4.5 and the wavenumber of the transition moves to larger values as the diffusivity coefficients are decreased. In the hyperdiffusive runs, the transition from near equipartition to $E_M(k)/E_V(k) = \epsilon_H^2 k^2$ is steeper than in the regular viscosity runs. When examining the ratios of the nonlinear terms in the magnetic vector potential (equivalent to the electric field equation), momentum, and "uncurled" $\mathbf{\Omega}_T$ equations for run RH2K4b (Figure 4.11c) similar features are seen to the regular diffusivity run shown in Figure 4.6a. The Hall term dominates the electric field at wavenumbers above $k \sim 8$. At $k_A \sim 28$ a transition occurs in the momentum equation where the Lorentz force becomes increasingly important and eventually dominates the equation. The wavenumber k_A also roughly coincides with the beginning of the transition to the magnetically dominated state in Figure 4.11b as also found in the regular diffusivity runs. Figure 4.11d shows the autocorrelation functions of $\mathbf{j}$, $\boldsymbol{\omega}$, and $\mathbf{e}$ for runs RH2K4b and RH2c (also see Figure 4.10 for another regular diffusivity example). Again the curves show similar general features between hyperdiffusive and regular diffusive runs. At small separations the $\boldsymbol{\omega}$ autocorrelation tends to be wider than the $\mathbf{j}$ autocorrelation with a crossover that occurs at larger separations. The $\mathbf{e}$ autocorrelation is similar to the $\mathbf{j}$ autocorrelation at small separations but ultimately wider at large separations. Other results discussed in this paper, but not shown in Figure 4.11, are likewise similar between hyperdiffusive and regular diffusivity runs.

4.3 Conclusions

In this study, 3D direct numerical simulations of Hall MHD turbulence are examined in both Fourier and configuration space and compared to MHD simulations. Runs using both traditional Laplacian dissipation and hyperdiffusive Laplacian-squared dissipation are performed and similar results are obtained regardless of the dissipation operator used. It is found that at small to moderate wavenumbers, which can extend to scales below the ion inertial length, $E_M(k)/E_V(k)$ is in near equipartition. Unlike MHD, at large wavenumbers the ratio becomes magnetically dominated and scales as $\epsilon_H^2 k^2$ which is consistent with the behavior of linear whistler waves. However, it is shown that this scaling is also consistent with nonlinear fluctuations when the $\mathbf{j} \times \mathbf{b}$ terms (Lorentz force

and Hall terms) are dominant in the equations. The transition to the magnetically dominated state, which may be akin to the electron MHD regime where ions are taken to be a dynamically unimportant neutralizing background, is found to occur when the $\mathbf{u}\cdot\nabla\mathbf{u}$ term becomes subdominant to dissipation. Unlike MHD, this length scale is potentially different than the overall dissipation scale of the system. The near equipartition of energy into the Hall regime is strongly linked to the nonlinearity of the system, since the $\mathbf{u}\cdot\nabla\mathbf{u}$ term does not contribute to the linearized system. While the simulations presented here are performed in the presence of viscous and resistive dissipation, the results suggest that examination of the ratio of magnetic to kinetic energy spectra may provide insight into the behavior of dissipation in collisionless plasmas or at least provide an indication of the relative importance of the various nonlinearities in the system.

The spectra of right and left polarized fluctuations in HMHD turbulence have also been examined in the manner proposed by *Meyrand and Galtier* [2012]. The ratio of $\left\langle|\mathbf{u}_R|^2\right\rangle / \left\langle|\mathbf{u}_L|^2\right\rangle$ in the initial conditions seems to have an effect on the relative amplitudes of the right and left polarized spectra and, therefore affects the exact ratio of $E_M(k)/E_V(k)$ in the near equipartition region. Smaller ratios of $\left\langle|\mathbf{u}_R|^2\right\rangle / \left\langle|\mathbf{u}_L|^2\right\rangle$ appear to be associated with more kinetic energy. The slope of the right and left polarized spectra have short regions that may be consistent with $k^{-7/3}$ and $k^{-11/3}$ respectively when considering moderate to large polarizations ($|P_M| > 0.3$) and regular diffusivity. However, when considering just strongly polarized fluctuations ($|P_M| > 0.7$) left polarized fluctuations show a much steeper spectrum than $k^{-11/3}$ while right polarization has a significant $k^{-7/3}$ region. When using hyperdiffusivity the region consistent with $k^{-7/3}$ is somewhat enhanced for $P_M < -0.3$.

Current structures in HMHD are found to be narrower and more intense than in MHD, as has been noted by various other authors [*Donato et al.*, 2012; *Miura and Hori*, 2009; *Miura and Araki*, 2011]. In particular, it is found that while current and vorticity structures have nearly equal sizes on average in MHD, in HMHD current structures become narrower and vorticity structures become broader. Evidence is also found that there may be a relationship between the strong current structures and alignment between the current and magnetic field. This behavior is somewhat different

than the idea of strong currents forming in the boundary between regions of strong alignment, which has been proposed in the context of MHD [*Meneguzzi et al.*, 1996; *Servidio et al.*, 2008]. Alignment between **j** and **b** within strong current structures may be of particular importance in collisionless plasmas where intense field-aligned currents can be unstable, as is discussed in more detail in Chapters 5 and 6.

Electric field autocorrelation functions are found to be significantly narrower in HMHD than in MHD and to behave similar to the current autocorrelation function at small separations. The similar behavior to the current autocorrelation may be of use for in situ measurements of space plasmas, since the electric field is often easier to obtain than the current. However, further understanding of how additional kinetic effects alter this behavior is necessary to use this feature in space plasmas.

Additional simulations may provide further insight into some of the results found here. In light of the $E_M(k)/E_V(k)$ findings, studies varying the magnetic Prandtl number such that $\nu \neq \eta$ (in particular $\nu < \eta$) may be interesting in HMHD, since this can alter the ordering of the various dissipation scales and could produce different behavior. Simulations with an explicitly imposed B_0 could provide more insight into the role of the double curl Beltrami configuration in the small scales. Finally, simulations with smaller scale initial conditions or forcing, such that more strong current structures are generated and better statistics are obtained, would help to characterize the relationship between current structures and alignments.

Chapter 5

The Role of Turbulence in Bursty Bulk Flows: THEMIS Observations

As discussed in Chapter 1.3.1, one region of the magnetosphere where turbulence is thought to be driven is in the bursty bulk flow (BBF) braking region, where strong Earthward flows driven by the magnetic tension released by magnetic reconnection, impinge on the near-Earth dipolar field. Simulations show the development of flow vortices and turbulence as the flow rebounds off of the dipole field [e.g. *Birn et al.*, 2011; *El-Alaoui et al.*, 2013]. The analysis of turbulence in the BBF braking region provides an opportunity to examine the role of turbulence in the dissipation of energy released by magnetic reconnection. Specifically, reconnection facilitates the conversion of energy stored in the magnetic field to bulk flow energy through the formation of reconnection jets. If dissipative processes are not sufficiently strong at the scale of the bulk flow, turbulence can then provide a means to transfer the large-scale energy into the small scales, where it can be dissipated into the plasma.

Burst data from the THEMIS mission also provides an opportunity to examine collisionless dissipation mechanisms. Observations have shown the presence of double layers and electron phase space holes (discussed in Chapter 2.2.2) in both the plasma sheet in general [*Ergun et al.*, 2009] and more specifically in association with BBF braking events [*Ergun et al.*, 2015]. The observations, discussed further in Chapter 5.1, are consistent with a sparsely distributed population of double layers, which are not always directly observed but that generate electron phase space holes that are often observed. The observations, therefore, suggest the presence of field-aligned currents, since most of the few known mechanisms for generating these structures are through current instabilities

[*Newman et al.*, 2001]. The question then becomes how are these currents generated in the BBF braking region? One possibility is that turbulence transfers the energy contained in large scale fluctuations to small kinetic scales and generates intermittent currents. As discussed in Chapter 4.2.2, in the context of HMHD, the intermittent currents formed by turbulence can have significant field-aligned components. In Chapter 5.2, the possibility that sufficient field-aligned current is generated through linear waves is considered and then observations are analyzed for the role of turbulence in the remainder of the chapter.

Finally, since BBFs drive turbulence within a confined region of the magnetosphere, namely the plasma sheet, it is possible that waves radiate from the region and provide a mechanism for the removal of energy from the turbulent fluctuations, as mentioned in Chapter 1.2. This process could be of geophysical significance because plasma waves radiated along the magnetic field could propagate to the auroral region (near the poles of the Earth), where they could deposit energy and drive Alfvénic aurora [e.g. *Chaston et al.*, 2007b].

5.1 Observations of Kinetic Structures and Spectra in the Braking Region

Ergun et al. [2015] performed a detailed analysis of large-amplitude **E** activity associated with BBF braking events. Using THEMIS data, *Ergun et al.* [2015] found that BBF braking events often contain strong **E** fluctuations in both the components perpendicular and parallel to **B** and high-frequency (above the ion cyclotron frequency) electrostatic activity. Electric field amplitudes were observed as high as 500 mV/m, whereas estimates based on the typical amplitude of **B** fluctuations would expect corresponding Alfvénic **E** fluctuations with amplitudes of ∼5–10 mV/m. Strong **E** activity was observed to be almost always embedded within intervals exhibiting **B** fluctuations, but not all intervals of **B** fluctuations show exceptionally high **E** amplitudes suggesting a threshold mechanism in the generation of strong **E** activity. Nonlinear electrostatic structures, namely double layers and electron phase space holes, were also observed in the braking region [*Ergun et al.*, 2009, 2015]. *Ergun et al.* [2015] report that for events where high resolution wave burst data (measuring fields at 8196 samples/s) is available electron phase space holes are present in 90% of events and

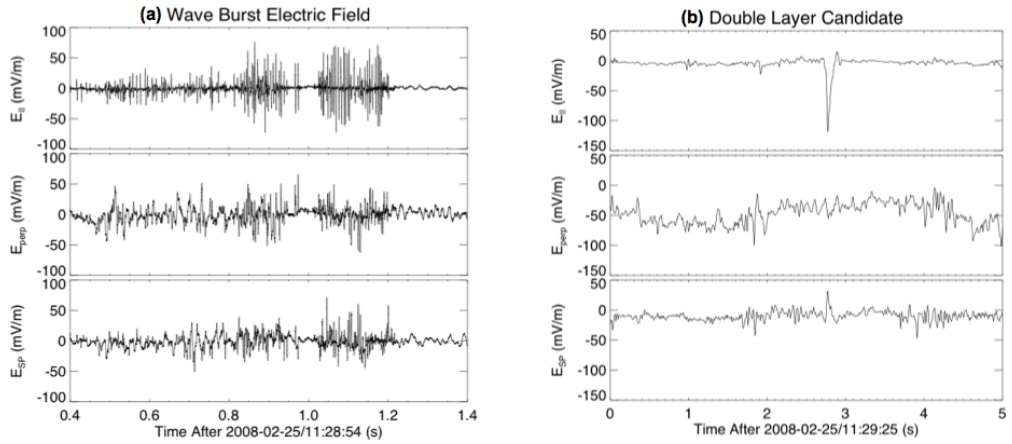

Figure 5.1: (a) Wave burst **E** measurements in magnetic field-aligned coordinates. The high resolution $E_{||}$ signatures have the distinct bipolar signatures of electron phase space holes when zoomed in. (b) Particle burst data showing a possible double layer (the $E_{||}$ feature at ~ 2.7 s). Both sets of data are from a BBF braking event observed by THEMIS.

double layers are present in 20% of events and a number of double layer candidates are found in the particle burst data (measuring fields at 128 samples/s), which were not captured by the wave burst data.

Figure 5.1a shows an example of the electron phase space holes captured by the wave burst data in a BBF braking event. The components of **E** are displayed in a field-aligned coordinate system with the top panel showing the component parallel to **B** (subscript "||"), the bottom panel showing the component perpendicular to **B** and in the spin-plane of the spacecraft (subscript "SP"), and the middle panel showing the perpendicular component that completes the right hand coordinate system (subscript "$PERP$"). The high-frequency **E** activity is dominated by $E_{||}$, which exhibit bipolar structure (all with a positive followed by negative peak) consistent with electron phase space holes. Figure 5.1b shows a potential double layer captured by the particle burst data and characterized by a strong unipolar $|E_{||}| > 100$ mV/m.

Ergun et al. [2015] also showed that low-frequency fluctuations (below the ion cyclotron frequency) appear to be, in part, Alfvénic in nature. The presence of Alfvénic fluctuations was inferred from the E/B ratio and the Poynting flux, which is largely aligned with $\mathbf{B}_0$. The spectra

of low-frequency fluctuations in **E** and **B** exhibit power law behavior that may be indicative of turbulence; perpendicular **B** fluctuations follow a $-5/3$ power law in frequency, while perpendicular **E** is closer to a $-3/2$ power law on average. At high frequencies, the **B** spectrum steepens and the **E** spectrum becomes shallower; behavior that appears to be common in plasma turbulence, as it is also seen in the Kelvin-Helmholtz instability discussed in Chapter 6 and in the solar wind [e.g. *Bale et al.*, 2005].

In this study, we investigate how the observed strong electric fields are generated. Observations of double layers and electron phase space holes within BBF braking events suggest that field-aligned currents may be present within the region that could destabilize into these structures. A hypothesis is examined in which turbulence within the braking region generates the necessary field-aligned currents to create the double layers and electron phase space holes. This process represents a dissipation mechanism in which energy is removed from the turbulent fluctuations by the destabilization of field-aligned currents into nonlinear kinetic structures. Heating of the plasma would then occur through the acceleration of particles within the kinetic structures, which offers an alternative to methods where heating occurs directly though the interactions of particles with the turbulent fluctuations.

5.2 Kinetic Alfvén Waves

The kinetic Alfvén wave is the generalization of the MHD shear Alfvén wave to length scales near or below the ion gyroradius. While fluid approximations exist, both based on the two-fluid equations [*Stringer*, 1963; *Streltsov and Lotko*, 1995] and using modifications to the single fluid equations [*Marchenko et al.*, 1996], the full treatment of the kinetic Alfvén wave requires the coupled system of Maxwell's equations to solve for **E** and **B** and the Vlasov equation to solve for the evolution of the particle distribution function (see Chapter 2.2). A comparison of approximations to the kinetic Alfvén wave dispersion relation can be found in *Bellan* [2012].

An important parameter for this wave mode is the plasma β defined as $\beta \equiv 2\mu_0 n_0 k_B T_0 / B_0^2$. For a proton-electron plasma, we can define $\beta_i \equiv 2\mu_0 n_{0i} k_B T_{0i} / B_0^2$ and $\beta_e \equiv 2\mu_0 n_{0e} k_B T_{0e} / B_0^2$

assuming $n_{0e} = n_{0i} = n_0$ due to quasineutrality, and with T_{0i} and T_{0e} the temperatures associated with the ion and electron populations. The total $\beta = \beta_i + \beta_e$.

For plasmas with $m_e/m_i \ll \beta/2 < 1$ and assuming small but non-zero ion gyroradius, analytic expressions for the kinetic Alfvén wave dispersion relation have been derived [*Hasegawa*, 1976]. Assuming $\beta < 1$ the dispersion relation can be written as [Eq. 6 in *Lysak and Lotko*, 1996]

$$\frac{\omega^2}{k_\parallel^2 V_A} = \frac{k_\perp^2 \rho_i^2}{1 - \Gamma_0\left(k_\perp^2 \rho_i^2\right)} + \frac{k_\perp^2 \rho_{sound}^2}{\Gamma_0\left(k_\perp^2 \rho_e^2\right)\left[1 + \xi_0 Z\left(\xi_0\right)\right]} \tag{5.1}$$

where $\rho_{sound} = \rho_i\sqrt{T_{0,e}/T_{0,i}}$ and ρ_e and ω_{ce} are defined to be negative (see Chapter 2.2.1 for definitions of the parameters and functions in Eq. 5.1). When $\beta/2$ becomes less than approximately m_e/m_i, the behavior of Equation 5.1 significantly changes and the kinetic Alfvén wave transitions into the inertial Alfvén wave regime [*Lysak and Lotko*, 1996]. However, this β regime is well below the regime of the data discussed in this study.

Although the low β limit allows for the simplification of the governing equations to a form that is more easily manipulated, it neglects the effect of ion damping. Linear damping on a species peaks when the parallel phase velocity of the wave ($\omega/k_{||}$) is approximately equal to $V_{T,s}$. For kinetic Alfvén waves, $\omega/k_{||}$ approaches V_A at small $k_\perp$ and then increases as $k_\perp$ increases. For ions, the ratio $V_A/V_{T,i} = \sqrt{B_0^2/(\mu_0 n_0 k_B T_{0i})} = \sqrt{2/\beta_i}$ and for electrons this ratio is given by $V_A/V_{T,e} = \sqrt{m_e B_0^2/(\mu_0 m_i n_0 k_B T_{0e})} = \sqrt{(m_e/m_i)(2/\beta_e)}$. It is apparent that in environments where β_i is approximately 2 or greater, ion damping potentially can be important for kinetic Alfvén waves since at some $k_\perp$ value there will be a wave with $\omega/k_\parallel \approx V_{T,i}$. In lower β_i environments, ion damping can be bypassed because even the lowest $\omega/k_\parallel$ that a kinetic Alfvén wave can attain is still larger than $V_{T,i}$. In this case, damping can occur on electrons for waves with the appropriate $k_\perp$ values.

Figures 5.2 and 5.3 show the behavior of $\omega/k_\parallel$ and the linear damping in different β regimes based on the numerical solution to the linearized Maxwell-Vlasov equations, which are valid for all values of β (see Appendix A.2). In all panels $n_0 = 3 \times 10^5$ m^{-3}, T_{0i} =15 keV, and T_{0e} = 3 keV. These values are selected based on the data examined in Section 5.3. The factor of 5 between T_{0i}

and T_{0e} is consistent with statistical studies of the plasma sheet that find ion temperatures greater than electron temperatures [*Paterson and Frank*, 1994]. The value of B_0 is adjusted to obtain the values 0.25, 0.5, 1.0, and 2.0 for β_i. The displayed solutions have the real part of the frequency given by $\omega_r = 0.1\omega_{ci}$.

In Figure 5.2, $\omega/k_\parallel$ approaches V_A at small $k_\perp\rho_i$ and increases with increasing $k_\perp\rho_i$ in all panels, as expected. However, as β increases the numerical solution diverges from the analytic approximation in Eq. 5.1, illustrating the need for a numerical solution.

Figure 5.3 shows the numerical solution for the ratio of the imaginary part of the angular frequency to the real part. The related quantity $\omega_r/(2\pi\omega_i)$ measures the number of oscillations that occur before the amplitude is damped by one e-folding. The ion and electron contributions to this ratio are plotted as blue dotted lines and red dashed lines respectively. At the lowest value of β_i, damping on electrons dominates the dissipation. This strong electron damping is due to the fact that this solution also has the lowest β_e. Therefore, V_A begins closer to $V_{T,e}$ and, as discussed above, strong electron damping occurs sooner as $\omega/k_\parallel$ approaches $V_{T,e}$. Conversely, at the largest value of β_i the electron damping is weaker and a peak due to damping on ions appears at $k_\perp\rho_i \sim 1$. At the middle value of β_i, the magnitude of the contributions due to both electrons and ions are smaller for a given value of $k_\perp\rho_i$. Taking a value of $|\omega_i/\omega_r| \sim 0.1$ as significant damping, plasma environments with $\beta_i \sim 0.5$–2.0 have the most potential for energy to cascade to wavenumbers several times larger than ρ_i. However, the value of T_{0e}/T_{0i} can alter this range of values, with larger T_{0e}/T_{0i} resulting in increased electron damping [*Lysak and Lotko*, 1996].

The development of field-aligned currents within Alfvén waves results from the polarization drift of ions combined with a nonzero $k_\perp$ [*Boyd and Sanderson*, 2003]. For Alfvén waves the polarization of $\mathbf{E}$ is dominantly perpendicular to $\mathbf{B}_0$ and, therefore a current is also present in that direction. In order for the plasma to maintain quasineutrality, the current must close along the field line. Although the exact details of the calculation may change, the basic concept of a polarization drift combined with quasineutrality requiring the presence of a field-aligned current is valid in both the linear and nonlinear regimes.

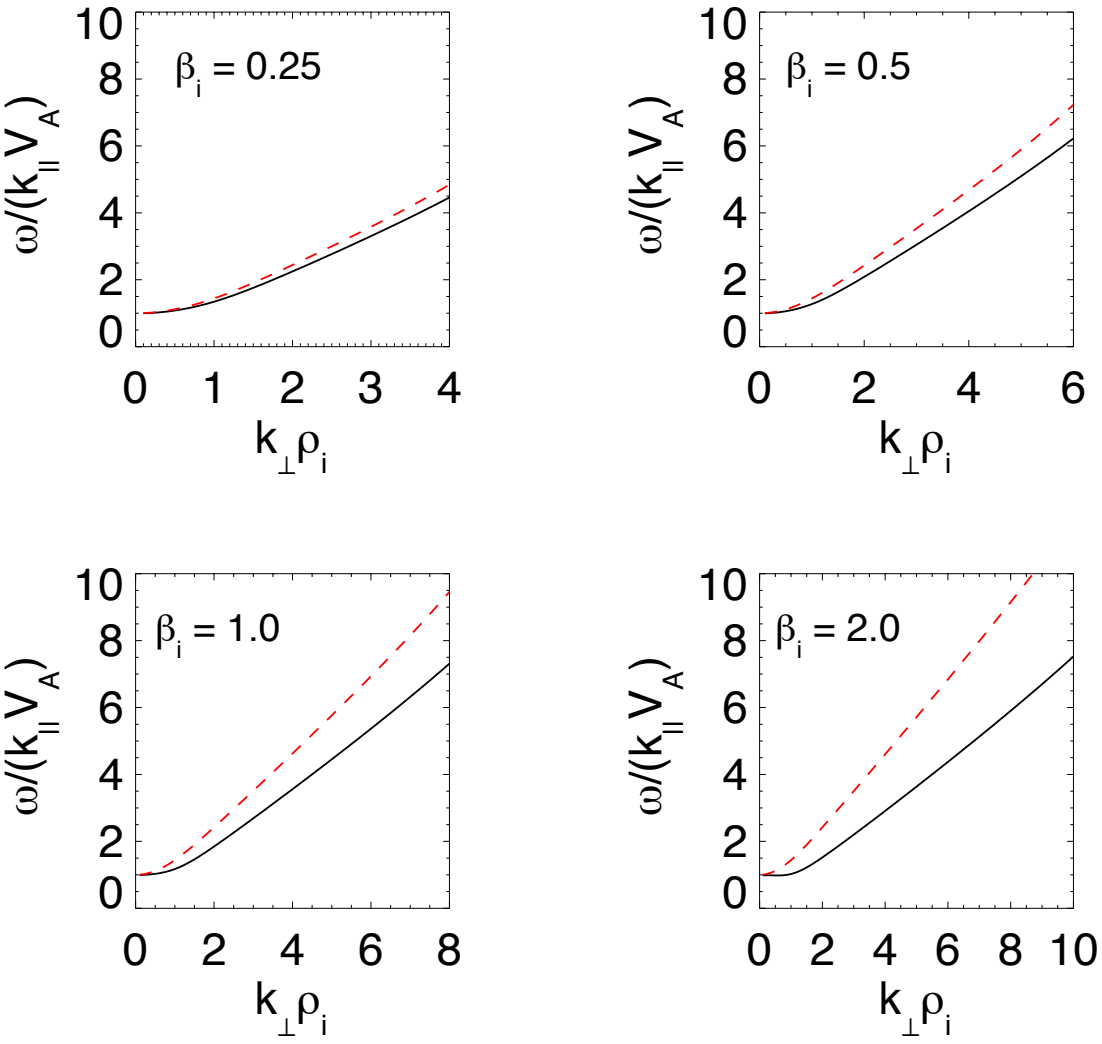

Figure 5.2: Solid black lines plot numerical solutions of the parallel phase velocity relative to V_A for kinetic Alfvén waves (see Eq. 2.46–2.53) at four different values of β as a function of $k_\perp \rho_i$. The background density and ion and electron temperatures are held fixed at $n_0 = 3 \times 10^5$ m^{-3}, T_{0i} =15 keV, and $T_{0e} = 3$ keV and the value of B_0 is adjusted so as to obtain the value 0.25, 0.5, 1.0, and 2.0 for β_i. The red dashed lines plot the low β approximation from Equation 5.1 for comparison. For all β values the phase velocity increases from V_A as $k_\perp \rho_i$ increases.

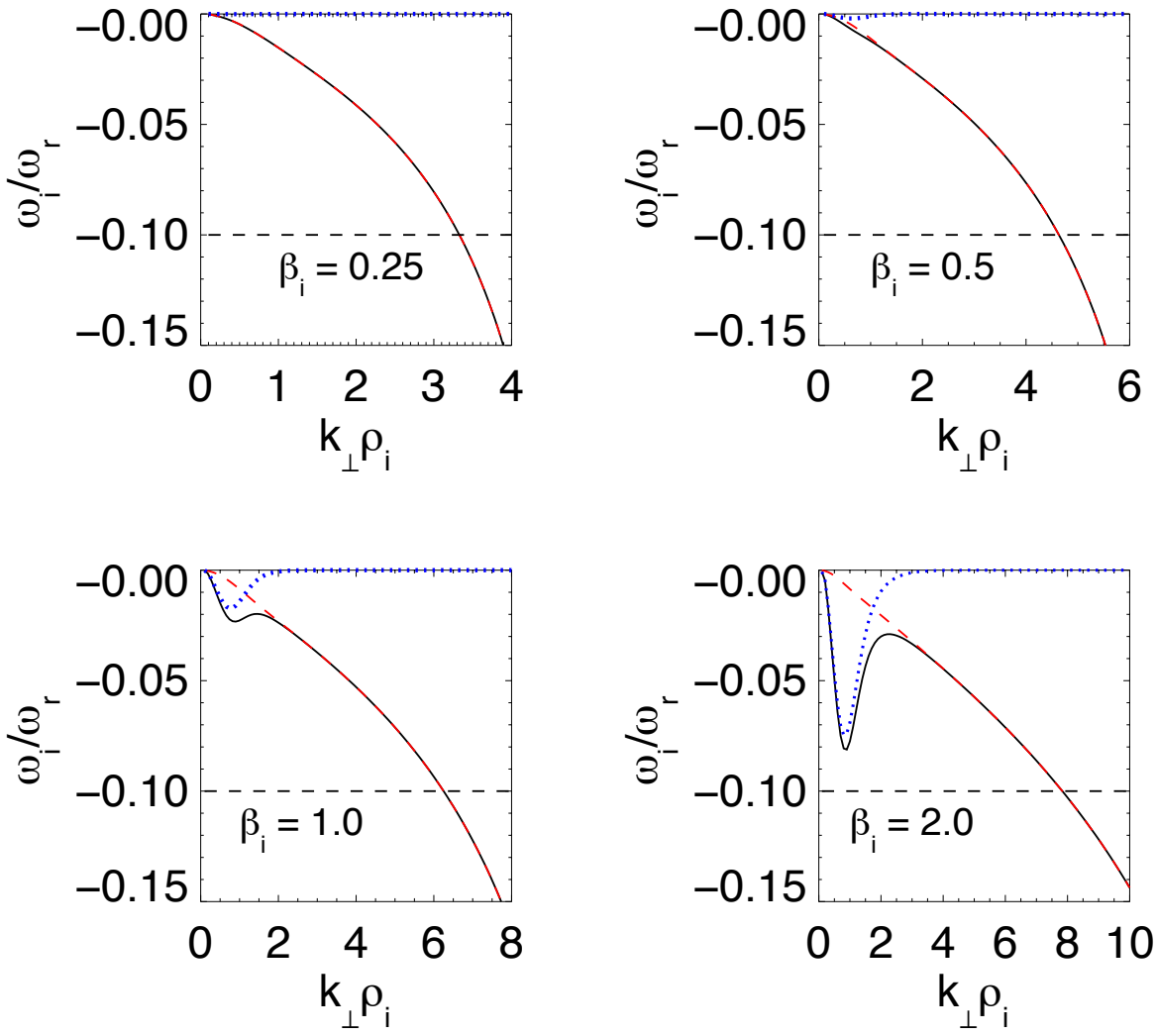

Figure 5.3: For the same parameters as in Figure 5.2, the black solid lines plot numerical solutions for ω_i/ω_r as a function of $k_\perp \rho_i$. Blue dotted lines and red dashed lines show the contributions to this ratio due to ion and electron damping respectively. Within the range $\beta_i \sim 0.5$–2.0 the damping remains below $|\omega_i/\omega_r| \sim 0.1$ for a relatively wide range of $k_\perp \rho_i$ and is thus the range of β that has the best chance of developing unstable field-aligned currents. At low values of β, electron damping dominates, while at larger values of β, ion damping can become important.

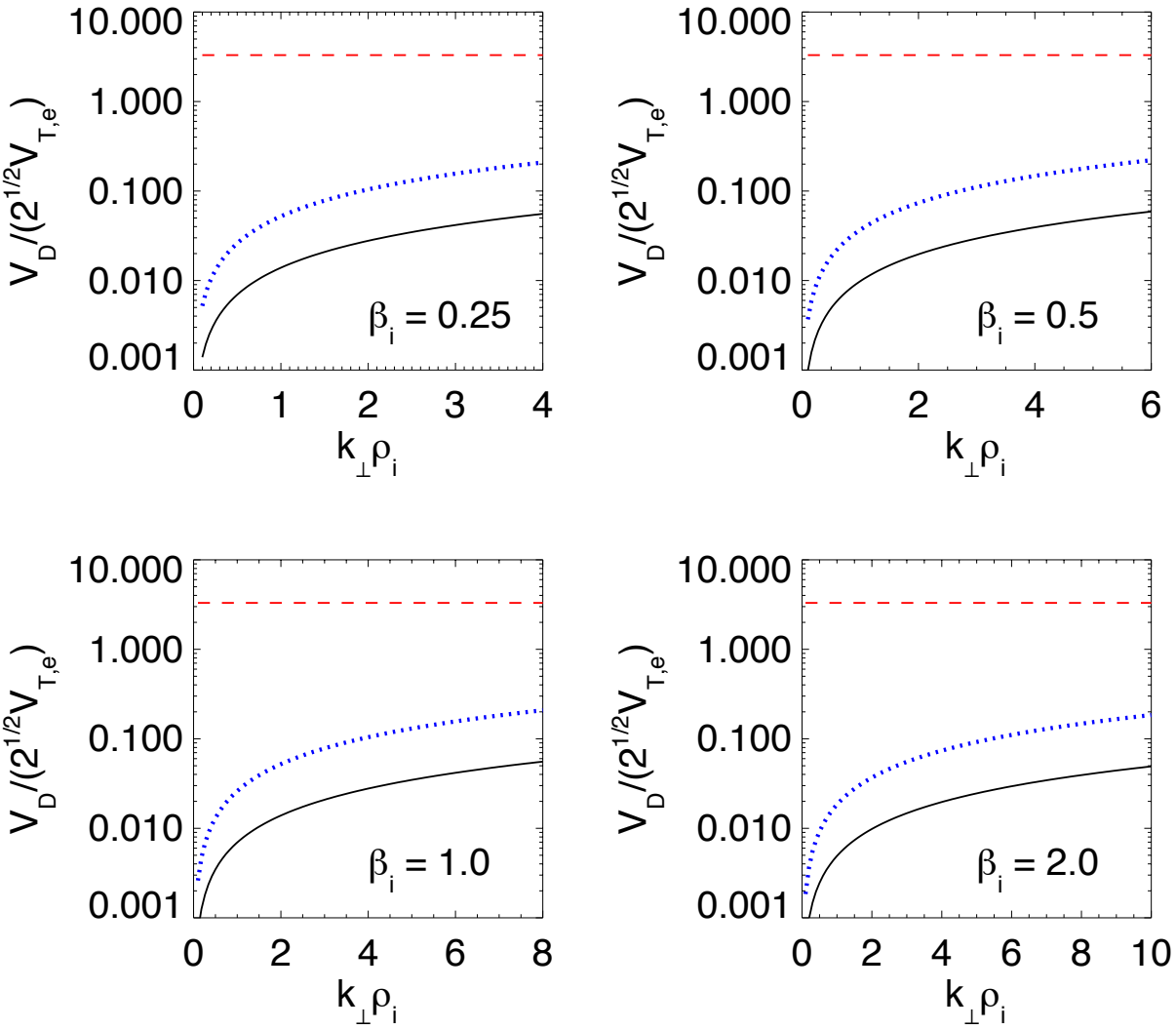

Figure 5.4: For the same parameters as Figure 5.2, the black solid lines and blue dotted lines plot the numerical solutions for the field-aligned currents expressed as a drift velocity between the ion and electron distribution functions relative to $\sqrt{2}V_{T,e}$ as a function of $k_\perp\rho_i$. The amplitude of the **B** perturbation is 4 nT for the black solid lines and 15 nT for the blue dotted lines. The red dashed lines show the Buneman instability threshold for $T_{0e}/T_{0i} = 0.2$ based on *Kindel and Kennel* [1971].

Figure 5.4 shows the field-aligned currents associated with Alfvén waves for the same parameter values shown in Figures 5.2 and 5.3. The current is expressed as a drift velocity between the ion and electron distribution functions, $V_D = J_\parallel/(n_0 q)$, scaled by $\sqrt{2}V_{T,e}$. The amplitude of the current is linearly proportional to the magnitude of the fluctuation and in Figure 5.4 the field-aligned current is displayed for two **B** fluctuation amplitudes. For the black solid curve the value is 4 nT based on root-mean-squared fluctuation amplitudes observed below ω_{ci} and for the blue dotted curve it is 15 nT based on the typical value for peak **B** differences over 10 s intervals within strong **E** events as examined by *Ergun et al.* [2015]. The current increases as $k_\perp \rho_i$ increases and, although at MHD scales field-aligned currents can be present, for a given fluctuation amplitude the currents at kinetic scales are significantly larger. The current reaches a larger value for smaller β; however, at moderate β_i linear damping does not reach the same level until larger $k_\perp \rho_i$. The dashed red lines give the instability threshold for the Buneman instability based on *Kindel and Kennel* [1971], which can lead to the growth of double layers [*Newman et al.*, 2001] (see Chapter 2.2.2). Within the range $0.5 < \beta_i < 2.0$, the current of a single linear wave with an amplitude of 4 nT can reach a value about 55 times less than the instability threshold before the damping reaches $|\omega_i/\omega_r| \sim 0.1$, and for 15 nT, it is a factor of 15 less. Note that for β_i of approximately 2 or greater, ion damping becomes stronger at smaller $k_\perp$ than electron damping and as such the field-aligned currents are even smaller.

From the above analysis, it is unlikely that Buneman unstable currents form from a linear combination of kinetic Alfvén waves as would arise from weak turbulence. However, it is possible that strong turbulence with intermittency can lead to extreme currents.

5.3 Observational Analysis

To test the proposed hypothesis, data from the Electric Field Instrument (EFI) [*Bonnell et al.*, 2008; *Cully et al.*, 2008], Fluxgate Magnetometer (FGM) [*Auster et al.*, 2008], Search Coil Magnetometer (SCM) [*Roux et al.*, 2008], Electrostatic Analyzer (ESA) [*McFadden et al.*, 2008a], and Solid State Telescopes (SST) on the THEMIS satellites [*Angelopoulos*, 2008] are examined.

The data used are particle burst intervals from the years 2008 and 2009, which are intervals of higher resolution data triggered by dipolarization events in the magnetotail and provide **E** and **B** measurements every 1/128 seconds and moments of the distribution function every 3 seconds [*Angelopoulos*, 2008]. Interval selection for this study is based on peak $|\mathbf{E}| > 10$ mV/m and spacecraft location between 8 and 12 R_E away from Earth in radial distance, within $\pm 30^\circ$ of the equatorial plane, and within $\pm 45^\circ$ of midnight. These requirements on position are made to limit the data to the BBF braking region and within the nominal location of the plasma sheet. These selection criteria differ from the criteria used for the analysis in *Ergun et al.* [2015] in the choice of peak threshold ($|\mathbf{E}| > 50$ mV/m), which this study takes to be substantially lower in order to get a sampling of both strong and weak events.

Based on these criteria, a database of 200 intervals with intense **E** activity is compiled. In Figure 5.5 an example of one such interval, plotted in geocentric solar magnetospheric (GSM) coordinates, is shown. A number of features typical of many of the events in this study can be seen in Figure 5.5. These intervals exhibit regions of heightened **B** fluctuations often associated with heightened **E** fluctuations. The peak amplitudes of **E** range from tens of mV/m up to a few hundred mV/m (see Figure 5.5c,d). The field activity is generally associated with a signature in the velocity on the order of several hundred km/s, the profile of which is consistent with the rebounding or deflection of the flow in a BBF braking event. For example, the velocities in Figure 5.5f are enhanced in the x GSM and y GSM components, as well as to a lesser extent in the z GSM component. The velocity signatures may be associated with the deflection of the BBF flow into vortical flow [*Panov et al.*, 2010; *Birn et al.*, 2011; *Ergun et al.*, 2015]. **E** activity is also generally associated with a dipolarization of **B** and increase in temperature consistent with observations of BBF events [*Angelopoulos et al.*, 1992]. Note the increase in $|B_z|$ GSM (red curve) and decrease in $|B_x|$ GSM (blue curve) in Figure 5.5c, as well as the increase in T_e and T_i (black curves in Figure 5.5a,b). As plotted in Figure 5.5e, the enhanced fluctuations are also associated with strong detrended Poynting flux ($d\mathbf{S} = \delta\mathbf{E} \times \delta\mathbf{B}/\mu_0$) with power that can be in excess of 1 mW/m^2 and with a significant field-aligned component indicative of Alfvénic fluctuations [*Wygant et al.*, 2002].

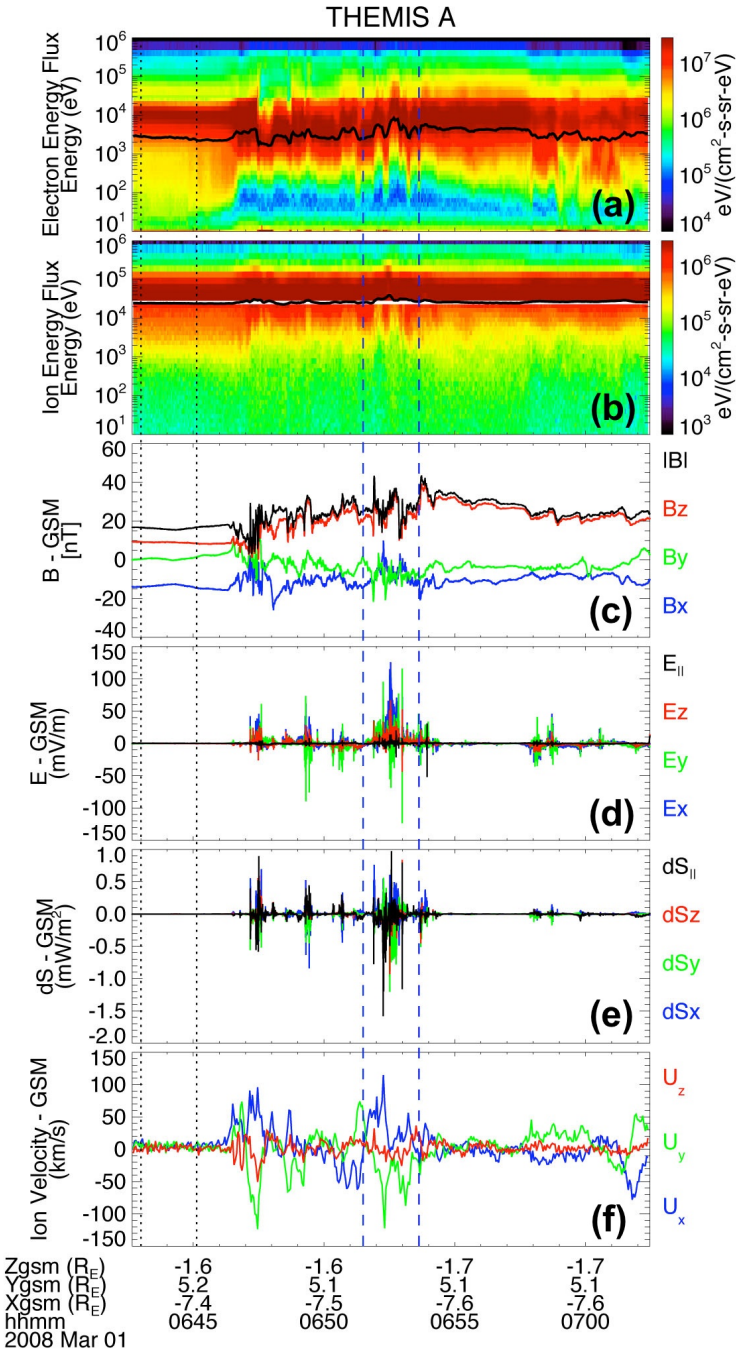

Figure 5.5: Summary plot of an example burst interval containing a strong **E** event. The data are plotted in GSM coordinates (blue, green, and red curves). Vertical dashed blue lines indicate the 128 s subinterval containing the most **E** power integrated over the spectrum. Vertical dotted black lines indicate the 128 s subinterval containing the least **E** power integrated over the spectrum. (a) Omnidirectional electron differential energy flux from both the ESA and SST with black solid curve indicating the electron temperature. (b) Omnidirectional ion differential energy flux from both the ESA and SST with black solid curve indicating the ion temperature. (c) The magnetic field with the magnitude plotted as the black curve. (d) Electric field with $E_{||}$ plotted as the black curve. (e) Detrended Poynting flux with $dS_{||}$ plotted in black. (f) Ion flow velocity computed from the ESA.

$\delta\mathbf{B}$ and $\delta\mathbf{E}$ are computed by subtracting a 128 s sliding average from the fields. Similar features were found and quantified by *Ergun et al.* [2015].

For many particle burst intervals, only a smaller subinterval shows evidence of heightened **E**. This feature is likely the result of strong **E** activity being generated in localized regions of the braking event since often **B** activity continues to be present. In order to avoid effects due to averaging together the properties of the heightened **E** regions with regions of very little activity, the data is trimmed to include only the 128 s subinterval within each particle burst interval that contained the largest **E** fluctuation amplitude when integrated over the spectrum. The length of 128 s is selected because it both allows for frequencies below ω_{ci} (typically at ~ 0.3 Hz) to be observed and because it is comparable to the typical durations of strong **E** events reported by *Ergun et al.* [2015]. For comparison, the 128 s subintervals that show the minimum **E** amplitude when integrated over the spectrum also are examined. In Figure 5.5, the 128 s subintervals used for the example interval are shown as dashed blue and dotted black lines (maximum and minimum fluctuation amplitude, respectively).

T_{0e}, T_{0i}, $\mathbf{B}_0$, and n_0 are computed as the average values over the 128 s subinterval. Derived quantities such as V_A or ω_{ci} are computed based on these averages. Characteristic amplitudes of **E** and **B** fluctuations (denoted by $d\mathbf{E}$ and $d\mathbf{B}$ respectively) are computed by integrating the respective power spectra over a frequency band and taking the square root. The two bands considered are "low frequencies" from 1/128 Hz to ω_{ci} and "high frequencies" from ω_{ci} to 64 Hz. To construct the power spectra for **B**, both the FGM and SCM are used with the FGM used for frequencies below 1 Hz, the SCM for frequencies above 8 Hz, and a linear combination of the two for intermediate frequencies. Low-frequency $d\mathbf{E}$ and $d\mathbf{B}$ are denoted by a superscript "LF" and the high-frequency quantities with a superscript "HF". The fields are rotated into the field-aligned coordinate system with respect to $\mathbf{B}_0$, as described in Chapter 5.1.

$V_A \sim 1000$ km/s and is larger than both the typical flow speeds (on the order of a few hundred km/s and nonuniform) and the speed of the spacecraft (approximately 1 km/s in the tail). As a result, obtaining spatial information about the flow through the use of the Taylor

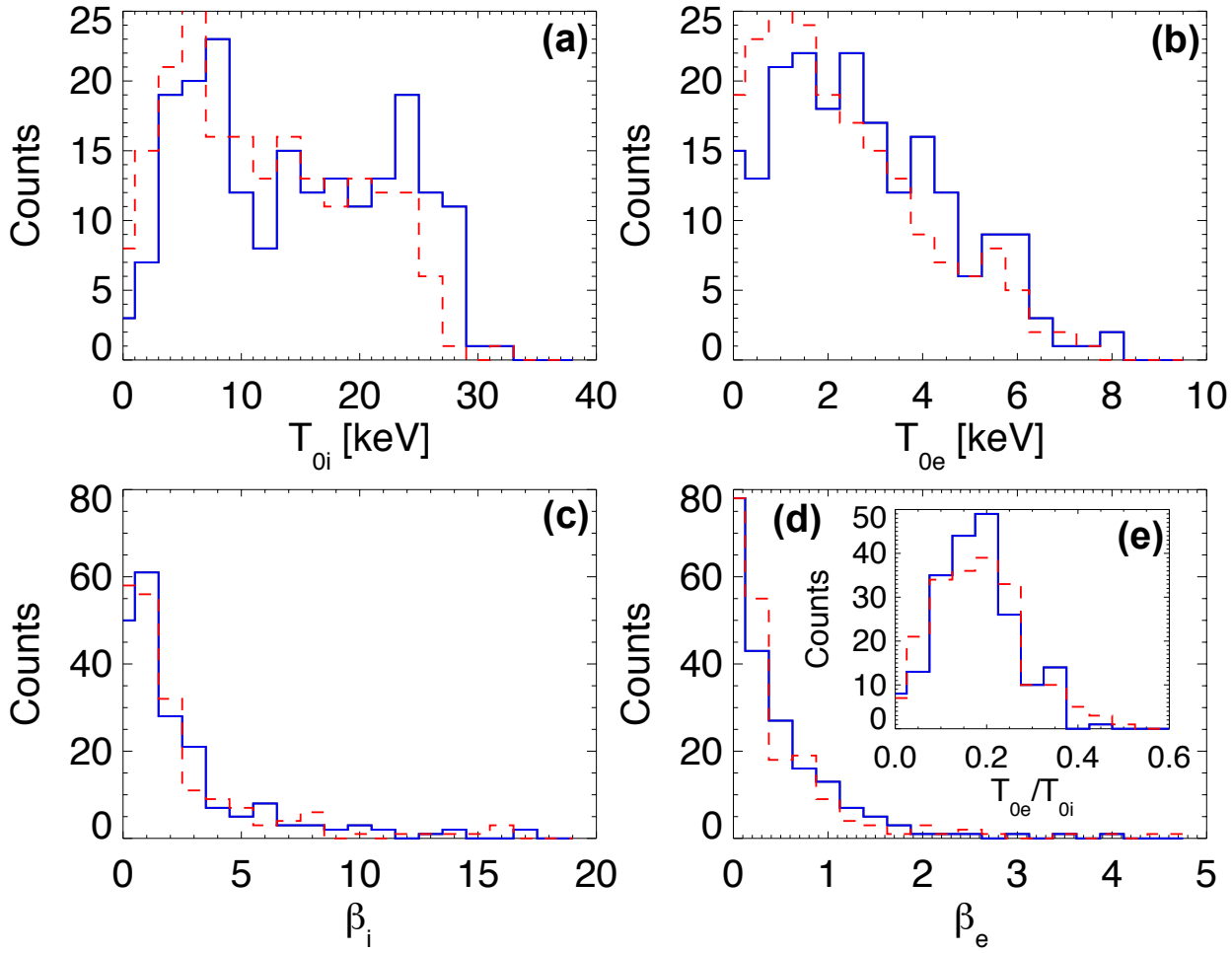

Figure 5.6: Distributions of (a) T_{0i}, (b) T_{0e}, (c) β_i, (d) β_e, and (e) T_{0i}/T_{0e} from the 128 s subintervals. Blue solid lines are from the 200 subintervals with the maximum **E** activity and red dashed lines are from the 200 subintervals with the minimum **E** activity.

hypothesis [*Taylor*, 1938], as is often done in turbulence studies of the solar wind [*Matthaeus and Goldstein*, 1982], is not generally possible. Also, a significant amount of the ion thermal energy and sometimes the electron thermal energy due to the increase in temperature associated with the events, goes above the energy range of the ESA and into the energy range of the SST. Therefore, the temperatures provided by the ESA can significantly underestimate the actual temperatures.

To obtain estimates of T_e, the combined ESA and SST differential energy fluxes (see Figure 5.5a) are numerically integrated. For T_i, ESA and SST measurements (Figure 5.5b) are combined and a characteristic energy is extracted from fits assuming an isotropic Maxwellian distribution. The details of these temperature estimates are given in Appendix B.

Figure 5.6 shows distributions of T_{0i}, T_{0e}, β_i, β_e, and T_{0e}/T_{0i} for the 200 subintervals with the maximum **E** activity and 200 subintervals with the minimum **E** activity. The averages of T_{0i} and T_{0e} within the subintervals of strong **E** activity are 15 keV and 3 keV respectively with an average T_{0e}/T_{0i} of 0.2. For subintervals with strong **E**, the median β_i is 1.7 with 50% of the intervals within the range 0.9 to 3.5 and the median β_e is 0.4 with 50% of the intervals within the range 0.2 to 0.8. These β span a range of values where, based on Figure 5.3, either electron damping could dominate or where ion damping could dominate. However, as found in Figure 5.4 it is unlikely that the linear regime could account for the necessary field–aligned currents (on the order of the Buneman instability threshold).

5.3.1 High and Low Frequency Fluctuations

Figure 5.7a compares dB^{LF}_{PERP} to dE^{LF}_{SP} for the 200 subintervals with high and low **E** activity. dE^{LF}_{SP} is used instead of dE^{LF}_{PERP} because the SP component does not include measurements from the axial electric field booms, which are less accurate than the spin-plane booms. For MHD scale Alfvén waves the ratio of the perpendicular **E** to perpendicular **B** fluctuations in orthogonal directions gives V_A. At kinetic scales, this ratio is modified and based on numerical results typically increases with increasing $k_\perp$ (as, for example, seen in *Lysak* [1998]). The subintervals with low **E** on average give a value of $dE^{LF}_{SP}/dB^{LF}_{PERP} = 1.1V_A$ distributed with 65% of the subintervals below V_A

and 35% of the subintervals above V_A adding support to the fluctuations being Alfvénic in nature. The subintervals showing high **E** activity have ratios that are generally above V_A with an average $dE_{SP}^{LF}/dB_{PERP}^{LF} = 1.9V_A$ distributed such that 75% of the subintervals are above V_A and 25% of the subintervals are below V_A. The fact that this ratio is generally above V_A is consistent with the presence of Alfvén waves with perpendicular length scales in the kinetic regime.

Wygant et al. [2000, 2002] examined the plasma sheet boundary layer from 4–6 R_E and also found strong field-aligned $d\mathbf{S}$ as seen in the events of this study. *Wygant et al.* [2002] also examined the ratio of perpendicular **E** to **B** for fluctuations with frequencies below ω_{ci} and found ratios of about 2 to 10 times V_A, which they associated with kinetic Alfvén waves. Integrated fluctuation amplitudes in Figure 5.7 are roughly consistent with the low end of the range found by *Wygant et al.* [2002]. *Chaston et al.* [2012, 2014] examined the ratio of the perpendicular **E** to **B** in spectral space finding that at low frequencies this ratio is roughly V_A and increases as the frequency increases, which they attributed to the dispersion relation of kinetic Alfvén waves. In this study it is not assumed that frequencies can be uniquely transformed into wavenumbers through the flow velocities. While the results in Figure 5.7a differ slightly from the *Chaston et al.* [2012, 2014] results, in that $dE_{SP}^{LF}/(dB_{PERP}^{LF}V_A)$ is greater than one in the high **E** activity regions, this could be the result of a mixture of wavenumbers (including kinetic Alfvén waves) making up the low frequencies or due to a mixture of Alfvénic and compressional waves as suggested in *Ergun et al.* [2015].

Based on the scenario proposed in Chapter 5.1, the strength of the field-aligned current is expected to be related to the amplitude of the low-frequency **B** fluctuations. Since the generation of high-frequency electrostatic waves and nonlinear structures are triggered by a threshold effect in the current, a threshold in the high-frequency **E** when compared to the low-frequency **B** might be expected. Figure 5.7b compares dB_{PERP}^{LF} to dE_{SP}^{HF}. The noise level of the quantities computed based on 128 s subintervals selected from 10 particle burst intervals (separate from the 200 particle bursts used in the analysis) that show no discernible **E** or **B** activity are plotted as dashed lines. A number of the low-amplitude electric field data points at the lowest dE_{SP}^{HF} values, where the

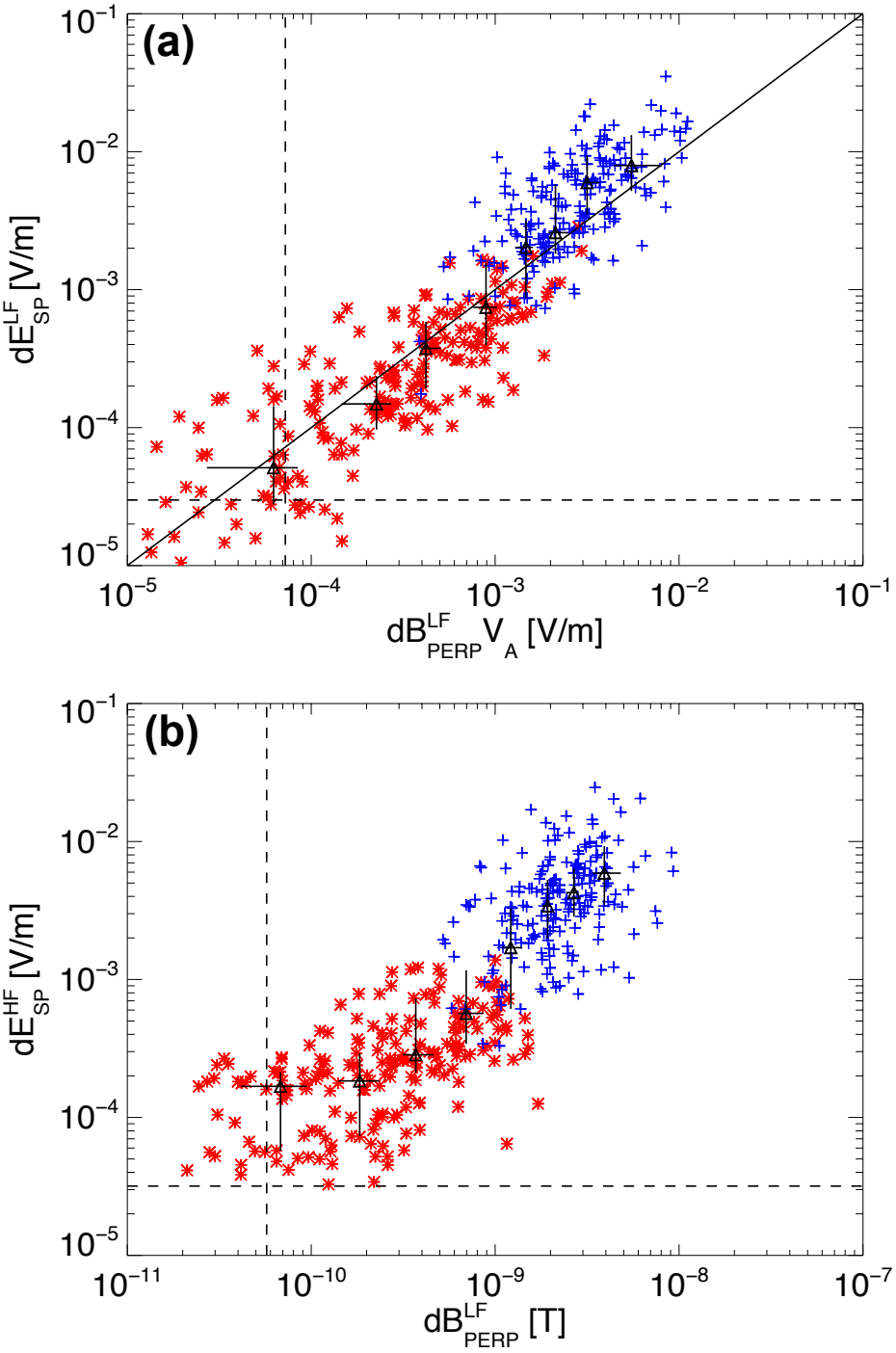

Figure 5.7: (a) Scatter plot of $dB^{LF}_{PERP}V_A$ compared to dE^{LF}_{SP} (both computed using frequencies from 1/128 Hz to ω_{ci}). The solid diagonal line is where $dE^{LF}_{SP} = V_A dB^{LF}_{PERP}$. (b) Scatter plot of dB^{LF}_{PERP} compared to dE^{HF}_{SP} (computed using frequencies from ω_{ci} to 64 Hz). Blue "+" are from 200 intervals with large **E** amplitudes when integrated over the spectrum. Red "*" are from 200 intervals with low **E** activity when integrated over the spectrum. The black triangles are median values from eight bins of $dB^{LF}_{PERP}V_A$ (a) or dB^{LF}_{PERP} (b) each containing 50 data points. The vertical and horizontal solid black lines mark the upper and lower quartiles around the median in each bin. Vertical and horizontal black dashed lines represent the estimated noise level of the quantities.

data level off at values of $\sim 3 \times 10^{-5}$ to 6×10^{-5} V/m, appear to have reached the noise floor of the EFI at high-frequencies and only provide an upper bound on dE_{SP}^{HF}. The intervals within the upper flattening at roughly 2×10^{-4} V/m seem to contain some amount of low amplitude real **E** signal. The exact nature of these fluctuations is beyond the scope of this study and is left for future investigation. There is a strong association between dB_{PERP}^{LF} and dE_{SP}^{HF} with larger dE_{SP}^{HF} associated with larger values of dB_{PERP}^{LF}. A strong rise in dE_{SP}^{HF} as a function of dB_{PERP}^{LF} occurs starting at ~ 0.6 nT suggestive of a threshold. Dividing the data into eight bins in dB_{PERP}^{LF} each containing 50 data points and computing the slope in log–log space associated with the jump between the median values within the 4^{th} and 5^{th} bins give a slope of ~ 2.0. Since this is a slope in log-log space, it corresponds to the dE_{SP}^{HF} increasing as a power law with exponent 2.0 as a function of dB_{PERP}^{LF}.

$d\mathbf{B}^{HF}$ (not shown) is much smaller than $d\mathbf{E}^{HF}$ leading to nearly electrostatic high-frequency fluctuations. The analysis of the exact nature of the high-frequency fluctuations (aside from the observation that electron phase space holes and double layers are often present, as seen in Figure 5.1) is beyond the scope of this study and left for future analysis.

5.3.2 Intermittency

Another feature of the proposed scenario is the presence of turbulence. While power law spectra in frequency were observed by *Ergun et al.* [2015], the lack of direct spatial information from the data makes it difficult to infer the presence of turbulence using the spatial power spectrum. Features associated with intermittency have been found in the temporal behavior of turbulent hydrodynamic and MHD flows numerically [*Chevillard et al.*, 2005; *Homann et al.*, 2007; *Yoshimatsu et al.*, 2011]. Observationally, distributions of temporal fluctuations have been attributed to intermittency in other studies in the magnetotail where the Taylor hypothesis was not strictly valid [*Weygand et al.*, 2005].

In Figure 5.8, distributions of $\Delta B_i / \Delta B_{i,rms}$ (defined in Eq. 2.63) with $\tau = 1$ s are displayed for the 3 components of **B** from the field-aligned coordinate system using FGM data. For the

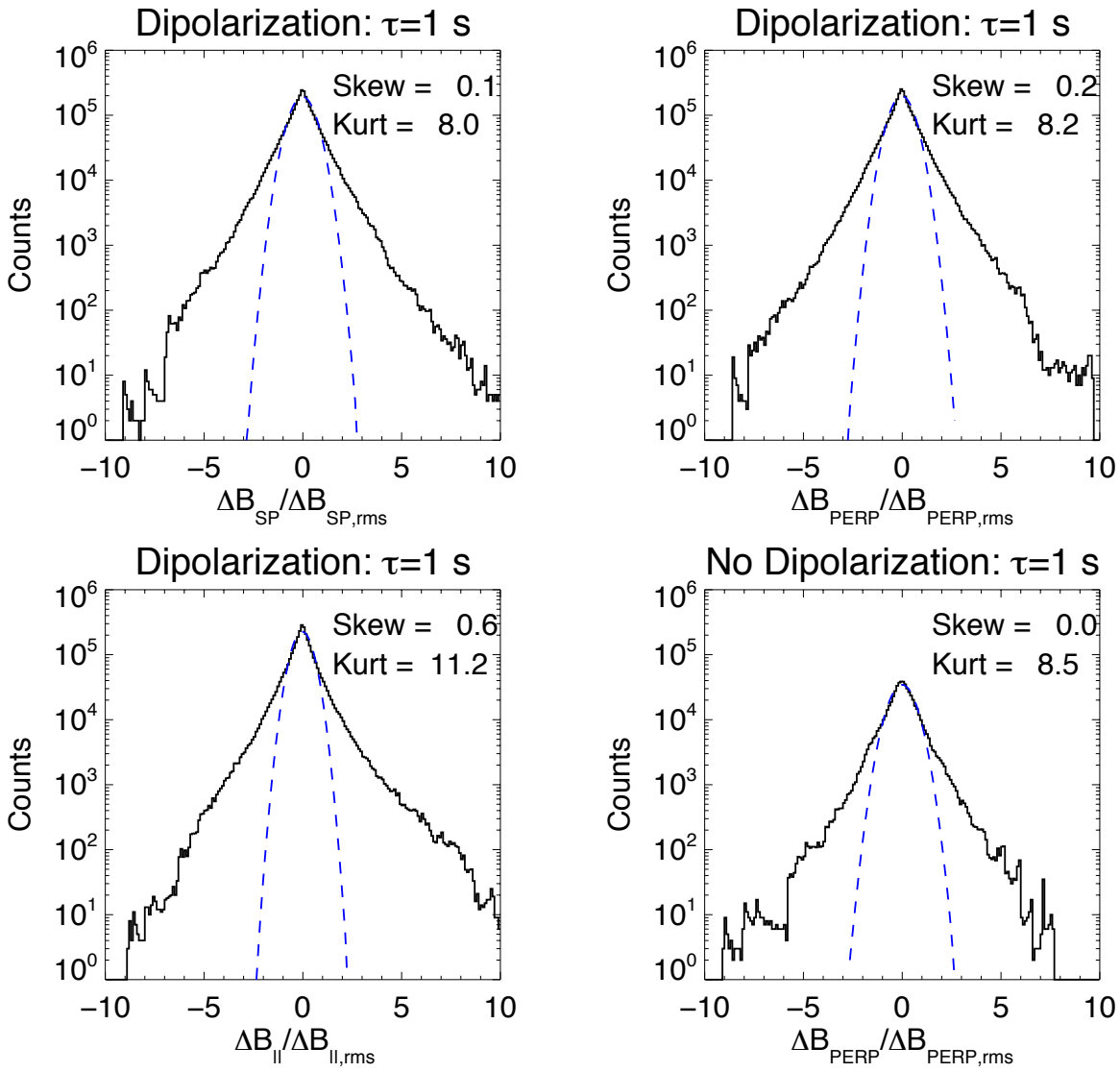

Figure 5.8: Distributions of $\Delta B_i/\Delta B_{i,rms}$ with $\tau = 1$ s in a field-aligned coordinate system. The three panels labeled "Dipolarization" show all three components of **B** and are created by co-adding the distributions from the 200 128 s subintervals with the maximum **E** activity. The panel labeled "No Dipolarization" shows the $\Delta B_{PERP}/\Delta B_{PERP,rms}$ distribution for 40 subintervals manually selected so as to include peak $|\mathbf{E}| > 10$ mV/m but avoid gradients associated with dipolarization. All other components show similar behavior. Dashed blue curves show Gaussian fits and the values of the skewness and kurtosis (defined so that a value of 3 is Gaussian) are given in the top right of each panel. All of the distributions show super-Gaussian wings that are expected from intermittency.

three panels labeled "Dipolarization," the distributions are computed using all 200 subintervals with high **E** activity and the subintervals are co-added so as to obtain better statistics. Co-adding is reasonable because the standard deviation has been normalized out and the mean of each subinterval is approximately zero. Many of the 200 subintervals selected by the automated routine contain the trends associated with dipolarization. Since often **E** and **B** activity continues even after the dipolarization trend has leveled off, the panel labeled "No Dipolarization" in Figure 5.8 uses 40 manually selected subintervals (not necessarily of 128 s in length) that occur once the large-scale trend in **B** (smoothed using a 128 s sliding average) has leveled off. The distributions for all three components appear similar and so only the B_{PERP} component is displayed.

Visually, the distributions exhibit super-Gaussian wings when compared to Gaussian fits shown as dashed blue curves. The degree to which these distributions depart from Gaussian is quantified in the upper right corner of each panel, which lists the skewness and kurtosis. The skewness, which is sensitive to the asymmetry of the distribution, of a Gaussian is zero and the kurtosis, which is sensitive to the wings of the distribution, is 3 for a Gaussian. The values of the skewness are small but nonzero and the values of the kurtosis are significantly above Gaussian as a result of the strong wings.

Figure 5.9 plots the distributions of $\Delta B_{PERP}/\Delta B_{PERP,rms}$ for larger values of τ (5 s and 25 s) computed from the two sets of data containing strong **E** activity used in Figure 5.8. The distributions become increasingly Gaussian as τ is increased as expected from intermittency. The distributions for all of the components appear similar, so only the B_{PERP} component is displayed. An intermediate value of $\tau = 10$ s is also examined, giving a kurtosis of 3.8 for the "Dipolarization" intervals and 4.1 for the "No Dipolarization" intervals, but is not displayed.

Figure 5.10 shows the distributions using $\tau = 1$ s for the 200 subintervals with the minimum **E** activity and 40 subintervals manually selected to contain peak $|\mathbf{E}| < 10$ mV/m. The manually selected intervals are chosen so as to occur prior to the regions of BBF braking, where there is also little activity in **B**. The distributions for the regions with only low **E** activity have lower values of the kurtosis than the distributions in Figure 5.8 but still have noticeably super-Gaussian wings,

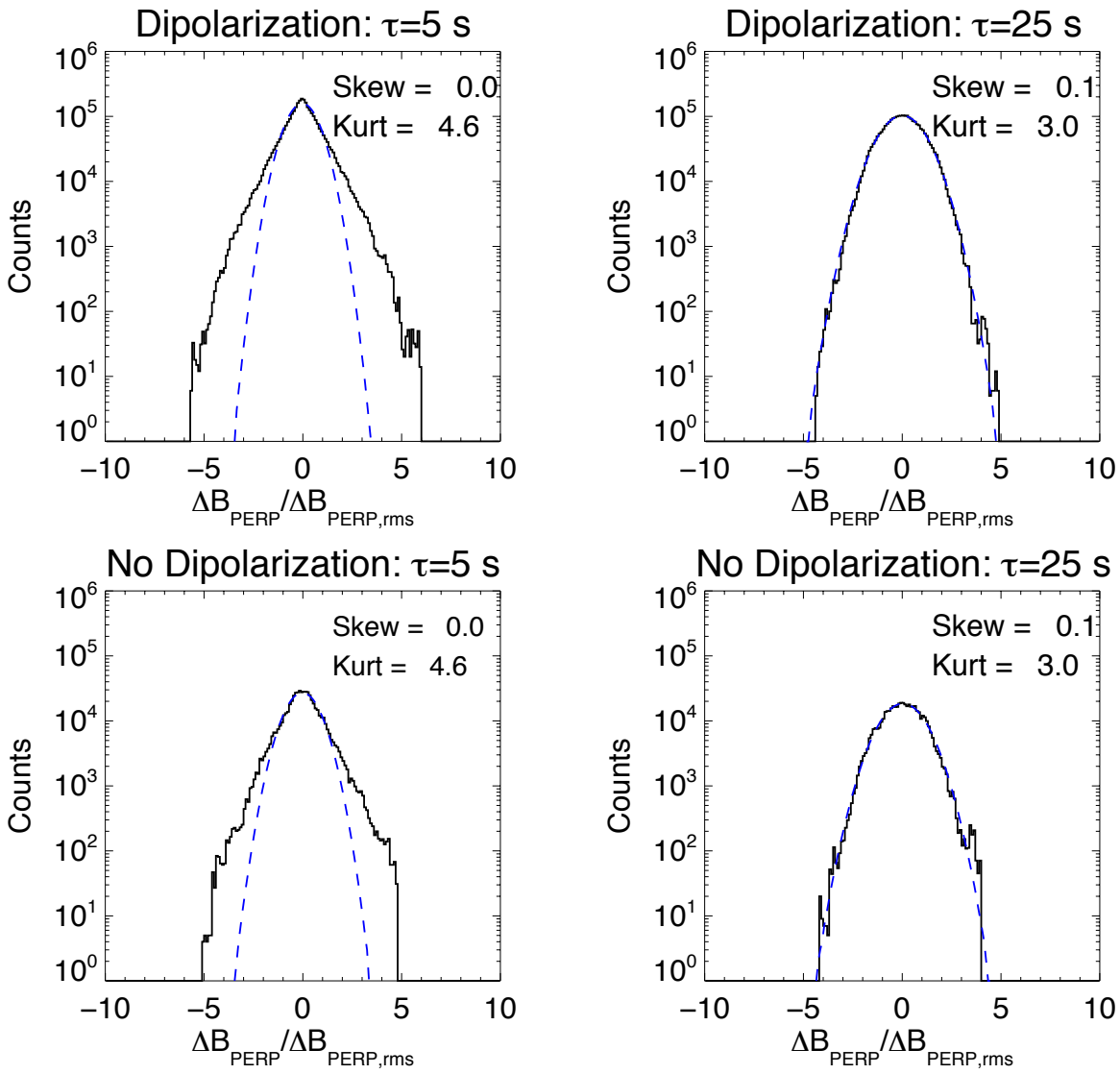

Figure 5.9: Distributions of $\Delta B_{PERP}/\Delta B_{PERP,rms}$ for $\tau = 5$ s (left column) and $\tau = 25$ s (right column) in the same format as Figure 5.8. The top row uses the 200 subintervals of data that have the maximum **E** activity and the bottom row uses 40 subintervals manually selected so as to include peak $|\mathbf{E}| > 10$ mV/m but avoid gradients associated with dipolarization. The distributions become increasingly Gaussian as τ increases, suggestive of intermittency. The behavior of the other two components is similar.

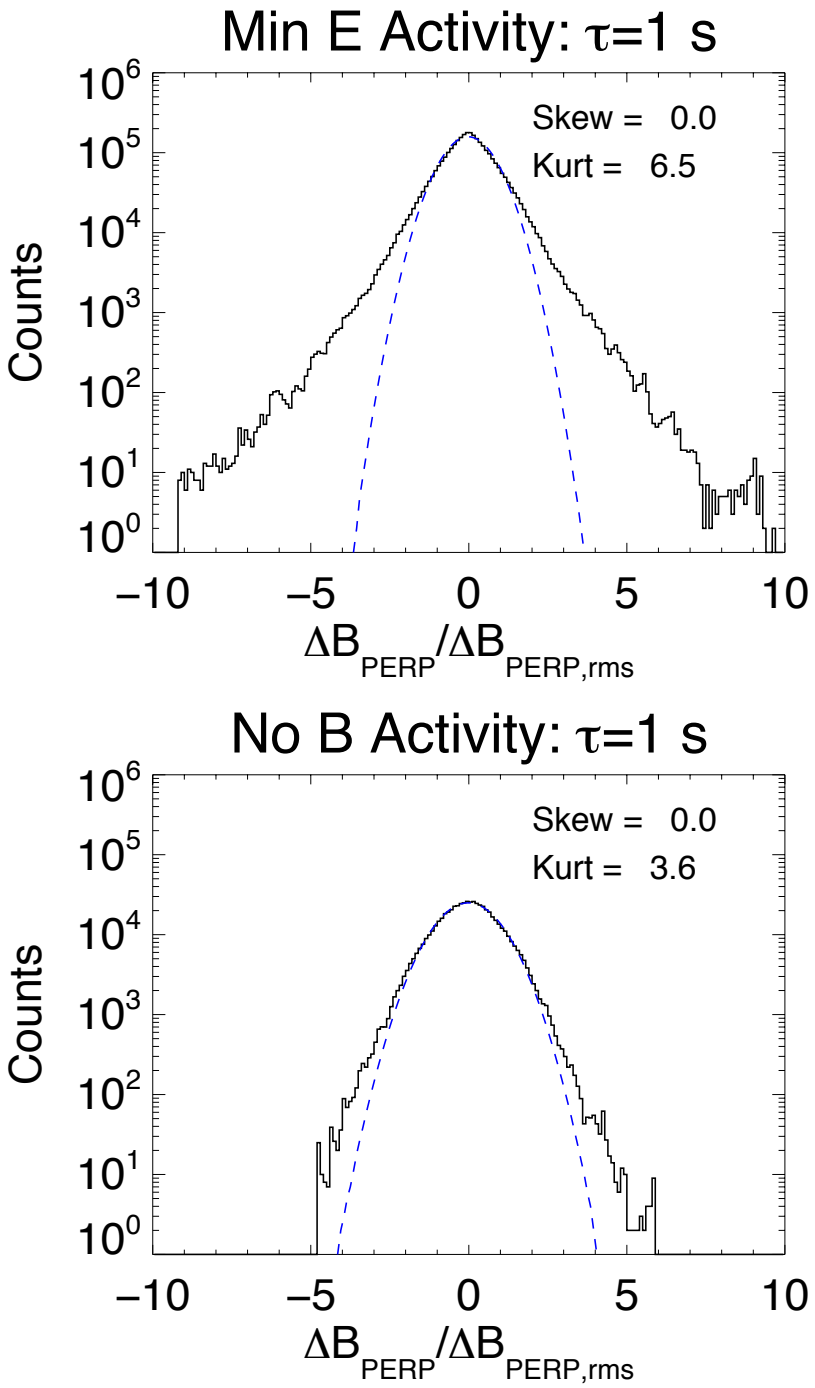

Figure 5.10: Distributions $\Delta B_{PERP}/\Delta B_{PERP,rms}$ with $\tau = 1$ s in the same format as Figure 5.8. The top panel uses the 200 128 s subintervals with the minimum **E** activity and the bottom panel uses 40 manually selected subintervals which contain peak $|\mathbf{E}| < 10$ mV/m and occur prior to a BBF braking event where little **B** activate is present. Regions with little **E** activity can still contain **B** activity that have super-Gaussian wings, but regions with little **E** and **B** activity have distributions that are significantly closer to Gaussian.

whereas the intervals that also contain little **B** activity are significantly closer to Gaussian even at the 1 s separation. The super-Gaussian wings in low **E** activity regions are potentially due to the fact that the automatically selected intervals are based on the minimum integrated **E** activity and in some cases could occur in regions where there is relatively low **E** activity, but still turbulent **B** activity resulting from the BBF braking. This interpretation would be consistent with a scenario where strong **E** activity is associated with the instability of the strongest currents in a turbulent environment.

Although direct measurements of the spatial increments or currents cannot be made with the current data set, the presence of temporal $\Delta B_i/\Delta B_{i,rms}$ that become increasingly non-Gaussian at smaller τ suggests that intermittent turbulence is active in the BBF braking region. If this is the case, then it is not unreasonable that exceptionally strong currents associated with the intermittency, as discussed in Chapter 2.3.2, may be present that would be the most likely currents to destabilize into nonlinear kinetic electric field structures. However, it is possible that additional mechanisms, such as flux tube oscillations generated by the BBF braking [*Panov et al.*, 2013], may also contribute to the non-Gaussian tails in the single spacecraft measurements.

5.4 Discussion and Energy Budget

The observational results presented in Section 5.3 are consistent with several features of the proposed hypothesis. A relationship between dB^{LF}_{PERP} and dE^{HF}_{SP} is found suggesting a threshold, as expected from a current instability. Furthermore, the presence of non-Gaussian wings in the distributions of $\Delta B_i/\Delta B_{i,rms}$ are suggestive of turbulence, which can lead to strong localized currents. The fact that **E** activity often occurs as isolated bursts within larger regions of **B** fluctuations also may be a result of intermittency since in that case one would expect the currents generating **E** signatures to be localized.

Some scatter is present in Figure 5.7 which could be attributed to several sources. Based on the 8 bins of 50 data points in each panel of Figure 5.7 (the medians of which are plotted as black triangles), the first and third quartiles of $dB^{LF}_{PERP}V_A$ and dB^{LF}_{PERP} are about 20% below or

above the respective medians. For dE_{SP}^{LF} and dE_{SP}^{HF} the first quartiles are located at roughly 50% below and the third quartiles are about 75% above the respective medians. The scatter could be associated with measurement uncertainties or variations in the physical mechanism for instability from event to event. Instrumental noise in the fields (plotted as dashed lines in Figure 5.7) is likely a minor contribution to the scatter for much of the data, which is well above the noise levels. Another source of uncertainty comes from the density (which enters the calculation of V_A) because high-energy electrons can generate false counts in the low-energy ion measurement in the ESA leading to a potential 25% overestimate [*McFadden et al.*, 2008b]. Another potential source of scatter comes from the characterization of "typical" values for the intervals based on 128 s samples of a turbulent environment. The current-driven instability threshold depends on T_{0e}/T_{0i}, so a trend in $d\mathbf{E}^{HF}$ with this ratio may blur out a threshold. However, the Buneman instability does not vary drastically with T_{0e}/T_{0i} and, as can be seen in Figure 5.6, T_{0e}/T_{0i} stays within a factor of 2 of T_{0e}/T_{0i}=0.2. Although not shown, there is no observed trend associated with T_{0e}/T_{0i} and $d\mathbf{E}^{HF}$. It is also possible that inhomogeneities in the plasma can play an important role, as has been observed in simulations [*Newman et al.*, 2001].

In order to quantify the importance of turbulent dissipation, estimates of the power input to the braking region, dissipated within the region, and leaving the region are provided in Table 5.1. The values in Table 5.1 are only meant to be order-of-magnitude estimates. High, medium, and low estimates are computed. In the leftmost column, "Input" denotes an energy input mechanism, "Loss" denotes a channel through which energy can be removed from the region, "Observed" indicates an observed constraint, and "Turb. Dis." indicates mechanisms that could contribute to the dissipation of turbulent energy. The BBF braking region is assumed to be a $2R_E \times 2R_E \times 2R_E$ cube. Although the size and shape of the braking region cannot be determined from the data, this size is used because it is comparable to estimates from *Angelopoulos et al.* [1996, 1997].

The power input by BBF events, given in the first row of Table 5.1, is based on distributions of the duration and total energy of BBF events [*Angelopoulos et al.*, 1994]. Row two estimates the power leaving as Alfvén waves by assuming the average magnitude of $dS_{||}$ leaves through an area of

Table 5.1: Estimated Power Budget for the Bursty Bulk Flow Braking Region

	Process	Low (Watts)	Medium (Watts)	High (Watts)
Input	BBF Energy[a]a	5×10^9	1×10^{10}	1×10^{11}
Loss	Alfvénic Poynting Flux	5×10^8	2×10^9	5×10^9
Loss	Deflected Flow	–	–	–
Loss	Adiabatic Heating	1×10^9	3×10^9	7×10^9
Loss	Strong Turbulent Cascade	4×10^8	1×10^9	2×10^9
	Weak Turbulent Cascade	3×10^7	1×10^8	4×10^8
Observed	Heating[b]	6×10^9	9×10^9	1.3×10^{10}
Turb. Dis.	Linear Damping: Alfvén	2×10^7	7×10^7	8×10^8
Turb. Dis.	Linear Damping: Electrostatic	1×10^6	1×10^7	1×10^8
Turb. Dis.	Double Layers	–	–	$< 10^{11}$

[a]Based on *Angelopoulos et al.* [1994].
[b]Due to a combination of both adiabatic heating and turbulent dissipation.

$2R_E \times 2R_E$. $d\mathbf{S}$ for the example interval is shown in Figure 5.5e with the field-aligned component plotted in black. The upper and lower values are the upper and lower quartiles when this quantity is computed for 50 subintervals, which are a subset of the intervals used in Chapter 5.3 and are used throughout the estimates provided in Table 5.1. It is not clear how to estimate the contribution of diverted flow around Earth and so the values in row three are left blank.

As demonstrated in Figure 5.5, increases in $|\mathbf{B}|$, T_i, and T_e are observed across most events. Row four estimates the amount of adiabatic heating ($E_{AH} = (3/2)n_0 k_B \Delta T_{AH}$) due to the conservation of magnetic moment, $\mu \equiv k_B T_0/(2B_0)$, assuming the increase occurs over a 2 minute period. Since μ is adiabatically conserved, the change in temperature associated with a change in $|\mathbf{B}|$ is given by $\Delta T_{AH} = T_0^{(1)}(B_0^{(2)}/B_0^{(1)} - 1)$. Superscripts (1) and (2) represent quantities before and after the BBF braking event respectively. $T_0^{(1)}$, $B_0^{(1)}$, and $B_0^{(2)}$ are estimated by manually identifying pre- and post event regions where the $\mathbf{B}$ strength and temperatures have stabilized and averaging the data within those regions.

Rows five and six estimate the dissipation required to support a steady state strong or weak turbulent cascade. The values are computed by assuming $|d\mathbf{B}^{LF}|^2/(2\mu_0)$ is distributed over the spectral forms seen in Eq. 2.57 ($k^{-5/3}$) and Eq. 2.59 ($k^{-3/2}$). The minimum wavenumber in the internal range is taken to be $2\pi/2R_E$ with a much larger maximum wave number. The high and

low values are the upper and lower quartiles for 50 subintervals.

Row seven gives the observed heating in the events. The temperatures pre- and post- event are computed by hand in the same way as described for the adiabatic heating calculation. The temperatures of ions and electrons roughly increase by $\Delta T_{heat} \sim 10^3 - 10^4 eV$. The power required to generate this heating is estimated by assuming the energy increase occurs over a two minute period.

Rows eight and nine estimate the linear damping of low-frequency Alfvénic fluctuations and high-frequency electrostatic waves. The high value gives an overestimate of the linear damping of Alfvén waves if all low-frequency perpendicular magnetic energy ($[(dB_{SP}^{LF})^2 + (dB_{PERP}^{LF})^2]/2\mu_0$) is taken to be at a length scale where the damping rate is $\omega_i/\omega_r \sim 0.1$ and $\omega_r = 2\pi(0.03$ Hz). The medium and low values assume $[(dB_{SP}^{LF})^2 + (dB_{PERP}^{LF})^2]/2\mu_0$ is distributed over a Kolmogorov spectrum and that a damping rate with $\omega_i/\omega_r \sim 0.1$ occurs on the energy at wavenumbers of $2\pi/\rho_i$ or $12\pi/\rho_i$ (based on where electron damping becomes strong in Figure 5.3) respectively with ρ_i taken to be roughly 350 km based on the data. The high-frequency data from the EFI, which is used to compute $d\mathbf{E}^{HF}$, is supplemented with **E** spectra computed on-board the spacecraft, which provide data up to 3580 Hz. The electric field energy is computed within 16 frequency bins between the ion cyclotron frequency and 3580 Hz. For the middle value the damping rate is $\omega_i/\omega_r = 0.1$. The high value assumes the damping rate equals the frequency, which is used as an upper limit because high-frequency fluctuations are seen in the data so it is expected to take more than one oscillation for the energy to dissipate. The low value assumes $\omega_i = 0.03\ s^{-1}$ corresponding to the typical frequency of low-frequency oscillations. This limit is chosen because high-frequency **E** fluctuations are generally seen within longer intervals of low-frequency **B** activity and so it is expected that the electrostatic waves would damp faster than the timescale associated with the low-frequency fluctuations.

Row ten gives an upper limit on the damping due to double layers. The power dissipated per unit volume by double layers is given by $J_\parallel E_\parallel$. The upper limit assumes every flux tube going through the BBF braking region has a double layer with an 800 V potential based on the double

layer potentials observed by *Ergun et al.* [2009] and $J_{\parallel} \sim qn_0V_{T,e}$.

Comparing the medium values in Table 5.1, the estimate of Alfvén wave Poynting flux leaving the region is within a factor of about 2 to the estimates for a strong turbulent cascade. The power required to generate the observed heating, which is likely a result of adiabatic heating and turbulent dissipation, is also roughly the same order to within a factor of 2 or 3 as the combined turbulent dissipation and adiabatic heating. However, adiabatic heating likely accounts for a larger fraction of the observed heating. Since these are only order of magnitude estimates, the fact that adiabatic heating, Alfvénic Poynting flux, and a strong turbulent cascade give values that are the same order of magnitude and sum to within an order unity constant of the input energy indicates that these are all potentially relevant loss mechanisms for BBF events and turbulent dissipation could be a significant sink when considering the energy budget.

The linear dissipation of high-frequency electrostatic waves is likely small compared to the total cascade rate. Although the upper limit for the linear damping of low-frequency Alfvénic fluctuations gives a value comparable to the estimates of the cascade rate, this value likely significantly overestimates the amount of energy dissipated through this channel since it assumes that all of the low-frequency energy is at a scale where damping is strong. The middle and low values are likely more reasonable and therefore linear damping of low-frequency fluctuations would be a minor contribution to the damping. The upper limit estimate of damping due to double layers is also likely a significant over estimate. Although double layers have been observed in these regions, they are not observed in all the data and it is unlikely that all of the flux tubes within the braking region contain a double layer. If flux tubes containing double layers fill 1% of the cross-sectional area of the braking region, then double layers could provide a significant amount of the damping associated with the turbulent cascade. This value is consistent with lower limits on the number of field lines with double layers in the plasma sheet as estimated by *Ergun et al.* [2009] and is likely a more reasonable estimate.

To summarize, a schematic diagram of energy flow through the BBF braking region is shown in Figure 5.11. Energy enters into the region via BBFs driven by reconnection. Internal dissipation

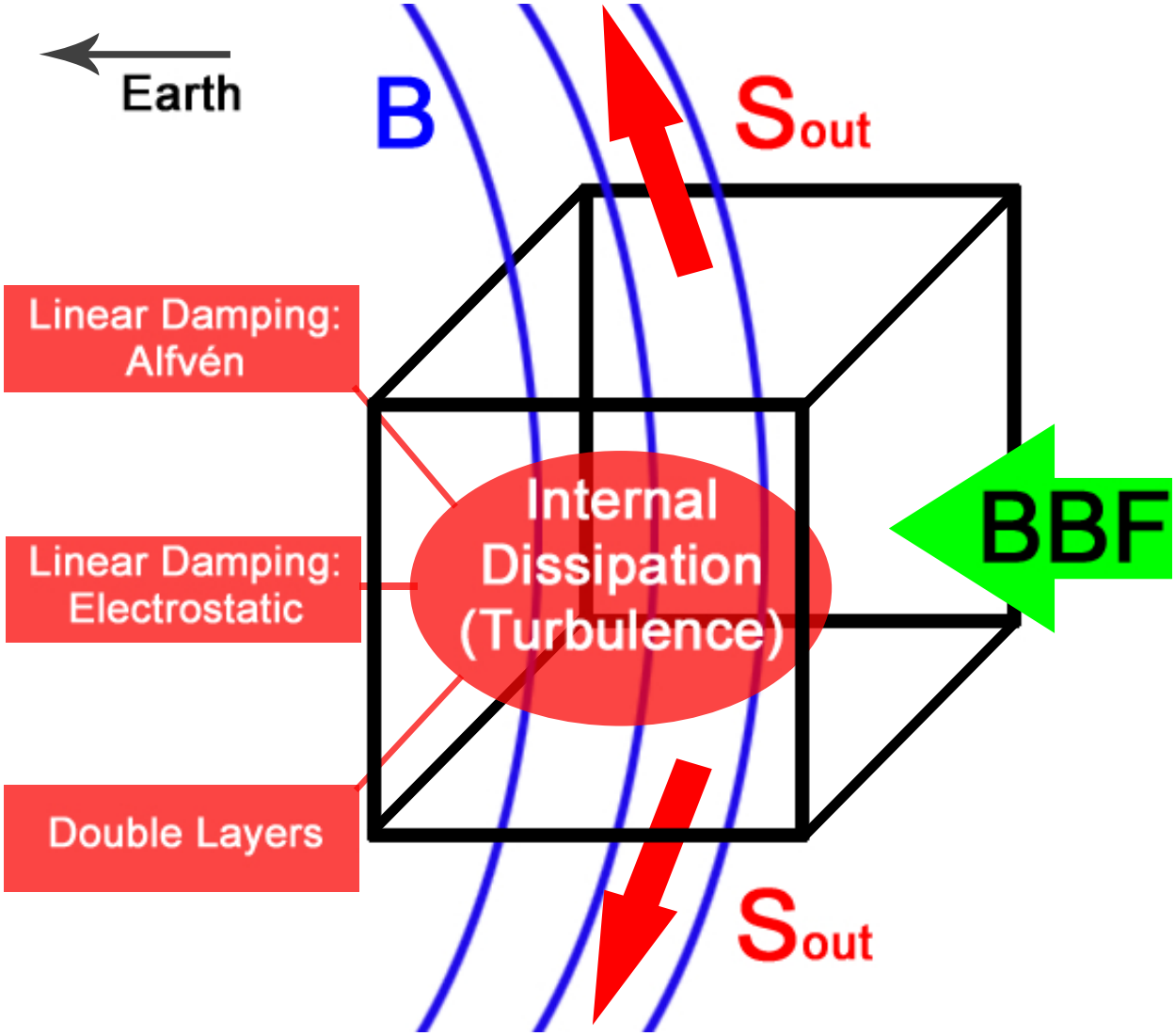

Figure 5.11: Diagram illustrating the energy flow through the BBF braking region. The black box represents the braking region. Energy is input by BBFs. Energy could then be dissipated into the plasma within the region and radiated out of the region by Alfvén waves. Turbulence could facilitate in distributing energy to these processes. Not shown is the deflection of flow around the Earth.

is facilitated by the transfer of energy from the large to small scales by turbulence and while there may be a number of possible dissipation mechanism, double layers generated by field-aligned current instabilities appear to provide adequate dissipation. Radiation of Alfvénic Poynting flux may also constitute a significant transfer of energy out of the region and could generate aurora.

5.5 Conclusions

In this chapter, we examine the generation of high-frequency **E** activity observed within BBF braking events by the THEMIS satellites. A theory is considered where a turbulent cascade of Alfvénic fluctuations drives energy to small perpendicular length scales. A dissipation mechanism where the instability of field-aligned currents transfers energy into high-frequency electrostatic wave modes or double layers could then occur. The presence of field-aligned currents in the BBF braking region is supported by observations of double layers and electron phase space holes [*Ergun et al.*, 2009, 2015]. This scenario is used to motivate the analysis of THEMIS data, which appears to support the hypothesis. Based on the linear theory of kinetic Alfvén waves it is found that for moderate values of β ($0.5 < \beta_i < 2$ with $T_{0e}/T_{0i} \sim 0.2$) it is possible for waves to bypass linear damping on ions and cascade to small perpendicular length scales. However, the field-aligned currents generated by a single linear kinetic Alfvén wave are still significantly less than the currents required for instability indicating that a strongly turbulent environment may be required.

Using **E** and **B** measurements, evidence is found that is consistent with a threshold in the high-frequency **E** activity with respect to the magnitude of the low-frequency **B** fluctuations, which is in agreement with the idea that currents associated with low-frequency fluctuations destabilize to generate the high-frequency activity. It is also found that the ratio of the low-frequency electric to magnetic field fluctuations are consistent with the Alfvén velocity except in intervals where high-frequency **E** activity is present. In these intervals the ratio is slightly larger than the Alfvén velocity, which is consistent with the presence of large $k_\perp$ kinetic Alfvén waves. The distributions of temporal increments in **B** become increasingly non-Gaussian as the temporal separation is decreased, which could be associated with turbulent intermittency. Intermittency in turbulence is also associated

with super-Gaussian wings on the distributions of spatial derivatives and, therefore, enhanced probabilities for strong currents in localized regions of the system. These distributions are therefore both suggestive of the presence of turbulence and a means through which currents can be enhanced in localized regions leading to instability.

Rough estimates of the energy budget associated with the BBF braking region indicate that, combined with additional sinks of energy such as adiabatic heating and Alfvén wave Poynting flux leaving the region, the proposed turbulent dissipation mechanism fits within the available energy input by BBF events. The power dissipated by the turbulent cascade can potentially be comparable to the other energy sinks considered. Dissipation associated with double layers is likely the main contribution to the dissipation of turbulent energy.

The findings of this study are consistent with a strongly turbulent environment. The presence of intermittency suggests nonlinear dynamics are playing an important role. Further analysis is required to determine the exact nature of the turbulence and is made difficult in this study by the lack of spatial information. However, future work with the MMS mission may provide insight into the spatial characteristics of turbulence within this region (see Chapter 7.2).

The work in this chapter offers a dissipation mechanism for turbulence that is distinct from other forms of dissipation that are often discussed in plasma physics (such as Landau or cyclotron damping), which transfer energy directly from the turbulent fluctuations into the particles. In this mechanism an extra step is added where the field-aligned currents generated by the turbulence destabilize due to kinetic effects and transfer energy into double layers or high-frequency electrostatic wave modes. Energy is then transferred to the particles by accelerating them in double layers or through dissipation of high-frequency electrostatic waves. This process could be relevant in other turbulent plasma environments where strong field-aligned currents develop. Based on linear analysis, this could occur in moderate-β environments where linear damping on ions can be small and linear electron damping does not become large until much smaller scales. However, in any plasma system, where field-aligned currents are comparable to the electron thermal speed, the potential exists for current driven kinetic instabilities.

Chapter 6

Turbulence in a Kelvin-Helmholtz Instability on the Magnetopause: MMS Observations

Another area of the magnetosphere where turbulence is thought to occur is within the Kelvin-Helmholtz instability, which can occur on the Earth's magnetopause as a result of the velocity shear induced by the magnetosheath flows (see Chapter 1.3.2 for more details). While simulations have shown the development of turbulence as a result of secondary instabilities within the large-scale KH wave, extensive observational analysis of KH-related turbulence hasn't been performed. With high-resolution, 4-spacecraft measurements, the recently launched Magnetospheric Multiscale (MMS) mission [*Burch et al.*, 2015] (see also Chapter 1.4.2) is well suited to examine the role of turbulence in the KHI. The capabilities of MMS also can aid in building an understanding of the kinetic physics associated with collisionless plasma turbulence.

On September 8, 2015 between 9 and 12 UTC, MMS observed a potential KHI event for which over an hour of high-resolution "burst" data was available. This event is also analyzed by *Eriksson et al.* [2016], who showed that the observed parameters are consistent with a KH unstable plasma and also found evidence for reconnection at periodic current sheets throughout the event. This chapter provides the first in-depth observational study of turbulence properties in association with a KHI. The study provides evidence for turbulence in the regions between the periodic current sheets, which may correspond to the interior of vortices depending on the stage of development, and several features are discussed that warrant further investigation. A diagram of the KHI on the magnetopause, showing the relative locations of periodic current sheets and turbulent regions,

is given in Figure 1.3. Unlike the THEMIS study of Chapter 5, MMS allows for the analysis of temporal and spatial features using the 4-spacecraft formation, which is of particular importance in the magnetosphere where the Taylor frozen-in hypothesis is often invalid [*Matthaeus and Goldstein*, 1982]. Additionally, both ion and electron flow velocities are examined observationally down to kinetic scales in a turbulent plasma for the first time.

6.1 Observational Analysis

In this study, **B** data from the Fluxgate Magnetometers (FGM) [*Russell et al.*, 2014] and Search-Coil Magnetometer (SCM) [*Le Contel et al.*, 2014], **E** data from the Electric Field Double Probes (EDP) [*Ergun et al.*, 2014; *Lindqvist et al.*, 2014], and $\mathbf{u}_i$ and $\mathbf{u}_e$ from the Fast Plasma Investigation (FPI) [*Pollock et al.*, 2016] on MMS are analyzed. 54 intervals are manually selected for analysis, such that they are located between the periodic current sheets associated with the KHI and contain enhanced fluctuations in **B** when a 10 s running average is subtracted. $\mathbf{B}_0$, V_A, ion cyclotron frequency ($f_{ci} = \omega_{ci}/2\pi$), and lower-hybrid frequency ($f_{LH} = [(\omega_{ci}\omega_{ce})^{-1} + \omega_{pi}^{-2}]^{-1/2}/2\pi$) are defined based on average parameters from each interval. Subscripts $\perp$ and $||$ will refer to components perpendicular and parallel to $\mathbf{B}_0$.

Figure 6.1 shows an example overview from one of the 54 intervals as observed by MMS1 plotted in geocentric solar ecliptic (GSE) coordinates. All four spacecraft appear similar, but not identical. Sharp changes in B_y GSE in Figure 6.1e at 11:00:25 UT and 11:01:20 UT are two of the periodic current sheets associated with the KHI. Sharp decreases in temperature and an increase in density occur at the current sheets consistent with a transition from the magnetospheric boundary layer to the magnetosheath and a more gradual transition back to boundary layer temperatures occurs between the current sheets, as expected in the KHI. Black dashed lines mark the interval analyzed for turbulence, which features fluctuations in **B**, **E**, $\mathbf{u}_i$, and $\mathbf{u}_e$. In many cases, periods of low fluctuations (peak **B** fluctuation amplitudes < 5nT) are located between the current sheets and turbulent intervals, which may be indicative of the path traveled through the event. The low-fluctuation regions are often associated with higher densities than the turbulent regions, as seen in

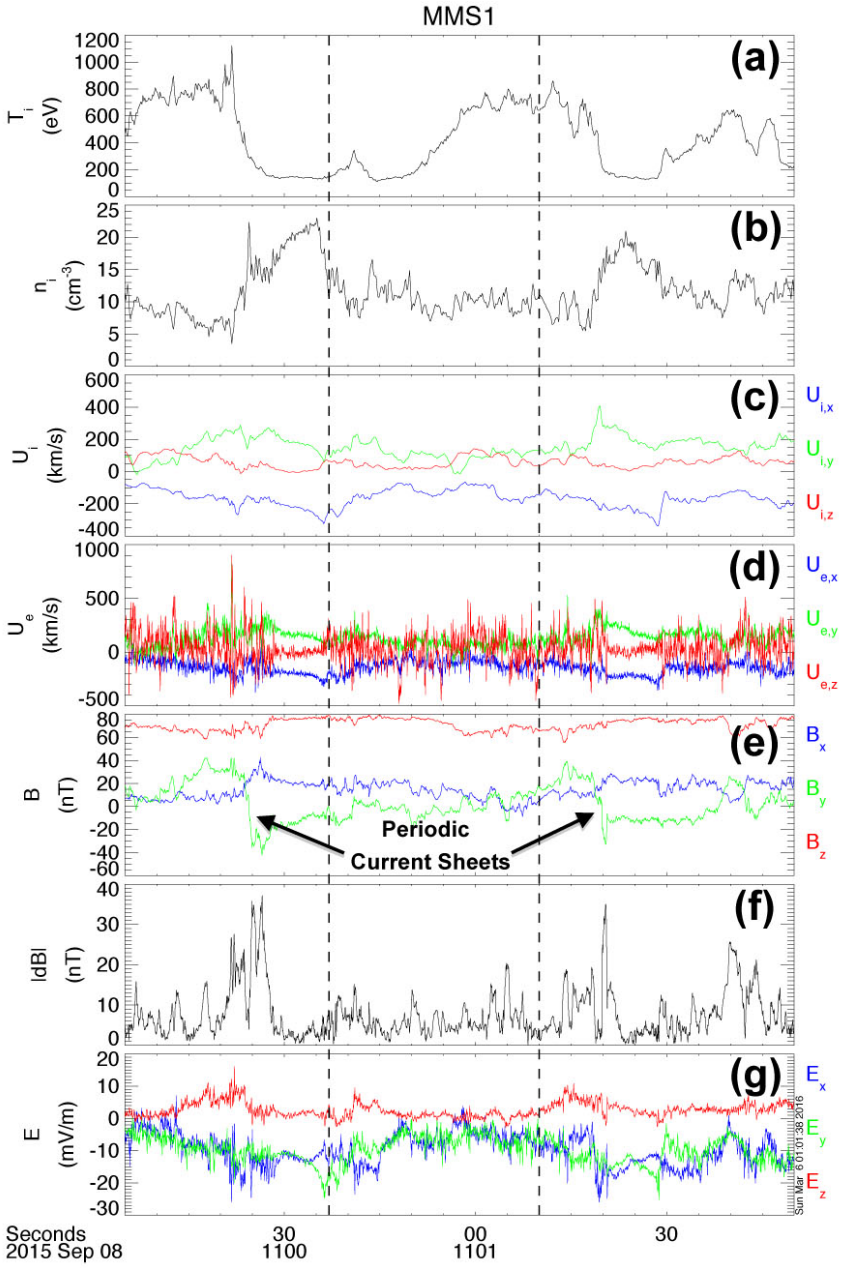

Figure 6.1: Example of a turbulent KH interval plotting (a) ion temperature, (b) ion density, (c) $\mathbf{u}_i$, (d) $\mathbf{u}_e$, (e) $\mathbf{B}$, (f) magnitude of $\mathbf{B}$ fluctuations when 10 s running average is removed, and (g) $\mathbf{E}$. Vector quantities are in GSE coordinates. Vertical dashed lines mark the region analyzed for turbulence. Two current sheets associated with the KHI are seen in B_y at roughly 11:00:25 and 11:01:20.

Figure 6.1b (for example, just after 11:00:30 UT), and so may be associated with the magnetosheath plasma.

In the following analysis of the turbulent intervals, linear trends (based on least-squared fits of the turbulent intervals) are subtracted from the quantities, instead of the 10 s running average mentioned above. With linear trends subtracted, root-mean-squared fluctuation amplitudes are $\delta B_{rms} \approx 11$ nT, $\delta E_{rms} \approx 5$ mV/m, $\delta u_{i,rms} \approx 67$ km/s and $\delta u_{e,rms} \approx 165$ km/s. B_0 is stronger than the fluctuations such that $\delta B_{rms}/B_0 \approx 0.14$.

6.1.1 Spectra

As discussed in Chapter 2.3.1, energy spectra are expected to follow power laws with k in turbulence theory. Using MMS, $f = \omega/2\pi$ instead of k spectra can be computed since the Taylor hypothesis is not valid in this event (background flow speeds are ≈ 200 km/s compared to $V_A \approx 450$ km/s), but, even so, power law behavior is found in both individual spectra from each interval and average spectra. In creating average spectra, standardized interval lengths of ≈ 32 s for each quantity are adopted, which omits 16 shorter intervals. Data gaps prevent the computation of spectra with SCM data in 7 intervals. Prior to averaging, the normalizations $\mathbf{B}/B_0$, $\mathbf{E}/(B_0 V_A)$, $\mathbf{u}_i/V_A$, and $\mathbf{u}_e/V_A$, which are appropriate for Alfvénic fluctuations in the MHD regime, are performed. For $\mathbf{B}$ spectra, FGM data are used for $f < 1$ Hz, SCM data are used for $f > 8$ Hz, and a linear combination is used in between. For the intervals examined, $f_{ci} \approx 1$ Hz and $f_{LH} \approx 50$ Hz, indicated by vertical solid and dashed lines respectively in Figure 6.2.

Figure 6.2 shows spectra averaged over the four spacecraft and multiple intervals. The $|\mathbf{B}|$ spectrum (Figure 6.2a) follows $f^{-5/3}$ for $f < f_{ci}$ and $f^{-3.2}$ for $f > f_{ci}$. For the individual intervals, the low-frequency power laws are generally in the vicinity of $f^{-3/2}$ or $f^{-5/3}$ consistent with the theoretical fluid predictions and observations of turbulence in the solar wind [*Matthaeus and Goldstein*, 1982] and BBF braking region (as discussed in Chapter 5.1) [*Ergun et al.*, 2015]. $\delta B_\perp$ contains most of the power below $f \approx 100$ Hz, where $\delta B_\perp$ and $\delta B_{||}$ are nearly equal (see inset of Figure 6.2a).

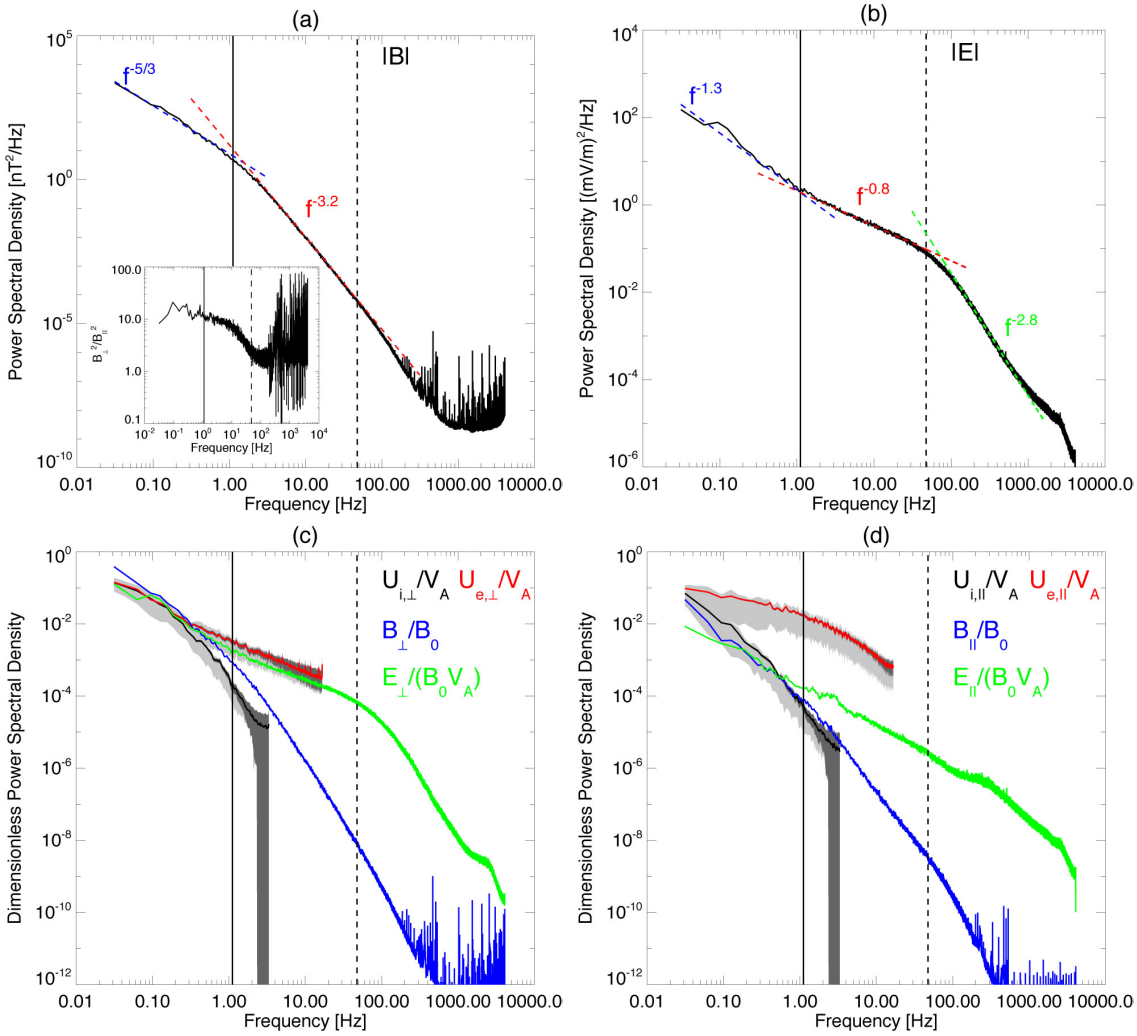

Figure 6.2: Average power spectra for (a) total **B** with inset showing ratio of $B_\perp$ to $B_{||}$ spectra, (b) total **E**, (c) perpendicular components of the normalized vectors, and (d) parallel component of the normalized vectors. Changes in spectral slope are seen in **B** and **E** near f_{ci} (vertical solid line) with **B** steepening and **E** becoming shallower. At f_{LH} (vertical dashed line), **E** steepens. Below f_{ci}, the perpendicular components of all normalized vectors are similar, consistent with Alfvénic fluctuations. $\mathbf{u}_i$, **B**, and **E** are dominated by the perpendicular components for most of the frequency range, while $\mathbf{u}_e$ is dominated by the parallel component. Dark gray regions mark the uncertainty in the velocity spectra based on the statistical uncertainty in the FPI data and light gray regions give upper and lower quartiles of the spectra used in averaging.

The $|\mathbf{E}|$ spectrum shows three power laws $f^{-1.3}$ for $f < f_{ci}$, $f^{-0.8}$ for $f_{ci} < f < f_{LH}$, and $f^{-2.8}$ for $f > f_{LH}$. $E_\perp$ is the dominant component below $f \approx 400$ Hz, where $E_{||}$ begins to dominate. Below f_{ci}, $\mathbf{E}/(B_0 V_A)$ is similar in amplitude to $\mathbf{B}/B_0$ consistent with Alfvénic fluctuations; however, it tends to have a shallower slope as also seen by *Ergun et al.* [2015] in the BBF braking region. Unlike $\mathbf{B}$, $\mathbf{E}$ becomes shallower above f_{ci}, as also observed in other space plasmas [*Bale et al.*, 2005; *Chaston et al.*, 2012; *Ergun et al.*, 2015].

$u_{i,\perp}/V_A$ spectra are similar to $B_\perp/B_0$ for $f < f_{ci}$ consistent with Alfvénic fluctuations and $u_{e,\perp}$ is similar to $u_{i,\perp}$. As f approaches f_{ci}, $u_{e,\perp}$ and $u_{i,\perp}$ diverge with $u_{e,\perp}$ becoming shallower similar to $E_\perp$, which is consistent with ions decoupling at these frequencies while the electrons remain frozen to the field. Similar behavior has been seen in the k spectra from kinetic simulations, where $\mathbf{u}_i$ and $\mathbf{u}_e$ diverge from each other at scales near the ion inertial length (≈ 65 km in this event) [*Karimabadi et al.*, 2013]. For reference, the periodic current sheets in this KH event are found to be of the order of the ion inertial length [*Eriksson et al.*, 2016], however, note that the periodic current sheets are not included in the spectra. While $u_{i,\perp}$ dominates over $u_{i,||}$, most of the $\mathbf{u}_e$ power is in $u_{e,||}$ (except at the lowest frequencies). Note that aliasing effects may be present in the high-frequencies of the velocity spectra.

The spectral behavior is consistent with the general behavior seen in the time domain. Strong fluctuations can be seen in $u_{e,z}$ GSE (nearly the field-aligned component) in Figure 6.1d as compared to the other components. Comparing Figure 6.1c to Figure 6.1d, while similar overall trends are seen in the components, there is generally smaller scale activity in $\mathbf{u}_e$.

Statistical uncertainties on the velocities are typically a few km/s for $\mathbf{u}_i$ and a few tens of km/s for $\mathbf{u}_e$ within this KHI observation. Dark shaded regions in Figures 6.2c,d show the standard deviation in the velocity spectra due to instrumental uncertainties based on an ensemble of time series where random noise given by the statistical uncertainties in the FPI moment calculations is applied to the data. Light shaded regions show the observed spread in spectral power for the averaged intervals quoted as the upper and lower quartiles for each frequency, which could include contributions from instrumental uncertainty and the physical variability of the system.

6.1.2 Intermittency

Unlike the study in Chapter 5, where only the temporal magnetic increments were able to be examined using THEMIS data, the small-scale, multi-spacecraft configuration allows for the measurement of increments both temporally and spatially. As discussed in Chapter 2.3.2, intermittency is linked to the formation of intense localized currents and can drive kinetic-scale instabilities as examined in Chapter 5, as well as magnetic reconnection [*Osman et al.*, 2014].

Using FGM data, $\Delta B_i/\Delta B_{i,rms}$ (defined in Eq. 2.63) can be examined at a variety of τ and roughly one Δx, corresponding to the separation of the four spacecraft. The average $\Delta x \approx 175$ km (4.3 ion gyroradii) when averaged over all intervals. Figure 6.3 shows distributions of $\Delta B_y/\Delta B_{y,rms}$ for temporal and spatial lags and the kurtosis of the distributions as a function of τ. Distributions from each spacecraft (or from the six different spacecraft pairs for spatial differences) and each interval are co-added to build up statistics in the wings of the distributions. As can be seen in the temporal distributions, at large $\tau > 8$ s, the distributions are nearly Gaussian with kurtosis near 3 and at smaller τ, the kurtosis is > 3 and the distributions develop super-Gaussian wings as expected from turbulence. While the distributions as a function of Δx cannot be examined with this data, the distribution at the obtainable Δx shows super-Gaussian wings with kurtosis ranging from 4.26 to 4.85 for the 3 components. Temporal distributions have kurtosis values in this range near $\tau \approx 1$ s. As a check for consistency, assuming temporal distributions are purely associated with advected spatial structures, this would give an advection velocity of ≈ 175 km/s, which is roughly consistent with the ion velocities seen in Figure 6.1 and estimates of the tailward propagation velocity of the periodic current sheets by *Eriksson et al.* [2016].

6.1.3 Anisotropy

The presence of a strong $\mathbf{B}_0$, as seen in Figure 6.1, is believed to introduce anisotropy to the turbulent fluctuations. One way of examining the anisotropy of the spatial scales is by considering the spatial autocorrelation function (A_Q) of a quantity $\mathbf{Q}$, as defined in Eq. 2.62. Since only one

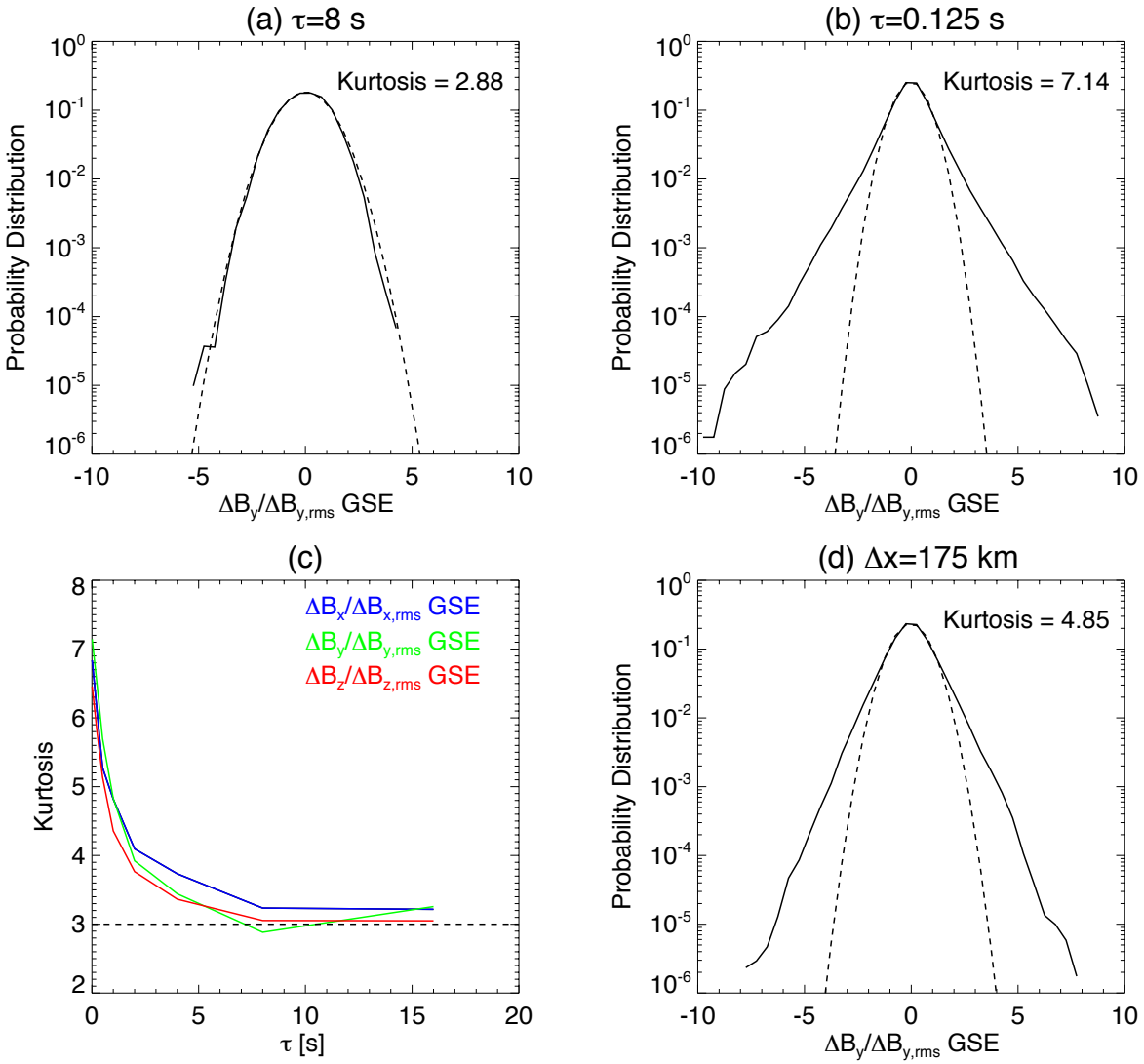

Figure 6.3: Panels (a) and (b) show distributions of $\Delta B_y(\tau)/\Delta B_{y,rms}$. Panel (c) shows the kurtosis of the temporal increments as a function of τ. Distributions are near Gaussian (kurtosis of 3) at large τ and have super-Gaussian wings (kurtosis > 3) at small τ consistent with turbulent intermittency. Panel (d) shows the spatial distribution of $\Delta B_y(\Delta x)/\Delta B_{y,rms}$ and super-Gaussian wings are seen in the spatial increment distribution. Dashed curves show Gaussian fits.

Table 6.1: Average correlation values in the parallel and perpendicular directions for $\mathbf{B}$, $\mathbf{E}$, $\mathbf{u}_i$, and $\mathbf{u}_e$. Values are the average and standard deviation of the MMS1-MMS2 correlation for the parallel direction and all other separations for the perpendicular direction.

Quantity	Parallel Direction	Perpendicular Direction
A_B	0.92 ± 0.03	0.53 ± 0.17
A_E	0.42 ± 0.10	0.21 ± 0.11
A_{U_i}	0.96 ± 0.02	0.62 ± 0.15
A_{U_e}	0.31 ± 0.08	0.08 ± 0.07

value of Δx is available during the KHI event, the values of the length scales cannot be determined. However, by examining A_Q for the 6 directions in the formation, MMS can provide an indication of the anisotropy in the length scales. During the KHI event, two of the spacecraft, MMS1 and MMS2, were separated within $\approx 10^\circ$ of $\mathbf{B}_0$, providing an ideal configuration for examining how the length scales differ respectively in the parallel and perpendicular directions to $\mathbf{B}_0$.

Figure 6.4 plots A_B, A_E, A_{U_i}, and A_{U_e} from each interval as scatter plots in the $\Delta x_\perp$–$\Delta x_{||}$ plane. In all cases A_Q is larger along $\Delta x_{||}$ than $\Delta x_\perp$, consistent with quasi-2D turbulence where small scales generated by the turbulence are mainly perpendicular to $\mathbf{B}_0$. Average values in the parallel versus perpendicular directions are given in Table 6.1. This type of anisotropy has been seen in the slow solar wind [*Matthaeus et al.*, 1990; *Dasso et al.*, 2005] and plasma sheet [*Weygand et al.*, 2009]. The anisotropy also coincides with the symmetries associated with the KHI. While A_B and A_{U_i} have similar values, A_E and A_{U_e} are smaller, which may be indicative of similar scales for the $\mathbf{B}$ and $\mathbf{U}_i$ fluctuations, and smaller scales for the $\mathbf{E}$ and $\mathbf{U}_e$ fluctuations. Smaller scale fluctuations in $\mathbf{E}$ may be consistent with the enhanced $\mathbf{E}$ power over $\mathbf{B}$ for $f > f_{ci}$ in Figure 6.2, assuming high frequencies correspond to large wavenumbers.

6.2 Discussion and Conclusions

In this chapter, the first results from MMS have been used to observationally demonstrate that turbulence is present in the Kelvin-Helmholtz instability and for the first time examine intermittency and anisotropy in this region. The properties of the ion and electron velocities down into

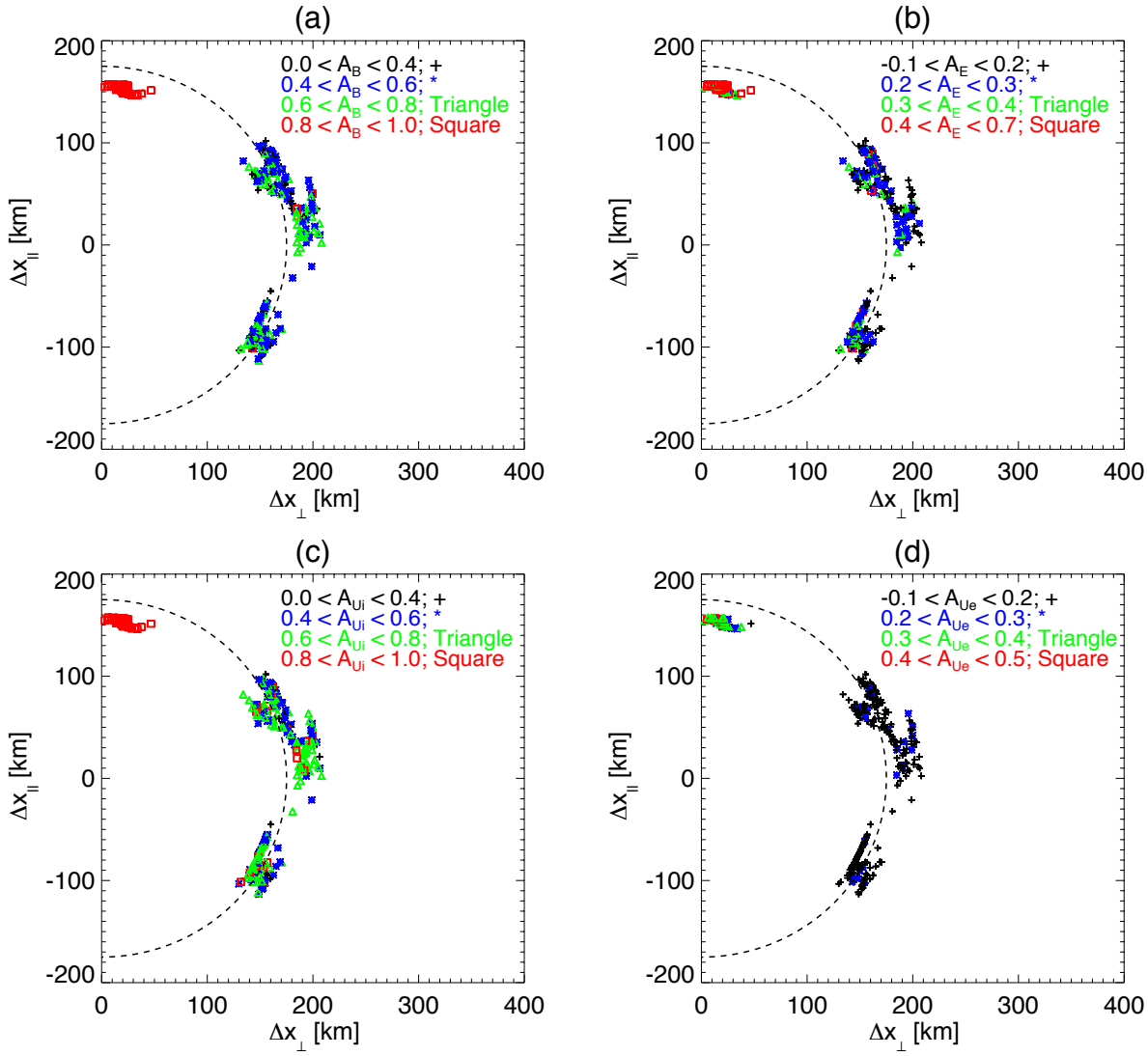

Figure 6.4: Scatter plot of the autocorrelation functions (a) A_B, (b) A_E, (c)A_{U_i}, and (d) A_{U_e} in the $\Delta x_\perp$–$\Delta x_{||}$ plane. Colors and symbols denote bins of correlation. Bins are different for A_E and A_{U_e}. Autocorrelations are systematically larger parallel to $\mathbf{B}_0$ compared to perpendicular for all quantities, consistent with quasi-2D turbulence in the perpendicular plane. A_B and A_{U_i} have similar values, while A_E and A_{U_e} are less correlated. Dashed curves mark a circle of radius 175 km.

the kinetic scales are also observationally examined for the first time in a turbulent environment. A variety of analysis techniques are used to probe the properties of turbulence in the region between the periodic current sheets associated with the large-scale KHI. The presence of power law spectra and distributions of magnetic field increments consistent with intermittency are suggestive of the presence of turbulence. FPI provides a unique opportunity to examine the behavior of $\mathbf{u}_i$ and $\mathbf{u}_e$ at kinetic scales and could provide valuable insight into the kinetic physics at play in turbulent plasmas.

Spectra exhibit power law behavior with changes in slope at f_{ci}, as expected from turbulence theory and observed in other turbulent plasmas. In other plasmas, such as the solar wind and plasma sheet, it has been proposed that shallowing of **E** spectra and steepening of **B** spectra at scales below the ion gyroradius may be linked to kinetic Alfvén waves, which have an increasing ratio of $E_\perp/B_\perp$ as a function of k (see Chapter 5.2 for a discussion of kinetic Alfvén waves) [*Bale et al.*, 2005; *Chaston et al.*, 2012] . The observations of the **E** and **B** spectra in the range between f_{ci} and f_{LH} presented here, could be related to kinetic Alfvén waves. However, it is not necessarily straight-forward to convert frequencies to wavenumbers in the parameter regime of this event. It has also been shown for the first time that the deviation of **E** and **B** in this frequency range is accompanied by deviations in $\mathbf{u}_e$ and $\mathbf{u}_i$.

An additional break in the **E** spectrum is found near f_{LH}, which may have implications for the dissipation of energy in the region or could indicate a change in nonlinear dynamics. One intriguing consequence of confined regions of turbulence is the radiation of plasma waves. Electrostatic whistler waves are associated with a cutoff frequency at f_{LH}. If these waves have large enough group velocities they may radiate out of the region before significantly participating in the turbulent cascade, so the steepening of the slope above f_{LH} may be associated with removal of energy through whistler wave radiation. In Chapter 5, a similar process of "dissipating" energy through plasma wave radiation was proposed in the context of BBF braking where it could lead to Alfvénic aurora [*Stawarz et al.*, 2015] and wave radiation has been seen in KHI simulations [*Karimabadi et al.*, 2013]. An in-depth examination of this possibility could prove interesting for

future work.

Observational evidence for turbulent intermittency has been found within the KHI and the formation of intermittent current structures may be important for the development of reconnection in the KHI vortices. For quasi-2D turbulence with a strong B_0, as observed in this event, the formation of field-aligned currents is expected since small-scale fluctuations in **B** develop in the perpendicular direction. The significant differences in the $u_{i,||}$ and $u_{e,||}$ spectra, which imply the presence of field-aligned currents, may be consistent with this scenario. If sufficiently strong field-aligned currents are generated, they may lead to signatures in the aurora or the generation of waves and double layers through field-aligned current instabilities (see Chapter 5).

Wilder et al. [2016] performs a detailed analysis of ion acoustic waves observed within one of the turbulent intervals examined in this study. The presence of ion acoustic waves was inferred from the frequencies (between 100 Hz and the ion plasma frequency) and phase speed of electrostatic oscillations with amplitudes up to 100 mV/m. Ion acoustic waves can be generated by field-aligned current instabilities, as examined by [*Kindel and Kennel*, 1971] and discussed in Chapter 2.2.2. *Wilder et al.* [2016] suggest that the enhancement in the $E_{||}$ spectra around 200 Hz for the case study interval, and as also can be seen in the average spectrum in Figure 6.2d, is the signature of the ion acoustic waves. The turbulence in this region may be providing currents that generate these waves and the damping of the ion acoustic waves could then dissipate energy from the turbulence.

Simulations often show a layer of turbulence, which envelopes the current sheets between the vortices, in the later stages of development of the KHI [*Karimabadi et al.*, 2013; *Daughton et al.*, 2014]. The presence of distinct periodic current sheets in this event may mean the turbulence is still in the relatively early stages of development. Later in the MMS mission, when the apogee is raised to study magnetotail reconnection, KHI further down tail may be encountered and provide insight into the later stages of KHI turbulence. While the separation of the MMS formation was ≈ 175 km in this study, the separations are varied down to 10 km over the course of the mission. Observations of KHI events at smaller separations could provide valuable insights into the kinetic scale behavior and individual current structures in the turbulence.

Chapter 7

Conclusions

The presented work uses a combination of numerical simulations and observational data to examine plasma turbulence. The first two studies (see Chapters 3 and 4) use numerical simulations of MHD and Hall MHD to examine the relaxation of turbulent flows and the role of the Hall effect in the small scales of plasma turbulence, respectively. The study of the relaxation of turbulent flows is relevant to understanding the implications of turbulence on systems that are allowed to decay (i.e. in the absence of forcing), whereas the study of HMHD turbulence provides insight into the dynamics as the fluctuations transition into the kinetic scales. The later two studies (presented in Chapters 5 and 6) observationally examine two regions within the magnetosphere where turbulence is thought to play a role; the bursty bulk flow (BBF) braking region in the Earth's magnetotail and Kelvin-Helmholtz instability (KHI) on the Earth's magnetopause. The BBF braking region study relates to the driving of turbulence by reconnection ejecta, while the KHI study relates to the role of turbulence in the coupling of the magnetosphere to the solar wind and provides the first in-depth observational study of the properties of turbulence in association with the KHI on the magnetopause. Both observational studies find kinetic scale phenomena in association with turbulence.

To summarize, the main conclusions of this work are:

(1) Except in the case of strong symmetries (i.e. the absence of helicity), decaying turbulent MHD systems tend to evolve towards states predicted by statistical mechanics in combination with a principle of energy minimization, which are characterized by a high degree of

alignment between the magnetic field and velocity (cross helicity) and magnetic field and magnetic vector potential (magnetic helicity). See Chapter 3.

(2) In the small scales of HMHD systems there is a transition from quasi-equipartition between magnetic and kinetic energy to a magnetically dominated state with the ratio of magnetic to kinetic energy scaling as $\epsilon_H^2 k^2$ (with ϵ_H the dimensionless ion inertial length), which appears to be associated with the nonlinear advection term becoming subdominant to dissipation. See Chapter 4.

(3) Observations demonstrate the presence of turbulence in the BBF braking region and KHI on the Earth's magnetopause and the turbulence could play a role in facilitating the dynamics associated with these systems and the magnetosphere as a whole. See Chapters 5 and 6.

(4) The instability of strong field-aligned currents associated with intermittency into electrostatic structures (e.g. double layers and electron phase space holes) or electrostatic waves (e.g. ion acoustic waves) appears to be a general process for the dissipation of energy in collisionless plasmas and may be aided by Hall physics. See Chapters 4, 5 and 6.

(5) In confined regions of turbulence, such as found in the magnetosphere, the radiation of plasma waves may be associated with the removal of energy from the turbulence and, as in the BBF braking region, could transport energy to the Earth's auroral region. See Chapters 5 and 6.

7.1 Perspectives on the Present Work

Turbulence is a challenging phenomenon to study; involving a high degree of nonlinearity and a wide range of interacting scales. At a basic level, the study of turbulence is an attempt to understand the dynamics associated with the nonlinear terms in the equations, which in general is not a straight-forward task. Collisionless plasma systems complicate matters by introducing a wide range of additional effects as the fluid approximation breaks down, which act both to alter

the behavior of the nonlinearities and provide pathways for the dissipation of energy. Despite the high degree of complexity, turbulence is likely present in a wide variety of systems and may have significant impacts on understanding the dynamics of these systems, as studied, for example, in this work in the context of the Earth's magnetosphere. Some potential consequences of turbulence on the Earth's magnetosphere, which were explored in this work, include:

(1) Allowing the transfer of energy from large-scale configurations, such as reconnection ejecta (for example, BBFs) or KH waves, into the thermal energy of the plasma.

(2) Exciting waves that transfer energy out of the turbulent region and into distant regions of the magnetosphere, such as the auroral region.

(3) Generating magnetic reconnection events that, for example, allow the mixing of magnetospheric and magnetosheath plasma.

Because turbulence allows the transfer of energy into the small kinetic scales, as more refined satellite missions continue to be launched examining ever smaller length and time scales, such as in the case of MMS, it will no doubt be necessary to expand our understanding of plasma turbulence to fully interpret the observations.

The study of plasma turbulence can have broad applicability to the field of magnetic reconnection research. As illustrated in points (1) and (3) above, magnetic reconnection and turbulence have a close relationship, in that reconnection jets can drive turbulence and turbulence can drive magnetic reconnection events through the tangling of magnetic fields by the turbulent fluctuations [*Matthaeus and Lamkin*, 1986; *Servidio et al.*, 2010, 2011]. Aside from driving reconnection, turbulence can have an impact on how reconnection manifests itself. For example, reconnection is expected to occur on the dayside magnetosphere as a result of the inflowing solar wind, even in the laminar case [*Dungey*, 1961]. However, turbulence in the magnetosheath could lead to more "patchy" 3D reconnection events than the extended line of reconnection expected in the laminar regime, which could result in the further tangling of the magnetic field by the initial reconnection and formation of secondary reconnection events with strong electric field signatures as proposed by

Ergun et al. [2016]. This impact on the nature of the reconnection could then have implications for the identification of reconnection events in observations.

A number of techniques are available for the exploration of plasma turbulence. Observational studies are useful in that, since they include the full range of physics, they provide, in a sense, the ground truth for the theoretical understanding of turbulence. However, as is particularly the case in space missions, data is often obtained from point measurements by single spacecraft (for example see the analysis of Chapter 5), which makes it difficult to get information about a wide range of length scales as is needed in turbulence theory. The MMS mission provides an exciting opportunity to try and disentangle the temporal and spatial behavior down into the kinetic scales through the use of multiple spacecraft and high-time-resolution data. Additionally, the ability to obtain relatively long periods of high-time-resolution burst data through the use of the SITL system (as was possible in the KHI event of Chapter 6) is useful for statistical studies of turbulence. However, even with the significant improvements provided by MMS, it is still challenging to measure the wide range of scale sizes inherent to turbulent systems since the nominal tetrahedral formation only provides approximately one separation distance at any given time. The exceptions to this limitation are systems such as the solar wind, where high-speed background flows allow the use of the Taylor "frozen-in" hypothesis and a unique mapping of temporal scales to length scales can be performed; although assumptions about isotropy (or anisotropy) are still required for single spacecraft measurements in this case [e.g. *Stawarz et al.*, 2009, 2011]. However, for magnetospheric flows, the Taylor hypothesis is often not a valid approximation.

Alternatively, numerical approaches provide an opportunity to examine in detail the spatial configurations of turbulent systems. By using simplified approximations to the full system, simulations can aid in disentangling the role of various physical effects (for example the Hall effect as studied in Chapter 4). Simulations, however, also have their limitations. It is often difficult to achieve the full scale separations present in real systems and it is challenging to simultaneously include both the large-scale fluid regime and all of the small-scale kinetic physics. As such, a piecemeal approach is often employed, where MHD simulations are employed to develop an under-

standing of the large-scales (as done in Chapter 3) and fully kinetic simulations, which often just barely resolve the fluid scales, are used to examine small-scale dynamics [e.g. *Karimabadi et al.*, 2013]. While this approach can provide useful insights, the issue is that it doesn't fully allow for the coupling between the fluid and kinetic scales; although intermediate approximations, such as the HMHD approximation studied in this work, can provide some insight into the transition to kinetic scales.

7.2 Future Work

The MMS mission will encounter a variety of potentially turbulent environments in the immediate vicinity of Earth, including KH unstable regions on the magnetopause, the magnetosheath, the solar wind, and BBF events in the magnetotail. In particular, as the apogee of MMS (located at $\approx 12\ R_E$ in radial distance) rotates through the magnetotail over the course of the summer of 2016, the formation will likely be in the vicinity of the nominal plasma sheet and at radial distances consistent with the BBF braking region. The optimal time for MMS to be in relatively close proximity to the plasma sheet, while still being in a region where BBF braking events are expected to be observed, will occur in August of 2016 and will provide a potential opportunity to perform a follow-up study to the one discussed in Chapter 5. The main advantages of this follow-up study will be the addition of spatial information about the turbulence, which was not able to be examined in Chapter 5 using THEMIS data, as well as the ability to obtain more high-time-resolution data. These advantages will translate into a better ability to examine the current structures formed by the intermittency and perhaps the radiation of waves using measurements of the Poynting flux from multiple points in space.

While the work presented here begins to address several issues, there are still a number of topics that need to be examined to fully understand collisionless plasma turbulence. One question that should continue to be explored is, "*What kinetic processes, in addition to the field-aligned current instabilities explored here, are driven by turbulence and what parameters determine the relative importance of these processes?*" The answers to this question will aid in determining the

processes of turbulent dissipation in the collisionless regime and would help in understanding the small-scale behavior of collisionless plasmas in general. A variety of kinetic phenomena have been studied in association with turbulence, for example, magnetic reconnection [*Matthaeus and Lamkin*, 1986; *Servidio et al.*, 2010; *Donato et al.*, 2012; *Osman et al.*, 2014], resonant damping mechanisms (such as Landau or cyclotron damping) [*Leamon et al.*, 1999; *Kasper et al.*, 2008], and temperature anisotropy driven instabilities [*Bale et al.*, 2009; *Osman et al.*, 2012]. However, other process may also play a role that have not yet been explored. Additionally, the parameters of the plasma could influence what kinetic processes are relevant and so analyzing different environments may provide additional insights. For example, the analysis of linear kinetic Alfvén waves in Chapter 5.2 showed that the plasma β can have an impact on the strength of dissipation at a given scale and the species of particle responsible for the dissipation, so perhaps β also has an impact on collisionless dissipation in the nonlinear regime. While linear wave dissipation mechanisms have been invoked to understand turbulent dissipation, one might expect that the extent to which this is a valid approach is dependent on whether the turbulence is in the strongly or weakly nonlinear regime.

One way to potentially move forward in exploring the driving of kinetic phenomena through turbulence is by observationally examining the configurations of individual intermittent structures in turbulent environments (as has been done in some numerical simulations [e.g. *Mininni et al.*, 2006a; *Dmitruk and Matthaeus*, 2006; *Lee et al.*, 2008; *Pouquet et al.*, 2010]). Along with statistical measures, this type of analysis could provide a more in depth understanding of the magnetic reconnection or instabilities that could form as a result of the intermittency. Missions such as MMS, with high-time-resolution data and small-scale multipoint measurements, in conjunction with fluid and kinetic simulations (for example, by comparing 1D trajectories through simulated structures to numerical data) could be employed in this effort.

A related question, which could be relevant to understanding the small-scale behavior of HMHD turbulence seen in Figure 4.4, is, "*To what extent do linear (or nearly linear) waves play a role in the dynamics?*" One way to numerically explore this is by examining the extent to which energy is concentrated onto the predicted linear dispersion relations when considering the frequency-

wavenumber spectra of turbulence simulations, as has begun to be done in some simulations [e.g. *Parashar et al.*, 2010; *Comişel et al.*, 2013; *Clark di Leoni et al.*, 2014]. The challenge with this is that a significant amount of computer resources are necessary to output the data with enough cadence to examine a wide range of frequencies for large computational domains, which can limit the analysis to relatively modest Reynolds numbers. The radiation of waves from confined regions of turbulence could also be explored numerically; however, again this puts a limit on the Reynolds numbers available since it would require driving turbulence in only a fraction of the domain and looking at the wave radiation far from the driving region.

Future work on HMHD turbulence could also involve using numerical simulations with forcing at small to moderate scales to study the effect of Hall physics on inverse cascades. As mentioned in Chapters 1.2 and 2.3.3, magnetic helicity is known to undergo an inverse cascade (i.e. a transfer from small to large scales) in MHD. *Servidio et al.* [2008b] have performed the statistical mechanics of the HMHD system (see Chapter 2.3.3 for the MHD case) and find that magnetic helicity also features a condensation to the smallest wavenumbers, indicative of the possibility of an inverse cascade, in HMHD. In addition the quantity $(H_G - H_M)/(2d_i)$, which is the generalized helicity with the magnetic helicity component removed, can also exhibit interesting behavior including a condensation at the small wavenumbers. While some work has been done on inverse cascades in electron MHD (HMHD neglecting the velocity) [*Wareing and Hollerbach*, 2010; *Kim and Cho*, 2015], the more general case of HMHD inverse cascades, which includes the generalized helicity, has not been explored. The inverse cascade problem in HMHD relates to understanding how kinetic effects alter the nonlinear dynamics of the turbulence and, in terms of applications to physical systems, to understanding the formation of large-scale magnetic structures and dynamos in the universe. The related problem of the extension of the relaxation problem (discussed for MHD in Chapter 3) to HMHD has also not been performed and would likely involve the more complex relaxed states associated with the generalized helicity, which involve non-force-free configurations [*Turner*, 1986].

7.2.1 Solar Probe Plus

Along with the MMS mission, future missions, such as Solar Probe Plus (SPP) [*Fox et al.*, 2015] scheduled to launch in mid-2018, provide a promising future for the study of collisionless plasma turbulence. SPP will examine solar wind turbulence, which is believed to play a role in heating the corona and accelerating the solar wind, as close as 10 solar radii from the Sun. SPP's perihelion is expected to be inside of the Alfvén critical point, where the solar wind transitions from sub-Alfvénic to super-Alfvénic and, as a result, the Taylor hypothesis, which is typically used in solar wind turbulence studies to translate temporal variations into spatial variations, may not be valid. Based on extrapolations of measurements from the Helios spacecraft, the anticipated solar wind flow speed is 210 km/s and $V_A = 500$ km/s at 10 solar radii [*Bale et al.*, 2016]. Analysis of turbulence near the Sun with SPP may, therefore, be similar to single spacecraft analysis of magnetospheric turbulence (see for example Chapter 5), where the Taylor hypothesis is also not valid. However, unlike the magnetosphere, the close proximity of SPP to the Sun at perihelion means that the spacecraft velocity will be significant with speeds of roughly 200 km/s, which may aid in some cases to the determination of spatial scales [*Klein et al.*, 2015].

The results from this work may provide some insights into the behavior that will be observed by SPP. The formation of field-aligned current instabilities due to intermittency may be a fairly general process in collisionless plasmas, potentially occurring in both the BBF braking region and the magnetopause KHI. It therefore may be reasonable to expect these instabilities to be also occurring in the solar wind observed by SPP. As a result, it would also be expected for double layers, electron phase space holes, and/or electrostatic waves, such as ion acoustic waves, to be present.

The expected $B_0 \approx 2000$ nT, $n_0 \approx 7000$ cm^{-3}, and $T_{0i} \approx T_{0e} \approx 85$ eV, which translates to $\beta_i \approx \beta_e \approx 0.06$ [*Bale et al.*, 2016]. If the fluctuations were to behave similar to kinetic Alfvén waves, as has been suggested in the solar wind [e.g. *Bale et al.*, 2005], then, as discussed in Chapter 5.2, ion damping would be expected to be negligible and energy may cascade past ion scales with

relatively little dissipation. Electron damping could potentially become significant or intermittent field-aligned current instabilities could take over. For reference, the expected value of β_e is just larger than that used in the top left panel of Figure 5.3 (note that $\beta_e = \beta_i/5$ in that figure). In the time until SPP's closest approach to the Sun, the MMS mission will no doubt reveal additional features of kinetic scale plasma turbulence that could potentially be translated to the solar wind environment at 10 solar radii and provide insight that could aid in the interpretation of solar probe observations.

Bibliography

Abramenko, V. I. (2008), Multifractal nature of solar phenomena, in *Solar Physics Research Trends*, edited by P. Wang, pp. 95–136, Nova Science Publishers, Inc., New York.

Alexakis, A., P. D. Mininni, and A. Pouquet (2005), Shell-to-shell energy transfer in magnetohydrodynamics. I. Steady state turbulence, *Phys. Rev. E*, *72*(4), 046301, doi:10.1103/PhysRevE.72.046301.

Alexandrova, O., V. Carbone, P. Veltri, and L. Sorriso-Valvo (2008), Small-Scale Energy Cascade of the Solar Wind Turbulence, *Astrophys. J.*, *674*, 1153–1157, doi:10.1086/524056.

Alexandrova, O., C. H. K. Chen, L. Sorriso-Valvo, T. S. Horbury, and S. D. Bale (2013), Solar Wind Turbulence and the Role of Ion Instabilities, *Space Sci. Rev.*, *178*, 101–139, doi:10.1007/s11214-013-0004-8.

Angelopoulos, V. (2008), The THEMIS Mission, *Space Sci. Rev.*, *141*, 5–34, doi:10.1007/s11214-008-9336-1.

Angelopoulos, V. (2011), The ARTEMIS Mission, *Space Sci. Rev.*, *165*, 3–25, doi:10.1007/s11214-010-9687-2.

Angelopoulos, V., W. Baumjohann, C. F. Kennel, F. V. Coronti, M. G. Kivelson, R. Pellat, R. J. Walker, H. Luehr, and G. Paschmann (1992), Bursty bulk flows in the inner central plasma sheet, *J. Geophys. Res.*, *97*, 4027–4039, doi:10.1029/91JA02701.

Angelopoulos, V., C. F. Kennel, F. V. Coroniti, R. Pellat, M. G. Kivelson, R. J. Walker, C. T. Russell, W. Baumjohann, W. C. Feldman, and J. T. Gosling (1994), Statistical characteristics of bursty bulk flow events, *J. Geophys. Res.*, *99*, 21, doi:10.1029/94JA01263.

Angelopoulos, V., F. V. Coroniti, C. F. Kennel, M. G. Kivelson, R. J. Walker, C. T. Russell, R. L. McPherron, E. Sanchez, C.-I. Meng, W. Baumjohann, G. D. Reeves, R. D. Belian, N. Sato, E. Friis-Christensen, P. R. Sutcliffe, K. Yumoto, and T. Harris (1996), Multipoint analysis of a bursty bulk flow event on April 11, 1985, *J. Geophys. Res.*, *101*, 4967–4989, doi:10.1029/95JA02722.

Angelopoulos, V., T. D. Phan, D. E. Larson, F. S. Mozer, R. P. Lin, K. Tsuruda, H. Hayakawa, T. Mukai, S. Kokubun, T. Yamamoto, D. J. Williams, R. W. McEntire, R. P. Lepping, G. K. Parks, M. Brittnacher, G. Germany, J. Spann, H. J. Singer, and K. Yumoto (1997), Magnetotail flow bursts: Association to global magnetospheric circulation, relationship to ionospheric activity and direct evidence for localization, *Geophys. Res. Lett.*, *24*, 2271–2274, doi:10.1029/97GL02355.

Auster, H. U., K. H. Glassmeier, W. Magnes, O. Aydogar, W. Baumjohann, D. Constantinescu, D. Fischer, K. H. Fornacon, E. Georgescu, P. Harvey, O. Hillenmaier, R. Kroth, M. Ludlam, Y. Narita, R. Nakamura, K. Okrafka, F. Plaschke, I. Richter, H. Schwarzl, B. Stoll, A. Valavanoglou, and M. Wiedemann (2008), The THEMIS Fluxgate Magnetometer, *Space Sci. Rev.*, *141*, 235–264, doi:10.1007/s11214-008-9365-9.

Baker, D. N., L. Riesberg, C. K. Pankratz, R. S. Panneton, B. L. Giles, F. D. Wilder, and R. E. Ergun (2015), Magnetospheric Multiscale Instrument Suite Operations and Data System, *Space Sci. Rev.*, *online first*, doi:10.1007/s11214-014-0128-5.

Bale, S. D., P. J. Kellogg, D. E. Larsen, R. P. Lin, K. Goetz, and R. P. Lepping (1998), Bipolar electrostatic structures in the shock transition region: Evidence of electron phase space holes, *Geophys. Res. Lett.*, *25*, 2929–2932, doi:10.1029/98GL02111.

Bale, S. D., P. J. Kellogg, F. S. Mozer, T. S. Horbury, and H. Reme (2005), Measurement of the Electric Fluctuation Spectrum of Magnetohydrodynamic Turbulence, *Phys. Rev. Lett.*, *94*(21), 215002, doi:10.1103/PhysRevLett.94.215002.

Bale, S. D., J. C. Kasper, G. G. Howes, E. Quataert, C. Salem, and D. Sundkvist (2009), Magnetic Fluctuation Power Near Proton Temperature Anisotropy Instability Thresholds in the Solar Wind, *Phys. Rev. Lett.*, *103*(21), 211101, doi:10.1103/PhysRevLett.103.211101.

Bale, S. D., K. Goetz, P. R. Harvey, P. Turin, J. W. Bonnell, T. D. de Wit, R. E. Ergun, R. J. MacDowall, M. Pulupa, M. Andre, M. Bolton, J.-L. Bougeret, T. A. Bowen, D. Burgess, C. A. Cattell, B. D. G. Chandran, C. C. Chaston, C. H. K. Chen, M. K. Choi, J. E. Connerney, S. Cranmer, M. Diaz-Aguado, W. Donakowski, J. F. Drake, W. M. Farrell, P. Fergeau, J. Fermin, J. Fischer, N. Fox, D. Glaser, M. Goldstein, D. Gordon, E. Hanson, S. E. Harris, L. M. Hayes, J. J. Hinze, J. V. Hollweg, T. S. Horbury, R. A. Howard, V. Hoxie, G. Jannet, M. Karlsson, J. C. Kasper, P. J. Kellogg, M. Kien, J. A. Klimchuk, V. V. Krasnoselskikh, S. Krucker, J. J. Lynch, M. Maksimovic, D. M. Malaspina, S. Marker, P. Martin, J. Martinez-Oliveros, J. McCauley, D. J. McComas, T. McDonald, N. Meyer-Vernet, M. Moncuquet, S. J. Monson, F. S. Mozer, S. D. Murphy, J. Odom, R. Oliverson, J. Olson, E. N. Parker, D. Pankow, T. Phan, E. Quataert, T. Quinn, S. W. Ruplin, C. Salem, D. Seitz, D. A. Sheppard, A. Siy, K. Stevens, D. Summers, A. Szabo, M. Timofeeva, A. Vaivads, M. Velli, A. Yehle, D. Werthimer, and J. R. Wygant (2016), The FIELDS instrument suite for Solar Probe Plus, *Space Sci. Rev.*, *online first*, doi:10.1007/s11214-016-0244-5.

Bardos, C., M. C. L. Filho, D. Niu, H. J. N. Lopes, and E. S. Titi (2013), Stability of two-dimensional viscous incompressible flows under three-dimensional perturbations and inviscid symmetry breaking, *SIAM J. Math. Anal.*, *45*(3), 1871–1885, doi:10.1137/120862569.

Baumjohann, W., G. Paschmann, and H. Luehr (1990), Characteristics of high-speed ion flows in the plasma sheet, *J. Geophys. Res.*, *95*, 3801–3809, doi:10.1029/JA095iA04p03801.

Bellan, P. M. (2012), Improved basis set for low frequency plasma waves, *J. Geophys. Res.*, *117*(A16), A12219, doi:10.1029/2012JA017856.

Bhattacharjee, A., Z. W. Ma, and X. Wang (2001), Recent developments in collisionless reconnection theory: Applications to laboratory and space plasmas, *Phys. Plasmas*, *8*, 1829–1839, doi:10.1063/1.1353803.

Birn, J., J. F. Drake, M. A. Shay, B. N. Rogers, R. E. Denton, M. Hesse, M. Kuznetsova, Z. W. Ma, A. Bhattacharjee, A. Otto, and P. L. Pritchett (2001), Geospace Environmental Modeling (GEM) magnetic reconnection challenge, *J. Geophys. Res.*, *106*, 3715–3720, doi:10.1029/1999JA900449.

Birn, J., R. Nakamura, E. V. Panov, and M. Hesse (2011), Bursty bulk flows and dipolarization in MHD simulations of magnetotail reconnection, *J. Geophys. Res.*, *116*, A01210, doi:10.1029/2010JA016083.

Biskamp, D., and W.-C. Müller (2000), Scaling properties of three-dimensional isotropic magnetohydrodynamic turbulence, *Phys. Plasmas*, *7*, 4889–4900, doi:10.1063/1.1322562.

Biskamp, D., and H. Welter (1989), Dynamics of decaying two-dimensional magnetohydrodynamic turbulence, *Phys. Fluids B*, *1*, 1964–1979, doi:10.1063/1.859060.

Biskamp, D., E. Schwarz, and J. F. Drake (1996), Two-Dimensional Electron Magnetohydrodynamic Turbulence, *Phys. Rev. Lett.*, *76*, 1264–1267, doi:10.1103/PhysRevLett.76.1264.

Biskamp, D., E. Schwarz, and J. F. Drake (1997), Two-fluid theory of collisionless magnetic reconnection, *Phys. Plasmas*, *4*, 1002–1009, doi:10.1063/1.872211.

Block, L. P. (1978), A double layer review, *Astrphys. Space Sci.*, *55*, 59–83, doi:10.1007/BF00642580.

Boldyrev, S., and J. C. Perez (2012), Spectrum of Kinetic-Alfvén Turbulence, *Astrophys. J. Lett.*, *758*, L44, doi:10.1088/2041-8205/758/2/L44.

Bonnell, J. W., F. S. Mozer, G. T. Delory, A. J. Hull, R. E. Ergun, C. M. Cully, V. Angelopoulos, and P. R. Harvey (2008), The Electric Field Instrument (EFI) for THEMIS, *Space Sci. Rev.*, *141*, 303–341, doi:10.1007/s11214-008-9469-2.

Borg, A. L., M. Øieroset, T. D. Phan, F. S. Mozer, A. Pedersen, C. Mouikis, J. P. McFadden, C. Twitty, A. Balogh, and H. Rème (2005), Cluster encounter of a magnetic reconnection diffusion region in the near-Earth magnetotail on September 19, 2003, *Geophys. Res. Lett.*, *32*, L19105, doi:10.1029/2005GL023794.

Borovsky, J. E., and H. O. Funsten (2003), MHD turbulence in the Earth's plasma sheet: Dynamics, dissipation, and driving, *J. Geophys. Res.*, *108*, 1284, doi:10.1029/2002JA009625.

Borovsky, J. E., R. C. Elphic, H. O. Funsten, and M. F. Thomsen (1997), The Earth's plasma sheet as a laboratory for flow turbulence in high-β MHD, *J. Plasma Phys.*, *57*, 1–34, doi:10.1017/S0022377896005259.

Boyd, T. J. M., and J. J. Sanderson (2003), *The Physics of Plasmas*, Cambridge University Press, New York.

Brachet, M. E., D. I. Meiron, S. A. Orszag, B. G. Nickel, R. H. Morf, and U. Frisch (1983), Small-scale structure of the Taylor-Green vortex, *J. Fluid Mech.*, *130*, 411–452, doi:10.1017/S0022112083001159.

Braginskii, S. I. (1965), Transport Processes in a Plasma, *Rev. Plasma Phys.*, *1*, 205.

Brandenburg, A., and K. Subramanian (2005), Astrophysical magnetic fields and nonlinear dynamo theory, *Phys. Rep.*, *417*, 1–209, doi:10.1016/j.physrep.2005.06.005.

Bruno, R., and V. Carbone (2013), The Solar Wind as a Turbulence Laboratory, *Living Rev. Solar Phys.*, *10*, doi:10.12942/lrsp-2013-2.

Burch, J. L., T. E. Moore, R. B. Torbert, and B. L. Giles (2015), Magnetospheric Multiscale Overview and Science Objectives, *Space Sci. Rev.*, *online first*, 1–17, doi:10.1007/s11214-015-0164-9.

Burlaga, L. F. (1991), Intermittent turbulence in the solar wind, *J. Geophys. Res.*, *96*, 5847–5851, doi:10.1029/91JA00087.

Cattell, C., J. Crumley, J. Dombeck, J. R. Wygant, and F. S. Mozer (2002), Polar observations of solitary waves at the Earth's magnetopause, *Geophys. Res. Lett.*, *29*, 1065, doi:10.1029/2001GL014046.

Cattell, C. A., J. Dombeck, J. R. Wygant, M. K. Hudson, F. S. Mozer, M. A. Temerin, W. K. Peterson, C. A. Kletzing, C. T. Russell, and R. F. Pfaff (1999), Comparisons of Polar satellite observations of solitary wave velocities in the plasma sheet boundary and the high altitude cusp to those in the auroral zone, *Geophys. Res. Lett.*, *26*, 425–428, doi:10.1029/1998GL900304.

Chandrasekhar, S. (1961), *Hydrodynamic and Hydromagnetic Stability*, Dover Publications, Inc., New York.

Chapman, S., and V. C. A. Ferraro (1931), A new theory of magnetic storms, *Terr. Magn. Atmos. Electr.*, *36*(3), 171–186, doi:10.1029/TE036i003p00171.

Charles, C., and R. Boswell (2003), Current-free double-layer formation in a high-density helicon discharge, *Applied Phys. Lett.*, *82*, 1356, doi:10.1063/1.1557319.

Chaston, C. C., M. Wilber, F. S. Mozer, M. Fujimoto, M. L. Goldstein, M. Acuna, H. Reme, and A. Fazakerley (2007a), Mode Conversion and Anomalous Transport in Kelvin-Helmholtz Vortices and Kinetic Alfvén Waves at the Earth's Magnetopause, *Phys. Rev. Lett.*, *99*(17), 175004, doi:10.1103/PhysRevLett.99.175004.

Chaston, C. C., C. W. Carlson, J. P. McFadden, R. E. Ergun, and R. J. Strangeway (2007b), How important are dispersive Alfvén waves for auroral particle acceleration?, *Geophys. Res. Lett.*, *34*, L07101, doi:10.1029/2006GL029144.

Chaston, C. C., J. W. Bonnell, L. Clausen, and V. Angelopoulos (2012), Energy transport by kinetic-scale electromagnetic waves in fast plasma sheet flows, *J. Geophys. Res.*, *117*, A09202, doi:10.1029/2012JA017863.

Chaston, C. C., J. W. Bonnell, J. R. Wygant, F. Mozer, S. D. Bale, K. Kersten, A. W. Breneman, C. A. Kletzing, W. S. Kurth, G. B. Hospodarsky, C. W. Smith, and E. A. MacDonald (2014), Observations of kinetic scale field line resonances, *Geophys. Res. Lett.*, *41*, 209–215, doi:10.1002/2013GL058507.

Chen, C. H. K., L. Leung, S. Boldyrev, B. A. Maruca, and S. D. Bale (2014), Ion-scale spectral break of solar wind turbulence at high and low beta, *Geophys. Res. Lett.*, *41*, 8081–8088, doi:10.1002/2014GL062009.

Chen, C. X., and R. A. Wolf (1993), Interpretation of high-speed flows in the plasma sheet, *J. Geophys. Res.*, *98*, 21, doi:10.1029/93JA02080.

Chen, F. F. (1984), *Introduction to Plasma Physics and Controlled Fusion, 2nd Ed.*, Plenum Press, New York.

Chevillard, L., S. G. Roux, E. Lévêque, N. Mordant, J.-F. Pinton, and A. Arnéodo (2005), Intermittency of Velocity Time Increments in Turbulence, *Phys. Rev. Lett.*, *95*(6), 064501, doi:10.1103/PhysRevLett.95.064501.

Cichowlas, C., P. Bonaïti, F. Debbasch, and M. Brachet (2005), Effective Dissipation and Turbulence in Spectrally Truncated Euler Flows, *Phys. Rev. Lett.*, *95*(26), 264502, doi:10.1103/PhysRevLett.95.264502.

Clark di Leoni, P., P. J. Cobelli, P. D. Mininni, P. Dmitruk, and W. H. Matthaeus (2014), Quantification of the strength of inertial waves in a rotating turbulent flow, *Physics of Fluids*, *26*(3), 035106, doi:10.1063/1.4868280.

Comişel, H., D. Verscharen, Y. Narita, and U. Motschmann (2013), Spectral evolution of two-dimensional kinetic plasma turbulence in the wavenumber-frequency domain, *Phys. Plasmas*, *20*(9), 090701, doi:10.1063/1.4820936.

Cranmer, S. R. (2009), Coronal Holes, *Living Rev. Solar Phys.*, *6*, 3, doi:10.12942/lrsp-2009-3.

Cranmer, S. R., M. Asgari-Targhi, M. P. Miralles, J. C. Raymond, L. Strachan, H. Tian, and L. N. Woolsey (2015), The role of turbulence in coronal heating and solar wind expansion, *Phil. Trans. R. Soc. A*, *373*, 20140148, doi:10.1098/rsta.2014.0148.

Cully, C. M., R. E. Ergun, K. Stevens, A. Nammari, and J. Westfall (2008), The THEMIS Digital Fields Board, *Space Sci. Rev.*, *141*, 343–355, doi:10.1007/s11214-008-9417-1.

Dallas, V., and A. Alexakis (2013), Symmetry breaking of decaying magnetohydrodynamic Taylor-Green flows and consequences for universality, *Phys. Rev. E*, *88*(6), 063017, doi:10.1103/PhysRevE.88.063017.

D'Asaro, E. A. (2014), Turbulence in the Upper-Ocean Mixed Layer, *Annual Review of Marine Science*, *6*, 101–115, doi:10.1146/annurev-marine-010213-135138.

Dasso, S., L. J. Milano, W. H. Matthaeus, and C. W. Smith (2005), Anisotropy in Fast and Slow Solar Wind Fluctuations, *Astrophys. J. Lett.*, *635*, L181–L184, doi:10.1086/499559.

Daughton, W., T. K. M. Nakamura, H. Karimabadi, V. Roytershteyn, and B. Loring (2014), Computing the reconnection rate in turbulent kinetic layers by using electron mixing to identify topology, *Phys. Plasmas*, *21*(5), 052307, doi:10.1063/1.4875730.

Davidson, P. A. (2004), *Turbulence: An Introduction for Scientists and Engineers*, Oxford University Press, New York.

Delamere, P. A., R. J. Wilson, S. Eriksson, and F. Bagenal (2013), Magnetic signatures of Kelvin-Helmholtz vortices on Saturn's magnetopause: Global survey, *J. Geophys. Res.*, *118*, 393–404, doi:10.1029/2012JA018197.

Delamere, P. A., F. Bagenal, C. Paranicas, A. Masters, A. Radioti, B. Bonfond, L. Ray, X. Jia, J. Nichols, and C. Arridge (2015), Solar Wind and Internally Driven Dynamics: Influences on Magnetodiscs and Auroral Responses, *Space Sci. Rev.*, *187*, 51–97, doi:10.1007/s11214-014-0075-1.

Desroche, M., F. Bagenal, P. A. Delamere, and N. Erkaev (2012), Conditions at the expanded Jovian magnetopause and implications for the solar wind interaction, *J. Geophys. Res.*, *117*, A07202, doi:10.1029/2012JA017621.

Dmitruk, P., and W. H. Matthaeus (2006), Structure of the electromagnetic field in three-dimensional Hall magnetohydrodynamic turbulence, *Phys.Plasmas*, *13*(4), 042307, doi:10.1063/1.2192757.

Dobrowolny, M., A. Mangeney, and P. Veltri (1980), Fully developed anisotropic hydromagnetic turbulence in interplanetary space, *Phys. Rev. Lett.*, *45*, 144–147, doi:10.1103/PhysRevLett.45.144.

Donato, S., S. Servidio, P. Dmitruk, V. Carbone, M. A. Shay, P. A. Cassak, and W. H. Matthaeus (2012), Reconnection events in two-dimensional Hall magnetohydrodynamic turbulence, *Phys. Plasmas*, *19*(9), 092307, doi:10.1063/1.4754151.

Drake, J. F., M. Swisdak, C. Cattell, M. A. Shay, B. N. Rogers, and A. Zeiler (2003), Formation of Electron Holes and Particle Energization During Magnetic Reconnection, *Science*, *299*, 873–877, doi:10.1126/science.1080333.

Dungey, J. W. (1961), Interplanetary Magnetic Field and the Auroral Zones, *Phys. Rev. Lett.*, *6*, 47–48, doi:10.1103/PhysRevLett.6.47.

El-Alaoui, M., R. L. Richard, M. Ashour-Abdalla, M. L. Goldstein, and R. J. Walker (2013), Dipolarization and turbulence in the plasma sheet during a substorm: THEMIS observations and global MHD simulations, *J. Geophys. Res.*, *118*, 7752–7761, doi:10.1002/2013JA019322.

Ergun, R. E., C. W. Carlson, J. P. McFadden, F. S. Mozer, G. T. Delory, W. Peria, C. C. Chaston, M. Temerin, I. Roth, L. Muschietti, R. Elphic, R. Strangeway, R. Pfaff, C. A. Cattell, D. Klumpar, E. Shelley, W. Peterson, E. Moebius, and L. Kistler (1998), FAST satellite observations of large-amplitude solitary structures, *Geophys. Res. Lett.*, *25*, 2041–2044, doi:10.1029/98GL00636.

Ergun, R. E., Y.-J. Su, L. Andersson, C. W. Carlson, J. P. McFadden, F. S. Mozer, D. L. Newman, M. V. Goldman, and R. J. Strangeway (2001), Direct Observation of Localized Parallel Electric Fields in a Space Plasma, *Phys. Rev. Lett.*, *87*(4), 045003, doi:10.1103/PhysRevLett.87.045003.

Ergun, R. E., L. Andersson, D. Main, Y.-J. Su, D. L. Newman, M. V. Goldman, C. W. Carlson, A. J. Hull, J. P. McFadden, and F. S. Mozer (2004), Auroral particle acceleration by strong double layers: The upward current region, *J. Geophys. Res.*, *109*(A18), A12220, doi:10.1029/2004JA010545.

Ergun, R. E., L. Andersson, J. Tao, V. Angelopoulos, J. Bonnell, J. P. McFadden, D. E. Larson, S. Eriksson, T. Johansson, C. M. Cully, D. N. Newman, M. V. Goldman, A. Roux, O. Lecontel, K.-H. Glassmeier, and W. Baumjohann (2009), Observations of Double Layers in Earth's Plasma Sheet, *Phys. Rev. Lett.*, *102*(15), 155002, doi:10.1103/PhysRevLett.102.155002.

Ergun, R. E., S. Tucker, J. Westfall, K. A. Goodrich, D. M. Malaspina, D. Summers, J. Wallace, M. Karlsson, J. Mack, N. Brennan, B. Pyke, P. Withnell, R. Torbert, J. Macri, D. Rau, I. Dors, J. Needell, P.-A. Lindqvist, G. Olsson, and C. M. Cully (2014), The Axial Double Probe and Fields Signal Processing for the MMS Mission, *Space Sci. Rev.*, *online first*, doi:10.1007/s11214-014-0115-x.

Ergun, R. E., K. A. Goodrich, J. E. Stawarz, L. Andersson, and V. Angelopoulos (2015), Large-amplitude electric fields associated with bursty bulk flow braking in the Earth's plasma sheet, *J. Geophys. Res.*, *120*, 1832–1844, doi:10.1002/2014JA020165.

Ergun, R. E., K. A. Goodrich, F. D. Wilder, J. C. Holmes, J. E. Stawarz, S. Eriksson, A. P. Sturner, D. M. Malaspina, M. A. Usanova, R. B. Torbert, P.-A. Lindqvist, Y. Khotyaintsev, J. L. Burch, R. J. Strangeway, C. T. Russel, C. J. pollock, B. L. Giles, M. Hesse, L. J. Chen, M. V. Goldman, D. L. Newman, S. J. Schwartz, T. D. Phan, F. S. Mozer, J. Drake, M. A. Shay, P. A. Cassal, and R. Nakamura (2016), MMS Observations of Parallel Electric Fields Associated with Magnetic Reconnection, *Phys. Rev. Lett.*, *submitted*.

Eriksson, S., B. Lavraud, F. D. Wilder, B. L. Giles, J. L. Burch, W. Baumjohann, R. Ergun, P.-A. Lindqvist, W. Magnes, C. Pollock, C. T. Russell, R. Strangeway, R. B. Torbert, D. J. Gershman, Y. V. Khotyaintsev, L. Avanov, E. Grimes, S. Schwartz, A. Sturner, T. D. Phan, J. E. Stawarz, and K. Goodrich (2016), MMS Observations of Kelvin-Helmholtz-Induced Magnetic Reconnection, *Geophys. Res. Lett.*, *submitted*.

Faganello, M., F. Califano, and F. Pegoraro (2008), Numerical Evidence of Undriven, Fast Reconnection in the Solar-Wind Interaction with Earth's Magnetosphere: Formation of Electromagnetic Coherent Structures, *Phys. Rev. Lett.*, *101*(10), 105001, doi:10.1103/PhysRevLett.101.105001.

Falceta-Gonçalves, D., G. Kowal, E. Falgarone, and A. C.-L. Chian (2014), Turbulence in the interstellar medium, *Nonlin. Proc. Geophys.*, *21*, 587–604, doi:10.5194/npg-21-587-2014.

Falgarone, E., J. Pety, and P. Hily-Blant (2009), Intermittency of interstellar turbulence: Extreme velocity-shears and CO emission on milliparsec scale, *Astron. Astrophys.*, *507*, 355–368, doi:10.1051/0004-6361/200810963.

Fox, N. J., M. C. Velli, S. D. Bale, R. Decker, A. Driesman, R. A. Howard, J. C. Kasper, J. Kinnison, M. Kusterer, D. Lario, M. K. Lockwood, D. J. McComas, N. E. Raouafi, and A. Szabo (2015), The Solar Probe Plus Mission: Humanity's First Visit to Our Star, *Space Sci. Rev.*, *online first*, doi:10.1007/s11214-015-0211-6.

Frisch, U. (1995), *Turbulence: The Legacy of A. N. Kolmogorov*, Cambridge University Press, Cambridge.

Frisch, U., A. Pouquet, J. Leorat, and A. Mazure (1975), Possibility of an inverse cascade of magnetic helicity in magnetohydrodynamic turbulence, *J. Fluid Mech.*, *68*, 769–778, doi:10.1017/S002211207500122X.

Fuselier, S. A., W. S. Lewis, C. Schiff, R. Ergun, J. L. Burch, S. M. Petrinec, and K. J. Trattner (2014), Magnetospheric Multiscale Science Mission Profile and Operations, *Space Sci. Rev.*, *online first*, doi:10.1007/s11214-014-0087-x.

Fyfe, D., and D. Montgomery (1976), High-beta turbulence in two-dimensional magnetohydrodynamics, *J. Plasma Phys.*, *16*, 181–191, doi:10.1017/S0022377800020158.

Galtier, S. (2006), Wave turbulence in incompressible Hall magnetohydrodynamics, *J. Plasma Phys.*, *72*, 721–769, doi:10.1017/S0022377806004521.

Galtier, S., and E. Buchlin (2007), Multiscale Hall-Magnetohydrodynamic Turbulence in the Solar Wind, *Astrophys. J.*, *656*, 560–566, doi:10.1086/510423.

Galtier, S., S. V. Nazarenko, A. C. Newell, and A. Pouquet (2000), A weak turbulence theory for incompressible magnetohydrodynamics, *J. Plasma Phys.*, *63*, 447–488, doi:10.1017/S0022377899008284.

Galtier, S., S. V. Nazarenko, A. C. Newell, and A. Pouquet (2002), Anisotropic Turbulence of Shear-Alfvén Waves, *Astrophys. J. Lett.*, *564*, L49–L52, doi:10.1086/338791.

Galtier, S., A. Pouquet, and A. Mangeney (2005), On spectral scaling laws for incompressible anisotropic magnetohydrodynamic turbulence, *Phys. Plasmas*, *12*(9), 092310, doi:10.1063/1.2052507.

Gargett, A. E. (1989), Ocean turbulence, *Annual Review of Fluid Mechanics*, *21*, 419–451, doi:10.1146/annurev.fl.21.010189.002223.

Gary, S. P., S. Saito, and Y. Narita (2010), Whistler Turbulence Wavevector Anisotropies: Particle-in-cell Simulations, *Astrophys. J.*, *716*, 1332–1335, doi:10.1088/0004-637X/716/2/1332.

Ghosh, S., E. Siregar, D. A. Roberts, and M. L. Goldstein (1996), Simulation of high-frequency solar wind power spectra using Hall magnetohydrodynamics, *J. Geophys. Res.*, *101*, 2493–2504, doi:10.1029/95JA03201.

Goertz, C. K., and G. Joyce (1975), Numerical Simulation of the Plasma Double Layer, *Astrophys. Space Sci.*, *32*, 165–173.

Goldman, M. V., M. M. Oppenheim, and D. L. Newman (1999), Nonlinear two-stream instabilities as an explanation for auroral bipolar wave structures, *Geophys. Res. Lett.*, *26*, 1821–1824, doi:10.1029/1999GL900435.

Goldreich, P., and S. Sridhar (1995), Toward a theory of interstellar turbulence. 2: Strong alfvenic turbulence, *Astrophys. J.*, *438*, 763–775, doi:10.1086/175121.

Gómez, D. O., P. D. Mininni, and P. Dmitruk (2005), Parallel Simulations in Turbulent MHD, *Physica Scripta*, *116*, 123–127, doi:10.1238/Physica.Topical.116a00123.

Gottlieb, D., and S. A. Orszag (1977), *Numerical Analysis of Spectral Methods: Theory and Applications*, Society for Industrial and Applied Mathematics, Philadelphia.

Greco, A., P. Chuychai, W. H. Matthaeus, S. Servidio, and P. Dmitruk (2008), Intermittent MHD structures and classical discontinuities, *Geophys. Res. Lett.*, *35*, L19111, doi:10.1029/2008GL035454.

Greco, A., W. H. Matthaeus, S. Servidio, P. Chuychai, and P. Dmitruk (2009), Statistical Analysis of Discontinuities in Solar Wind ACE Data and Comparison with Intermittent MHD Turbulence, *Astrophys. J. Lett.*, *691*, L111–L114, doi:10.1088/0004-637X/691/2/L111.

Gurnett, D. A., and A. Bhattacharjee (2005), *Introduction to Plasma Physics*, Cambridge University Press, New York.

Harned, D. S. (1982), Quasineutral hybrid simulation of macroscopic plasma phenomena, *J. Comp. Phys.*, *47*, 452–462, doi:10.1016/0021-9991(82)90094-8.

Hasegawa, A. (1976), Particle acceleration by MHD surface wave and formation of aurora, *J. Geophys. Res.*, *81*, 5083–5090, doi:10.1029/JA081i028p05083.

Hasegawa, H., M. Fujimoto, T.-D. Phan, H. Rème, A. Balogh, M. W. Dunlop, C. Hashimoto, and R. TanDokoro (2004), Transport of solar wind into Earth's magnetosphere through rolled-up Kelvin-Helmholtz vortices, *Nature*, *430*, 755–758, doi:10.1038/nature02799.

Homann, H., R. Grauer, A. Busse, and W. C. Müller (2007), Lagrangian statistics of Navier-Stokes and MHD turbulence, *J. Plasma Phys.*, *73*, 821–830, doi:10.1017/S0022377807006575.

Hori, D., and H. Miura (2008), Spectrum Properties of Hall MHD Turbulence, *Plasma Fusion Res.*, *3*, S1053, doi:10.1585/pfr.3.S1053.

Howes, G. G., J. M. Tenbarge, W. Dorland, E. Quataert, A. A. Schekochihin, R. Numata, and T. Tatsuno (2011), Gyrokinetic Simulations of Solar Wind Turbulence from Ion to Electron Scales, *Phys.Rev. Lett.*, *107*(3), 035004, doi:10.1103/PhysRevLett.107.035004.

Hwang, K.-J., M. M. Kuznetsova, F. Sahraoui, M. L. Goldstein, E. Lee, and G. K. Parks (2011), Kelvin-Helmholtz waves under southward interplanetary magnetic field, *J. Geophys. Res.*, *116*, A08210, doi:10.1029/2011JA016596.

Iroshnikov, P. S. (1964), Turbulence of a Conducting Fluid in a Strong Magnetic Field, *Sov. Astron.*, *7*(4), 566–571.

Ishihara, T., T. Gotoh, and Y. Kaneda (2009), Study of High - Reynolds Number Isotropic Turbulence by Direct Numerical Simulation, *Ann. Rev. Fluid Mech.*, *41*, 165–180, doi:10.1146/annurev.fluid.010908.165203.

Ivey, G. N., K. B. Winters, and J. R. Koseff (2008), Density Stratification, Turbulence, but How Much Mixing?, *Ann. Rev. Fluid Mech.*, *40*, 169–184, doi:10.1146/annurev.fluid.39.050905.110314.

Joselyn, J. A. (2001), State of the Art in Space Weather Services and Forecasting, in *Space Storms and Space Weather Hazards*, vol. 38, edited by I. A. Daglis, pp. 419–436, doi:10.1007/978-94-010-0983-6_17.

Karimabadi, H., V. Roytershteyn, M. Wan, W. H. Matthaeus, W. Daughton, P. Wu, M. Shay, B. Loring, J. Borovsky, E. Leonardis, S. C. Chapman, and T. K. M. Nakamura (2013), Coherent structures, intermittent turbulence, and dissipation in high-temperature plasmas, *Phys. Plasmas*, *20*(1), 012303, doi:10.1063/1.4773205.

Kasper, J. C., A. J. Lazarus, and S. P. Gary (2008), Hot Solar-Wind Helium: Direct Evidence for Local Heating by Alfvén-Cyclotron Dissipation, *Phys. Rev. Lett.*, *101*(26), 261103, doi:10.1103/PhysRevLett.101.261103.

Kavosi, S., and J. Raeder (2015), Ubiquity of Kelvin-Helmholtz waves at Earth's magnetopause, *Nature Communications*, *6*, 7019, doi:10.1038/ncomms8019.

Kim, H., and J. Cho (2015), Inverse Cascade in Imbalanced Electron Magnetohydrodynamic Turbulence, *Astrophys. J.*, *801*, 75, doi:10.1088/0004-637X/801/2/75.

Kindel, J. M., and C. F. Kennel (1971), Topside current instabilities, *J. Geophys. Res.*, *76*, 3055–3078, doi:10.1029/JA076i013p03055.

Kiyani, K. H., K. T. Osman, and S. C. Chapman (2015), Dissipation and heating in solar wind turbulence: from the macro to the micro and back again, *Phil. Trans. R. Soc. A*, *373*, 20140155, doi:10.1098/rsta.2014.0155.

Klein, K. G., J. C. Perez, D. Verscharen, A. Mallet, and B. D. G. Chandran (2015), A Modified Version of Taylor's Hypothesis for Solar Probe Plus Observations, *Astrophys. J. Lett.*, *801*, L18, doi:10.1088/2041-8205/801/1/L18.

Klimchuk, J. A. (2006), On Solving the Coronal Heating Problem, *Solar Phys.*, *234*, 41–77, doi:10.1007/s11207-006-0055-z.

Kolmogorov, A. N. (1941), The Local Structure of Turbulence in Incompressible Viscous Fluid for Very Large Reynolds Numbers, *Dokl. Akad. Nauk SSSR*, *30*, 301, (reprinted in *Proc. R. Soc. A*, 434, 9-13, 1990).

Kraichnan, R. H. (1965), Inertial-Range Spectrum of Hydromagnetic Turbulence, *Phys. Fluids*, *8*, 1385–1387, doi:10.1063/1.1761412.

Kraichnan, R. H. (1967), Inertial Ranges in Two-Dimensional Turbulence, *Phys. Fluids*, *10*, 1417–1423, doi:10.1063/1.1762301.

Krishan, V., and S. M. Mahajan (2005), Modeling of short scale turbulence in the solar wind, *Nonlin. Proc. Geophys.*, *12*, 75–81, doi:10.5194/npg-12-75-2005.

Krstulovic, G., M. E. Brachet, and A. Pouquet (2014), Forced magnetohydrodynamic turbulence in three dimensions using Taylor-Green symmetries, *Phys. Rev. E*, *89*(4), 043,017, doi:10.1103/PhysRevE.89.043017.

Le Contel, O., P. Leroy, A. Roux, C. Coillot, D. Alison, A. Bouabdellah, L. Mirioni, L. Meslier, A. Galic, M. C. Vassal, R. B. Torbert, J. Needell, D. Rau, I. Dors, R. E. Ergun, J. Westfall, D. Summers, J. Wallace, W. Magnes, A. Valavanoglou, G. Olsson, M. Chutter, J. Macri, S. Myers, S. Turco, J. Nolin, D. Bodet, K. Rowe, M. Tanguy, and B. de la Porte (2014), The Search-Coil Magnetometer for MMS, *Space Sci. Rev.*, *online first*, doi:10.1007/s11214-014-0096-9.

Leamon, R. J., C. W. Smith, N. F. Ness, and H. K. Wong (1999), Dissipation range dynamics: Kinetic Alfvén waves and the importance of β_e, *J. Geophys. Res.*, *104*, 22,331–22,344, doi:10.1029/1999JA900158.

Lecoanet, D., and E. Quataert (2013), Internal gravity wave excitation by turbulent convection, *Mon. Not. R. Astron. Soc.*, *430*, 2363–2376, doi:10.1093/mnras/stt055.

Lee, E., M. E. Brachet, A. Pouquet, P. D. Mininni, and D. Rosenberg (2008), Paradigmatic flow for small-scale magnetohydrodynamics: Properties of the ideal case and the collision of current sheets, *Phys. Rev. E*, *78*(6), 066401, doi:10.1103/PhysRevE.78.066401.

Lee, E., M. E. Brachet, A. Pouquet, P. D. Mininni, and D. Rosenberg (2010), Lack of universality in decaying magnetohydrodynamic turbulence, *Phys. Rev. E*, *81*(1), 016,318, doi:10.1103/PhysRevE.81.016318.

Lindqvist, P.-A., G. Olsson, R. B. Torbert, B. King, M. Granoff, D. Rau, G. Needell, S. Turco, I. Dors, P. Beckman, J. Macri, C. Frost, J. Salwen, A. Eriksson, L. Åhlén, Y. V. Khotyaintsev,

J. Porter, K. Lappalainen, R. E. Ergun, W. Wermeer, and S. Tucker (2014), The Spin-Plane Double Probe Electric Field Instrument for MMS, *Space Sci. Rev.*, *online first*, doi:10.1007/s11214-014-0116-9.

Liu, C., X. Feng, J. Guo, and Y. Ye (2013), Study of small-scale plasmoid structures in the magnetotail using Cluster observations and Hall MHD simulations, *J. Geophys. Res.*, *118*, 2087–2100, doi:10.1002/jgra.50248.

Lysak, R. L. (1998), The relationship between electrostatic shocks and kinetic Alfvén waves, *Geophys. Res. Lett.*, *25*, 2089–2092, doi:10.1029/98GL00065.

Lysak, R. L., and W. Lotko (1996), On the kinetic dispersion relation for shear Alfvén waves, *J. Geophys. Res.*, *101*, 5085–5094, doi:10.1029/95JA03712.

Ma, X., and A. Otto (2013), Mechanisms of field-aligned current formation in magnetic reconnection, *J. Geophys. Res.*, *118*, 4906–4914, doi:10.1002/jgra.50457.

Ma, Z. W., and L. C. Lee (2001), Hall effects on the generation of field-aligned currents in three-dimensional magnetic reconnection, *J. Geophys. Res.*, *106*, 25,951–25,960, doi:10.1029/2000JA000290.

Mahajan, S. M., and Z. Yoshida (1998), Double Curl Beltrami Flow: Diamagnetic Structures, *Phys. Rev. Lett.*, *81*, 4863–4866, doi:10.1103/PhysRevLett.81.4863.

Marchenko, V. A., R. E. Denton, and M. K. Hudson (1996), A magnetohydrodynamic model of kinetic Alfvén waves with finite ion gyroradius, *Phys. Plasmas*, *3*, 3861–3863, doi:10.1063/1.871935.

Marino, R., L. Sorriso-Valvo, V. Carbone, A. Noullez, R. Bruno, and B. Bavassano (2008), Heating the Solar Wind by a Magnetohydrodynamic Turbulent Energy Cascade, *Astrophys. J. Lett.*, *677*, L71–L74, doi:10.1086/587957.

Martin, L. N., P. Dmitruk, and D. O. Gomez (2012), Energy spectrum, dissipation, and spatial structures in reduced Hall magnetohydrodynamic, *Phys.Plasmas*, *19*(5), 052305, doi:10.1063/1.4717728.

Martin, L. N., G. De Vita, L. Sorriso-Valvo, P. Dmitruk, G. Nigro, L. Primavera, and V. Carbone (2013), Cancellation properties in Hall magnetohydrodynamics with a strong guide magnetic field, *Phys. Rev. E*, *88*(6), 063107, doi:10.1103/PhysRevE.88.063107.

Masters, A., N. Achilleos, M. G. Kivelson, N. Sergis, M. K. Dougherty, M. F. Thomsen, C. S. Arridge, S. M. Krimigis, H. J. McAndrews, S. J. Kanani, N. Krupp, and A. J. Coates (2010), Cassini observations of a Kelvin-Helmholtz vortex in Saturn's outer magnetosphere, *J. Geophys. Res.*, *115*, A07225, doi:10.1029/2010JA015351.

Matsumoto, H., H. Kojima, T. Miyatake, Y. Omura, M. Okada, I. Nagano, and M. Tsutsui (1994), Electrotastic Solitary Waves (ESW) in the magnetotail: BEN wave forms observed by GEOTAIL, *Geophys. Res. Lett.*, *21*, 2915–2918, doi:10.1029/94GL01284.

Matsumoto, Y., and M. Hoshino (2004), Onset of turbulence induced by a Kelvin-Helmholtz vortex, *Geophys. Res. Lett.*, *31*, L02807, doi:10.1029/2003GL018195.

Matsumoto, Y., and K. Seki (2010), Formation of a broad plasma turbulent layer by forward and inverse energy cascades of the Kelvin-Helmholtz instability, *J. Geophys. Res.*, *115*, A10231, doi:10.1029/2009JA014637.

Matthaeus, W. H., and M. L. Goldstein (1982), Measurement of the rugged invariants of magnetohydrodynamic turbulence in the solar wind, *J. Geophys. Res*, *87*, 6011–6028, doi:10.1029/JA087iA08p06011.

Matthaeus, W. H., and S. L. Lamkin (1986), Turbulent magnetic reconnection, *Physics of Fluids*, *29*, 2513–2534, doi:10.1063/1.866004.

Matthaeus, W. H., and D. Montgomery (1980), Selective decay hypothesis at high mechanical and magnetic Reynolds numbers, *Ann. N. Y. Acad. Sci.*, *357*, 203–222, doi:10.1111/j.1749-6632.1980.tb29687.x.

Matthaeus, W. H., and Y. Zhou (1989), Extended inertial range phenomenology of magnetohydrodynamic turbulence, *Phys. Fluids B*, *1*, 1929–1931, doi:10.1063/1.859110.

Matthaeus, W. H., M. L. Goldstein, and D. A. Roberts (1990), Evidence for the presence of quasi-two-dimensional nearly incompressible fluctuations in the solar wind, *J. Geophys. Res.*, *95*, 20,673–20,683, doi:10.1029/JA095iA12p20673.

Matthaeus, W. H., J. W. Bieber, and G. P. Zank (1995), Unquiet on any front: Anisotropic turbulence in the solar wind, *Rev. Geophys. Suppl.*, *33*, 609–614, doi:10.1029/95RG00496.

Matthaeus, W. H., P. Dmitruk, D. Smith, S. Ghosh, and S. Oughton (2003), Impact of Hall effect on energy decay in magnetohydrodynamic turbulence, *Geophys. Res. Lett.*, *30*, 2104, doi:10.1029/2003GL017949.

Matthaeus, W. H., A. Pouquet, P. D. Mininni, P. Dmitruk, and B. Breech (2008), Rapid Alignment of Velocity and Magnetic Field in Magnetohydrodynamic Turbulence, *Phys. Rev. Lett.*, *100*(8), 085,003, doi:10.1103/PhysRevLett.100.085003.

Matthaeus, W. H., M. Wan, S. Servidio, A. Greco, K. T. Osman, S. Oughton, and P. Dmitruk (2015), Intermittency, nonlinear dynamics and dissipation in the solar wind and astrophysical plasmas, *Phil. Trans. R. Soc. A*, *373*, 20140154, doi:10.1098/rsta.2014.0154.

McFadden, J. P., C. W. Carlson, D. Larson, M. Ludlam, R. Abiad, B. Elliott, P. Turin, M. Marckwordt, and V. Angelopoulos (2008a), The THEMIS ESA Plasma Instrument and In-flight Calibration, *Space Sci. Rev.*, *141*, 277–302, doi:10.1007/s11214-008-9440-2.

McFadden, J. P., C. W. Carlson, D. Larson, J. Bonnell, F. Mozer, V. Angelopoulos, K.-H. Glassmeier, and U. Auster (2008b), THEMIS ESA First Science Results and Performance Issues, *Space Sci. Rev.*, *141*, 477–508, doi:10.1007/s11214-008-9433-1.

McKee, C. F., and E. C. Ostriker (2007), Theory of Star Formation, *Ann. Rev. Astron. Astrophys.*, *45*, 565–687, doi:10.1146/annurev.astro.45.051806.110602.

Meneguzzi, M., H. Politano, A. Pouquet, and M. Zolver (1996), A Sparse-Mode Spectral Method for the Simulation of Turbulent Flows, *J. Comp. Phys.*, *123*, 32–44, doi:10.1006/jcph.1996.0003.

Meyrand, R., and S. Galtier (2012), Spontaneous Chiral Symmetry Breaking of Hall Magnetohydrodynamic Turbulence, *Physical Review Letters*, *109*(19), 194501, doi:10.1103/PhysRevLett.109.194501.

Mininni, P., A. Alexakis, and A. Pouquet (2005), Shell-to-shell energy transfer in magnetohydrodynamics. II. Kinematic dynamo, *Phys. Rev. E*, *72*(4), 046,302, doi:10.1103/PhysRevE.72.046302.

Mininni, P. D., and A. Pouquet (2007), Energy Spectra Stemming from Interactions of Alfvén Waves and Turbulent Eddies, *Phys. Rev. Lett.*, *99*(25), 254502, doi:10.1103/PhysRevLett.99.254502.

Mininni, P. D., and A. Pouquet (2009), Finite dissipation and intermittency in magnetohydrodynamics, *Phys. Rev. E*, *80*(2), 025401, doi:10.1103/PhysRevE.80.025401.

Mininni, P. D., A. Alexakis, and A. Pouquet (2007), Energy transfer in Hall-MHD turbulence: cascades, backscatter, and dynamo action, *J. Plasma Phys.*, *73*, 377–401, doi:10.1017/S0022377806004624.

Mininni, P. D., D. Rosenberg, R. Reddy, and A. Pouquet (2011), A hybrid MPI-OpenMP scheme for scalable parallel pseudospectral computations for fluid turbulence, *Parallel Comput.*, *37*, 316–326, doi:10.1016/j.parco.2011.05.004.

Mininni, P. D., A. G. Pouquet, and D. C. Montgomery (2006a), Small-Scale Structures in Three-Dimensional Magnetohydrodynamic Turbulence, *Physical Review Letters*, *97*(24), 244503, doi:10.1103/PhysRevLett.97.244503.

Miura, A., and P. L. Pritchett (1982), Nonlocal stability analysis of the MHD Kelvin-Helmholtz instability in a compressible plasma, *J. Geophys. Res.*, *87*, 7431–7444, doi:10.1029/JA087iA09p07431.

Miura, H., and K. Araki (2011), Local structures of homogeneous Hall MHD turbulence, *J. Phys. Conf. Ser.*, *318*(7), 072032, doi:10.1088/1742-6596/318/7/072032.

Miura, H., and D. Hori (2009), Hall effects on local structures in decaying MHD turbulence, *J. Plasma Fusion Res. SERIES*, *8*, 73–76.

Moffett, H. K. (1969), The degree of knottedness of tangled vortex lines, *J. Fluid Mech.*, *35*(1), 117–129, doi:10.1017/S0022112069000991.

Mozer, F. S., S. D. Bale, and T. D. Phan (2002), Evidence of Diffusion Regions at a Subsolar Magnetopause Crossing, *Phys. Rev. Lett.*, *89*(1), 015002, doi:10.1103/PhysRevLett.89.015002.

Nakamura, T. K. M., and W. Daughton (2014), Turbulent plasma transport across the Earth's low-latitude boundary layer, *Geophys. Res. Lett.*, *41*, 8704–8712, doi:10.1002/2014GL061952.

Nakamura, T. K. M., and M. Fujimoto (2005), Magnetic reconnection within rolled-up MHD-scale Kelvin-Helmholtz vortices: Two-fluid simulations including finite electron inertial effects, *Geophys. Res. Lett.*, *32*, L21102, doi:10.1029/2005GL023362.

Nakamura, T. K. M., W. Daughton, H. Karimabadi, and S. Eriksson (2013), Three-dimensional dynamics of vortex-induced reconnection and comparison with THEMIS observations, *J. Geophys. Res.*, *118*, 5742, doi:10.1002/jgra.50547.

Nazarenko, S. (2011), *Lecture Notes in Physics 825: Wave Turbulence*, Springer-Verlag, Berlin.

Nelson, N. J., B. P. Brown, A. S. Brun, M. S. Miesch, and J. Toomre (2013), Magnetic Wreaths and Cycles in Convective Dynamos, *Astrophys. J.*, *762*, 73, doi:10.1088/0004-637X/762/2/73.

Newman, D. L., M. V. Goldman, R. E. Ergun, and A. Mangeney (2001), Formation of Double Layers and Electron Holes in a Current-Driven Space Plasma, *Phys. Rev. Lett.*, *87*(25), 255001, doi:10.1103/PhysRevLett.87.255001.

Nishimura, Y., J. Wygant, T. Ono, M. Iizima, A. Kumamoto, D. Brautigam, and F. Rich (2008), Large-amplitude wave electric field in the inner magnetosphere during substorms, *J. Geophys. Res.*, *113*, A07202, doi:10.1029/2007JA012833.

Nykyri, K., and A. Otto (2001), Plasma transport at the magnetospheric boundary due to reconnection in Kelvin-Helmholtz vortices, *Geophys. Res. Lett.*, *28*, 3565–3568, doi:10.1029/2001GL013239.

Omura, Y., H. Matsumoto, T. Miyake, and H. Kojima (1996), Electron beam instabilities as generation mechanism of electrostatic solitary waves in the magnetotail, *J. Geophys. Res.*, *101*, 2685–2698, doi:10.1029/95JA03145.

Orszag, S. A. (1971), On the Elimination of Aliasing in Finite-Difference Schemes by Filtering High-Wavenumber Components., *J. Atmos. Sci.*, *28*, 1074, doi:10.1175/1520-0469(1971)028⟨1074:OTEOAI⟩2.0.CO;2.

Osman, K. T., M. Wan, W. H. Matthaeus, B. Breech, and S. Oughton (2011), Directional Alignment and Non-Gaussian Statistics in Solar Wind Turbulence, *Astrophys. J.*, *741*, 75, doi:10.1088/0004-637X/741/2/75.

Osman, K. T., W. H. Matthaeus, M. Wan, and A. F. Rappazzo (2012), Intermittency and Local Heating in the Solar Wind, *Phys. Rev. Lett.*, *108*(26), 261102, doi:10.1103/PhysRevLett.108.261102.

Osman, K. T., W. H. Matthaeus, K. H. Kiyani, B. Hnat, and S. C. Chapman (2013), Proton Kinetic Effects and Turbulent Energy Cascade Rate in the Solar Wind, *Phys. Rev. Lett.*, *111*(20), 201101, doi:10.1103/PhysRevLett.111.201101.

Osman, K. T., W. H. Matthaeus, J. T. Gosling, A. Greco, S. Servidio, B. Hnat, S. C. Chapman, and T. D. Phan (2014), Magnetic Reconnection and Intermittent Turbulence in the Solar Wind, *Phys. Rev. Lett.*, *112*(21), 215002, doi:10.1103/PhysRevLett.112.215002.

Oughton, S., P. Dmitruk, and W. H. Matthaeus (2004), Reduced magnetohydrodynamics and parallel spectral transfer, *Phys. Plasmas*, *11*, 2214–2225, doi:10.1063/1.1705652.

Panov, E. V., R. Nakamura, W. Baumjohann, V. Angelopoulos, A. A. Petrukovich, A. Retinò, M. Volwerk, T. Takada, K.-H. Glassmeier, J. P. McFadden, and D. Larson (2010), Multiple overshoot and rebound of a bursty bulk flow, *Geophys. Res. Lett.*, *37*, L08103, doi:10.1029/2009GL041971.

Panov, E. V., M. V. Kubyshkina, R. Nakamura, W. Baumjohann, V. Angelopoulos, V. A. Sergeev, and A. A. Petrukovich (2013), Oscillatory flow braking in the magnetotail: THEMIS statistics, *Geophys. Res. Lett.*, *40*, 2505–2510, doi:10.1002/grl.50407.

Parashar, T. N., S. Servidio, M. A. Shay, W. H. Matthaeus, and P. A. Cassak (2010), Orszag Tang vortex-Kinetic study of a turbulent plasma, *Twelfth International Solar Wind Conference*, *1216*, 304–307, doi:10.1063/1.3395861.

Parashar, T. N., W. H. Matthaeus, M. A. Shay, and M. Wan (2015), Transition from Kinetic to MHD Behavior in a Collisionless Plasma, *Astrophys. J.*, *811*, 112, doi:10.1088/0004-637X/811/2/112.

Paterson, W. R., and L. A. Frank (1994), Survey of plasma parameters in Earth's distant magnetotail with the Geotail spacecraft, *Geophys. Res. Lett.*, *21*, 2971–2974, doi:10.1029/94GL02105.

Patterson, G. S., Jr., and S. A. Orszag (1971), Spectral Calculations of Isotropic Turbulence: Efficient Removal of Aliasing Interactions, *Phys. Fluids*, *14*, 2538–2541, doi:10.1063/1.1693365.

Podvigina, O., and A. Pouquet (1994), On the non-linear stability of the 1:1:1 ABC flow, *Physica D*, *75*, 471–508, doi:10.1016/0167-2789(94)00031-X.

Politano, H., and A. Pouquet (1995), Model of intermittency in magnetohydrodynamic turbulence, *Phys. Rev. E*, *52*, 636–641, doi:10.1103/PhysRevE.52.636.

Politano, H., A. Pouquet, and P. L. Sulem (1995), Current and vorticity dynamics in three-dimensional magnetohydrodynamic turbulence, *Phys. Plasmas*, *2*, 2931–2939, doi:10.1063/1.871473.

Pollock, C., T. Moore, A. Jacques, J. Burch, U. Gliese, Y. Saito, T. Omoto, L. Avanov, A. Barrie, V. Coffey, J. Dorelli, D. Gershman, B. Giles, T. Rosnack, C. Salo, S. Yokota, M. Adrian, C. Aoustin, C. Auletti, S. Aung, V. Bigio, N. Cao, M. Chandler, D. Chornay, K.Christian, G. Clark, G. Collinson, T. Corris, A. D. L. Santos, R. Devlin, T. Diaz, T. Dickerson, C. Dickson, A. Diekmann, F. Diggs, C. Duncan, A. Figueroa-Vinas, C. Firman, M. Freeman, N. Galassi, K. Garcia, G. Goodhart, D. Guererro, J. Hageman, J. Hanley, E. Hemminger, M. Holland, M. Hutchins, T. James, W. Jones, S. Kreisler, J. Kujawski, V. Lavu, J. Lobell, E. LeCompte, A. Lukemire, E. MacDonald, A. Mariano, T. Mukai, K. Narayanan, Q. Nguyan, M. Onizuka, W. Paterson, S. Persyn, B. Piepgrass, F. Qian, A. Rager, T. Raghuram, A. Ramil, L. Reichenthal, H. Rodriguez, J. Rouzaud, A. Rucker, Y. Saito, M. Samara, J.-A. Sauvaud, D. Schuster, M. Shappirio, K. Shelton, D. Sher, D. Smith, K. Smith, S. Smith, D. Steinfeld, R. Szymkiewicz, K. Tanimoto, J. Taylor, C. Tucker, K. Tull, A. Uhl, J. Vlolet, P. Walpole, S. Weidner, D. White, G. Winkert, P.-S. Yeh, and M. Zeuch (2016), Fast Plasma Investigation for Magnetospheric Multiscale, *Space Sci. Rev.*, *online first*, doi:10.1007/s11214-016-0245-4.

Pope, S. B. (2000), *Turbulent Flows*, Cambridge University Press, New York.

Pouquet, A. (1993), Magnetohydrodynamic turbulence., in *Astrophysical Fluid Dynamics - Les Houches 1987*, edited by J.-P. Zahn and J. Zinn-Justin, pp. 139–227.

Pouquet, A., U. Frisch, and J. Leorat (1976), Strong MHD helical turbulence and the nonlinear dynamo effect, *J. Fluid Mech.*, *77*, 321–354, doi:10.1017/S0022112076002140.

Pouquet, A., E. Lee, M. E. Brachet, P. D. Mininni, and D. Rosenberg (2010), The dynamics of unforced turbulence at high Reynolds number for Taylor-Green vortices generalized to MHD, *Geophys. Astrophys. Fluid Dyn.*, *104*, 115–134, doi:10.1080/03091920903304080.

Pouquet, A., M.-E. Brachet, E. Lee, P. D. Mininni, D. Rosenberg, and V. Uritsky (2010), Lack of Universality in MHD Turbulence, and the Possible Emergence of a New Paradigm?, in *Astrophysical Dynamics: From Stars to Galaxies, IAU Symposium*, vol. 271, edited by N. H. Brummell, A. S. Brun, and M. Miesch, pp. 304–316, doi:10.1017/S174392131101773X.

Pu, Z. Y., M. Yei, and Z. X. Liu (1990), Generation of vortex-induced tearing mode instability at the magnetopause, *J. Geophys. Res.*, *95*, 10,559–10,566, doi:10.1029/JA095iA07p10559.

Rast, M. P., and J.-F. Pinton (2009), Point-vortex model for Lagrangian intermittency in turbulence, *Phys. Rev. E*, *79*(4), 046314, doi:10.1103/PhysRevE.79.046314.

Reynolds, O. (1883), An Experimental Investigation of the Circumstances Which Determine Whether the Motion of Water Shall Be Direct or Sinuous, and of the Law of Resistance in Parallel Channels, *Phil.Trans. R. Soc.*, *174*, 935–982.

Richardson, L. F. (1926), Atmospheric Diffusion Shown on a Distance-Neighbour Graph, *Proc. R. Soc. A*, *110*, 709–737, doi:10.1098/rspa.1926.0043.

Riley, J. J., and M.-P. Lelong (2000), Fluid Motions in the Presence of Strong Stable Stratification, *Ann. Rev. Fluid Mech.*, *32*, 613–657, doi:10.1146/annurev.fluid.32.1.613.

Roberts, M., and J. C. Bowman (2011), Dealiased convolutions for pseudospectral simulations, *J. Phys. Conf. Ser.*, *318*(7), 072037, doi:10.1088/1742-6596/318/7/072037.

Rodriguez Imazio, P., L. N. Martin, P. Dmitruk, and P. D. Mininni (2013), Intermittency in Hall-magnetohydrodynamics with a strong guide field, *Phys. Plasmas*, *20*(5), 052506, doi:10.1063/1.4807378.

Roux, A., O. Le Contel, C. Coillot, A. Bouabdellah, B. de La Porte, D. Alison, S. Ruocco, and M. C. Vassal (2008), The Search Coil Magnetometer for THEMIS, *Space Sci. Rev.*, *141*, 265–275, doi:10.1007/s11214-008-9455-8.

Russell, C. T., B. J. Anderson, W. Baumjohann, K. R. Bromund, D. Dearborn, D. Fischer, G. Le, H. K. Leinweber, D. Leneman, W. Magnes, J. D. Means, M. B. Moldwin, R. Nakamura, D. Pierce, F. Plaschke, K. M. Rowe, J. A. Slavin, R. J. Strangeway, R. Torbert, C. Hagen, I. Jernej, A. Valavanoglou, and I. Richter (2014), The Magnetospheric Multiscale Magnetometers, *Space Sci. Rev.*, *online first*, doi:10.1007/s11214-014-0057-3.

Sahraoui, F., S. Galtier, and G. Belmont (2006), On waves in incompressible hall magnetohydrodynamics, *J. Plasma Phys.*, *73*(5), 723–730, doi:10.1017/S0022377806006180.

Sahraoui, F., M. L. Goldstein, P. Robert, and Y. V. Khotyaintsev (2009), Evidence of a Cascade and Dissipation of Solar-Wind Turbulence at the Electron Gyroscale, *Phys. Rev. Lett.*, *102*(23), 231102, doi:10.1103/PhysRevLett.102.231102.

Sahraoui, F., M. L. Goldstein, G. Belmont, P. Canu, and L. Rezeau (2010), Three Dimensional Anisotropic k Spectra of Turbulence at Subproton Scales in the Solar Wind, *Phys. Rev. Lett.*, *105*(13), 131101, doi:10.1103/PhysRevLett.105.131101.

Saur, J., H. Politano, A. Pouquet, and W. H. Matthaeus (2002), Evidence for weak MHD turbulence in the middle magnetosphere of Jupiter, *Astron. Astrophys.*, *386*, 699–708, doi:10.1051/0004-6361:20020305.

Saur, J., A. Pouquet, and W. H. Matthaeus (2003), An acceleration mechanism for the generation of the main auroral oval on Jupiter, *Geophys. Res. Lett.*, *30*, 1260, doi:10.1029/2002GL015761.

Servidio, S., W. H. Matthaeus, and P. Dmitruk (2008), Depression of Nonlinearity in Decaying Isotropic MHD Turbulence, *Phys. Rev. Lett.*, *100*(9), 095005, doi:10.1103/PhysRevLett.100.095005.

Servidio, S., W. H. Matthaeus, and V. Carbone (2008b), Statistical properties of ideal three-dimensional Hall magnetohydrodynamics: The spectral structure of the equilibrium ensemble, *Phys. Plasmas*, *15*(4), 042314, doi:10.1063/1.2907789.

Servidio, S., W. H. Matthaeus, M. A. Shay, P. Dmitruk, P. A. Cassak, and M. Wan (2010), Statistics of magnetic reconnection in two-dimensional magnetohydrodynamic turbulence, *Phys. Plasmas*, *17*(3), 032,315, doi:10.1063/1.3368798.

Servidio, S., P. Dmitruk, A. Greco, M. Wan, S. Donato, P. A. Cassak, M. A. Shay, V. Carbone, and W. H. Matthaeus (2011), Magnetic reconnection as an element of turbulence, *Nonlin. Proc. Geophys.*, *18*, 675–695, doi:10.5194/npg-18-675-2011.

Shaikh, D., and P. K. Shukla (2009), Spectral properties of electromagnetic turbulence in plasmas, *Nonlinear Processes in Geophysics*, *16*, 189–196, doi:10.5194/npg-16-189-2009.

Shay, M. A., and J. F. Drake (1998), The role of electron dissipation on the rate of collisionless magnetic reconnection, *Geophys. Res. Lett.*, *25*, 3759–3762, doi:10.1029/1998GL900036.

Shiokawa, K., W. Baumjohann, and G. Haerendel (1997), Braking of high-speed flows in the near-Earth tail, *Geophys. Rev. Lett.*, *24*(10), 1179–1182, doi:10.1029/97GL01062.

Shiokawa, K., I. Shinohara, T. Mukai, H. Hayakawa, and C. Z. Cheng (2005), Magnetic field fluctuations during substorm-associated dipolarizations in the nightside plasma sheet around X= -10 R_E, *J. Geophys. Res.*, *110*, A05212, doi:10:1029/2004JA010378.

Simon, J. B., G. Lesur, M. W. Kunz, and P. J. Armitage (2015), Magnetically driven accretion in protoplanetary discs, *Mon. Not. R. Astron. Soc.*, *454*, 1117–1131, doi:10.1093/mnras/stv2070.

Sorriso-Valvo, L., V. Carbone, P. Veltri, G. Consolini, and R. Bruno (1999), Intermittency in the solar wind turbulence through probability distribution functions of fluctuations, *Geophys. Res. Lett.*, *26*, 1801–1804, doi:10.1029/1999GL900270.

Sorriso-Valvo, L., V. Carbone, P. Veltri, H. Politano, and A. Pouquet (2000), Non-Gaussian probability distribution functions in two-dimensional magnetohydrodynamic turbulence, *Europhys. Lett.*, *51*, 520–526, doi:10.1209/epl/i2000-00369-6.

Sorriso-Valvo, L., R. Marino, V. Carbone, A. Noullez, F. Lepreti, P. Veltri, R. Bruno, B. Bavassano, and E. Pietropaolo (2007), Observation of Inertial Energy Cascade in Interplanetary Space Plasma, *Phys. Rev. Lett.*, *99*(11), 115,001, doi:10.1103/PhysRevLett.99.115001.

Sreenivasan, K. R. (1995), On the universality of the Kolmogorov constant, *Phys. Fluids*, *7*, 2778–2784, doi:10.1063/1.868656.

Staquet, C., and J. Sommeria (2002), Internal gravity waves: from instabilities to turbulence, *Ann. Rev. Fluid Mech.*, *34*, 559–593, doi:10.1146/annurev.fluid.34.090601.130953.

Stawarz, J. E., and A. Pouquet (2015), Small-scale behavior of Hall magnetohydrodynamic turbulence, *Phys. Rev. E*, *92*(6), 063102, doi:10.1103/PhysRevE.92.063102.

Stawarz, J. E., C. W. Smith, B. J. Vasquez, M. A. Forman, and B. T. MacBride (2009), The Turbulent Cascade and Proton Heating in the Solar Wind at 1 AU, *Astrophys. J.*, *697*, 1119–1127, doi:10.1088/0004-637X/697/2/1119.

Stawarz, J. E., C. W. Smith, B. J. Vasquez, M. A. Forman, and B. T. MacBride (2010), The Turbulent Cascade for High Cross-Helicity States at 1 AU, *Astrophys. J.*, *713*, 920–934, doi:10.1088/0004-637X/713/2/920.

Stawarz, J. E., B. J. Vasquez, C. W. Smith, M. A. Forman, and J. Klewicki (2011), Third Moments and the Role of Anisotropy from Velocity Shear in the Solar Wind, *Astrophys. J.*, *736*, 44, doi:10.1088/0004-637X/736/1/44.

Stawarz, J. E., A. Pouquet, and M.-E. Brachet (2012), Long-time properties of magnetohydrodynamic turbulence and the role of symmetries, *Phys. Rev. E*, *86*(3), 036307, doi:10.1103/PhysRevE.86.036307.

Stawarz, J. E., R. E. Ergun, and K. A. Goodrich (2015), Generation of high-frequency electric field activity by turbulence in the Earth's magnetotail, *J. Geophys. Res.*, *120*, 1845–1866, doi:10.1002/2014JA020166.

Stawarz, J. E., S. Eriksson, F. D. Wilder, R. E. Ergun, S. J. Schwartz, A. Pouquet, J. L. Burch, B. L. Giles, Y. Khotyaintsev, O. Le Contel, P.-A. Lindqvist, W. Magnes, C. J. Pollock, C. T. Russell, R. J. Strangeway, R. B. Torbert, L. A. Avanov, J. C. Dorelli, D. J. Gershman, K. A. Goodrich, D. M. Malaspina, G. T. Marklund, L. Mirioni, and A. P. Sturner (2016), Observations of Turbulence in a Kelvin-Helmholtz Event on September 8, 2015 by the Magnetospheric Multiscale Mission, *Geophys. Res. Lett.*, *submitted*.

Stix, T. H. (1992), *Waves in Plasmas*, Springer-Verlag, New York.

Streltsov, A., and W. Lotko (1995), Dispersive field line resonances on auroral field lines, *J. Geophys. Res.*, *100*, 19,457–19,472, doi:10.1029/95JA01553.

Stribling, T., and W. H. Matthaeus (1990), Statistical properties of ideal three-dimensional magnetohydrodynamics, *Phys. Fluids*, *2*, 1979–1988, doi:10.1063/1.859419.

Stribling, T., and W. H. Matthaeus (1991), Relaxation processes in a low-order three-dimensional magnetohydrodynamics model, *Physics of Fluids B*, *3*, 1848–1864, doi:10.1063/1.859654.

Stringer, T. E. (1963), Low-frequency waves in an unbounded plasma, *J. Nucl. Energy*, *5*, 89–107, doi:10.1088/0368-3281/5/2/304.

Sun, J., C. J. Nappo, L. Mahrt, D. Belušić, B. Grisogono, D. R. Stauffer, M. Pulido, C. Staquet, Q. Jiang, A. Pouquet, C. Yagüe, B. Galperin, R. B. Smith, J. J. Finnigan, S. D. Mayor, G. Svensson, A. A. Grachev, and W. D. Neff (2015), Review of wave-turbulence interactions in the stable atmospheric boundary layer, *Rev. Geophys.*, *53*, 956–993, doi:10.1002/2015RG000487.

Swift, D. W., and Y. Lin (2001), Substorm onset viewed by a two-dimensional, global-scale hybrid code, *J. Atmos. Sol.-Terr. Phys.*, *63*, 683–704, doi:10.1016/S1364-6826(00)00188-7.

Taylor, G. I. (1938), The Spectrum of Turbulence, *Proc. R. Soc. A*, *164*, 476–490, doi:10.1098/rspa.1938.0032.

Taylor, J. B. (1986), Relaxation and magnetic reconnection in plasmas, *Rev. Mod. Phys.*, *58*, 741–763, doi:10.1103/RevModPhys.58.741.

TenBarge, J. M., and G. G. Howes (2013), Current Sheets and Collisionless Damping in Kinetic Plasma Turbulence, *Astrophys. J. Lett.*, *771*, L27, doi:10.1088/2041-8205/771/2/L27.

Torbert, R. B., C. T. Russell, W. Magnes, R. E. Ergun, P.-A. Lindqvist, O. LeContel, H. Vaith, J. Macri, S. Myers, D. Rau, J. Needell, B. King, M. Granoff, M. Chutter, I. Dors, G. Olsson, Y. V. Khotyaintsev, A. Eriksson, C. A. Kletzing, S. Bounds, B. Anderson, W. Baumjohann, M. Steller, K. Bromund, G. Le, R. Nakamura, R. J. Strangeway, H. K. Leinweber, S. Tucker, J. Westfall, D. Fischer, F. Plaschke, J. Porter, and K. Lappalainen (2014), The FIELDS Instrument Suite on MMS: Scientific Objectives, Measurements, and Data Products, *Space Sci. Rev.*, *online first*, doi:10.1007/s11214-014-0109-8.

Tsurutani, B. T., and E. J. Smith (1979), Interplanetary discontinuities: Temporal variations and the radial gradient from 1 to 8.5 AU, *J. Geophys. Res.*, *84*, 2773–2787, doi:10.1029/JA084iA06p02773.

Tu, C.-Y., and E. Marsch (1995), MHD structures, waves and turbulence in the solar wind: Observations and theories, *Space Sci. Rev.*, *73*, 1–210, doi:10.1007/BF00748891.

Turner, L. (1986), Hall effects on magnetic relaxation, *IEEE Trans. Plasma Sci.*, *14*, 849–857, doi:10.1109/TPS.1986.4316633.

Uritsky, V. M., A. Pouquet, D. Rosenberg, P. D. Mininni, and E. F. Donovan (2010), Structures in magnetohydrodynamic turbulence: Detection and scaling, *Phys. Rev. E*, *82*(5), 056326, doi:10.1103/PhysRevE.82.056326.

Uzdensky, D. A., and S. Rightley (2014), Plasma physics of extreme astrophysical environments, *Rep. Prog. Phys.*, *77*(3), 036902, doi:10.1088/0034-4885/77/3/036902.

Voitenko, Y., and J. de Keyser (2011), Turbulent spectra and spectral kinks in the transition range from MHD to kinetic Alfvén turbulence, *Nonlin. Proc. Geophys.*, *18*, 587–597, doi:10.5194/npg-18-587-2011.

Voitenko, Y. M. (1998), Three-wave coupling and weak turbulence of kinetic Alfvén waves, *J. Plasma Phys.*, *60*, 515–527, doi:10.1017/S0022377898007107.

Volwerk, M., K.-H. Glassmeier, R. Nakamura, T. Takada, W. Baumjohann, B. Klecker, H. Rème, T. L. Zhang, E. Lucek, and C. M. Carr (2007), Flow burst-induced Kelvin-Helmholtz waves in the terrestrial magnetotail, *Geophys. Res. Lett.*, *34*, L10102, doi:10.1029/2007GL029459.

Vörös, Z., W. Baumjohann, R. Nakamura, M. Volwerk, A. Runov, T. L. Zhang, H. U. Eichelberger, R. Treumann, E. Georgescu, A. Balogh, B. Klecker, and H. RéMe (2004), Magnetic turbulence in the plasma sheet, *J. Geophys. Res.*, *109*(A18), A11215, doi:10.1029/2004JA010404.

Vörös, Z., W. Baumjohann, R. Nakamura, A. Runov, M. Volwerk, Y. Asano, D. Jankovičová, E. A. Lucek, and H. Rème (2007), Spectral scaling in the turbulent Earth's plasma sheet revisited, *Nonlin. Proc. Geophys.*, *14*, 535–541, doi:10.5194/npg-14-535-2007.

Wan, M., S. Servidio, S. Oughton, and W. H. Matthaeus (2009), The third-order law for increments in magnetohydrodynamic turbulence with constant shear, *Phys. Plasmas*, *16*(9), 090703, doi: 10.1063/1.3240333.

Wan, M., S. Servidio, S. Oughton, and W. H. Matthaeus (2010), The third-order law for magnetohydrodynamic turbulence with shear: Numerical investigation, *Phys. Plasmas*, *17*(5), 052307, doi:10.1063/1.3398481.

Wan, M., W. H. Matthaeus, H. Karimabadi, V. Roytershteyn, M. Shay, P. Wu, W. Daughton, B. Loring, and S. C. Chapman (2012), Intermittent Dissipation at Kinetic Scales in Collisionless Plasma Turbulence, *Phys. Rev. Lett.*, *109*(19), 195001, doi:10.1103/PhysRevLett.109.195001.

Wareing, C. J., and R. Hollerbach (2010), Cascades in decaying three-dimensional electron magnetohydrodynamic turbulence, *J. Plasma Phys.*, *76*, 117–128, doi:10.1017/S0022377809990158.

Weygand, J. M., M. G. Kivelson, K. K. Khurana, H. K. Schwarzl, S. M. Thompson, R. L. McPherron, A. Balogh, L. M. Kistler, M. L. Goldstein, J. Borovsky, and D. A. Roberts (2005), Plasma sheet turbulence observed by Cluster II, *J. Geophys. Res.*, *110*, A01205, doi: 10.1029/2004JA010581.

Weygand, J. M., W. H. Matthaeus, S. Dasso, M. G. Kivelson, L. M. Kistler, and C. Mouikis (2009), Anisotropy of the Taylor scale and the correlation scale in plasma sheet and solar wind magnetic field fluctuations, *J. Geophys. Res.*, *114*, A07213, doi:10.1029/2008JA013766.

Wilder, F., J. E. Stawarz, S. J. Schwartz, S. Eriksson, R. E. Ergun, D. M. Malaspina, K. A. Goodrich, J. L. Burch, R. B. Torbert, P.-A. Lindqvist, O. Le Contel, Y. Khotyaintsev, R. J. Strangeway, C. T. Russell, C. J. Pollock, B. L. Giles, A. P. Sturner, and J. H. Holmes (2016), Observations of Ion Acoustic Waves Associated With the Kelvin-Helmholtz Instability by the Magnetospheric Multiscale Mission, *Geophys. Res. Lett.*, *submitted*.

Woltjer, L. (1958a), A Theorem on Force-Free Magnetic Fields, *Proc. Nat. Acad. Sci.*, *44*, 489–491, doi:10.1073/pnas.44.6.489.

Woltjer, L. (1958b), On Hydromagnetic Equilibrium, *Proc. Nat. Acad. Sci.*, *44*, 833–841, doi: 10.1073/pnas.44.9.833.

Wu, P., M. Wan, W. H. Matthaeus, M. A. Shay, and M. Swisdak (2013), von Kármán Energy Decay and Heating of Protons and Electrons in a Kinetic Turbulent Plasma, *Phys. Rev. Lett.*, *111*(12), 121105, doi:10.1103/PhysRevLett.111.121105.

Wygant, J. R., A. Keiling, C. A. Cattell, M. Johnson, R. L. Lysak, M. Temerin, F. S. Mozer, C. A. Kletzing, J. D. Scudder, W. Peterson, C. T. Russell, G. Parks, M. Brittnacher, G. Germany, and J. Spann (2000), Polar spacecraft based comparisons of intense electric fields and Poynting flux near and within the plasma sheet-tail lobe boundary to UVI images: An energy source for the aurora, *J. Geophys. Res.*, *105*, 18, doi:10.1029/1999JA900500.

Wygant, J. R., A. Keiling, C. A. Cattell, R. L. Lysak, M. Temerin, F. S. Mozer, C. A. Kletzing, J. D. Scudder, V. Streltsov, W. Lotko, and C. T. Russell (2002), Evidence for kinetic Alfvén waves and parallel electron energization at 4-6 R_E altitudes in the plasma sheet boundary layer, *J. Geophys. Res.*, *107*, 1201, doi:10.1029/2001JA900113.

Yamada, M., Y. Ren, H. Ji, J. Breslau, S. Gerhardt, R. Kulsrud, and A. Kuritsyn (2006), Experimental study of two-fluid effects on magnetic reconnection in a laboratory plasma with variable collisionality, *Phys. Plasmas*, *13*(5), 052119, doi:10.1063/1.2203950.

Yoshimatsu, K., K. Schneider, N. Okamoto, Y. Kawahara, and M. Farge (2011), Intermittency and geometrical statistics of three-dimensional homogeneous magnetohydrodynamic turbulence: A wavelet viewpoint, *Phys. Plasmas*, *18*(9), 092304, doi:10.1063/1.3628637.

Zeldovich, Y. B., and A. A. Ruzmaĭkin (1987), REVIEWS OF TOPICAL PROBLEMS: The hydromagnetic dynamo as the source of planetary, solar, and galactic magnetism, *Sov. Phys. Uspekhi*, *30*, 494–506, doi:10.1070/PU1987v030n06ABEH002852.

Zelenyi, L., A. Artemyev, and A. Petrukovich (2014), Properties of Magnetic Field Fluctuations in the Earth's Magnetotail and Implications for the General Problem of Structure Formation in Hot Plasmas, *Space Sci. Rev.*, *online first*, doi:10.1007/s11214-014-0037-7.

Appendix A

Numerical Methods

A.1 The Pseudospectral Method

The Geophysical High Order Suite for Turbulence (GHOST) code is a pseudospectral code that has been parallelized up to in excess of 130000 processors using a hybrid (MPI-OpenMP) methodology [*Mininni et al.*, 2011]. For the computations performed in Chapters 3 and 4, an explicit, second-order Runge-Kutta time-stepping scheme is used to advance **b** and **u** (described by Eq. 2.7 and 2.8) discretely in time. Since the temporal integration scheme is explicit, the time step must be set to be smaller than any of the dynamical timescales in the equations. Typically the nonlinear timescale is the limiting timescale in the problem and, therefore, the necessary time step will follow the scalings for the nonlinear timescales discussed in Chapter 2.3.1.

The pseudospectral method is a numerical technique for computing the spatial derivatives and nonlinear terms that contribute to the time derivatives and feed into the time-stepping scheme through the right-hand-sides of Eq. 2.7 and 2.8. The basic premise of spectral methods is to re-express the spatial domain using a spectral decomposition. The exact type of decomposition depends on the boundary conditions of the computational domain. For periodic boundary conditions, as used by GHOST, the appropriate decomposition is the Fourier transform, which expresses the domain as a series of sine and cosine functions. The advantage of performing this decomposition is that spatial derivatives become multiplications with **k**, which can be straightforwardly and accurately computed. However, the nonlinear terms become convolutions in Fourier space instead of multiplications. Therefore, in the pseudospectral method, the domain is transformed into Fourier

space to perform derivatives and then transformed back into real space to compute the nonlinear terms. See, for example, *Patterson and Orszag* [1971], *Gottlieb and Orszag* [1977], and *Gómez et al.* [2005], for further discussion of this method as applied to fluid equations.

In order to obtain a numerical solution, it is necessary to express the domain on a discrete, finite-sized grid, the consequence of which is to discretize the available wavevectors and truncate the Fourier transform at a maximum wavenumber. GHOST uses a 3D cubic domain with N^3 grid points and sides of length 2π. In 1D, the discrete Fourier transform of a function $g(x_n)$ defined at discrete positions x_n can be expressed as

$$g(x_n) = \frac{1}{N} \sum_{l=-N/2+1}^{N/2} g(k_l) e^{i x_n k_l} \tag{A.1}$$

$$g(k_l) = \sum_{n=0}^{N-1} g(x_n) e^{-i x_n k_l}. \tag{A.2}$$

The discrete Fourier transform is straight-forwardly generalized to 3D by applying the 1D transformation to each dimension. For a domain of length 2π, $x_n = 2\pi n/N$, $k_l = l$, and $g(k_l) = g^*(-k_l)$ for real signals in configuration space (with $*$ denoting the complex conjugate).

The truncation of the Fourier transform combined with periodicity results in an issue known as aliasing. The issue arises because on the discrete grid $e^{i x_n k_l}$ is indistinguishable from $e^{i x_n (k_l + mN)}$ where m is an integer. Based on the discrete convolution of two functions $g(k_l)$ and $h(k_l)$, nonlinear terms will have Fourier transforms of the form

$$[g(x_n)h(x_n)]_{k_\alpha} = \sum_{k_\alpha = k_\beta + k_\gamma} g(k_\beta) h(k_\gamma). \tag{A.3}$$

Therefore, nonlinear terms can give rise to wavenumbers larger than the maximum wavenumber on the discrete grid, which will be aliased onto the wavenumber $k_{\alpha'} = k_\alpha - N$. One remedy to this issue is to further truncate the Fourier transform to a new maximum wavenumber ($k_{max'}$) using the so-called 2/3-rule, where $k_{max'} = (2/3)(N/2)$ [*Orszag*, 1971]. The factor of 2/3 comes from considering, which value of $k_{max'}$ will result in no sum of two wavenumbers in the range $-k_{max'}$ to $k_{max'}$ exceeding $N/2$ (or being less than $-N/2$). While the 2/3-rule is the method used by GHOST to deal with aliasing, other dealiasing methods are also available [e.g. *Roberts and Bowman*, 2011].

A.2 Numerically Solving the Linear Maxwell-Vlasov Equations

In Chapter 5.2, solutions to the linear Maxwell-Vlasov equations are found numerically in order to explore the behavior of kinetic Alfvén waves in the BBF braking region. The numerical solution requires finding the combinations of $k_{\parallel}$, $k_{\perp}$, and ω that make $D(\mathbf{k},\omega) = 0$ (where $D(\mathbf{k},\omega)$ is the determinant of the matrix defined by Eq. 2.46 and Eq. 2.48–2.53) for a given set of the plasma parameters B_0, n_{0s}, and T_{0s}. The contribution of the terms in the infinite sums in Eq. 2.48–2.53 decrease as $|l|$ increases and so the sums can be truncated once the value of a given term decreases below a specified level.

An additional assumption that simplifies the numerical computation of the dispersion relation is to assume that ω_i is much smaller than ω_r. Defining $D_r(\mathbf{k},\omega)$ and $D_i(\mathbf{k},\omega)$ as the real and imaginary parts of $D(\mathbf{k},\omega)$ such that $D(\mathbf{k},\omega) = D_r(\mathbf{k},\omega) + iD_i(\mathbf{k},\omega)$ and Taylor expanding for small ω_i results in the equations [*Gurnett and Bhattacharjee*, 2005]

$$D_r(\mathbf{k},\omega_r) = 0 \tag{A.4}$$

$$\omega_i = \frac{-D_i(\mathbf{k},\omega_r)}{\partial D_r(\mathbf{k},\omega_r)/\partial\omega} \tag{A.5}$$

and so ω_r can be computed independent of the value of ω_i.

Once a solution is found, the associated eigenvector can be determined based on the values of the dielectric tensor and index of refraction using the relations

$$\frac{E_{1y}}{E_{1x}} = -\left(\frac{\epsilon_{xx} - N_{\parallel}^2}{\epsilon_{xy}} + \frac{\left(\epsilon_{xz} + N_{\parallel}N_{\perp}\right)^2}{\epsilon_{xy}\left(\epsilon_{zz} - N_{\perp}^2\right)}\right)\left(1 - \frac{\left(\epsilon_{xz} + N_{\parallel}N_{\perp}\right)\epsilon_{yz}}{\epsilon_{xy}\left(\epsilon_{zz} - N_{\perp}^2\right)}\right)^{-1} \tag{A.6}$$

$$\frac{E_{1z}}{E_{1x}} = \frac{\epsilon_{yz}}{\epsilon_{zz} - N_{\perp}^2}\frac{E_{1y}}{E_{1x}} - \frac{\epsilon_{xz} + N_{\parallel}N_{\perp}}{\epsilon_{zz} - N_{\perp}^2}. \tag{A.7}$$

A value of E_{1x}, which is arbitrary in the linear regime, must be supplied in order to fully determine $\mathbf{E}_1$. In Chapter 5.2, estimates of the observed low-frequency magnetic field fluctuations can be related to E_{1x} through Faraday's Law.

The current density associated with the linear solution can be computed as

$$\mathbf{J}_1 = -i\omega\epsilon_0\left(\boldsymbol{\epsilon} - \mathbf{1}\right)\cdot\mathbf{E}_1 \tag{A.8}$$

where ϵ_0 is the permittivity of free space and $\mathbf{1}$ is the identity matrix.

Appendix B

Estimating Ion and Electron Temperatures from the THEMIS ESA and SST Instruments

Since particle energies, particularly for the ions, can exceed the energy range of the ESA on THEMIS in the BBF braking region, ESA data must be combined with the higher energy data from the SST to obtain temperature estimates in Chapter 5. To provide estimates of the ion and electron temperatures, two methods are considered. In the first one, the combined ESA and SST omnidirectional differential energy fluxes are fitted assuming the distribution function of the plasma is Maxwellian. The omnidirectional differential energy flux is related to the distribution function such that $j_s \propto v^4 F_s$ where j_s is the omnidirectional differential energy flux for species s, v is the particle velocity, and F_s is the omnidirectional particle distribution function for species s. The functional form of the fit is given by

$$j_s = Ae^2 \exp(-e/T_s) \tag{B.1}$$

where A is a free parameter dependent on the density, temperature, and constants, $e = m_s v^2/2$ is the particle energy, and T_s is the temperature of species s in units of energy.

In the second method, j_s is numerically integrated to obtain the second moment of F_s, which can be related to a "temperature" by

$$T_s \equiv \frac{m_s}{3}\left(\int v^2 F_s v^2 dv\right)\left(\int F_s v^2 dv\right)^{-1} = \frac{2}{3}\left(\int j_s dv\right)\left(\int \frac{j_s}{e} dv\right)^{-1} \tag{B.2}$$

where the relationship between F_s and j_s is used and it is noted that the omnidirectional quantities are already integrated over solid angle.

For the ions, data from 100 eV to 10^6 eV is used for both methods with the lower limit set to reduce the effects of energetic electron contamination in the low energies of the ion sensor [*McFadden et al.*, 2008b]. For the electrons, data from 30 eV to 10^6 eV is used for both methods with the lower limit set to avoid contamination associated with internally produced secondary electrons [*McFadden et al.*, 2008b]. The lowest energy SST channel is known to be unreliable (D. Larson, personal communication, 2014) resulting in an apparent discontinuity between the ESA and SST differential energy fluxes; as a result, this data point is neglected when performing fits and interpolated from the surrounding points when performing numerical integrations.

Figure B.1 shows examples of j_s and fits for the ions (top) and electrons (middle and bottom). The ions are reasonably well described by a Maxwellian distribution function aside from the flattening in j_i due to energetic electron contamination, which in some cases can extend above the imposed 100 eV cutoff. The fitting method tends to be more robust to this contamination and, thus, Maxwellian fits are used to estimate the ion temperatures. The electrons are generally less affected by contamination, as long as energies below 30 eV are removed. On occasion the electrons have significantly non-Maxwellian distributions (see for example, the data points between 30 eV and the peak of j_e in the middle panel of Figure B.1) and, therefore, the numerical integration procedure is used to estimate the electron temperatures. The high energy (above the peak) tails in the electron distributions are a common feature of j_e; however, the points above the peak do not count as much towards the temperature as the lower energy points. The differences between the fitting and numerical integration methods for the ions are about 25% on average (largely associated with unremoved electron contamination in the numerical integration estimate) and for the electrons they are about 40% on average, giving a rough idea of the uncertainty associated with these estimates. Visual examination of the intervals driving up the percent difference for the electrons shows that generally this is associated with the distribution being poorly fit by a Maxwellian and/or by the signature of secondary electrons extending to energies above the 30 eV cutoff for a few points within the intervals.

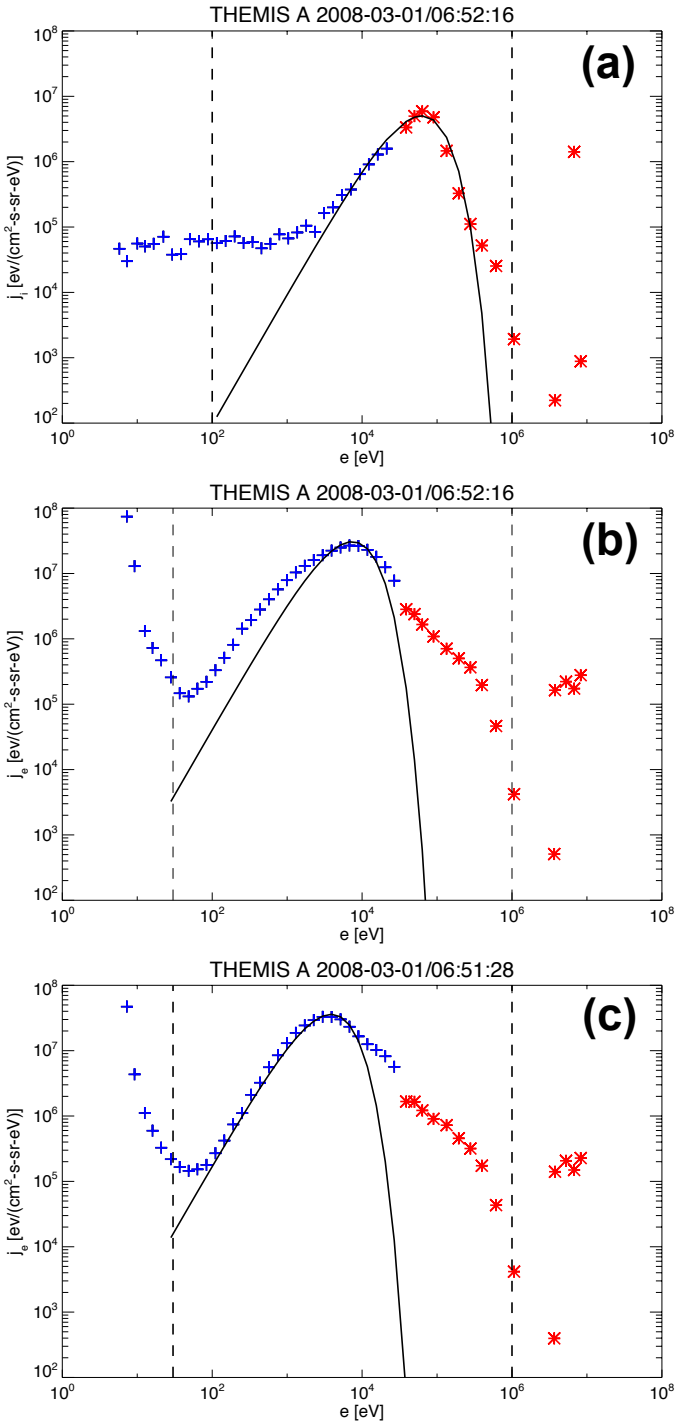

Figure B.1: Example j_s distributions for times selected from the interval in Figure 5.5 as a function of particle energy for (a) an ion distribution, (b) an electron distribution, which is inconsistent with a Maxwellian at low energies, and (c) a different electron distribution, which is consistent with the Maxwellian fit at low energies. Blue "+" are ESA data points and red "*" are SST data points. Vertical dashed lines mark the range of energies used to estimate the temperature either through fitting or numerical integration. The black solid curve shows the fit using the functional form given in Equation B.1. The first SST energy channel, which has a larger uncertainty and is often inconsistent with the rest of the data points has been omitted.